Analysis and Simulation of Macroscopic Defects in $Cu(In,Ga)Se_2$ Photovoltaic Thin Film Modules

Von der Fakultät für Elektrotechnik und Informationstechnik
der Rheinisch-Westfälischen Technischen Hochschule Aachen
zur Erlangung des akademischen Grades eines Doktors der
Ingenieurwissenschaften genehmigte Dissertation

vorgelegt von

Dipl.-Ing.
Boris Misic
aus Stuttgart

Berichter:
Universitätsprofessor Prof. Dr. Uwe Rau
Universitätsprofessor Prof. Dr. Jürgen H. Werner

Tag der mündlichen Prüfung: 20.10.2015

Contents

Summary

The present work deals with production induced defects in CIGS thin film modules which can deteriorate the electrical performance of the module. The motivation of this work is to both find ways how these defects can be diagnosed, e.g. in a quality control in the production site, and to gain a better understanding of the actual defect influence on the voltage and current in the surrounding of the defect. Thus, I investigate the use of electroluminescence and thermography as diagnostic tools to detect and identify common defects occurring in CIGS production.

I begin this work with a study of the CIGS production process and list potential defect origins for relevant production steps. In order to allow an experimental investigation of defects, I intentionally implement them into CIGS photovoltaic modules in a real CIGS production site environment. The defect implementation includes e.g. interrupted P1, P2, and P3 scribing lines for the monolithic series connection, as they can be caused by faulty scribing tools, and changes in the normal CIGS layer structure, as they can be caused by local contamination. Furthermore, I vary the geometry of the implemented defects. I characterise the implemented defects with microscope, electroluminescence (EL), and dark lock-in thermography (DLIT) measurements. EL and DLIT are chosen as they are spatially resolved measurements and therefore allow a comparatively fast investigation of a complete module. In addition to the defect measurements, I implement a software that is based on the principle of network simulation model and allows to model and simulate the implemented defect types in a CIGS module. The software models the CIGS module with a network, that consists of equivalent circuits of a solar cell and resistances, and translates the network into a non-linear system of equations that are solved. Finally, I investigate methods to repair an incomplete insulation of the Mo back contacts of two neighbouring cells.

The measurements on defects yield that P1, P2, and P3 scribing defects have characteristic EL and DLIT patterns. I show that the scribing defects can be reliably identified by these patterns if the length of the scribing line interruptions is sufficiently resolved in the EL and DLIT images. The explanation of the characteristic El and DLIT patterns of scribing defects is facilitated by the simulation software that yields the voltage distribution, which can explain the El images, and the current flow, which can explain the DLIT images.

With regard to the simulation software itself, I present an alternative solving approach for

the non-linear system of equations, that differs from the standard Newton-Raphson procedure and allows a scaling behaviour of the simulation duration with the number of equations close to the linear optimum.

Moreover, EL measurements of point defects with implemented abnormal layer sequences show that the i-ZnO/CdS buffer layer combination has a shunt mitigating effect. From comparison of various point defect types I conclude that the CdS has during chemical bath deposition a surface smoothing effect and fills up cavities and holes in the CIGS absorber. I suggest that this surface smoothing allows the sputtered i-ZnO to form a uniform and unbroken layer, and thus prevent shunting contact between the front and back electrode. In contrast, when I remove the CdS layer locally, the point defects show strong shunting in EL and DLIT measurements if the defect implementation has caused sharp edges or flakes at the Mo or CIGS layer.

Furthermore, Cu-rich debris is a potential contamination during CIGS co-evaporation, where it can fall down from the Cu evaporation source onto the module. For Cu-rich debris I find that its position within the cell determines whether it can be reliably identified by EL and DLIT measurements. Cu-rich debris on the P1 line evokes among all defects a unique EL brightness pattern, which I explain by the simulation software as an overlay of a P1 defect with two shunting defects, one located in each of the neighbouring cells.

Eventually, I develop two repair processes for defective Mo back contact insulation (P1 line). The first process is a thermal repair which uses thermally induced mechanical stress to create insulating fractures at the defect position. The second process is an electrical repair, where an applied current melts and evaporates remaining conductive Mo at the defect position, which finally results in an insulation, too.

To draw a conclusion, the present work contributes to the understanding and diagnostics of production induced defects in $Cu(In,Ga)Se_2$ photovoltaic thin film modules, and in case of the P1 scribing defects even shows ways how they can be repaired.

Zusammenfassung

Die vorliegende Arbeit behandelt herstellungsbedingte Defekte in CIGS Dünnschichtmodulen, welche die elektrische Leistung des Moduls verschlechtern können. Die Motivation dieser Arbeit ist es, sowohl Wege zu finden, wie diese Defekte diagnostiziert werden können, beispielsweise in Form einer Qualitätskontrolle in der Produktionstätte, als auch ein besseres Verständnis des tatsächlichen Defekteinflusses auf Ströme und Spannungen in der Defektumgebung zu erlangen.

Ich beginne mit einer Untersuchung des CIGS Herstellungsverfahrens und liste mögliche Defektursachen für die relevanten Produktionsschritte auf. Um eine experimentelle Untersuchung von Fehlern zu ermöglichen, bringe ich diese in der Umgebung einer realen CIGS Produktionsstätte in CIGS Photovoltaikmodule gezielt ein. Das gezielte Einbringen der Fehler beinhaltet beispielsweise unterbrochene P1-, P2- und P3-Strukturierungslinien, wie sie durch fehlerhafte Strukturierungsanlagen entstehen können, ebenso wie Veränderungen des CIGS Schichtenaufbaus, wie sie durch lokale Verschmutzungen verursacht werden können. Darüber hinaus verändere ich die Geometrie der eingebrachten Fehler. Ich charakterisiere die gezielt eingebrachten Defekte anhand von Mikroskopmessungen, Elektrolumineszenzmessungen (EL) und phasenempfindlichen Thermographiemessungen (DLIT). Die Messverfahren EL und DLIT wähle ich, weil sie ortsaufgelöste Messungen sind und daher eine vergleichsweise schnelle Untersuchung eines vollständigen Moduls erlauben. Zusätzlich zu den Messungen an den Defekten implementiere ich eine Software, die auf dem Prinzip des Netzwerksimulationsmodells beruht, und die es ermöglicht, die gezielt eingebauten Defekte in CIGS Photovoltaikmodulen zu modellieren und zu simulieren. Die Software modelliert das CIGS Photovoltaikmodul mit einem Netzwerk, welches aus Ersatzschaltbildern einer Solarzelle und Widerständen besteht, und überführt das Netzwerk in ein nichtlineares Gleichungssystem um dieses dann zu lösen. Abschließend untersuche ich Methoden zur Reparatur einer unvollständigen Isolierung zwischen den Molybdänrückkontakten zweier benachbarter Zellen.

Die Messungen an Defekten ergeben, dass P1-, P2- und P3-Strukturierungsfehler charakteristische EL and DLIT Muster hervorrufen. Ich weise nach, dass Strukturierungsfehler anhand dieser Muster verlässlich identifiziert werden können, sofern die Länge der Strukturierungslinienunterbrechungen in den EL- und DLIT-Bildern ausreichend aufgelöst wird.

Die Erklärung dieser EL- und DLIT-Muster der Strukturierungsfehler wird durch die Simulationssoftware erleichtert, welche die Spannungsverteilung ermittelt, die wiederum das EL-Bild zu erklären vermag, und welche den Stromfluss ermittelt, welcher wiederum das DLIT-Bild zu erklären vermag.

Hinsichtlich des Simulationsprogrammes stelle ich einen alternativen Lösungsansatz vor, welcher vom standardisierten Newton-Raphson Verfahren abweicht und ein Skalieren der Simulationsdauer mit der Anzahl der Gleichungen nahe des linearen Optimums erlaubt.

Darüber hinaus zeigen EL-Messungen von punktförmigen Defekten mit unnatürlicher CIGS-Schichtenfolge, dass die Pufferschichtkombination bestehend aus i-ZnO und CdS einen fehlermildernden Effekt hat. Anhand des Vergleichs verschiedener Punktdefekte ziehe ich den Schluss, dass das CdS während der chemischen Badabscheidung eine oberflächenglättende Eigenschaft hat und Hohlräume wie auch Löcher im CIGS-Absorber auffüllt. Ich schlage als Erklärung vor, dass diese Oberflächenglättung es dem i-ZnO ermöglicht, eine gleichmäßige und ununterbrochene Schicht auszubilden, und somit einen Kurzschlusskontakt zwischen Front- und Rückelektrode vermeidet. Im Gegensatz dazu zeigen die punktförmigen Defekte, wenn ich die CdS-Schicht lokal entferne, ein starkes Kurzschlussverhalten in EL- und DLIT-Bildern, wenn durch den gezielt eingebauten Defekt scharfe Kanten oder spanartige Abblätterungen am Mo oder CIGS hervorgerufen worden sind.

Zudem stellen kupferreiche Partikel, wie sie während der Abscheidung des CIGS von den Kupferverdampfungsquellen herab auf das Modul fallen können, eine potentielle Verschmutzung dar. In Bezug auf diese kupferreichen Partikel finde ich heraus, dass ihre Lage in der Zelle darüber entscheidet, ob sie in EL- und DLIT-Messungen verlässlich identifiziert werden können. Ein kupferreicher Partikel auf ein einer P1 Strukturierungslinie ruft ein einzigartiges Fehlerbild in der EL hervor, welches ich mithilfe der Simulationssoftware als eine Überlagerung eines P1 Strukturierungsfehlers mit zwei zu Kurzschlüssen führenden Punktdefekten, von denen jeweils einer in den benachbarten Zellen liegt, erkläre.

Abschließend entwickele ich zwei Reparaturverfahren für die fehlerhafte Isolierung von Molybdänrückkontakten (durch die P1-Linie). Das erste Reparaturverfahren ist thermisch bedingt und verwendet thermisch induzierte, mechanische Spannung um isolierende Risse an der Defektstelle zu erzeugen. Das zweite Reparaturverfahren ist elektrisch bedingt und beruht darauf, dass an der Defektstelle ein angelegter Strom das leitfähige Molybdän aufschmilzt und verdampft.

Zusammenfassend kann man sagen, dass die vorliegende Arbeit einen Beitrag dazu leistet, produktionsbedingte Fehler in Photovoltaikdünnschichtmodulen auf Basis von $Cu(In,Ga)Se_2$ zu verstehen, sie zu detektieren und identifizieren, und sie im Falle von P1 Strukturierungsfehlern sogar zu reparieren.

Chapter 1

Introduction

The first silicon-based p-n junction solar cell, which was developed in 1954 at the Bell Telephone Laboratories by Chapin and his colleagues Fuller and Pearson [1], marked the starting point of a world wide photovoltaic research activity. Since then research and development have achieved astonishing progress in terms of device efficiency, durability, and cost reduction, and made photovoltaics become a technology that reliably provides clean and renewable energy at the beginning of the 21st century. The intensive research in photovoltaics has lead to a diversity of used materials and working principles [2]. The material compound which consists of copper (Cu), indium (In), gallium (Ga), and selenide (Se), and forms the CIGS absorber, is among those materials. CIGS solar cells have competitive record efficiencies above 20 % on both glass substrates [3, 4], and flexible substrates [5], which has lead to CIGS large scale production in recent years.

In analogy to other photovoltaic technologies, CIGS module efficiencies are lower than cell efficiencies. In CIGS this is on the one hand caused by the currently used monolithic series connection of the cells with its cell connection and electrode insulation at each cell transition, which reduces the active solar cell area in comparison to a single cell measurement. Furthermore, it is more difficult to reach a homogeneous layer deposition on a large module scale than on a small laboratory cell scale. Usually, many laboratory cells of 1 cm x 1 cm size are produced and the best is picked in order to achieve a record. This is more difficult in case of modules with cells of 0.4 cm x 120 cm, where there are cell areas with better and worse electrical performance, and finally the latter deteriorates the total cell performance. Additionally, defects can affect the module efficiency. Defects can originate e.g. from contamination that occurs in rough production site environments, or faulty production equipment. One example for faulty production equipment is if the mechanical or laser scribing for the insulation of the front and back electrodes at the cell transitions is insufficient. In that case the neighbouring cells can be shunted. In order to minimise these production induced defects, it is essential to monitor both the parameters of the production equipment and the module quality. In a good quality control there are diagnostic tools that reliably

detect and identify defects so that the responsible production equipment and processes can be re-adjusted and the defect source can be eliminated.

In the present work I investigate the use of electroluminescence and thermography as diagnostic tools to detect and identify various common production induced defects. For the testing and evaluation of the defect diagnostics I need a comprehensive set of defects, which is why I deliberately implement defects that can theoretically occur during CIGS module production. These intentionally implemented defects include interruptions of each of the scribing lines that are required for the monolithic series connection. Furthermore, these intentionally implemented defects include abnormalities in the CIGS layer structure, as they for instance occur when one layer (or a combination of layers) is locally missing or has been damaged. I investigate all these defects with spatially resolved electroluminescence and thermography measurements, and search for a correlation between a defect type and its appearance in the measured images. In many cases either electroluminescence or thermography, or the combination of them respectively, yields a characteristic pattern that allows a reliable identification of the defect type. Owing the nature of a defect, that is here an abnormality of either the normal monolithic series connection or the normal layer structure within the cell, the observed characteristic defect patterns are caused by abnormal current flows and voltage distributions, which in some cases makes it impossible to intuitively explain the occurring defect patterns. To overcome this issue and gain a better understanding of the resulting defect appearance in the measurements, I implement a software that is based on the principle of the network simulation model [6]. This software allows to model and simulate the current flow, voltage distribution, electroluminescence image, and thermography image of a module containing defects, and therefore can explain the observed characteristic defect patterns in the measured images.

After a short introduction into the structure and working principle of both a single CIGS cell and a CIGS module in Chapter 2, I present in Chapter 3 an overview of the CIGS production process and discuss potential defect origins.

The two measurement techniques electroluminescence and thermography, which I apply for the defect diagnostics, are introduced in Chapter 4. For each measurement technique I show the physical fundamentals, the general measurement setup, and the measurement practice i.e. the measurement parameters and sample preparation.

Chapter 5 introduces the software which I have implemented in this thesis and which is based on the principle of the network simulation model. Beginning with an introduction into the structure of the network, I show how its single elements are calculated and how I vary the network density in dependence of the defect position. Special attention is paid to the setting of the network's non-linear system of equations, as I present an alternative solving approach in contrast to the standard Newton-Raphson procedure. Eventually, I verify my simulation by comparing it with the tool developed in [6].

I describe the implementation of both defects in scribing lines and in the CIGS layer sequence in Chapter 6. The quantitative EL analysis of the defective CIGS layer sequence sheds light on the role of the i-ZnO/CdS buffer combination. In contrast, the defective scribing lines are measured with both EL and DLIT, and additionally need to be modelled and simulated in the network simulation model in order to explain the measurements.

Based on the knowledge of the actual defect mechanism, which is gained in Chapter 6, I show the defect diagnostics consisting of detection and identification of defects in Chapter 7. In contrast to the measurements in Chapter 6, in Chapter 7 I additionally take into account the influence of the measurement resolution, defect geometry, defect position, and interaction between defects. Most of the defects can be identified either by EL or DLIT, or the combination of them.

Finally, I dedicate Chapter 8 to the repair of the incomplete insulation between the Mo back electrodes of two neighbouring cells. First, I present an inherent thermal repair that I have discovered to occur during CIGS co-evaporation. Furthermore, I show how this thermal repair can be applied intentionally in order to optimise the repair process. Second, I show an electrical repair that I have developed, and which is equally efficient as the thermal repair but additionally provides information like defect position and defect number per defective cell insulation within a fully automatised setup.

Chapter 2

CIGS Cells and Modules

"The purpose of this chapter is to introduce briefly the working principle of a CIGS solar cell and module."

2.1 Introduction

In the following, both the CIGS cell and module structure are introduced. With regard to the CIGS cell working principle, the role of each layer is discussed in Chapter 2.2. The CIGS cell's equivalent circuit and the correspondent current-voltage curve is shown. It is explained briefly how the components of the equivalent circuit can be measured in experiments. Similarly, the CIGS module is introduced in Chapter 2.3 with its equivalent circuit and current-voltage curve. The knowledge of these fundamentals is necessary in order to understand the network simulation model (NSM) in Chapter 5 and the experiments on defects in Chapters 6 and 7.

2.2 CIGS Cells

2.2.1 Structure

Figure 2.1 (a) depicts a CIGS solar cell with its (i) soda lime glass substrate, (ii) molybdenum (Mo) back contact, (iii) cupper-indium-gallium-diselenide (CIGS) absorber, (iv) cadmium-sulfide (CdS) and (v) intrinsic zinc oxide (i-ZnO) as buffer layers, (vi) aluminium doped zinc oxide (ZnO:Al) front contact, (vii) sealing polymer foil and (viii) the soda lime front glass. The role of each layer is briefly introduced in the following with regard to the solar cell working principle. In contrast, the role of each layer with regard to the manufacturing process is introduced in Chapter 3.

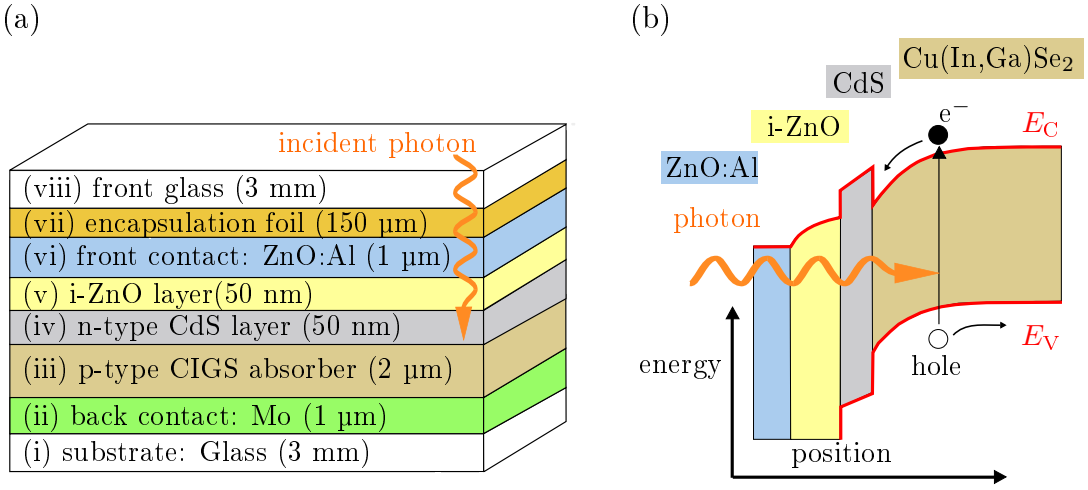

Figure 2.1: *Schematic CIGS cell structure and chalcogenide absorber structure. (a) The CIGS cell consists of 8 components: The soda lime glass substrate, the Mo back contact, the p-type CIGS absorber, the n-type CdS layer, the i-ZnO layer, the ZnO:Al front contact, the encapsulation foil and the front glass. The incident light enters the cell through the front glass. (b) Band diagram of a CIGS cell. In the p-type CIGS absorber the incident photon generates an electron-hole pair. The electron is excited from the valence band E_V to the conduction band E_C.*

(i) Substrate:

The substrate is formed by 3 mm thick soda lime glass. With a Young's modulus of $E_{glass} = 72$ GPa [7] the glass substrate allows the CIGS module to withstand mechanical stress in an outdoor environment (hail, snow).

(ii) Back Contact:

The back contact is formed by 1 µm thick molybdenum (Mo). The Mo back contact is highly conductive with a resistivity of $\rho = 54$ x 10^{-9} Ωm in order to reduce voltage loss within the cell and module, respectively. Moreover, Mo reflects 60 % of the incident light within the wavelength range of $\lambda = 500 - 1000$ nm [8] which increases the light path through the CIGS absorber and therefore increases the light absorption [8, 9].

(iii) p-type Absorber:

The p-type absorber is formed by a 2 µm thick $Cu(In_{1-x}Ga_x)Se_2$ composition with $x \approx 0.3$. In the absorber the absorption of incident photons creates electron-hole pairs. The electron is excited from the valence band into the conduction band and leaves a hole behind as shown in (b). CIGS is a direct bang gap semiconductor. Thus, there is neither phonon emission nor phonon absorption required for the excitation of the electron to the conduction band [2]. The CIGS absorber has typically a band gap of $E_{G,\,CIGS} \approx 1.15$ eV for $x \approx 0.3$ [10] which is the parameter for cells with highest efficiencies [11]. The band gap can be adjusted by the Ga/(In + Ga) ratio in the range of $E_{G,\,CIGS} = 1.04...1.67$ eV [10, 12, 13], where it is mainly the conduction band E_C that is increased [14].

(iv) n-type CdS Layer:

The n-type of the heterojunction is formed by a 50 nm thick cadmium sulphide (CdS) layer.

The CdS has a band gap of $E_{\mathrm{G,\,CdS}} \approx 2.42$ eV [15] and forms a heterojunction [16–18] with the CIGS absorber [19–21].

(v) i-ZnO Layer:

The intrinsic zinc oxide (i-ZnO) layer on the CdS layer has a thickness of 50 nm and a resistivity of $\rho = 2.5$ x 10^6 Ωm [22]. It prevents electrical inhomogeneities from deteriorating the solar cell performance [21, 23], leads to a higher reproducibility in the CIGS production [24] and increases the cell's resistivity to damp-heat stress [25].

(vi) Front Contact:

The front contact is formed by a 1 µm thick aluminium doped zinc oxide (ZnO:Al) window layer. With its Al dopant, the ZnO:Al is electrically conductive ($\rho = 9$ x 10^{-6} Ωm) and at the same time highly transmissive in the interesting wavelength region up to about 1100 nm [11].

(vii) Encapsulation Foil:

An ethylene vinyl-acetate (EVA) foil is used to encapsulate the CIGS cell and module, respectively. The EVA foil improves the mechanical stability, acts as electrical insulation, protects the module against corrosion as a moisture barrier, and prevents contamination from entering the module [26–28].

(viii) Front Glass:

The front glass provides the same mechanical stability as the substrate glass does. It is light-transmissive and allows the incident light to enter the CIGS cell / module.

2.2.2 Equivalent Circuit

Two possible equivalent circuits of a CIGS cell, as shown in Figure 2.1, are depicted in Figure 2.2 [11].

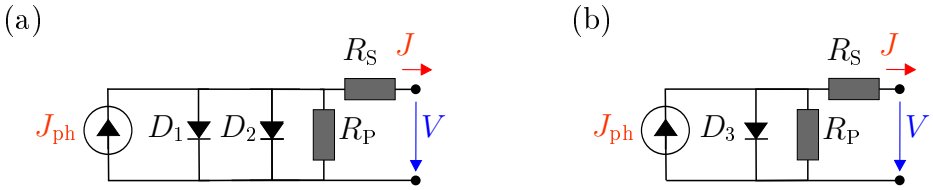

Figure 2.2: *Equivalent circuits of a CIGS solar cell. (a) Two-diode model with series resistance R_S and parallel resistance R_P. (b) Simplified one-diode model.*

The conversion of photons into electric charge carriers within the CIGS solar cell is represented by the current source and its photo-current density J_{ph} in both circuits (a) and (b). Generally, for a good solar cell performance, the highest possible J_{ph} is desired, which is given by

$$J_{\mathrm{ph}} = q \int_{\lambda} \phi(\lambda)\,[1 - R(\lambda)]\,\mathrm{IQE}(\lambda) d\lambda, \tag{2.1}$$

where q is the electron charge, $\phi(\lambda)$ is the wavelength dependent photon flux per time and area, $R(\lambda)$ is the wavelength dependent reflection, and IQE(λ) is the wavelength dependent internal quantum efficiency defined as

$$\mathrm{IQE}(\lambda) = \frac{\text{charge carriers collected at the cell's contacts}}{\text{photons absorbed in the solar cell}}. \tag{2.2}$$

Figure 2.2 (a) shows the ideal two-diode model of a solar cell without parasitic resistors. It consists of two diodes D_1 and D_2 and yields the following term for the solar cell's J-V curve

$$J = J_{\mathrm{ph}} - J_{01}\left\{exp\left(\frac{qV}{n_{\mathrm{id},1}k_{\mathrm{B}}T}\right) - 1\right\} - J_{02}\left\{exp\left(\frac{qV}{n_{\mathrm{id},2}k_{\mathrm{B}}T}\right) - 1\right\} - \frac{V + JR_{\mathrm{S}}}{R_{\mathrm{P}}}, \tag{2.3}$$

where J_{01} and J_{02} respectively are the dark saturation current densities, and $n_{\mathrm{id},1}$ and $n_{\mathrm{id},2}$ respectively are the diode ideality factors of the two diodes, k_{B} is the Boltzmann constant, and T is the temperature. The two-diode model takes into account that the diode ideality factor n_{id} is voltage dependent. For high junction voltages, the recombination in the solar cell is dominated by the quasi-neutral regions and the ideality factor comes close to $n_{\mathrm{id},1} = 1$, which is represented by D_1. In contrast, for low junction voltages, the recombination in the solar cell is dominated by the space-charge region and the ideality factor comes close to $n_{\mathrm{id},2} = 2$, which is represented by D_2. Consequently, J_{01} represents the dark saturation current density due to the recombination in the quasi-neutral regions, and J_{02} represents the dark saturation current density due to the recombination in the space-charge region of the p-n-junction [2, 29].

Nonetheless, for a good solar cell with a small J_{02} it is a common and sound assumption to neglect diode D_2 [2]. The resulting equivalent circuit is shown in Figure 2.2 (b) where only one diode, namely D_3 is used, and the correspondent J-V curve can be described by

$$J = J_{\mathrm{ph}} - J_{03}\left\{exp\left(\frac{qV}{n_{\mathrm{id},3}k_{\mathrm{B}}T}\right) - 1\right\} - \frac{V + JR_{\mathrm{S}}}{R_{\mathrm{P}}}. \tag{2.4}$$

In contrast to the two-diode model, the one-diode model requires to apply an ideality factor $n_{\mathrm{id},3}$ between 1 and 2. Thus, in order to describe a CIGS cell correctly, the ideality factor needs to be determined experimentally. It is shown in [2] how the saturation current density J_{03}, the ideality factor $n_{\mathrm{id},3}$, the series resistance R_{S}, and the parallel resistance R_{P} can be extracted from the $\log(J_{\mathrm{SC}})$ plottet versus V_{OC} (where both the short circuit current density J_{SC} and the open circuit voltage V_{OC} are measured for varying illumination intensities). The resistor R_{P} represents detrimental shunt paths in the solar cell that bypass the diode. For a good solar cell performance a high R_{P} is desired. The influence of a reduced R_{P} on the solar cell performance is discussed in detail in Chapters 6 and 7. The resistor R_{S} represents the series resistance in the solar cell. For a vertical current flow in the CIGS cell, the ZnO:Al contact, i-ZnO buffer layer, CdS buffer layer, CIGS absorber, Mo contact, as well as the

interfaces between each of the five layers contribute to R_S. Generally, a low R_S is desired in order to reduce the parasitic voltage loss. Figure 2.3 shows a measured current-voltage curve under illumination (red, solid) and in the dark (blue, dashed) and the power (orange, dotted) for the illuminated case.

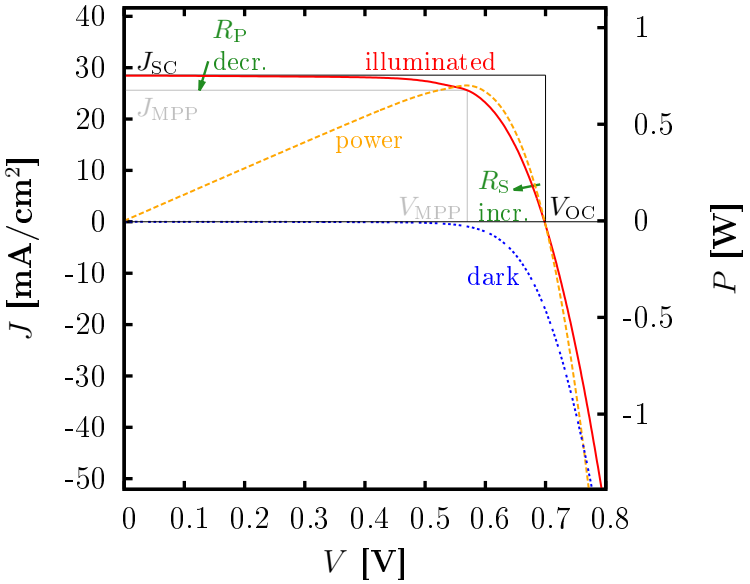

Figure 2.3: *Illuminated and dark current-voltage curve of a CIGS cell. Current density J on cell area $A_{cell} = 120\ cm \cdot 0.4\ cm = 48\ cm^2$ is shown as function of cell voltage V. The dark curve is approximately shifted by the short circuit current density J_{SC}. The orange, dashed curve shows the power $P = UJA_{cell}$ for the illuminated case. Current density J_{MPP} and voltage V_{MPP} in the maximum power point span the gray rectangle. Short circuit current density J_{SC} and open circuit voltage V_{OC} span the black rectangle. The fill factor FF is the ratio of gray to black rectangle.*

For the illuminated (red, solid) curve, the short circuit current density J_{SC} at $V = 0$ V and the open circuit voltage V_{OC} at $J = 0$ mA/cm^2 are labelled. For an ideal solar cell ($R_P \to \infty$) one can resolve Eq. (2.4) for V_{OC} by

$$V_{OC} = \frac{k_B T}{q} \ln\left(\frac{J_{SC} + J_{03}}{J_{03}}\right). \tag{2.5}$$

At the maximum power point (MPP), there is $P_{MPP} = V_{MPP} J_{MPP} A_{cell}$. Obviously, the gray rectangle cannot exceed the black one because $V_{MPP} < V_{OC}$ and $J_{MPP} < J_{SC}$ is always valid (in both the short circuit and the open circuit there is $P = 0$ W). The "squareness" of the J-V curve can be regarded as figure of merit as the resulting power P will increase the closer the gray rectangle comes to the black one. The fill factor FF quantifies this figure of merit by

$$FF = \frac{V_{MPP} J_{MPP}}{V_{OC} J_{SC}} = \frac{P_{MPP}}{V_{OC} J_{SC}}. \tag{2.6}$$

Figure 2.3 shows that a realistic $R_S \neq 0$ and $R_P \neq \infty$ deteriorate the fill factor FF. An increasing R_S causes a decreasing slope (abs. value) around V_{OC}, and a decreasing R_P causes an increasing slope (abs. value) around J_{SC} (both is indicated by the green arrows). The most important figure of merit is the cell's conversion efficiency η, given by

$$\eta = \frac{P_{MPP}}{P_{opt}} = \frac{FF\ V_{OC}\ J_{SC}}{P_{opt}}, \tag{2.7}$$

where P_{opt} is the incident light power.

2.3 CIGS Modules

In a CIGS module there are multiple CIGS solar cells connected in a monolithic series connection. In Figure 2.4 the combined schematic layer structure and equivalent circuit of a CIGS thin film module, consisting of three cells, is contained. The ZnO:Al front contact of each cell is connected with the Mo back contact of the adjacent cell. Furthermore, the front and back contacts of neighbouring cells need to be insulated in order to prevent short circuits between the cells. Insulation of the Mo back contacts of neighbouring cells is called P1 scribing (Chapter 3.2.4) and is performed after the Mo sputtering (Chapter 3.2.3). Here the letter "P" stands for process and the index "1" stands for the first performed scribing process. The P2 scribing is needed to create a channel through which the ZnO:Al front contact can be deposited onto the Mo back contact. The P3 scribing is needed to insulate the ZnO:Al front contacts of neighbouring cells. The positions of the P1, P2 and P3 scribing lines are shown in Figure 2.4.

The monolithic series connection requires to extend the equivalent circuit of a solar cell by the three resistances R_{Mo}, $R_{ZnO:Al}$ and R_C, as shown in Figure 2.4. In contrast to the CIGS cell, where for the sake of simplicity a solely vertical current flow can be assumed, the module current flows from left to right in Figure 2.4 through both the front and back contact of each cell. The module current J_{module} is schematically shown in the right cell of Figure 2.4 with the red arrows. Thus, the resistances R_{Mo} and $R_{ZnO:Al}$, as introduced by the front and back contacts, are regarded within the equivalent circuit of the CIGS thin film module. R_C represents the contact resistance between the front and back contact. In analogy to Eq. (2.4), the J-V curve of a CIGS module can be described by

$$J_{module} = J_{ph} - J_0 \left\{ exp\left(\frac{qV_M}{n_{id}k_BT}\right) - 1 \right\} - \frac{V_M + JR_S^*}{R_P^*}. \tag{2.8}$$

In contrast to Eq. (2.4), here the series resistance R_S^* additionally takes into account the sheet resistances of the front and back contact layers ($R_{ZnO:Al}$ and R_{Mo}) due to lateral current flow through the contacts, the contact resistances R_C and the connection resistance

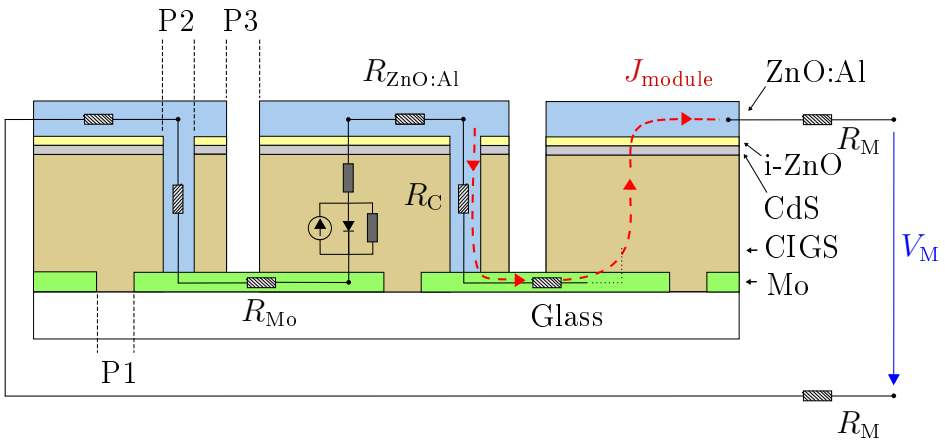

Figure 2.4: *Monolithic series connection in CIGS thin film modules. The insulation of cells is done by a P1 (Mo back contact) and P3 (ZnO:Al front contact) scribing. For contacting the front contact and back contact, a P2 (CIGS absorber and buffer layers) scribing is performed. For an illuminated module, the resulting current I_{module} is shown. The contact resistance between front and back contact is regarded by R_C. The sheet resistances of the front and back contact layers are taken into account by $R_{ZnO:Al}$ and R_{Mo}. The connection between active solar cell layers and external module junction box is represented by R_M. V_M is the external module voltage.*

R_{M}. The parallel resistance R_{P}^{*} additionally takes into account insufficient insulation by the P1 and P3 lines, insufficient laser edge insulation, and defects within the cells, of course. Furthermore, the module voltage V_{M} is now given by the sum of i single cell output voltages by

$$V_{\mathrm{M}} = \sum_{i=1}^{n} V_{\mathrm{i}}, \tag{2.9}$$

where n is the number of cells in the module.

Chapter 3

Origins of CIGS Defects

"The purpose of this chapter is to introduce the defects that I investigate within this thesis with regard to their origin in the CIGS production."

3.1 Introduction

The key topic of this thesis is the detection and identification of defects in CIGS thin film modules. It is essential to define the field of interest in a first step as the general term *defects* spans a wide range. In this thesis I explicitly deal with defects that are introduced by realistic and imperfect mass production equipment. Thus, most of the defects that are investigated within this thesis can be avoided on a laboratory scale - which is the case when it comes to world record efficiency CIGS solar cells [3]. However, the existence of the investigated defects is mainly owed to the circumstance that in mass production the criterion of solar cell quality is competing with the criterion of profitability. The competition of these two criteria eventually leads to a trade-off that affects any photovoltaic large scale production site. For instance, due to cost reasons there is no clean room environment in a CIGS production site which introduces many pollution related defects.

Because mass production is the background of the investigated defects, in this Chapter the defects are introduced in the order of the manufacturing processes which evoke them. I label the defects which I investigate by identification numbers from *D-1* to *D-6*. Furthermore, I name variations of defects. This is because defects can occur in multiple variations, e.g. a contamination on the glass, which has the ID *Mo-01*, can cause a hole only in the Mo back contact layer or in any of the following layers, too (as is shown in Chapter 3.2.3). Hence, five variations of *D-1* may exist which is why I name them from *Mo-01* to *Mo-05*.

Table 3.1 provides an overview of all defects and their variations which are investigated in this work. The first column presents the manufacturing processes in which the defects occur. The second column shows the defect IDs that I use in this work to refer to the defects.

Process	ID	Defect	Origin(s)	Variations	Details	Chapter
Mo sputtering	***D-1***	Holes in Mo and following layers	Contamination on glass & Mo fracture due to insufficient adhesion	Mo-01 Mo-02 Mo-03 Mo-04 Mo-05	Introduction	3.2.3
					Quantitative EL Analysis	6.2.4
					Detection & Identification	7.5
P1 scribing	***D-2***	P1 interruption	Tilted or polluted laser setup & damaged or polluted glass		Introduction	3.2.4
					Simulation	6.3.4.1
					Detection & Identification	7.2
CIGS evaporation	***D-3***	Cu-rich shunt path	Debris of Cu evaporation source		Introduction	3.2.6
					Simulation	7.6
					Detection & Identification	7.6
	D-4	Holes in CIGS and following layers	Contamination on Mo	CIGS-06 CIGS-07 CIGS-08 CIGS-09	Introduction	3.2.6
					Quantitative EL Analysis	6.2.4
					Detection & Identification	7.5
P2 scribing	***D-5***	P2 line interruption	Mechanical wear of the graver		Introduction	3.2.9
					Detection & identification	7.3
P3 scribing	***D-6***	P3 interruption	Mechanical wear of the graver		Introduction	3.2.11
					Simulation	6.3.4.2
					Detection & identification	7.4

Table 3.1: *Investigated defects. 1^{st} column shows affected processes, 2^{nd} column presents the used defect ID in this work, 3^{rd} column contains the defect descriptions, 4^{th} column names potential defect origins, 5^{th} column lists possible variations, 6^{th} and 7^{th} list the chapters that contain introductions, measurements or simulations of the correspondent defects in this work.*

The third column contains a short description of the defect itself. The fourth column names possible defect origins. The fifth column lists variations of the defects, here only for the point defects. The sixth and seventh column list the chapters that contain introductions, measurements or simulations of the correspondent defects in this work. Throughout this thesis Table 3.1 can be used for orientation.

3.2 CIGS Thin Film Module Production

In this chapter each production step which is needed for creating the monolithic series connection, as shown in Figure 2.4, is briefly introduced. Whenever it is possible, defects that can typically occur within the shown production steps are introduced. If it is one of the defects that I have investigated within this thesis then I mention its ID and point to the correspondent Chapter where it is discussed.

3.2.1 Soda Lime Glass Production

The production of the substrate glass and the window glass is not integral part of the CIGS production site, at least not nowadays. Defects occurring during glass production are typically impurities like bubbles in the glass or scratches as result of damages. The consequences mainly affect the P1 laser scribing where the laser beam must pass the substrate glass. Incomplete P1 scribing as a result of glass impurities is discussed in Chapter 3.2.4

3.2.2 Glass Washing

Cleaning of the glass substrate before Mo deposition onto the soda-lime glass is generally assumed to be necessary for avoiding defects [30–33]. The cleaning removes contaminations that can cause holes within the Mo and following layers. This scenario is introduced in Chapter 3.2.3 as defect ***D-1*** in detail. Furthermore, contaminations can lead to faulty P1 scribing which is introduced in Chapter 3.2.4 and labelled as ***D-2***. In this thesis the glass has been washed with demineralised water and lint-free brushes. There are alternative cleaning methods, e.g. consisting of multiple cleaning steps and even pre-sputtering processes, which have been presented in [34, 35].

3.2.3 Molybdenum Sputtering

The Mo back contact is usually deposited on soda lime glass using direct current (DC) magnetron sputtering with a metal Mo target in an argon (Ar) gas environment [8, 34, 36, 37]. Usually, the Mo is deposited as a bilayer [11, 34, 38, 39] with each layer fulfilling a different requirement: The first layer needs to provide good adhesion to the glass substrate which is achieved with an Ar pressure of approximately 13 mTorr [34]. The second layer is deposited onto the first layer with a lower Ar pressure of about 3 mTorr [34] which leads to a low resistivity of about $\rho = 54 \text{ x } 10^{-9}$ Ωm at a thickness of 900 nm of the second layer. In contrast, the first layer has a resistivity that is about ten times higher. As the first layer is only needed for good adhesion to the glass it is made only 100 nm thick.

The different Ar pressures during Mo sputtering cause different film stresses within the Mo. As shown in Figure 3.1 (a), the film stress within the Mo changes from tensile to compressive for falling pressures at about 8 mTorr. The change in Mo film stress is a potential defect origin for the P1 laser scribing process as it makes the minimum required laser peak fluence $F_{\text{Peak, min}}$ (laser spot energy density in Joule/cm^2 [40]) increase significantly by 20 % as shown in Figure 3.1 (b) [41]. The P1 scribing must remove both Mo layers. In order to reduce loss of active solar cell area the P1 line is scribed as thin as necessary for sufficient insulation of two neighbouring Mo back contacts [23] (current P1 thicknesses are about 50 µm [42]). For obtaining a thin P1 line the smallest required laser peak fluence $F_{\text{Peak,min}}$ is applied. If due to fluctuations in the Mo sputtering process the required laser peak fluence is higher than the applied one, then the P1 laser scribing can be incomplete. P1 defects and further potential defect origins are discussed more detailed in Chapter 3.2.4.

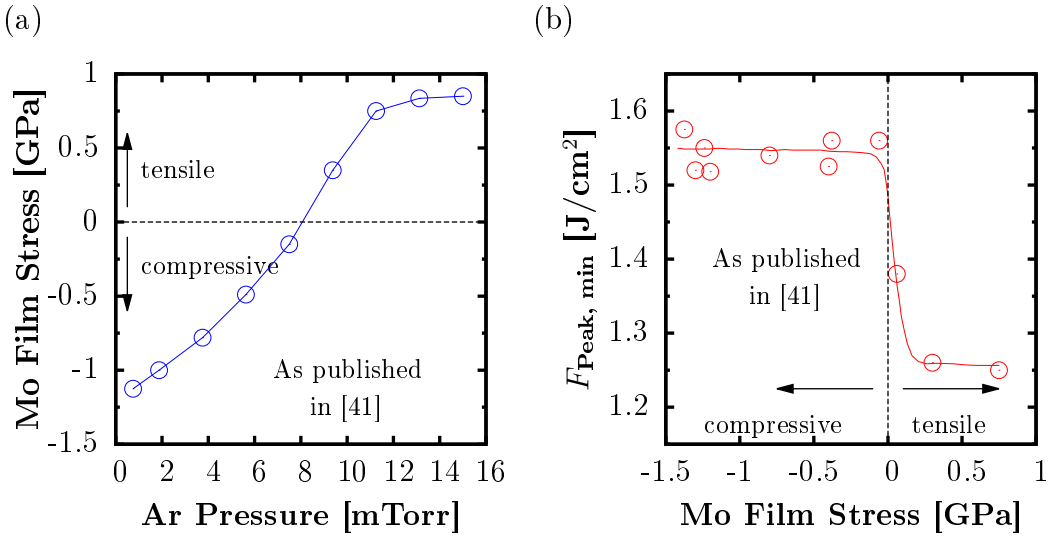

Figure 3.1: *Mo film stress as origin of P1 defects. (a) Mo film stress changes from tensile to compressive for falling pressures at about 8 mTorr. (b) Minimum required laser peak fluence $F_{Peak,\ min}$ increases significantly at change from tensile to compressive stress. An abrupt change in $F_{Peak,\ min}$ can lead to incomplete P1 scribing lines.*

D-1: Holes in Mo and following layers can be caused by contamination on the glass substrate. Contaminations on the glass, as a result of insufficient glass washing, can cause holes both in the sputtered Mo layer and in the following layers which is shown in Figure 3.2 schematically. In (a) a defect free layer sequence is given as a reference. In (b) a contamination is schematically depicted which can prevent a proper Mo sputtering. The contamination is exemplified by a globular defect with a diameter of 10 µm (height of the Mo layer is about 1 µm). Images (b) - (f) just give a schematic view of the possible defect mechanism as the exact shape and size of the defect can strongly vary. If the contamination in (b) falls off or is washed off before the CIGS co-evaporation, a hole only within the Mo layer can remain. I experimentally investigate the situation shown in (b) in Chapter 6.2 and name this case of *D-1* as ***Mo-01***.

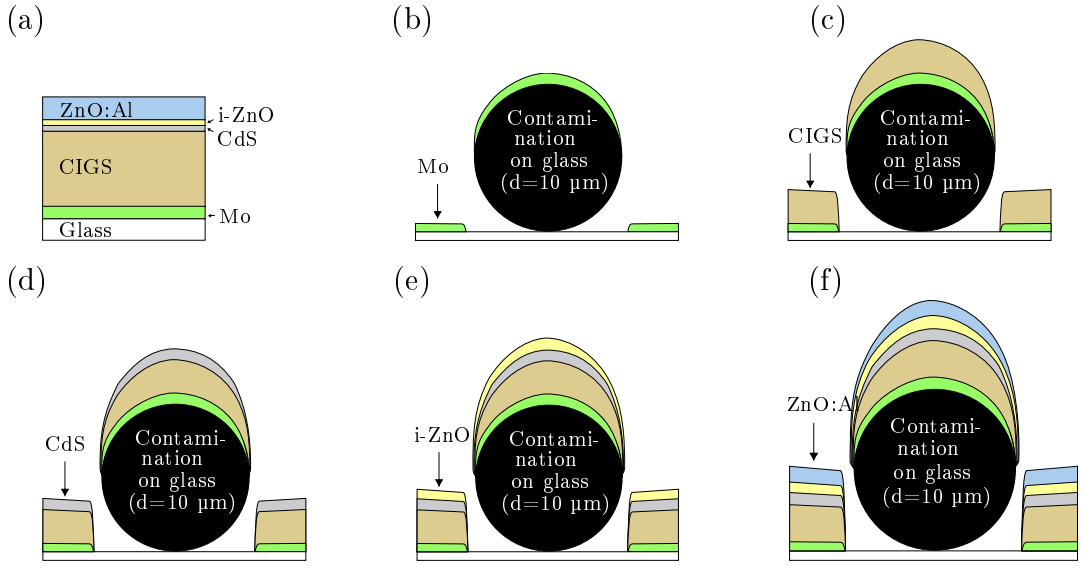

Figure 3.2: *Schematic drawing of possible holes originating from contamination on glass (defect* ***D-1****). (a) Defect free layer sequence. (b) Hole in Mo layer, named as* ***Mo-01****. (c) Hole in Mo and CIGS layer, named as* ***Mo-02****. (d) Hole in Mo, CIGS and CdS layer, designated as* ***Mo-03****. (e) Hole in Mo, CIGS, CdS and i-ZnO layer, named as* ***Mo-04****. (f) Hole in all layers, described as* ***Mo-05****. Situations (c) - (f) are shunt paths through the absorber and shed light on the isolating role of the CdS and i-ZnO buffer layers. Layer thickness is not drawn to scale for the sake of visibility.*

If the contamination from (b) remains at the same position during CIGS co-evaporation then a situation as shown in (c) can occur where both the Mo and CIGS layer contain a hole. For this case the contamination must be heat-resistant (thus, remains practically solid) for CIGS deposition temperatures $T > 600$ °C which makes Mo splinters (Mo debris resulting from P1 scribing) and glass splinters (glass damage due to transport) the most likely candidates. I study the situation where the contamination falls off after CIGS deposition in Chapter 6.2 experimentally and name this case of *D-1* as ***Mo-02***.

Assuming that the contamination remains at the same position till CdS chemical bath deposition (CBD), as shown in (d), then the three subsequent layers Mo, CIGS and CdS can locally contain a hole. For this case a sufficient adhesion between contamination and glass is required as the CBD is capable of rinsing off contaminations during its initial phase, the so called incubation phase (0 - 30 seconds) [11]. Within this incubation phase there is practically no CdS growth but surface contaminations on the CIGS absorber like Na_2O/NaOOH, Na_2CO_3 and Ga_2O_3 are removed effectively [11]. The experimental investigation of the case where the contamination falls off after CBD is presented in Chapter 6.2 and I label this case of *D-1* as ***Mo-03***.

In the event that the contamination remains till i-ZnO sputtering, a situation as shown in (e) can occur where the Mo, CIGS, CdS and i-ZnO layer can contain a hole. I explore the situation where the contamination falls off after i-ZnO sputtering experimentally in Chapter 6.2 with the defect ID *D-1* and its variation ***Mo-04***.

In case the contamination remains on the glass substrate even until the ZnO:Al is sputtered, then the situation shown in (f) can occur where all layers contain a hole at the same position. The experiments that shed light on the situation shown in (f) are contained as variation ***Mo-05*** of *D-1* in Chapter 6.2.

The actual growth progress can differ significantly from those shown in Figure 3.2. For instance, uninterrupted CIGS or ZnO:Al layers can occur, covering the contamination, if the contamination size or form is negligible compared to the correspondent layer thickness. Thus, the main benefit of Chapter 6.2 is to gain general knowledge about how the presented situations in (b) - (f) influence the voltages and currents in a solar cell. In contrast, Chapter 6.2 does not cover any possible permutation of defective layers because I assume an upwards directed error propagation as the most likely case. For example, an upwards directed error propagation excludes the Mo layer and the i-ZnO layer to be defective at the same position, while the CIGS and CdS layers in between are defect free - this is unlikely if they have the same defect origin.

3.2.4 P1 Scribing

Within this thesis the Mo was scribed by a laser from substrate side through the glass as shown in Figure 3.3. The laser pulse travels through the glass, as the glass is transparent for the applied laser wavelength of $\lambda = 532$ nm [41], and irradiates the interface between glass and Mo. The applied laser pulse duration is $t_{\text{pulse}} = 300 - 800$ ps at a feed range of $v_{\text{P1}} = 1 - 2$ m/s. The laser pulse overlap is $o_{\text{P1}} \approx 20\%$ at a laser pulse width of about $w_{\text{P1}} \approx 45$ µm.

In [42] the laser scribing process has been described as a process consisting of three steps: In a first step, the interface between the glass substrate and the Mo film absorbs the optical laser pulse energy which leads to a steep temperature increase at the interface. In a second step, the steep temperature increase causes local melting and evaporation of the Mo layer. In a third step, the strain caused by the partial evaporation at the substrate/film interface leads to fractures in the Mo layer where the Mo preferably is ablated. Any deviation from the aforementioned laser parameters (λ, t_{pulse}, v_{P1}, o_{P1}, w_{P1}) can eventually cause an insufficient Mo laser scribing.

In the following I discuss three P1 defect sources (i-iii) which are relevant for industrial practice. **(i)** P1 scribing equipment contains movable parts, among which are the lenses for laser guiding. If tilting of the setup due to motion (acceleration and deceleration) causes the lenses to leave their initially calibrated positions, then the required laser focus can be lost. **(ii)** Furthermore, the machines for P1 scribing in photovoltaic production sites are not operated in a clean-room environment due to cost reasons. This leads to pollution on the lenses which can either cause laser beam absorption or change the reflectivity of the lenses, finally resulting in an interrupted P1 scribing process as well. **(iii)** The above

introduced three step P1 laser ablation process [42] demonstrates the need for an obstacle free light path through the glass substrate to the substrate/Mo interface. Therefore, the glass substrate itself can cause incomplete P1 scribing if it locally forms an obstacle for the laser beam.

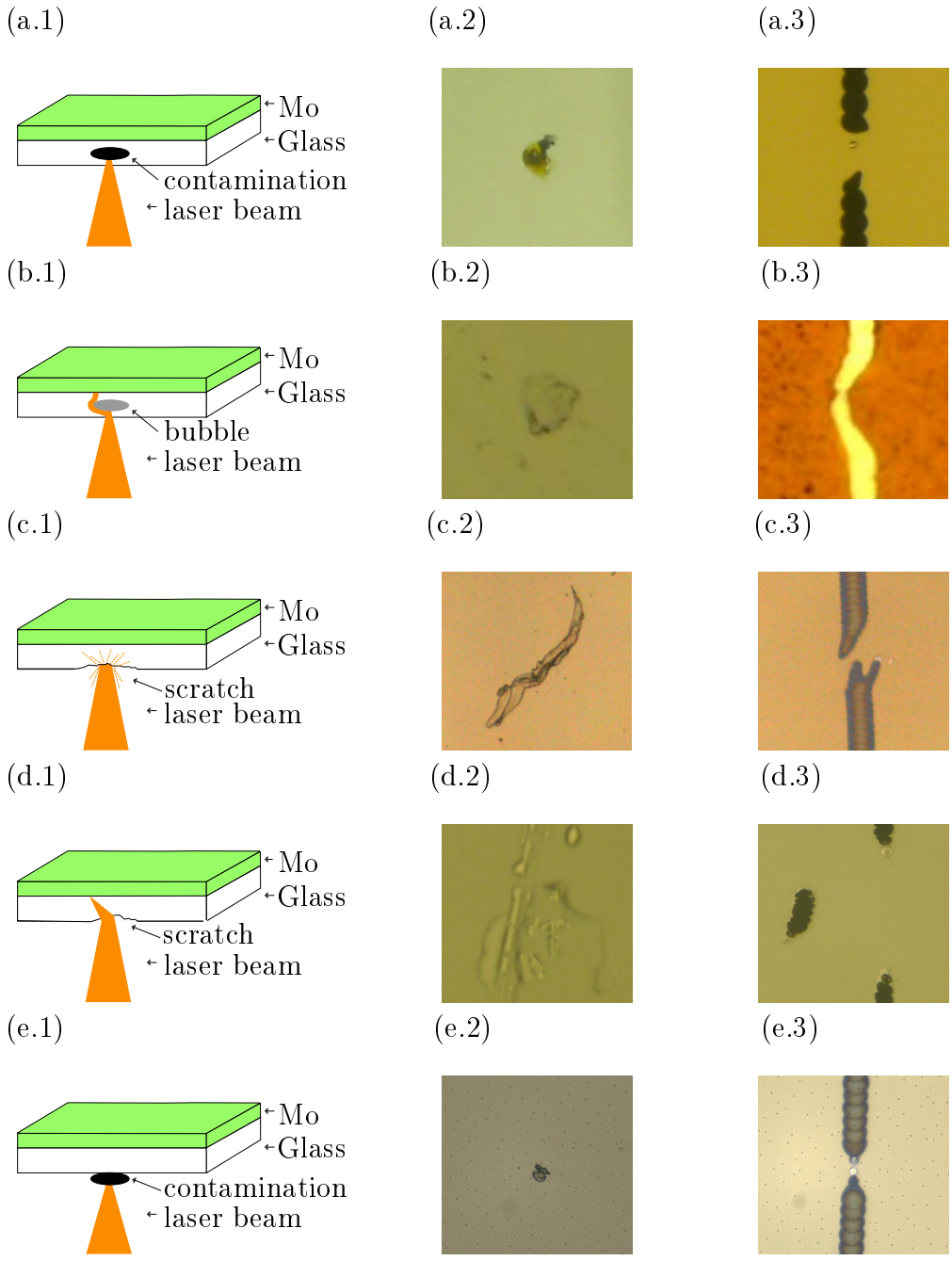

Figure 3.3: *P1 defects due to laser beam obstacles in or on the glass. The first column schematically illustrates the interruption of the P1 scribing line for cases (a)-(e). Second column shows microscope images of the obstacles. Third column contains microscope images of the correspondent interrupted P1 lines. (a) Contamination within glass. (b) Bubble within glass. (c) and (d) show scratches within or on the glass. (e) Contamination on glass.*

Figure 3.3 (a.1) shows schematically how a laser beam is either absorbed, scattered, reflected or deflected by a contamination within the glass. (a.2) shows the microscope image of the contamination and (a.3) contains the microscope image of the resulting laser line interruption. In contrast to the contamination which causes *Mo-01* - *Mo-05*, a contamination within the glass cannot be avoided by the glass washing (Chapter 3.2.2). These contaminations originate from the float glass production [43]. Bubbles within the glass can be a further obstacle for the laser beam as shown in (b.1)-(b.3). A detailed discussion of bubbles in float glass is given in [43] where bubbles are described as inclusions of atmospheric gases during the initial phase of batch melting, or decomposition of batch components, in the float glass production. Additionally, scratches on or within the glass can form an obstacle for the laser beam as shown in (c.1)-(c.3). Scratches can either occur during float glass production [43] or during transport in a photovoltaic production line. In (c.1)-(c.3) reflection and scattering are the main mechanisms to interrupt the laser beam. However, the main mechanism can also be deflection as shown for the scratch in (d.1)-(d.3). The only obstacle that can be prevented within a production site by glass washing is contamination on the glass surface as shown in (e.1)-(e.3). Most of the contamination that I have observed is point-like as shown in (e.3). Nonetheless, it can also be stripe-like contamination which is mainly caused by the substrate transport on polluted roles.

D-2: P1 scribing line interruption is therefore the second defect that I investigate within this thesis. It occurs due to the aforementioned defect sources (i)-(iii). The influence of *D-2* on currents and voltages is shown both experimentally and by modelling in a network simulation model in Chapter 6.3. Furthermore, the detection and identification of *D-2* in EL and DLIT measurements is introduced in Chapter 7.2.

3.2.5 Mo Washing

After P1 scribing the substrate is washed again with demineralized water and lint-free brushes. At this stage the most likely pollutions are Mo splinters that have been ablated as a result of the P1 scribing process. Alternative cleaning methods have been presented in [44].

3.2.6 CIGS Absorber Deposition

In the present work the CIGS absorber has been deposited by the process of co-evaporation. Co-evaporation means that the elements Cu, In, Ga and Se are evaporated simultaneously [11, 45, 46] and the chalcogenide formation takes place directly out of the gas phase. A detailed discussion of the chemical, physical, and technical background of the co-evaporation and its derivations can be found in [11].

For the identification of defects it is relevant that a top-down coating configuration has been used. In the top-down configuration the substrate is placed on a moving carrier which passes the evaporation sources that are positioned above it. The top-down configuration allows to exceed the glass transition temperature of about 560 °C [43] as the soft glass is held by the carrier and cannot fall down. This allows to operate up to 700 °C which has been reported to be a key to a higher homogeneity of the absorber layer (both laterally and vertically) and enhances the open circuit voltage V_{OC} [45]. In contrast, the bottom-up coating configuration (where the glass substrate is held above the deposition sources) does not allow to exceed the glass transition temperature.

D-3: Accumulated debris of the evaporation source falling down onto the substrate is a significant disadvantage of the top-down configuration as described in [11]. Cu-rich debris from the Cu evaporation source is most detrimental due to its high conductivity. Figure 3.4 shows a microscopic image of two Cu-rich contaminations close to each other.

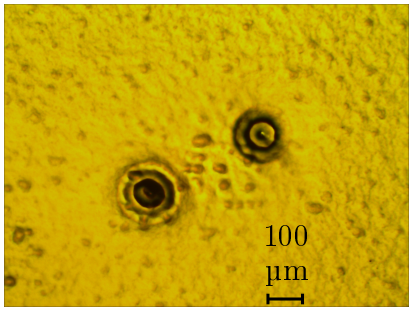

Figure 3.4: *Microscope image of two Cu-rich contaminations (defect **D-3**) which have fallen onto the substrate during CIGS co-evaporation.*

The microscope image is recorded from glass side. By applying destructive EDX material analysis to the phenomenon shown in Figure 3.4 I have found that it mainly consists of Cu. The Cu-rich contaminations typically appear like water drops within the surrounding Mo back contact (yellow surrounding). Furthermore, Figure 3.4 provides ground for speculation that the Cu-rich contamination should have a temperature at least close to the melting point of Mo (which is 2896 °C [47]) as it obviously penetrates the Mo layer. I could not observe any damage of the glass substrate at the positions where the Cu-rich debris was located. In Chapter 7.6 I show how Cu-rich debris can be detected and identified.

D-4 Holes in CIGS and following layers are the second type of defect that I investigate with regard to the CIGS deposition process. During CIGS co-evaporation contamination (Mo or glass splinters) can lead to holes in the deposited CIGS absorber and following layers. Assuming upwards directed error propagation (in the same way as I introduced it before for *D-1*), holes in the CIGS layer can lead to situations as shown in Figure 3.5.

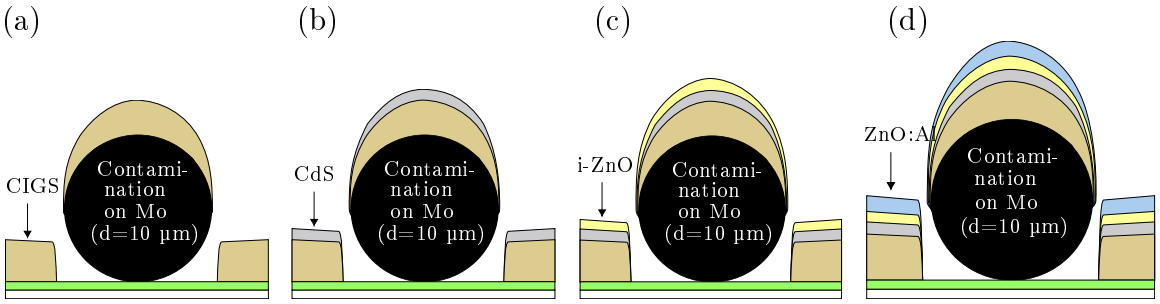

Figure 3.5: *Schematic drawing of holes originating from a contamination on the Mo layer, which is indicated by green colour (defect* ***D-4****). (a) Hole only in the CIGS absorber named as* ***CIGS-06****. (b) Hole in CIGS and CdS layer, named as* ***CIGS-07****. (c) Hole in CIGS, CdS and i-ZnO layer, named as* ***CIGS-08****. (d) Hole in CIGS and all following layers:* ***CIGS-09****. Situations (a)-(c) represent shunt paths through the absorber and shed light on the isolating role of the CdS and i-ZnO buffer layers. Layer thickness not drawn to scale for the sake of visibility.*

Figure 3.5 (a) depicts a contamination on the Mo layer that can cause a hole in the evaporated CIGS layer if it is heat-resistant at temperatures above 600 °C (see discussion in *D-1*). The experiments on the case as shown in (a), where the contamination falls off after CIGS deposition, is subject of discussion in Chapter 6.2 and the correspondent name for this variation of *D-4* is ***CIGS-06***.

If the contamination from (a) remains during CdS chemical bath deposition (CBD) as well (see comments on necessary adhesion in *D-1*), then a situation as shown in (b) can occur. I study the situation in (b), where the contamination falls off after CBD, experimentally and show the results in Chapter 6.2 for the variation ***CIGS-07*** of defect type *D-4*.

Assuming that the contamination from (b) that does not fall off after CBD, a hole in the layer sequence of CIGS, CdS, and i-ZnO can occur as shown in (c). The situation shown in (c) includes that the contamination falls off after i-ZnO sputtering, which I experimentally investigate in Chapter 6.2 under ***CIGS-08***.

Finally, in the event that the contamination remains through all following deposition processes at the same position, then a defect type as shown in (d) can occur. In this case the CIGS, CdS, i-Zno, and ZnO:Al layers are all locally missing which I study with my experiments on variation ***CIGS-09*** of defect type *D-4* in Chapter 6.2.

Note that the shown figures only schematically illustrate the creation of the point defects ***Mo-01*** - ***CIGS-09***, while the reality can include a much higher complexity of geometries. However, the shown local deteriorations of the layer structure will allow to gain specific knowledge about the shunt mitigating role of the i-ZnO/CdS buffer combination.

3.2.7 CdS Chemical Bath Deposition

Apart from forming the n-type, the CdS layer plays an important role in preserving a high carrier lifetime in the CIGS absorber. CIGS films that are exposed to air show a significant degradation of the carrier lifetime τ_{CIGS}. It has been reported in [48] that storing a module after CIGS deposition for 24 hours reduces the lifetime from $\tau_{\mathrm{CIGS}} =$ 100 ns to $\tau_{\mathrm{CIGS}} = 2$ ns. The degradation has been explained in [48] by oxidation of the CIGS surface leading to high surface recombination. The strong lifetime degradation in CIGS can be avoided by deposition of CdS as soon as possible after CIGS deposition. It has been suggested in [48] that CIGS surface passivation is the underlying effect. Once the CdS layer is deposited, the module can be stored for months without further lifetime degradation.

During chemical bath deposition (CDB) the substrate is immersed into a tank which contains the chemical solution consisting of thiourea, Cd salt and ammonia. The solutions, their molecular formula, their concentration within the solution of the tank and their purpose are listed in Table 3.2.

Table 3.2: *Sources and precursors of CBD. The following sources with the given concentrations are used for CBD of CdS on standard* $CuIn_{0.7}Ga_{0.3}Se_2$ *[49].*

Sources	**Molecular Formula**	**Concentration**	**Purpose**
thiourea	$SC(NH_2)_2$	0.12 mol/L	sulfur source
Cd salt	$Cd(CH_3COO)_2$	0.0013 mol/L	cadmium-ammonia complex as cadmium precursor
ammonia	NH_3	1.0 mol/L	

Thiourea is used as sulfur (S) source. The cadmium salt and the ammonia form cadmium-ammonia complex ions as cadmium precursors [11]. With the concentrations given in Table 3.2, the chemical reaction within the tank can be described by [49]

$$\mathrm{Cd(NH_3)_4^{2+} + SC(NH_2)_2 + 2OH^- \rightarrow CdS + CN_2H_2 + 4NH_3 + 2H_2O.} \tag{3.1}$$

The chemical reaction takes place at $T \approx 60$°C and pH ≈ 11 [49]. Two competing growth mechanisms have been described in [49, 50]: (i) Atom by atom growth of the CdS layer on the CIGS surface. (ii) Aggregation of colloids within the solution. Within the first 30 seconds there is practically no CdS layer growth. Instead, contaminations such as Na_2/NaOH, Na_2CO_3 and Ga_2O_3 are rinsed off by the solution in the tank [11]. The CdS layer growth starts after $t = 30$ s and after $t = 60$ s the complete module surface is covered by a grown CdS layer. The thickness of the CdS layer increases almost linearly with $v_{\mathrm{CdS}} = 0.3$ nm/s and is finished after $t = 300$ s at a CdS thickness of about 50 nm. It has been shown in

[51, 52] that the oxygen concentration in the grown CdS layer can be up to 10 %, and in [53] that Se and In atoms appear to diffuse from the CIGS absorber into the CdS.

Holes in the CdS and following layer can occur due to contamination that has an adhesion to the CIGS layer which is stronger than the rinsing effect of the CBD. Assuming upwards directed error propagation, three situations can occur as shown schematically in Figure 3.6.

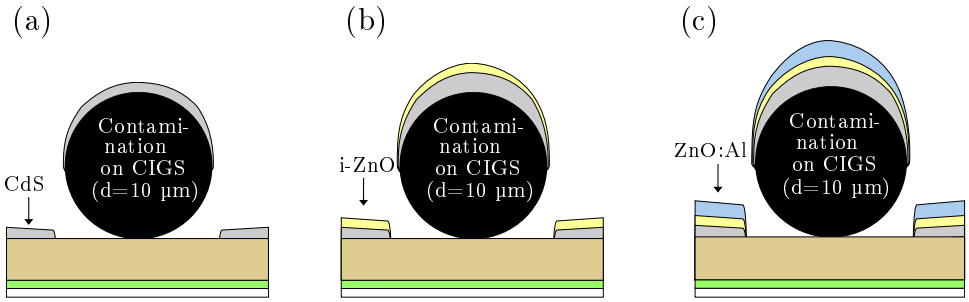

Figure 3.6: *Schematic drawing of holes originating from a contamination on the CIGS layer, which is indicated by brown colour. (a) Contamination can cause a hole in the CdS buffer layer, as well as in the following (b) i-ZnO and (c) ZnO:Al layers, if does not fall down after the correspondent process. Layer thickness is not drawn to scale for the sake of visibility. These cases are not investigated in this thesis.*

Figure 3.6 (a) depicts a contamination on the CIGS layer that can cause a hole in the CdS layer. In the case the contamination from (a) remains after CBD, situations like in (b) and (c) can occur. These cases are not investigated in this thesis.

3.2.8 Intrinsic ZnO Deposition

The intrinsic ZnO buffer layer is sputtered from a ceramic target at a radio frequency of about 13.56 MHz [11]. In analogy to the aforementioned point defects, two situations, as shown schematically in Figure 3.7, can occur due to upwards directed error propagation.

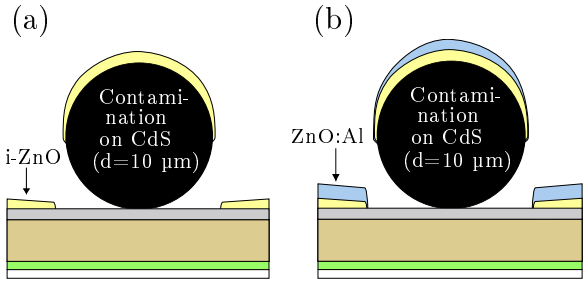

Figure 3.7: *Schematic drawing of holes within the i-ZnO layer originating from a contamination on the CdS layer, leading (a) to either only a hole in the i-ZnO layer or (b) to holes in both i-ZnO and ZnO:Al. Layer thickness is not drawn to scale for the sake of visibility.*

In Figure 3.7 I illustrate two possible scenarios for contaminations that are located on the CdS layer. If they persist during i-ZnO sputtering, then a hole in the i-ZnO layer results, as

drawn in (a). If the contamination does not fall off before ZnO:Al sputtering, then it can cause even an additional hole in the ZnO:Al layer, which is depicted in (b). Note that these scenarios are mentioned only for the sake of completeness, but are not investigated in this thesis.

3.2.9 P2 Scribing

The P2 scribing was done with a mechanical graver. Figure 3.8 depicts schematically how the mechanical graver removes the CIGS, CdS and i-ZnO layer.

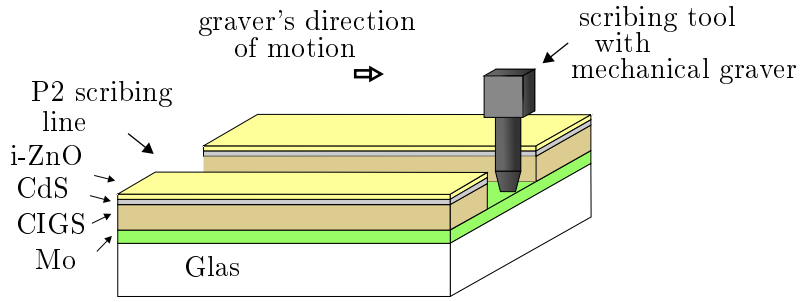

Figure 3.8: *Schematic P2 scribing. Mechanical graver scribes CIGS, CdS and i-ZnO layer.*

D-5: P2 scribing line interruption is the fifth defect type that I investigate within this thesis. The most likely reason for incomplete P2 lines is mechanical wear for which two wear mechanisms are introduced in the following. The first wear mechanism is diffusion of the scribing/cutting tool's coating into a interlayer between the tool and the work material. With regard to this first mechanism, I basically summarize metal machining literature and the essential equations in this section.

The second wear mechanism is increased adhesion due to an increased tool contact pressure p_{Tool}. The substrate to be scribed has a both unavoidable and unforeseeable warping due to the thermal stress which it experiences during CIGS co-evaporation. CIGS manufacturers increase the contact tool pressure p_{Tool} which ensures the tool to stay in contact with the module - despite of the unforeseeable warping. As a result, the increased p_{Tool} increases both diffusion and adhesion as wear mechanisms.

Both wear mechanisms are introduced in the following. The fundamentals discussed in this chapter are valid for the mechanical P3 scribing as well because it is based on the same scribing process. Figure 3.9 depicts schematically the two wear mechanisms and is the starting point for my discussion in this chapter.

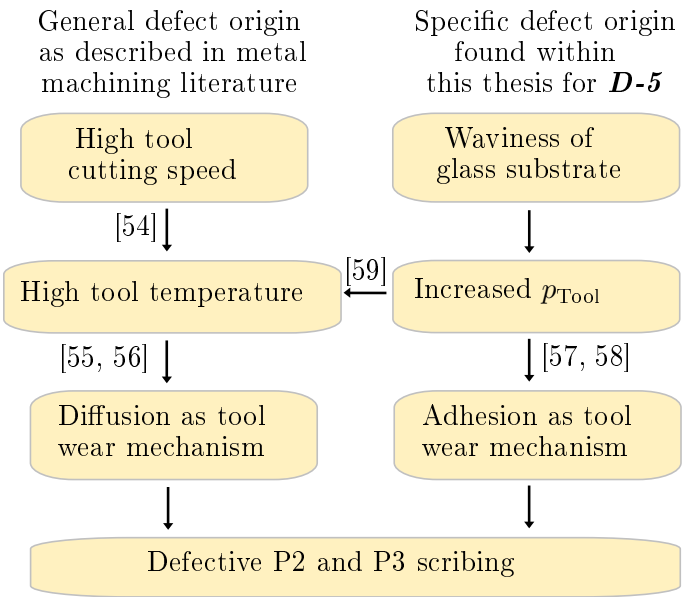

Figure 3.9: *Two wear mechanisms causing defective P2/P3 scribing. Left branch: High scribing speed (as a consequence of short production cycle time) leads to a high tool temperature during P2/P3 scribing (the tool is a mechanical graver) [54]. The high temperature makes diffusion as wear mechanism dominate over abrasion and adhesion [55, 56]. Right branch: Additionally, the waviness of the glass substrate after CIGS deposition makes a tool contact pressure p_{tool} onto the work material necessary which is higher than the required minimum contact pressure for flat substrates (see Figure 3.11). The increased p_{tool} additionally increases the temperature due to friction which enhances diffusion as wear mechanism [59]. At the same time an increased p_{tool} increases adhesion as wear mechanism [57, 58]. I have confirmed the detrimental effect of an increased p_{tool} with SEM and EDX measurements. The final result is for both branches a defective P2/P3 scribing as the tool's tungsten carbide layer is worn out. The effects of the two branches superimpose for both P2 and P3 scribing.*

In order to keep the production cycle time in a CIGS production site as small as possible, a P2/P3 scribing speed $v \approx 1$ m/s is applied. The mechanical graver, in the following just referred to as "tool", is covered by a tungsten carbide (WC) compound which is usually used for abrasion resistive cutting tools [60]. It has been shown in [54] that the tool temperature T_{t} can be regarded as linearly dependent of the tool cutting speed v by

$$T_{\mathrm{t}} = C_{\mathrm{t}} v^{d_{\mathrm{t}}}, \tag{3.2}$$

where C_{t} and d_{t} are constants [60] which have been determined experimentally in dependence of tool material, work material, tool geometry, cut thickness and cutting speed [60–64]. For cutting speeds in the range of $v \approx 1$ m/s it has been shown that the dominant wear mechanism for tungsten carbide compounds is thermal diffusion [55, 56, 65–72] due to temperatures of $T > 800$ °C. Diffusion wear means that atoms of the tool material, respectively

work material, migrate through the interface between tool and work material and form a local alloy [60]. In literature both tungsten and carbide have been observed to diffuse from the tool material into the work material [66, 67]. As a consequence, a diffusion based mass loss M_d (with regard to the tungsten carbide compound) has been observed with a wear rate [72] that can be described by Arrhenius type equation

$$\frac{\mathrm{d}M_\mathrm{d}}{\mathrm{d}t} = D_\mathrm{d} \cdot \exp^{-E_\mathrm{d}/(K_\mathrm{d}T_\mathrm{t})}, \tag{3.3}$$

where D_d and K_d are constants [72], and E_d is the activation energy of the tungsten carbide compound [73]. Hence, increasing the cutting speed v leads to an increased tool temperature T_t (Eq. 3.2); an increased tool temperature T_t leads to an increased wear rate $\mathrm{d}M_\mathrm{d}/\mathrm{d}t$ (Eq. 3.3); finally, the increased wear rate leads to an increased mass loss M_d which decreases the life time t_t of the cutting tool:

$$v \uparrow\rightarrow T_\mathrm{t} \uparrow\rightarrow \frac{\mathrm{d}M_\mathrm{d}}{\mathrm{d}t} \uparrow\rightarrow M_\mathrm{d} \uparrow\rightarrow t_\mathrm{t} \downarrow . \tag{3.4}$$

Once the mass loss M_d becomes too large, the tungsten carbide layer cannot ensure sufficient cutting performance any more. I have observed that worn tool tips tend to start kind of stuttering which finally leads to incomplete scribing lines, as shown in Figure 3.10.

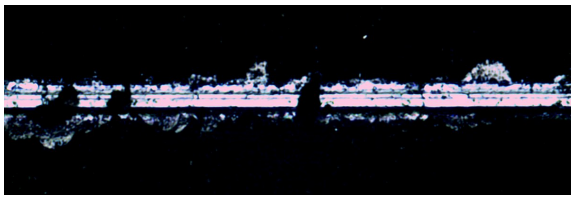

Figure 3.10: *Interrupted P2 scribing line. Worn tool tips tend to start kind of stuttering which makes the tool locally lose the contact to the substrate and eventually leads to interruptions in the scribing line.*

The aforementioned Equations 3.2, 3.3, and 3.4 have been described in literature. In contrast, a more specific reason for the mechanical wear, and therefore for the resulting defective P2 and P3 scribing, is an increase of the contact tool pressure p_tool .This is a consequence of the not precisely foreseeable warping of the glass substrate after CIGS co-evaporation. As discussed in Chapter 3.2.6, during CIGS deposition the glass substrate temperature exceeds the glass transition temperature of $T_\mathrm{g} \approx 560$ °C which is why the glass can warp during cooling down to room temperature [11]. The warping leads to different heights of the glass surface as shown schematically in Figure 3.11.

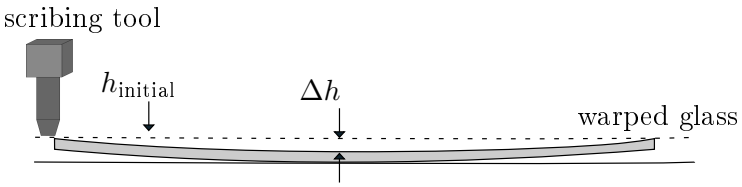

Figure 3.11: *Schematic warping of glass substrate after CIGS deposition. Wrapping of the glass substrate can lead to deviations from the initial scribing height $h_{initial}$. Δh can be in the range of several millimeters. In order to adjust the tool contact pressure p_{Tool} onto the work material, manufacturers often apply a too high pressure p_{Tool}.*

When scribing an uneven substrate, the pressure p_{Tool} of the scribing tool onto the work material must be higher than in case of an even substrate. This is because at a scribing speed $v \approx 1$ m/s there is less time for the scribing tool to adjust to an occurring height difference Δh (one can imagine a snowboarder jumping into the air when hitting a small snow hill). Hence, for a constantly appropriate height adjustment an increased p_{Tool} is applied in practice. While investigating the appropriate p_{Tool}, I have found that an increase of p_{Tool} increases M_{d} as well. This is depicted in Figure 3.12, where I present the EDX measurement of tungsten within a P2 scribing line for two different p_{Tool} at the same cutting speed $v = 1$ m/s.

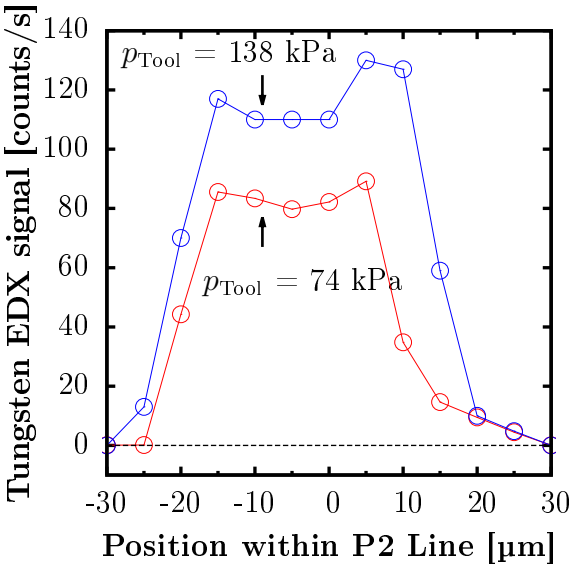

Figure 3.12: *Role of p_{Tool} on mechanical wear. Tungsten(W) has been measured with EDX within the P2 line. An increase in p_{Tool} increases M_d as well. Both measurements were performed at $v = 1$ m/s. At the edges of the 50 µm thick P2 line, the EDX signals are generally higher as the graver pushes material to the left and right while scribing.*

The result of Figure 3.12 is also visible in scanning electron microscope (SEM) images as shown in Figure 3.13, where (a.1) shows a comparatively smooth P2 scribing line with some few and small spots or strains in the upper right part. The correspondent energy dispersive X-ray (EDX) image taken at the position of the orange rectangle is shown in (a.2). The

tungsten (W) signal is clearly visible but still small when compared to the molybdenum (Mo) signal. This is the case for tool wear at $p_{\text{tool}} = 74$ kPa. In general, as long as the tungsten carbide layer of the tool is not significantly worn, the Mo signal can be expected as the dominant signal as all layers above the Mo (for both P2 and P3 scribing) are completely removed (ideally).

In contrast, (b.1) depicts a P2 scribing line with multiple and comparatively huge spots or strains measured for $p_{\text{tool}} = 138$ kPa. The tungston (W) mass loss M_{d} seems to have taken place on a much larger area and with a higher intensity than in (a.1). The EDX image taken

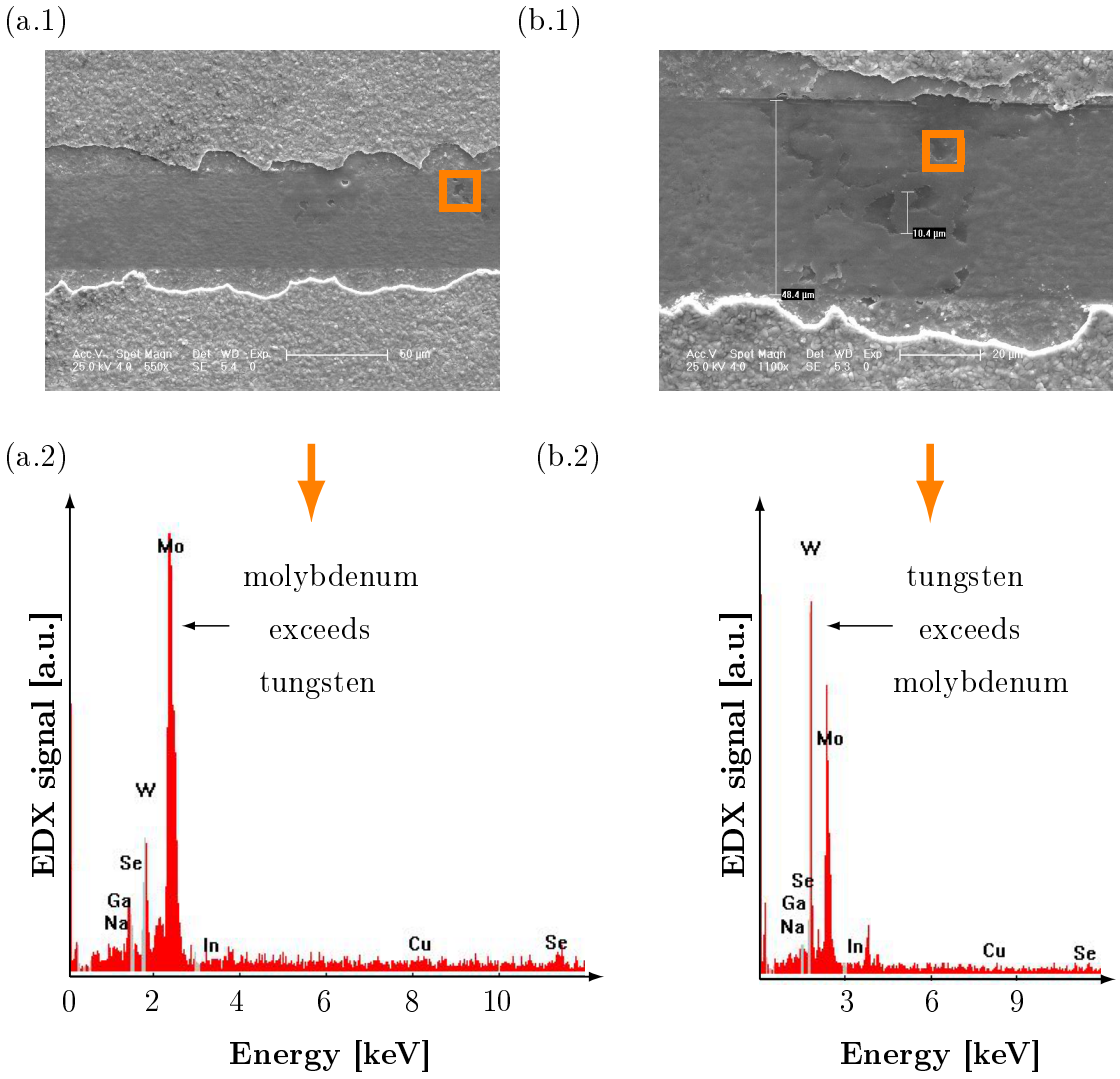

Figure 3.13: *SEM and REM images of tungsten in P2 scribing line resulting from different contact tool pressures p_{tool}. (a.1) SEM image with few and comparatively small stains containing W as measured for $p_{tool} = 74$ kPa. (a.2) Mo signal exceeds the W signal. (b.1) SEM image with multiple and comparatively huge stains containing W as measured for $p_{tool} = 138$ kPa. (b.2) W signal exceeds the Mo signal. The two measurements are made for two different gravers after the same tool usage time. The results indicate that an increased p_{tool} increases M_d of W as well.*

at the position of the orange rectangle is shown in (b.2). The visual impression of (b.1) is confirmed by the correspondent EDX image in (b.2) where the tungsten (W) signal exceeds the molybdenum (Mo) signal.

To draw a conclusion, Figure 3.13 shows that tungsten material loss due to mechanical wear can be visually ascertained in SEM and EDX images. Furthermore, the number of visible spots or strains increases significantly with the contact tool pressure p_{tool}. In accordance to the results shown in Figures 3.12 and 3.13, there is a right branch drawn in Figure 3.9. It has been shown in [59] that an increased p_{tool} leads to an increased temperature as well. Thus, in Figure 3.13 the increased p_{tool} of th right branch is drawn to enhance diffusion in the left branch. Furthermore, it has been shown in [57, 58] that an increased p_{tool} introduces adhesion as wear mechanism. The effect of high cutting speed v (in the left branch) and increased tool contact pressure p_{Tool} (in the right branch) superimpose and finally lead to defective P2/P3 scribing. In practice, I have found that the applied $p_{\mathrm{Tool,applied}}$ typically exceeds the minimum required $p_{\mathrm{Tool,min}}$ by a factor of 2 - 3.

I investigate the influence of ***D-5*** on currents and voltages both experimentally and by modelling in a network simulation model in Chapter 6.3. Moreover, I investigate its detection and identification in EL and DLIT measurements in Chapters 7.3 and 7.4.

3.2.10 ZnO:Al Deposition

The ZnO:Al front contact layer is deposited by magnetron sputtering. The ceramic ZnO:Al targets, which are used for DC magnetron sputtering [74, 75], typically contain 2 wt% Al_2O_3 [76]. As introduced in Chapter 2.2.1, this provides light transmittance and electrical conductivity. Holes in ZnO:Al can occur due to contamination on the i-ZnO layer as shown schematically in Figure 3.14. Note that the scenario in Figure 3.14 is only shown for the sake of completeness, but no investigated in this thesis.

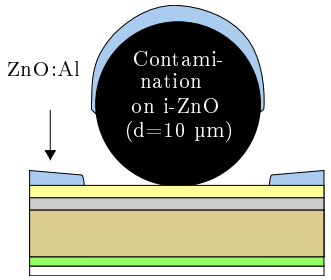

Figure 3.14: *Schematic drawing of a contamination on the i-ZnO layer, indicated by the yellow colour, which causes a hole in the ZnO:Al layer. Layer thickness is not drawn to scale for the sake of visibility.*

3.2.11 P3 Scribing

The P3 scribing is done mechanically in the present work. It is based on the same process as the P2 scribing and even performed on the same machines. Figure 3.15 depicts the mechanical P3 scribing process schematically.

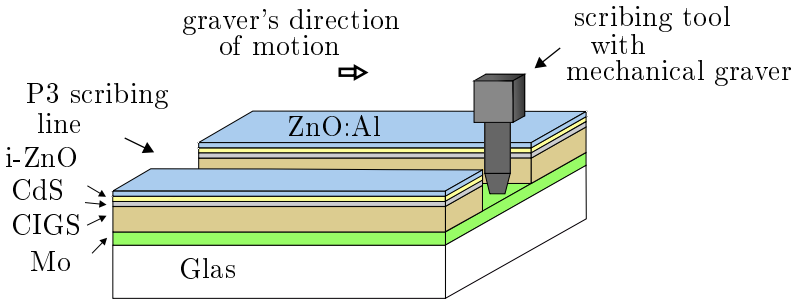

Figure 3.15: *P3 scribing. Mechanical graver scribes CIGS, CdS, i-ZnO and ZnO:Al layer.*

D-6: P3 scribing line interruption is the sixth defect that I investigate within this thesis. The most likely reason for incomplete P3 lines is mechanical wear. With regard to mechanical wear I have introduced all fundamentals in Chapter 3.2.9.

Due to the hardness of the ZnO [77] the minimum applied tool contact pressure $p_{\mathrm{Tool,P3}}$ for P3 scribing is higher than that of the P2 scribing. Hands on values for the production are $p_{\mathrm{Tool,P2}} \approx 120$ kPa in contrast to $p_{\mathrm{Tool,P3}} \approx 184$ kPa, which is an increase by about 50 %. Hence, the influence of the right branch in Figure 3.9, for an increased contact tool pressure p_{Tool} as the second wear mechanism, is even higher for P3 scribing than for P2 scribing.

In analogy to ***D-5***, the simulation of ***D-6*** can be found in Chapter 6.3 and its detection and identification in Chapter 7.4.

3.3 Conclusions

All defects that I have investigated with regard to detection and identification are summarized in Table 3.1. They can be divided into point defects (***D-1***, ***D-3***, ***D-4***) and scribing line defects (***D-2***, ***D-5***, ***D-6***).

I have correlated the mechanical wear of the graver tip with the applied tool contact pressure by SEM and EDX measurements. My investigation shows that the applied tool contact pressure, as it is used in a standard industry mechanical scribing process for the P2 and P3 lines, is chosen 2-3 times higher than actually required. While the original idea of an increased tool contact pressure is to avoid scribing line interruptions due to the glass waviness, which results from CIGS deposition process, at the same time the increased pressure leads to accelerated graver wear, and thus requires to exchange the graver earlier, in order to avoid P2 and P3 defects because of a worn out graver tip. Table 3.1 can be used as orientation within this work with regard to the investigated defects.

Chapter 4

EL & DLIT Measurements

"The purpose of this chapter is to introduce the two measurement techniques which I use within this thesis for the identification of defects: the electroluminescence measurement (EL) and the dark lock-in thermography measurement (DLIT)."

4.1 Introduction

This work has been written in close cooperation with industry partners. In an industrial production environment the photovoltaic module's electrical performance is typically measured as J-V curve, according to Eq. (2.8) in Chapter 2.3. This is a well standardised quality control to check whether the photovoltaic module fulfils the specifications.

Nonetheless, for defective modules one cannot extract from a measured J-V curve what the defect origin is. If the module's parallel resistance (see Chapter 2.2.2, Fig. 2.2) is reduced, then the origin can be, for instance, insufficient cell insulation (by P1 and P3 lines), insufficient laser edge insulation, or simply ohmic-like point defects within the cells. It is important to know what the defect origin is in order to take action for avoiding its occurrence in the production. For instance, realizing that P2 or P3 scribing defects occur, one can reduce the intervals for the exchange of the mechanical graver. Both EL and DLIT can address this issue as they are spatially resolved measurements. As it is shown in Chapters 6 and 7, both scribing defects and Cu-rich debris mostly have characteristic EL and DLIT patterns. These characteristic defect patterns can be detected and identified if the resolution of the EL and DLIT measurement setup is in the range of the defect size (which is discussed in Chapter 7).

Furthermore, EL allows cost reduction as it can be placed inline in a production environment. The EL measurement is usually performed after the ZnO:Al front contact has been deposited. If the module fails on the EL test (because of criteria which are specifically defined by each manufacturer), then the following production steps (i.e. contacting with conductive

tape, lamination with a polymer foil, placing and sticking of the front glass, installation of the contact box) can be avoided which reduces the costs.

EL measurements usually take only a few seconds (less than the production cycle time of currently about 24 seconds) and can therefore economically be integrated into the inline quality control. In contrast, DLIT measurements usually are performed offline in a laboratory environment due to their duration of up to several minutes.

4.2 Sample Preparation

The measured CIGS samples are of 30 x 30 cm^2 dimension with $n_{\text{cells}} = 69$ cells, a cell width of $w_{\text{cell}} = 4$ mm and a cell length of $l_{\text{cell}} = 300$ mm. The samples are not completely finished with regard to the production steps in a CIGS production site. All production steps after the ZnO:Al deposition are left out for the used samples. This allows the small samples to be cut out from a whole CIGS module of the dimensions 120 x 60 cm^2 as only one glass (the substrate) has to be cut. The first and the last cell of each sample is contacted with a conductive tape. For both EL and DLIT measurements, the conductive tapes are connected to the cables of the source-measurement-units (SMU) in four-terminal sensing mode.

None of the samples is exposed to light before EL measurement. Exposure to light can significantly change the EL appearance. The underlying effect has been explained in [78].

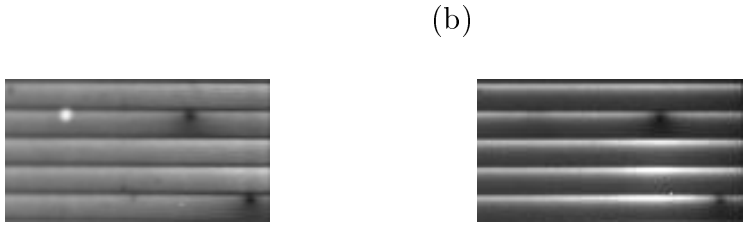

Figure 4.1: *Influence of light soaking on EL image. EL image (a) before and (b) after 48 hours of light soaking at 800 W/m^2 intensity. White spot in the upper left part disappears and image contrast is increased during light soaking. This effect has been explained in [78].*

There is a general trend that defects, or deviations from normal layer sequence in general, are better visible before light soaking (LS) than after. For instance, in Figure 4.1 the bright spot in the upper left part of (a) before LS disappears after LS in (b). As it is helpful to have as much information about defects as possible, none of the samples has been illuminated before EL measurements.

4.3 Electroluminescence

Electro - Luminescence (EL) is the physical phenomenon where a device (having p-type and n-type contacts) is electrically stimulated (*electro*), and as a result radiative recombination

of electrons and holes within the device leads to the emission of photons (*luminescence*). The electrical stimulation of the solar cell is done by applying a suitable forward current density j_{EL} (which is the control variable in this thesis for all measurements). The induced charge carriers recombine in the device, and the emitted photons have a photon energy which is around the device's band gap E_{G} (this is basically the inversion of the normal cell's operating mode). For CIGS modules this band gap is approximately $E_{\mathrm{G,\,CIGS}} \approx 1.15$ eV.

The radiative recombination of the charge carriers is recorded by a charge coupled device (CCD) camera which allows a visual and quantitative analysis of the solar cell's radiative light emission. This works reliably although solar cells are (compared to LEDs) suboptimal light emitters [79, 80]. In the following Chapter 4.3.1 I summarize some basic theory that is required for the quantitative analysis and interpretation of EL images.

4.3.1 EL Basics

It has been shown in [80] that the current induced radiative photon emission (electroluminescence operation) and the photon induced separation of electrons and holes (photovoltaic operation) are complementary physical actions in a solar cell. The link between these two operations has been called *reciprocity* and expressed quantitatively in [80] by

$$\phi_{\mathrm{em}}(E) = Q_{\mathrm{e}}(E)\phi_{\mathrm{bb}}(E)\left[\exp\left(\frac{qV}{k_{\mathrm{B}}T}\right)\right], \tag{4.1}$$

where $\phi_{\mathrm{em}}(E)$ is the emitted spectral photon density, $Q_{\mathrm{e}}(E)$ is the photovoltaic external quantum efficiency, $\phi_{\mathrm{bb}}(E)$ is the spectral photon density of a black body, q is the elementary charge, V is the p-n-junction voltage, k_{B} is the Boltzmann constant and T is the temperature of the solar cell. $\phi_{\mathrm{bb}}(E)$ can furthermore be written as

$$\phi_{\mathrm{bb}}(E) = \frac{2\pi E^2/(h^3c^2)}{\exp(E/k_{\mathrm{B}}T) - 1}, \tag{4.2}$$

where h is the Planck's constant and c is the vacuum speed of light. In an EL measurement setup the CCD camera plays a fundamental role as it records $\phi_{\mathrm{em}}(E)$. Multiplying the energy-dependent (respectively wavelength-dependent) sensitivity $Q_{\mathrm{cam}}(E)$ of the CCD camera with Eq. (4.1), and introducing the surface position r on the solar cell, yields the following expression for the detected signal S_{cam} in each camera pixel [81]

$$S_{\mathrm{cam}}(r) = \int Q_{\mathrm{cam}}(E)\phi_{\mathrm{em}}(E,r)dE = \exp\left(\frac{qV(r)}{k_{\mathrm{B}}T}\right)\int Q_{\mathrm{cam}}(E)Q_{\mathrm{e}}(E,r)\phi_{\mathrm{bb}}(E)dE. \tag{4.3}$$

$S_{\mathrm{cam}}(r)$ can be quantified as the camera sensitivity $Q_{\mathrm{cam}}(E)$ and external quantum efficiency $Q_{\mathrm{e}}(E,r)$ can be experimentally determined, and the black body photon density $\phi_{\mathrm{bb}}(E)$ can

be calculated. Eq. (4.3) can be rearranged by

$$V(r) = \frac{k_\mathrm{B}T}{q}\left\{\ln\left\{S_\mathrm{cam}(r)\right\} - \ln\left[\int Q_\mathrm{cam}(E)Q_\mathrm{e}(E,r)\phi_\mathrm{bb}(E)dE\right]\right\} \tag{4.4}$$

in order to calculate the voltage $V(r)$ of the solar cell at the position r from the correspondent pixel. Actually, here r represents an area $A(r)$ seen by one pixel and $V(r)$ is therefore the average solar cell voltage within the area $A(r)$. From external quantum efficiency measurements of CIGS cells [82] one can extract the relevant wavelength range from about $\lambda \approx 300\ \mathrm{nm} - 1200\ \mathrm{nm}$ which yields integration limits from $E_1 \approx 1.03$ eV to $E_2 \approx 4.13$ eV for Eq. (4.4) which can be rewritten as

$$V(r) = \Delta V(r) + V_\mathrm{offset}\,, \tag{4.5}$$

where $\Delta V(r) = \frac{k_\mathrm{B}T}{q}\ln\left(S_\mathrm{cam}\right)$ and V_offset is a constant value (assuming, for the sake of simplicity, that Q_e may be independent of r) [81].

4.3.2 EL Measurement Setup

The EL measurement setup is shown in Figure 4.2. Either a housing or a dark environment is used for protecting the setup from ambient light which introduces noise. The source-measure-unit (SMU), which sets J_EL and measures V_EL, is controlled by a human-machine-interface (HMI) (consisting of a personal computer, screen and input devices). The integration time T_int for the camera is set via the HMI. The camera data is read out and processed by the signal processing, which is basically a software installed on the personal computer. The conductive tapes on the first and last cell of the substrates are connected to the cables of the source-measurement-units (SMU) in four-terminal sensing mode.

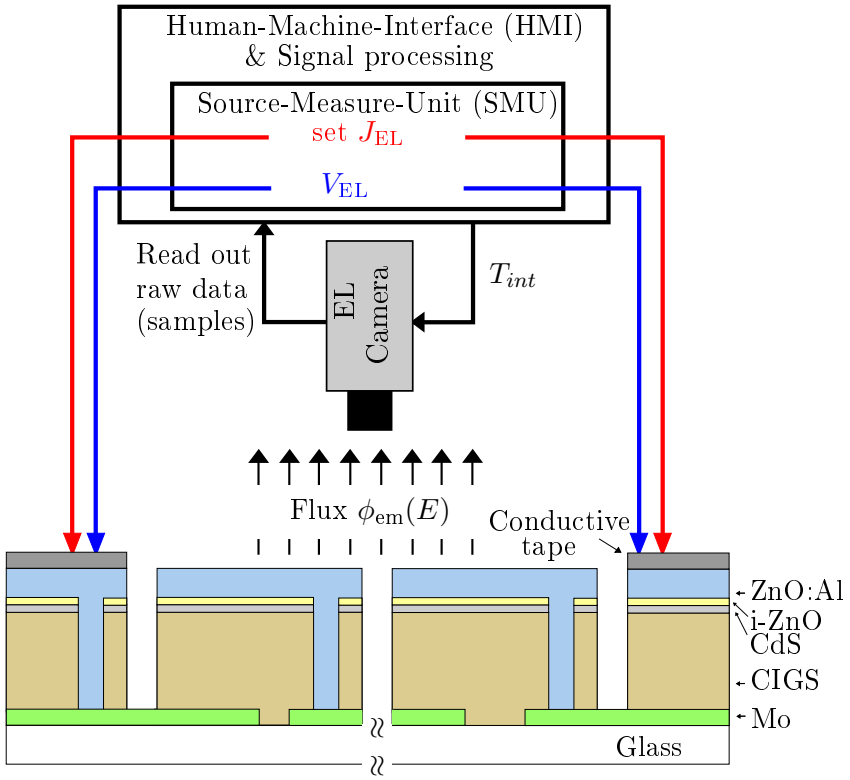

Figure 4.2: *Schematic EL setup. For the EL measurements a charge coupled device (CCD) camera with a silicon chip, providing a resolution of 3000 x 3000 pixel, has been used. The CCD chip is cooled 50° C below ambient. The current density J_{EL} is set as the control variable. The integration time T_{int} is set via the HMI.*

4.3.3 EL Measurement Practice

In the following the EL measurement practice is introduced that has been applied in this work. It describes a practice that has shown to be suitable for the purpose of this work.

The short circuit current density $J_{SC} \approx 29$ mA/cm^2 is not exceeded during EL measurements for the sake of cell protection.

Transient phenomena as published in [83] are practically avoided by operating in a static state for $\mathrm{d}V/\mathrm{d}t = 0$, which is reached several minutes after biasing the sample.

Before each EL measurement a dark-frame subtraction is done with a closed camera shutter. Dark-frame subtraction helps to correct the noise caused by dark current [84]. The term "dark current" describes a current that flows through photosensitive camera pixels even if they are not illuminated. For instance, the reason for dark currents can be thermal generation of charge carriers or defects in the sensor crystal. In order to reduce thermal generation of charge carriers the CCD chip is cooled before each EL measurement to 50° C below ambient.

Furthermore, a 3×3 pixel binning is applied, which means that 9 pixel on the chip are combined to one image pixel, in order to improve the signal S to noise N ratio SNR $= S/N$ albeit the expense of reduced spatial resolution.

The integration time is chosen to be $T = 6$ sec for all EL measurements in this work in order to allow comparability between the images.

4.4 Dark Lock-In Thermography

Each body of temperature $T > -273.15$ °C emits electromagnetic radiation, also called thermal radiation, due to the black body radiation law (introduced in Chapter 4.4.1). The thermal radiation increases with increasing temperature. Using thermography cameras that are sensitive in the IR range, one can visualize the spatial distribution of thermal radiation.

With regard to solar cells or modules, thermal radiation distributions among the cell occur due to changes in the thermal emissivity and temperature. In this work I don't investigate the thermal emissivity of the CIGS modules, but focus on temperature changes which are caused by the local power dissipation.

The local power dissipation is roughly proportional to $P = JU = J^2R$. Changes in the dissipated power can occur due to (i) the sheet resistance of the front/back contact layer which causes an uneven distribution of the dissipated power along the cell width. Furthermore, changes in the dissipated power can occur due to (ii) shunt resistances R_{shunt} and the power $P = J^2R_{\text{shunt}}$ that is dissipated within these shunts. While (i) is practically an inherent effect, (ii) points to abnormalities of the normal solar cell layer structure.

The term *dark* indicates that the solar cell is not illuminated during the lock-in measurement. A detailed overview of existing infrared imaging techniques, for both illuminated and not illuminated samples, has been published in [85]. In the following Chapter 4.4.1 I introduce some basic principles of infrared thermography.

4.4.1 Infrared Thermography Basics

The basic principle of DLIT is to detect an object's thermal radiation [86]. Eq. (4.2) is based on Planck's law [87] for a black body which is usually written as

$$B_{\upsilon}^{\text{bb}}(T) = \frac{2h\upsilon^3}{c^2} \frac{1}{\exp\left(\frac{h\upsilon}{k_{\text{B}}T}\right) - 1}, \tag{4.6}$$

where B_{υ}^{bb} is the spectral radiance of the black body and $\upsilon = c/\lambda$ is the frequency. The electromagnetic power P_{bb}, which is irradiated from an area A into a hemisphere above A, can be calculated by integrating the spectral radiance B_{υ}^{bb} over all frequencies υ and both

the polar angle θ and azimuthal angle ϕ for a hemisphere. The integration yields for the electromagnetic power P_{bb} of a black body

$$P_{\mathrm{bb}}(T) = A \int_0^{\infty} d\upsilon \int_0^{\pi/2} \cos(\theta) \sin(\theta)\, d\theta \int_0^{2\pi} d\phi\; B_{\upsilon}^{\mathrm{bb}}(T) = A\sigma T^4. \tag{4.7}$$

Eq. (4.7) is known as the Stefan-Boltzmann law containing the Stefan-Boltzmann constant $\sigma \approx 5.67 \text{ x } 10^{-8}$ $\mathrm{Js^{-1}m^{-2}K^{-4}}$. When applying Eq. (4.7) to a real solar cell, an emissivity $\varepsilon_{\mathrm{real}}$ must be introduced by

$$P_{\mathrm{real}}(T) = \varepsilon_{\mathrm{real}} A\sigma T^4, \tag{4.8}$$

with $\varepsilon_{\mathrm{real}} < 1 = \varepsilon_{\mathrm{bb}}$, where $\varepsilon_{\mathrm{bb}}$ is the emissivity of a black body. P_{real} is the quantity that has to be measured by a thermography camera. The temperature ranges that one is dealing with when operating a solar cell in a laboratory, practically allow only detection within the infrared (IR) range. Although Eq. (4.8) indicates a proportionality to the fourth power of the temperature, close to room temperature Eq. (4.8) is practically linear, as has been shown in [88], while the linear function has a very small slope. Thus, small ΔT around room temperature cause only small ΔP_{real} which aggravates the distinction of the signal from the surrounding statistical noise. In order to achieve good distinction between statistical noise and the beneficial signal that has to be measured, the lock-in principle is applied to infrared thermography. The lock-in principle is introduced in the following Chapter 4.4.2.

4.4.2 Lock-in Basics

For a thermography measurement on a photovoltaic device under test (DUT), a stimulus is applied to the DUT, while the stimulus is in its simplest form a voltage. The measured response signal $F(\mathrm{t})$ contains basically two components: (i) The beneficial signal which is the "true" response of the DUT, and (ii) statistical noise.

For the sake of simplicity, in its simplest form the approach of the lock-in principle can be described as the application of a practically noise free and alternating current (AC) like stimulus at a certain frequency - in contrast to the statistical noise that - theoretically - contains all frequencies.

The lock-in principle allows to suppress any signal that has not the stimulus frequency and, thus, to correctly detect only the beneficial signal S of the DUT [86, p. 15]. In its simplest form the lock-in principle can be mathematically described by

$$S = \frac{1}{t_{\mathrm{int}}} \int_0^{t_{\mathrm{int}}} F(t)K(t)dt, \tag{4.9}$$

where S is the beneficial response signal of the DUT without noise, $F(t)$ is the measured response signal of the DUT containing noise, t_{int} is the integration time, and $K(t)$ is a

symmetric square wave correlation function given by

$$K(t) = \begin{cases} +2, & \text{for } 0 \leq t < \frac{T}{2} \text{ within one period } T \\ -2, & \text{for } \frac{T}{2} \leq t < T \text{ within one period } T. \end{cases} \tag{4.10}$$

Eq. (4.9) yields a linear averaging over the integration time t_{int}. Figure 4.3 depicts an example for the (red) stimulus signal $E(t)$, the (orange) noise, the resulting (blue) response $F(t)$ and the (green) correlation function $K(t)$.

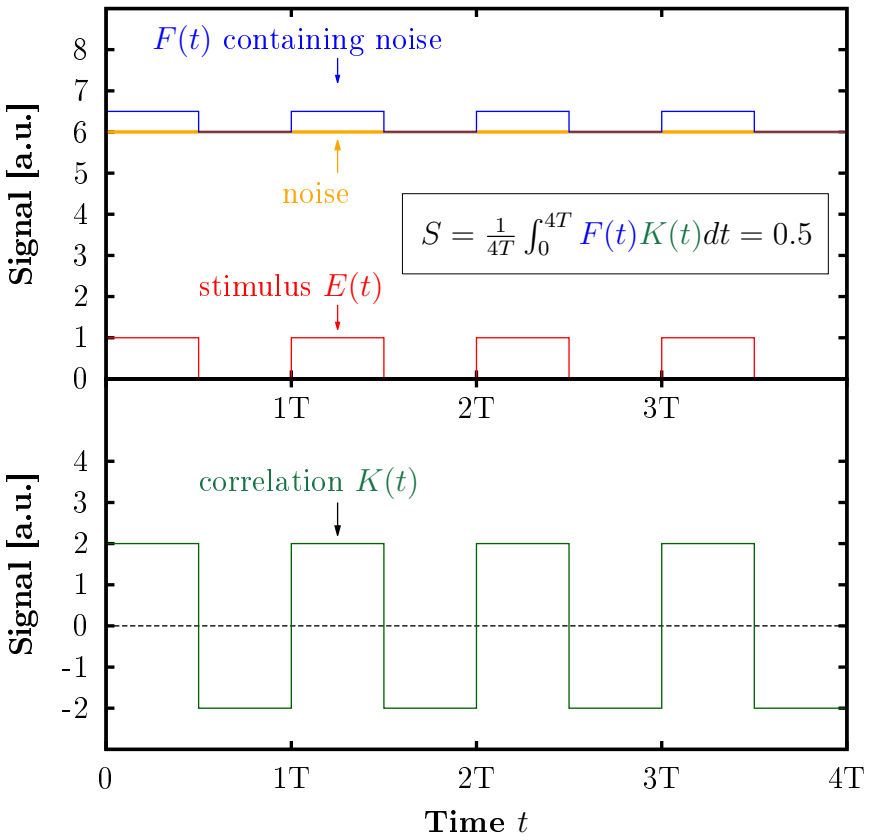

Figure 4.3: *Visual explanation of lock-in principle. A stimulus $E(t)$ with an amplitude of 1 causes a response of the DUT. The response is superimposed by the noise which leads to the signal $F(t)$. The signal $F(t)$ is multiplied with the correlation function $K(t)$, as introduced by Eq. (4.10), which finally yields $S = 0.5$ in arbitrary units as DC output signal which is the amplitude of the DUT's beneficial response.*

State of the art lock-in systems use a digital approach. The noisy response $F(t)$ is digitized by an analogue-digital-converter (ADC) which results in a series of numbers F_{j}, and a series of numbers K_{j}, respectively. The frequency of digitizing the noisy response $F(t)$ is f_{fr} which is basically the frame rate of the thermography camera and is therefore usually fixed. A digitizing event is synonymous with recording a thermography image. The variable n labels in the following the number of recorded thermography images during one lock-in period and the variable N labels the number of lock-in periods. For instance, Figure 4.3 shows $N = 4$

lock-in periods of T length. Hence, the integral from Eq. (4.10) becomes a sum

$$S = \frac{1}{nN} \sum_{i=1}^{N} \sum_{j=1}^{n} K_{\mathrm{j}} F_{\mathrm{i,j}}, \tag{4.11}$$

which means that n x N is the total number of recorded images and the measurement result is averaged by n x N images. For Eq. (4.11) the digitizing events are assumed to take place synchronously with the correlation function $K(t)$. Non-synchronous approaches are also known [89]. However, the synchronous approach allows the best suppression of DC signals while, in contrast, an incomplete N in general introduces additional noise [86, p. 17]. In modern thermography setups, harmonic correlation functions $K(t)$ are used which provide a narrow-band correlation, in contrast to the wide-band correlation of the square-wave $K(t)$ from Eq. (4.10) [86, p. 17]. The harmonic correlation allows to regard practically only the basic harmonic of $F(t)$ which contains the dominant information.

Furthermore, the thermal response of a device has a time delay with regard to its stimulus. Assuming harmonic stimulus and therefore harmonic response, the time delay can be regarded as a phase shift ϕ between stimulus and response. In order to detect both amplitude and phase of the beneficial DUT signal, two kinds of so called weighting factors K_{j} are used: the weighting factors $K_{\mathrm{j}}^{0^\circ}$ which approximate the sine function

$$K_{\mathrm{j}}^{0^\circ} = 2 \sin \frac{(2\pi(j-1))}{n} \tag{4.12}$$

and the weighting factors $K_{\mathrm{j}}^{\text{-}90^\circ}$ which approximate the cos function

$$K_{\mathrm{j}}^{\text{-}90^\circ} = -2 \cos \frac{(2\pi(j-1))}{n}, \tag{4.13}$$

where the indices "0°" and "-90°" refer to the phase shift, and the factor 2 needs to be added in order to obtain the correct amplitude. In analogy to Eq. (4.11) two components of S can be calculated. The so called "in-phase" component S^{0°, which has no phase shift, given by

$$S^{0^\circ} = \frac{1}{nN} \sum_{i=1}^{N} \sum_{j=1}^{n} K_{\mathrm{j}}^{0^\circ} F_{\mathrm{i,j}} \tag{4.14}$$

and the "quadrature" component, which has a phase shift of $\phi = -90°$, given by

$$S^{\text{-}90^\circ} = \frac{1}{nN} \sum_{i=1}^{N} \sum_{j=1}^{n} K_{\mathrm{j}}^{\text{-}90^\circ} F_{\mathrm{i,j}}. \tag{4.15}$$

A phase shift is counted in the direction of negative angles and, thus, using a negative algebraic sign for the cosine function in Eq. (4.13), one finally obtains positive values for

$S^{\text{-}90^\circ}$ in Eq. (4.15). The resulting DC signal S can be regarded as a complex number formed by

$$S = S^{0^\circ} - \mathrm{i}S^{\text{-}90^\circ} = S^{0^\circ} + \mathrm{i}S^{90^\circ}, \tag{4.16}$$

where S^{0° is the real part and $S^{\text{-}90^\circ}$ (or S^{90° respectively) is the imaginary part. In [88] it is derived in detail that

$$S^{0^\circ} = A\ \cos(\phi) \tag{4.17}$$

$$S^{\text{-}90^\circ} = A\ \sin(\phi) \tag{4.18}$$

for a harmonic response. The amplitude A of the beneficial response S is calculated by

$$A = \sqrt{(S^{0^\circ})^2 + (S^{\text{-}90^\circ})^2} \tag{4.19}$$

as known from complex numbers. The phase ϕ of the beneficial response can be calculated from the arctangent of the angle between S^{0° and $S^{\text{-}90^\circ}$. Knowing the phase shift ϕ, one can calculate S^{ψ} for any arbitrary phase shift ψ by

$$S^{\psi} = A\ \cos(\psi - \phi)\,. \tag{4.20}$$

The relation between lock-in frequency $f_{\text{lock-in}}$, sampling frequency f_{s} (which is practically the fixed camera frame rate f_{fr}) and the number n of images per lock-in period of length T is given by

$$f_{\text{lock-in}} = \frac{f_{\text{s}}}{n} = \frac{1}{T}. \tag{4.21}$$

The aforementioned Eq. (4.12) and 4.13 are valid for a harmonic response of the DUT. A discussion of the correlation factors $K_{\text{j}}^{0^\circ}$ and $K_{\text{j}}^{\text{-}90^\circ}$ for step-like stimulus and response can be found in [88]. Also in [88] it has been explained that the S^{45° signal is the most suitable one for the description of thin film modules. As shown in [88] the physical phase shift between response and stimulus in thin film modules turns out to be $\phi = 45°$ which is why S^{45° is the strongest measurable signal. Hence, S^{45° is the signal which I use within this work for DLIT measurements.

4.4.3 Heat Diffusion

As the DLIT measurement detects the sample temperature, it is not only of interest where the temperature within the sample is created (for instance in local shunts) due to power dissipation, but also how the temperature diffusion within the sample takes place (for example in the surrounding of the shunts).

Very detailed discussions of the heat diffusion can be found in Breitenstein [86] and Siegloch [88], which is why I only briefly summarize them. In order to quantitatively describe the thermal diffusion, thermal models are used [86, 88] with a simple point heat source on the surface of a solid. Furthermore, harmonically oscillating heating at the point heat source is assumed. With regard to the lock-in principle, the frequency is named $f_{\text{lock-in}}$, and the angular frequency is named $w_{\text{lock-in}} = 2\pi f_{\text{lock-in}}$, respectively. A heat wave can propagate into x, y and z direction within the solid, originating from the point heat source. The heat diffusion differential equation which describes the temperature difference ΔT between a position (x, y, z) and that of the point heat source is given by [88]

$$\Lambda^2 \left(\frac{\partial^2}{\partial x^2} + \frac{\partial^2}{\partial y^2} + \frac{\partial^2}{\partial z^2} \right) \Delta T = i\Delta T, \tag{4.22}$$

where t is the time and $i\Delta T$ is an imaginary part. Λ is the thermal diffusion length given by

$$\Lambda = \sqrt{\frac{\lambda}{\rho c_{\text{p}} \pi f_{\text{lock-in}}}}, \tag{4.23}$$

where λ is the heat conductivity, ρ is the solid's mass density, and c_{p} is the solid's specific heat capacity. The thermal diffusion length Λ causes a dampening of the heat wave (described by Eq. (4.22)) which depends on $f_{\text{lock-in}}$. For frequencies $f_{\text{lock-in}}$ = 1 Hz - 10 Hz, which are typically applied in DLIT measurements of thin film modules ([88], explained in Chapter 4.4.5), this dampening is strong. The strong dampening of the thermal diffusion is the reason for the improved spatial resolution of DLIT in contrast to steady-state thermography.

As long as Λ is smaller than the length and width of the area which is recorded by a pixel, the effect of heat diffusion can be neglected in DLIT images. However, if Λ becomes larger than the length and width of the area which is recorded by a pixel, a blurring of the heat signal will deteriorate the DLIT image.

4.4.4 DLIT Measurement Setup

The DLIT measurement setup is shown in Figure 4.4. Either a housing or a dark environment is used for protecting the setup from the ambient thermal radiation. In analogy to the EL measurement setup, the source-measure-unit (SMU), which sets J_{DLIT} and measures V_{DLIT}, is controlled by a human-machine-interface (HMI) (consisting of a personal computer, screen and input devices). The lock-in frequency $f_{\text{lock-in}}$ for the source-measurement-unit (SMU) and the camera is set via the HMI. The camera data is read out and processed by the signal processing, which is a software installed on the personal computer. The conductive tapes on the first and last cell of the substrates are connected to the cables of the SMU in four-terminal sensing mode.

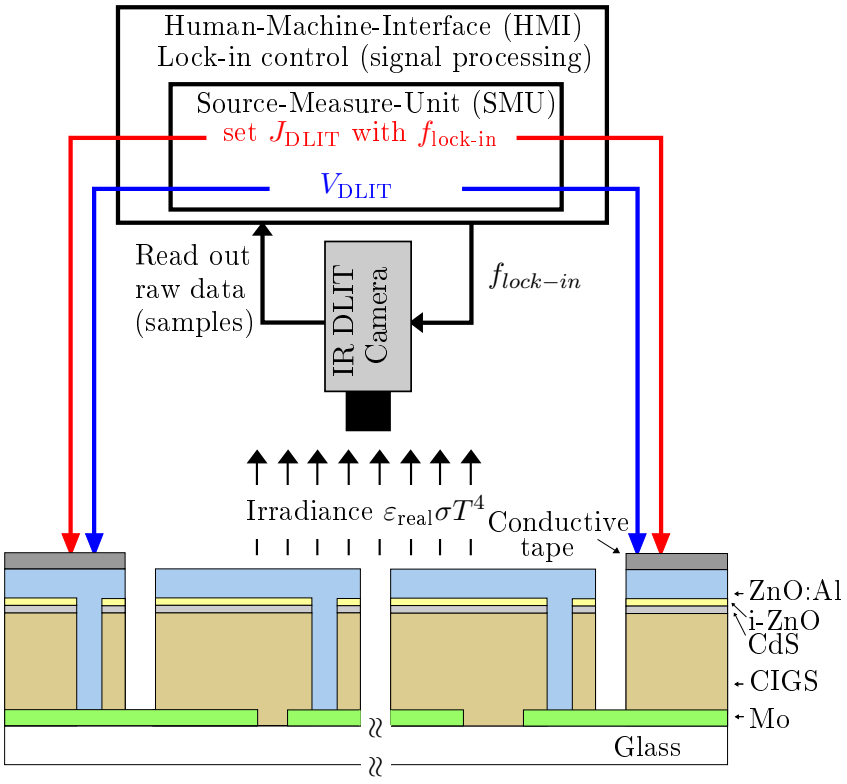

Figure 4.4: *Schematic DLIT setup. For the DLIT measurements an infrared (IR) thermography camera with a resolution of 288 x 288 pixels has been used. The current density J_{DLIT} is set by a SMU as the control variable. The measurement of the current/voltage is realized by a four-terminal sensing. The current/voltage is pulsed with $f_{lock\text{-}in}$ which is configured in the HMI. Furthermore, the IR camera receives $f_{lock\text{-}in}$ as trigger signal in order to synchronize $f_{lock\text{-}in}$ with the frame rate f_s of the camera. The measured samples, namely the raw data of the camera, are read out and further processed as introduced in Chapter 4.4.2.*

4.4.5 DLIT Measurement Practice

In the following I briefly introduce the role of the lock-in frequency $f_{\text{lock-in}}$ on DLIT measurements of thin film modules, as it has been published by Siegloch [88]. The given advantages and disadvantages constitute the choice of my own measurement practice.

According to Eq. (4.21), for a constant sampling frequency f_s (because in most cameras the frame rate f_{fr} is not changeable), a high lock-in frequency $f_{\text{lock-in}}$ in general results in a low number n of samples. A low number n of samples, however, leads to a poor signal approximation within a lock-in period T.

Siegloch [88] has shown that the lock-in thermography of thin film modules at frequencies $f_{\text{lock-in}} < 1$ Hz benefits from a high signal-to-noise ratio (SNR), due to the high n, and ,therefore, leads to a shorter measurement time. Nonetheless, the disadvantage is that due to heat

spreading within the DUT at low frequencies $f_{\text{lock-in}}$ a strong blurring at defects occurs in thermography images.

The opposite phenomena is observed for $f_{\text{lock-in}} > 10$ Hz: the SNR reduces due to a poor signal approximation within a lock-in period T while the spatial resolution close to the defects can be improved due to less heat spreading. Thus, Siegloch [88] suggests moderate frequencies $1\text{Hz} \leq f_{\text{lock-in}} < 10$ Hz which allow both a good SNR and a spatial resolution that can be compared to that for $f_{\text{lock-in}} > 10$ Hz. Note that a good SNR additionally reduces the total measurement time as less lock-in periods N are needed for averaging in order to improve the DLIT image.

For the aforementioned reasons I perform all my measurements at $f_{\text{lock-in}} = 1$ Hz for a number $n = 196$ of images. In [88] the use of $n > 100$ is recommended which is fulfilled hereby. All DLIT measurements are done using the S^{45° signal, according to the findings in [88]. I chose $N = 500$ lock-in periods which provides sufficient averaging by N x n, and I observe that the "on-the-fly" averaged thermography image practically does not change for more than $N = 200$ recorded single images - which means that N is chosen safely. I use sine/-cosine correlation factors $K_{\text{j}}^{0^\circ}$ and $K_{\text{j}}^{-90^\circ}$ as introduced in Chapter 4.4.2.

The control variable for DLIT measurements within this work is the current density J_{DLIT}. The short circuit current density $J_{\text{SC}} \approx 29$ mA/cm^2 was not exceeded during DLIT measurements for the sake of cell protection. Transient phenomena affecting the bulk and junction resistance, as published in [83], have been practically avoided by operating at $\mathrm{d}V/\mathrm{d}t = 0$. None of the samples was exposed to light before DLIT measurement because of the reasons introduced in Chapter 4.3.3. Before each measurement a dark-frame subtraction has been performed as introduced in Chapter 4.3.3.

A software-based correction of defective and therefore dark remaining pixels had to be performed as the used IR camera was affected by some dark pixels. The dark pixel correction was done by

$$S_{\text{corrected}} = \frac{1}{8} \sum_{i=1}^{8} S_{\text{i}}, \tag{4.24}$$

where $S_{\text{corrected}}$ is the signal of a dark pixel after correction, and S_{i} is the correspondent signal of each pixel in the surrounding of the dark pixel. Hence, the signals in the surrounding eight pixels are averaged, and the obtained average is allocated to the defective pixel.

Chapter 5

Network Simulation Model

"The purpose of this chapter is to introduce the software that I have implemented in this work. This software is based on the network simulation model (NSM) and allows to model and simulate defects and their influence on voltages and currents in a module, and therefore also to simulate the correspondent EL and DLIT images."

5.1 Introduction

A network simulation model (NSM) allows to model a CIGS module, simulate various operation modes (both forward and reverse bias under both illumination and in the dark), and simulate the correspondent EL and DLIT images. Network simulation models have already been used before by several groups in order to model solar cells or complete thin-film modules [85, 90–92].

I use the simulated current flow (which allows to draw current vector fields) and simulated voltage distribution (which allows to draw voltage surface plots) for a better understanding and interpretation of real EL and DLIT images, as it will be shown in the case of scribing defects in Chapter 6.3.

Furthermore, a NSM makes it possible to implement defects of various types into the module and simulate the defect's influence on the module's electrical parameters like e.g. the efficiency η or open circuit voltage V_{OC}.

The simulations add to the experimental investigations of Cu-rich debris (as will be shown in Chapter 7.6) and of scribing defects (as will be shown in Chapter 6.3.2) the ability to continuously adjust defect parameters like the shunt resistance for Cu-rich debris and the scribing line interruption length for scribing defects. This is a significant benefit as in contrast any set of real experiments is practically limited by time and costs.

This Chapter is therefore devoted to the introduction of the NSM and to the explanation of its working principle.

5.2 Network Circuit

The NSM can be regarded as a translation of the CIGS layer structure into an electrical equivalent circuit. The electrodes, namely the TCO front and the Mo back contact, are represented by networks of resistances. These two electrodes are at every segment (see Figure 5.1) in the network connected by the equivalent circuit of a solar cell (Chapter 2.2.2). Furthermore, the NSM models the monolithic series connection (Chapter 2.3) of the CIGS module.

Figure 5.1 (a) illustrates schematically the monolithic series connection of three cells and (b) its representation in the NSM.

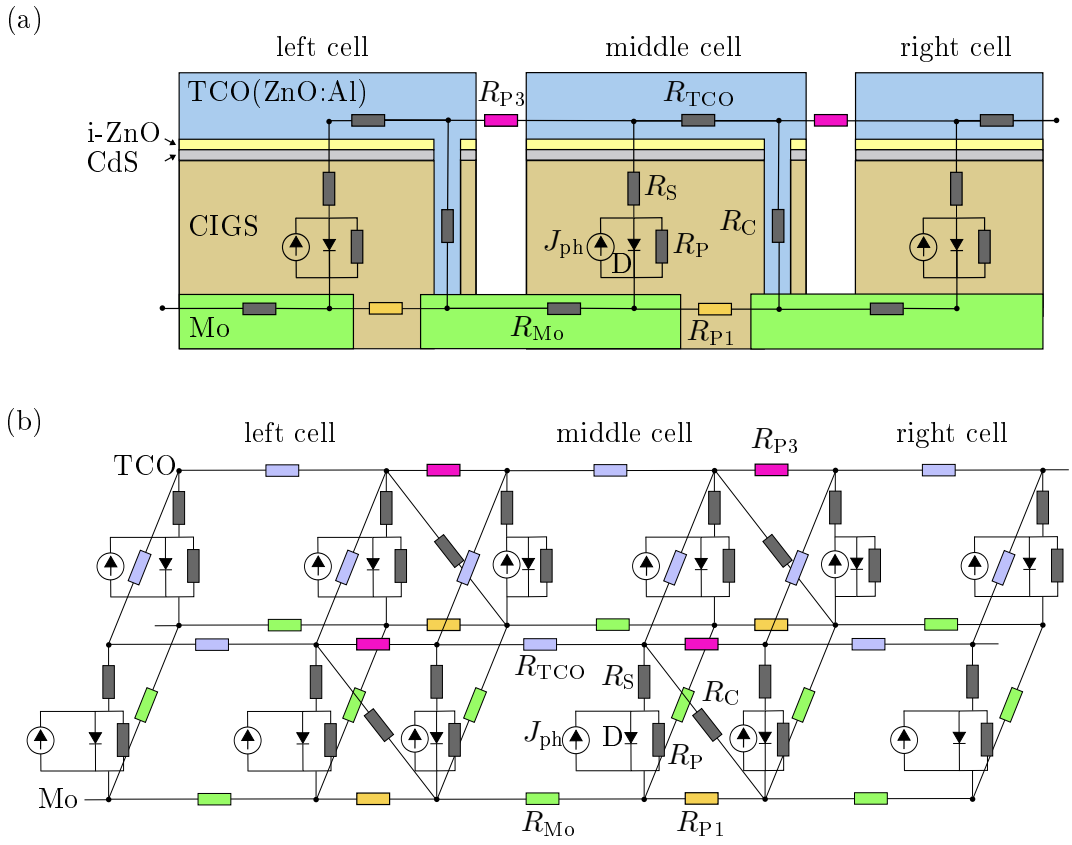

Figure 5.1: *NSM models CIGS module. (a) Layer structure and monolithic series connection in a CIGS module. (b) Example for a NSM that has two rows and six columns which form twelve segments, of which each contains the equivalent circuit of a solar cell.*

In Figure 5.1 the electronic components are labelled only within the middle cell for the sake of clarity. The equivalent circuit of a single solar cell [93] contains the parallel resistance R_P, the series resistance R_S, the diode D, and the photo current source driving J_{ph}. The resistance of the TCO front contact and the Mo back contact is represented by R_{TCO} and R_{Mo}. The contact resistance between the cells, located in the P2 scribing line (Chapter 3.2.9), is taken into account with R_C. The insulation of the cells, located in the P1 (insulation of Mo back contacts) and P3 (insulation of TCO front contact) scribing lines, is taken into account with R_{P1}, and R_{P3} respectively.

Figure 5.2 shows the geometry parameters that are used for the calculation of the network components inside a cell.

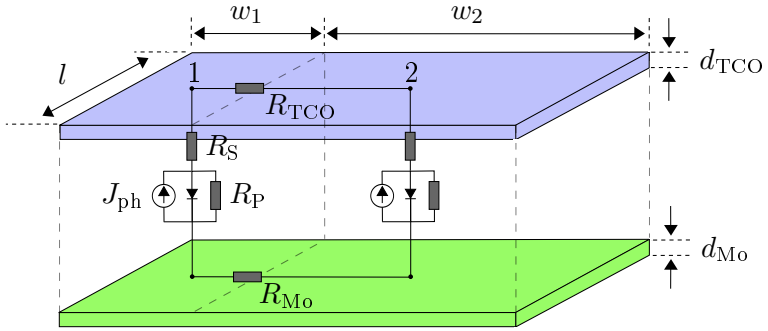

Figure 5.2: *Geometry parameters used for the calculation of network components inside a cell. Two neighbouring segments "1" and "2" are shown which are connected within the TCO front contact layer by R_{TCO}, and within the Mo back contact layer by R_{Mo}.*

Figure 5.2 illustrates two segments, labelled by 1 and 2, inside a cell. Both segments have the same length l, layer thickness d_{TCO} of the front contact and d_{Mo} of the back contact, while the left segment has a smaller width $w_1 < w_2$. For the sake of clarity only the network connections alongside the width are drawn, but not alongside the length. Nodes 1 and 2 are in the centres of the correspondent segment areas. In the following the calculation of the segment parameters is exemplified for the left segment. The photo current is calculated by

$$I_{\mathrm{ph}} = J_{\mathrm{sc}} A_1 = J_{\mathrm{sc}} w_1 l, \tag{5.1}$$

where J_{sc} [mA/cm^2] is the short circuit current density, and $A_1 = l w_1$ is the area of the left segment. The short circuit current density J_{sc} has been measured (see Table 5.1 further below). The shown CIGS series resistance is

$$R_{\mathrm{S}} = \frac{\rho_{\mathrm{CIGS,ser}}}{A_1} = \frac{\rho_{\mathrm{CIGS,ser}}}{w_1 l}, \tag{5.2}$$

with the specific series resistivity of the CIGS absorber $\rho_{\mathrm{CIGS,ser}}$ [Ωm^2]. The value for $\rho_{\mathrm{CIGS,ser}}$ is based on measurements, too (Table 5.1). The CIGS parallel resistance

$$R_{\mathrm{P}} = \frac{\rho_{\mathrm{CIGS,par}}}{A_1} = \frac{\rho_{\mathrm{CIGS,par}}}{w_1 l} \tag{5.3}$$

can be obtained by applying the specific parallel resistivity of the CIGS absorber $\rho_{\mathrm{CIGS,par}}$ [Ωm^2] (Table 5.1). The TCO network resistance R_{TCO} is given by

$$R_{\mathrm{TCO}} = \rho_{\mathrm{TCO}} \left(\frac{w_1 + w_2}{2} \right) \frac{1}{l \cdot d_{\mathrm{TCO}}}, \tag{5.4}$$

where ρ_{TCO} [Ωm] is the specific ZnO:Al resistivity of the TCO front contact (Table 5.1). As shown, different segment widths w and lengths l, as they are needed for the mesh variation

around defects, which will be shown in Chapter 5.7, are taken into account when calculating the network resistances. The Mo network resistance is calculated in analogy to Eq. (5.4).

Figure 5.3 illustrates the calculation of the network components at a cell transition.

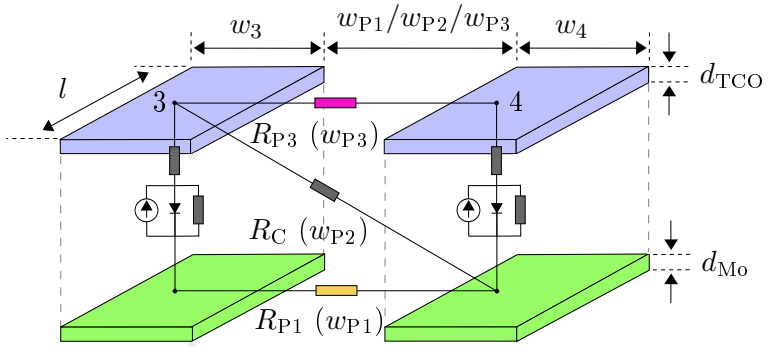

Figure 5.3: *Geometry parameters used for the calculation of network components at a cell transition between segments "3" and "4".*

In Figure 5.3 the scribing line width w_{P1} is used for the calculation of the isolation resistance

$$R_{P1} = \left(\rho_{Mo}\frac{w_3}{2} + \rho_{P1}w_{P1} + \rho_{Mo}\frac{w_4}{2}\right)\frac{1}{l \cdot d_{Mo}} \tag{5.5}$$

in the P1 scribing line with the specific isolation resistivity ρ_{P1} [Ωm]. Note that although the P1 scribing line is basically filled with CIGS absorber material, its conductivity is different from the absorber volume because of the different CIGS growth inside of the P1 line. Consequently, the isolation resistance in the P3 scribing line is

$$R_{P3} = \left(\rho_{TCO}\frac{w_3}{2} + \rho_{P3}w_{P3} + \rho_{TCO}\frac{w_4}{2}\right)\frac{1}{l \cdot d_{TCO}}. \tag{5.6}$$

The contact resistance between the two cells is

$$R_C = \rho_{TCO}\frac{w_3}{2}\frac{1}{l \cdot d_{TCO}} + \rho_C\frac{1}{l \cdot w_{P2}} + \rho_{Mo}\frac{w_4}{2}\frac{1}{l \cdot d_{Mo}}, \tag{5.7}$$

where ρ_C [Ωm^2] is the measured contact resistance when depositing ZnO:Al on Mo (Table 5.1).

Table 5.1: *Simulation parameters for the network simulation model, all measured at Manz CIGS Technology GmbH.*

Parameter	Symbol	Value	Reference
Short circuit current density	j_{SC}	290 Am^{-2}	measured
TCO resistivity	ρ_{TCO}	7.0 x 10^{-5} Ωm	measured
Mo resistivity	ρ_{Mo}	54 x 10^{-9} Ωm	measured
CIGS series resistivity	$\rho_{CIGS,\,ser}$	6.0 x 10^{-5} Ωm^2	measured
CIGS parallel resistivity	$\rho_{CIGS,\,par}$	0.11 Ωm^2	measured
P3-TCO isolation resistivity	ρ_{P3}	2.0 x 10^{10} Ωm	measured
P2-Cell contact resistivity	ρ_{C}	5.0 x 10^{-7} Ωm^2	measured
P1-Mo isolation resistivity	ρ_{P1}	2.0 x 10^{10} Ωm	measured

5.3 Solving the Network's System of Equations

5.3.1 Introduction

The NSM translates the network circuit into a system of equations (SOE). This Chapter presents the SOE and shows how it can be solved. For the sake of simplicity, in the following a simplified network is used which contains a single cell with only two segments, as shown in Figure 5.4.

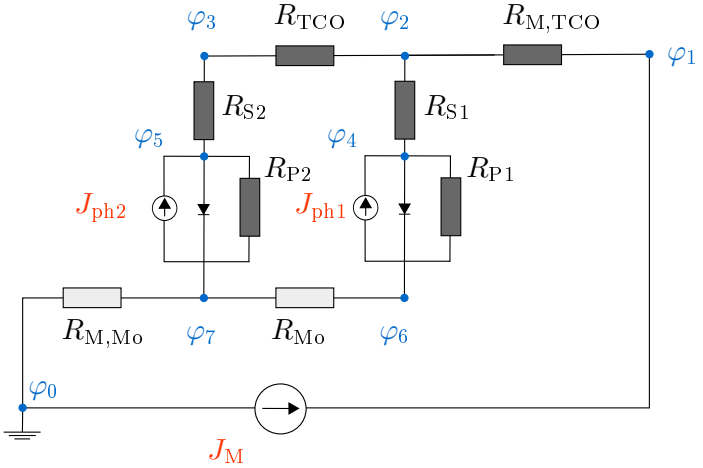

Figure 5.4: *Simplified network consisting of only one cell with only two segments.*

In Figure 5.4 the module entrance/exit resistances $R_{M,TCO}$ and $R_{M,Mo}$ have been added in order to take into account the voltage loss at the connection box at the back of the module. The potential φ_0 is grounded and J_M denotes the module current. The circuit in Figure 5.4 represents all relevant components of the NSM and leads to a small SOE which facilitates its discussion in the following. First, the standard Newton-Raphson procedure is introduced

as it is usually applied in non-linear circuit analysis. Afterwards, I show an alternative approach that I have developed in this work.

5.3.2 Standard Newton-Raphson Procedure

Applying Kirchhoff's current law (KCL) to the circuit in Figure 5.4 yields the following SOE

$$\begin{aligned}
-\frac{\varphi_1-\varphi_2}{R_{\mathrm{M,TCO}}}+J_{\mathrm{M}}&=0\\
-\frac{\varphi_2-\varphi_3}{R_{\mathrm{TCO}}}-\frac{\varphi_2-\varphi_4}{R_{\mathrm{S1}}}+\frac{\varphi_1-\varphi_2}{R_{\mathrm{M,TCO}}}&=0\\
-\frac{\varphi_3-\varphi_5}{R_{\mathrm{S2}}}+\frac{\varphi_2-\varphi_3}{R_{\mathrm{TCO}}}&=0\\
-\frac{\varphi_4-\varphi_6}{R_{\mathrm{P1}}}-J_{01}\left(\exp\left(\frac{q\left(\varphi_4-\varphi_6\right)}{nk_BT}\right)-1\right)+J_{\mathrm{ph1}}+\frac{\varphi_2-\varphi_4}{R_{\mathrm{S1}}}&=0\\
-\frac{\varphi_5-\varphi_7}{R_{\mathrm{P2}}}-J_{02}\left(\exp\left(\frac{q\left(\varphi_5-\varphi_7\right)}{nk_BT}\right)-1\right)+J_{\mathrm{ph2}}+\frac{\varphi_3-\varphi_5}{R_{\mathrm{S2}}}&=0\\
-\frac{\varphi_6-\varphi_7}{R_{\mathrm{Mo}}}+J_{01}\left(\exp\left(\frac{q\left(\varphi_4-\varphi_6\right)}{nk_BT}\right)-1\right)-J_{\mathrm{ph1}}+\frac{\varphi_4-\varphi_6}{R_{\mathrm{P1}}}&=0\\
-\frac{\varphi_7}{R_{\mathrm{Mo}}}+J_{02}\left(\exp\left(\frac{q\left(\varphi_5-\varphi_7\right)}{nk_BT}\right)-1\right)-J_{\mathrm{ph2}}+\frac{\varphi_5-\varphi_7}{R_{\mathrm{P2}}}&=0,
\end{aligned} \tag{5.8}$$

which can be expressed by

$$\boldsymbol{g}(\boldsymbol{\varphi})=0. \tag{5.9}$$

Eq. (5.9) can be solved by applying the Newton-Raphson procedure [94]

$$\boldsymbol{\varphi}^{(\nu+1)}=\boldsymbol{\varphi}^{(\nu)}-\boldsymbol{J}_{\mathrm{jac}}^{-\mathbf{1}}\left(\boldsymbol{\varphi}^{(\boldsymbol{\nu})}\right)\boldsymbol{g}\left(\boldsymbol{\varphi}^{(\nu)}\right), \tag{5.10}$$

where ν denotes the iteration step. The Jacobian is labelled by the index "jac" for better distinction from the currents in the circuit. For the SOE in Eq. (5.9) the Jacobian can be written as

$$\boldsymbol{J}_{\mathrm{jac}}\left(\boldsymbol{\varphi}^{\nu}\right)=\begin{bmatrix}
\frac{\partial g_1}{\partial\varphi_1^{\nu}} & \frac{\partial g_1}{\partial\varphi_2^{\nu}} & \cdots & \frac{\partial g_1}{\partial\varphi_7^{\nu}}\\
\frac{\partial g_2}{\partial\varphi_1^{\nu}} & \ddots & \cdots & \cdots\\
\vdots & \cdots & \ddots & \cdots\\
\frac{\partial g_7}{\partial\varphi_1^{\nu}} & \cdots & \cdots & \frac{\partial g_7}{\partial\varphi_7^{\nu}}
\end{bmatrix} \tag{5.11}$$

The computational cost for inverting the Jacobian is n^3 long operation counts, where one long operation count means the multiplication of one matrix element with one vector element [94]. In order to avoid the computational cost of inverting the Jacobian in each iteration step, as it is required in Eq. (5.10), one can alternatively either solve

$$\boldsymbol{J}_{\mathrm{jac}}\left(\boldsymbol{\varphi}^{(\boldsymbol{\nu})}\right)\left(\boldsymbol{\varphi}^{(\nu)}-\boldsymbol{\varphi}^{(\nu+1)}\right)=\boldsymbol{g}\left(\boldsymbol{\varphi}^{(\nu)}\right) \tag{5.12}$$

or

$$\boldsymbol{J}_{\mathrm{jac}}\left(\boldsymbol{\varphi}^{(\nu)}\right)\boldsymbol{\varphi}^{(\nu+1)} = \boldsymbol{J}_{\mathrm{jac}}\left(\boldsymbol{\varphi}^{(\nu)}\right)\boldsymbol{\varphi}^{(\nu)} - \boldsymbol{g}\left(\boldsymbol{\varphi}^{(\nu)}\right). \tag{5.13}$$

In both Eq. (5.12) and (5.13) the Jacobian needs to be recalculated in each iteration step after it has been inverted only once at the beginning of the numerical calculation. The Jacobian is usually highly sparse which is why sparse matrix techniques are used. For both Eq. (5.12) and (5.13) the Gaussian elimination method (GEM) is applied. The Newton-Raphson procedure is known to converge fast and reliably if the initial guess is good enough [95].

5.3.3 Alternative Approach

In this work I have tried out an alternative approach without the above introduced Newton-Raphson procedure. As shown in Figure 5.5 the electrical equivalent circuit of a solar cell can be replaced by a voltage source.

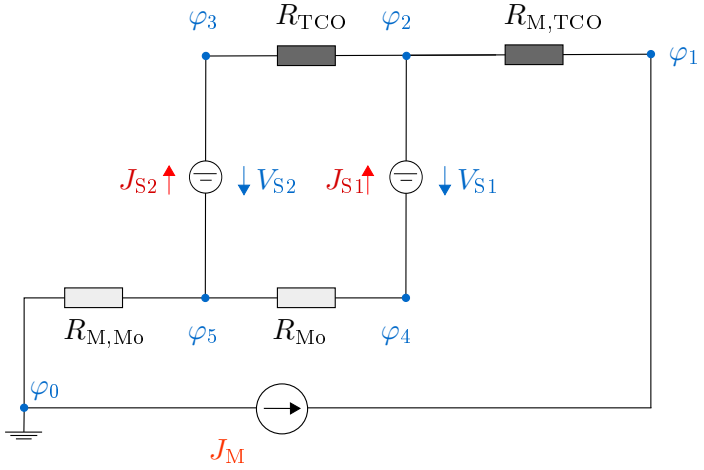

Figure 5.5: *Replacement of the solar cell's equivalent circuit by a voltage source. The replacement reduces the number of nodes per segment by one.*

The replacement of the solar cell's equivalent circuits by the voltage sources V_{S1} and V_{S2} reduces the number of nodes per segment by one. Application of the KCL leads to the following SOE

$$\begin{aligned}
-\frac{\varphi_1-\varphi_2}{R_{\mathrm{M,TCO}}} + J_{\mathrm{M}} &= 0\\
-\frac{\varphi_2-\varphi_3}{R_{\mathrm{TCO}}} + \frac{\varphi_1-\varphi_2}{R_{\mathrm{M,TCO}}} + J_{\mathrm{S1}} &= 0\\
+\frac{\varphi_2-\varphi_3}{R_{\mathrm{TCO}}} + J_{\mathrm{S2}} &= 0\\
-\frac{\varphi_4-\varphi_5}{R_{\mathrm{Mo}}} - J_{\mathrm{S1}} &= 0\\
-\frac{\varphi_5}{R_{\mathrm{M,Mo}}} + \frac{\varphi_4-\varphi_5}{R_{\mathrm{Mo}}} - J_{\mathrm{S2}} &= 0\\
\varphi_2-\varphi_4 &= V_{\mathrm{S1}}\\
\varphi_3-\varphi_5 &= V_{\mathrm{S2}}.
\end{aligned} \tag{5.14}$$

In Eq. (5.14) the currents through the passive elements are represented by potential differences $\varphi_x - \varphi_y$ at resistors, and the only currents, namely J_{S1}, J_{S2} and J_M, are driven by the voltage/current sources. Each voltage source is expressed by a node potential difference in a correspondent equation. This procedure is in accordance with the modified nodal analysis (MNA) [96, 97] which allows to handle current/voltage sources without having to transform them into their Norton's equivalent according to Norton's theorem [98]. Eq. (5.14) can be written in matrix form as

$$\begin{bmatrix} -1/R_{M,TCO} & 1/R_{M,TCO} & 0 & 0 & 0 & 0 & 0 \\ 1/R_{M,TCO} & -1/R_{TCO} - 1/R_{M,TCO} & 1/R_{TCO} & 0 & 0 & +1 & 0 \\ 0 & 1/R_{TCO} & -1/R_{TCO} & 0 & 0 & 0 & +1 \\ 0 & 0 & 0 & -1/R_{Mo} & 1/R_{Mo} & -1 & 0 \\ 0 & 0 & 0 & 1/R_{Mo} & -1/R_{M,Mo} - 1/R_{Mo} & 0 & -1 \\ 0 & +1 & 0 & -1 & 0 & 0 & 0 \\ 0 & 0 & +1 & 0 & -1 & 0 & 0 \end{bmatrix} \begin{bmatrix} \varphi_1 \\ \varphi_2 \\ \varphi_3 \\ \varphi_4 \\ \varphi_5 \\ J_{S1} \\ J_{S2} \end{bmatrix} = \begin{bmatrix} -J_M \\ 0 \\ 0 \\ 0 \\ 0 \\ V_{S1} \\ V_{S2} \end{bmatrix} \tag{5.15}$$

and Eq. (5.15) can be generalised as

$$\begin{bmatrix} & Y & & \cdots & \cdots \\ & & & \cdots & \cdots \\ & & & \cdots & \cdots \\ & & & \cdots & \cdots \\ & & & \cdots & \cdots \\ \vdots & \vdots & \vdots & \vdots & \vdots & \ddots & \cdots \\ \vdots & \vdots & \vdots & \vdots & \vdots & \vdots & \ddots \end{bmatrix} \begin{bmatrix} \varphi \\ J_S \end{bmatrix} = \begin{bmatrix} -J_M \\ 0 \\ 0 \\ 0 \\ 0 \\ V_S \end{bmatrix} \tag{5.16}$$

On the left side of the equation the section $[Y]$ contains the nodal admittance matrix, the dots represent either 0, or -1, or +1. The section $[\varphi]$ contains the node potentials, while the section $[J_S]$ contains the segments currents. On the right side of the equation there is only the module current J_M (which is the constant control variable of the simulation), and the section $[V_S]$ contains the segment voltages.

The initial guess in the iteration $\nu = 0$ is made for the segment voltages $\boldsymbol{V}_S^{\nu=0} = \boldsymbol{V}_{MPP}$, where V_{MPP} is the voltage in the MPP. The SOE is solved by applying the GEM and the LU factorisation [99–101]. A detailed introduction of the LU factorisation is attached in Appendix A. After each iteration step ν, new potentials $\boldsymbol{\varphi}^\nu$ and segment currents $\boldsymbol{I}_S^\nu$ are available and inserted into

$$\boldsymbol{V}_S^{\nu+1} = \frac{nk_BT}{q} log\left(\frac{\boldsymbol{J}_{ph} - \boldsymbol{J}_S^\nu - \left(\boldsymbol{V}_S^\nu + \boldsymbol{J}_S^\nu R_S\right)/R_P}{\boldsymbol{J}_0} + 1\right), \tag{5.17}$$

where $\boldsymbol{J}_0$ denotes the saturation currents in the segments. Eq. (5.17) yields the segment voltages $\boldsymbol{V}_S^{\nu+1}$ for the next iteration step $\nu+1$. Due to the exponential diode behaviour, small changes in $\boldsymbol{V}_S^\nu$ can have a huge impact on $\boldsymbol{J}_S^\nu$. This is taken into account by limiting the allowed voltage/current step per iteration.

5.4 Efficient Matrix Processing

In order to process the resulting matrices efficiently, I take the following three measures: (i) I use sparse matrices. Furthermore, (ii) for a smallest possible memory allocation when initialising a sparse matrix, the number of non-zero elements in the matrix is assigned as a size hint. The size hint is possible because I use a predetermined mesh, which I introduce in Chapter 5.7, and therefore all links in the network (determining the number of non-zero matrix entries) are predetermined, too. (iii) The left-hand side matrix in Eq. (5.16) is symmetrical which is why I save and process only the upper part. This both saves allocated memory and increases the speed of all matrix related operations like multiplications.

5.5 Simulation Performance

Figure 5.6 shows the simulation performance of the NSM developed in this work. The number of iterations (blue points belonging to left y-axis) and the total simulation duration (red circles belonging to right y-axis) are shown as functions of the number n of equations on the x-axis.

A defect free module is modelled and the number of cells is increased in order to increase the number of equations, while keeping the number of rows and columns per cell constant. The applied termination criterion is

$$\max|\boldsymbol{\varphi}^{(\nu+1)} - \boldsymbol{\varphi}^{(\nu)}| \leq 1\ \mu\mathrm{V} \tag{5.18}$$

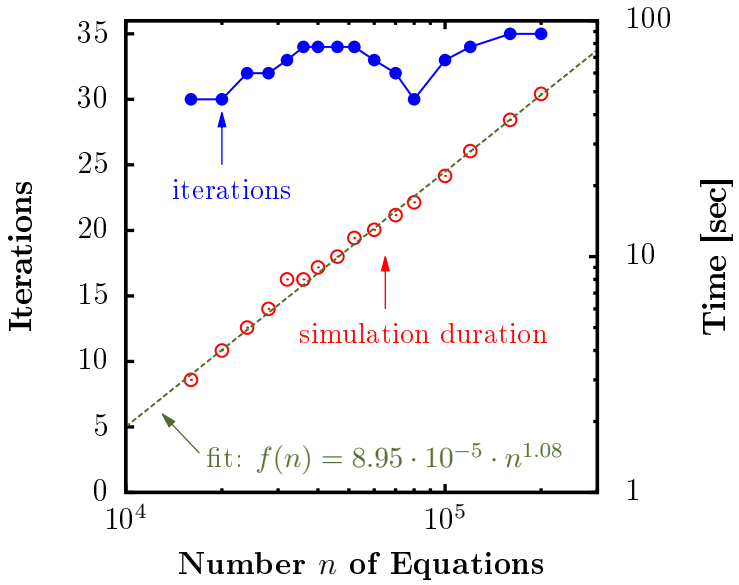

Figure 5.6: *Simulation performance of the NSM developed in this work. A defect free module is simulated. The number of cells is increased in order to increase the number of equations n. Blue points represent the number of iterations till convergence. Red circles represent the simulation duration and are fitted by the green dashed line. The fit shows that the simulation duration scales almost linearly with the number of equations.*

The simulation duration is fitted (green dashed line belonging to right y-axis) by

$$\begin{aligned} f(n) &= a \cdot n^b \\ &= 8.95 \cdot 10^{-5} \cdot n^{1.08} \end{aligned} \tag{5.19}$$

in gnuplot [102]. As the simulation is calculated on one core of the central processing unit (CPU), a linear scaling of the simulation duration, which equals $b = 1$, would be the best possible result one can obtain. The aforementioned fitting shows that my simulation comes quite close to this optimum with $b = 1.08$.

For implementations of network simulation models, which have been used for the modelling of photovoltaic devices, several values for b have already been reported like $b = 2..3$ in [103] and $b = 2$ in [6]. Thus, my approach, as introduced in Chapter 5.3.3, in combination with the efficient matrix processing, as introduced in Chapter 5.4, turns out to be advantageous for large scale simulations as it comes with a slope of $b = 1.08$ close to the theoretical optimum of linearity for calculations on one CPU core.

The actual simulation time increases if e.g. a severe shunt is modelled, as it is done for instance in Chapter 5.10. Then the NSM needs more iterations for the numerical calculation of the transition from defect-free to defective segments.

5.6 Comparison of Approaches

Both approaches, shown in Chapter 5.3.2 and 5.3.3, basically linearise a non-linear SOE.

Furthermore, both approaches lead to SOEs with the same number of equations n. Although the alternative approach reduces the number of nodes per segment from three to two, one equation per segment is added to the SOE for each voltage source due to the convention of the MNA.

Moreover, both approaches are basically fixed-point iterations, where

$$\boldsymbol{\varphi}^{(\nu+1)} = \boldsymbol{g}(\boldsymbol{\varphi}^{(\nu)}) \tag{5.20}$$

leads to a sequence $\boldsymbol{\varphi}^{(0)}$, $\boldsymbol{\varphi}^{(1)}$, $\boldsymbol{\varphi}^{(2)}$, ... that eventually converges to $\boldsymbol{\varphi}^{(\nu+1)} \approx \boldsymbol{\varphi}^{(\nu)}$.

My original interest was to try out an alternative approach that could reduce the long operation counts. This interest arised when studying the work of McCalla [94]. McCalla discusses different approaches to solve linear and non-linear SOEs in terms of long operation counts. He describes that Eq. (5.12) and (5.13) are used instead of Eq. (5.10) in order to avoid the costly inversion of the Jacobian in each iteration step. He furthermore explains, that the Gaussian elimination method (GEM) is applied to Eq. (5.12) and (5.13), while the LU factorisation can not be applied, as the Jacobian is recalculated in each iteration step. This leads to the total long operation count of

$$\Upsilon_{\mathrm{Jac,GEM}} = m_{\mathrm{J}} \cdot \left(\frac{n^3}{3} + n^2 - \frac{n}{3} \right) \tag{5.21}$$

for m_{J} iterations until convergence for Eq. (5.12) and (5.13). In contrast, the alternative approach, developed in this work, uses a LU factorisation and has a total long operation count of

$$\Upsilon_{\mathrm{LU}} = \frac{n^3}{3} + m_{\mathrm{LU}} \cdot n^2 - \frac{n}{3} \tag{5.22}$$

for m_{LU} iterations until convergence. However, McCalla also claims that matrix processing techniques, like e.g. sparse matrix techniques or pivoting strategies, have a much stronger influence on the computational cost than the theoretical number of long operations counts, as expressed by Eq. (5.21) and (5.22).

That this is indeed the case can be seen from the almost linear scaling I found for my tool with the number of equations, which is considerably better than the predicted scaling according to Eq. 5.22. For this reason a proper comparison of the computational cost is a numerical mathematics problem and as such falls beyond the scope of this thesis.

However, I have demonstrated an alternative approach which provides a reliable numerical analysis (as will be shown in Chapter 5.10) and scales very well with the number of equations.

5.7 Network Mesh Variation

5.7.1 Introduction

In order to model defects, which are small compared to the module size, the network mesh must provide segment sizes at the defect position that are sufficiently small. Finding an appropriate network mesh density has to take into account the following two aspects: (i) The smallest segment sizes are usually located at the defect position. Pieters [6] has shown that the defect must be modelled by more than one segment in order to reduce the simulation error. (ii) The computational time of a simulation increases with the number of equations in a SOE [103, 104].

An evenly spaced mesh, which fulfils the condition of aspect (i), puts a limitation to problem sizes and accuracy due to aspect (ii). This problem can be mitigated if the mesh is not evenly spaced but provides more segments in the region of the defect and less further away. Further away from the defect, where there is practically no defect influence any more, the mesh can be less dense. Hence, I implement a variable mesh in the NSM which is introduced in the following. The characteristic of this variable mesh is that it is predetermined with regard to its smallest segment at the defect position. This is in contrast to the approach of a self-adapting mesh that has been published in [6]. As [6] provides an even more appropriate solution to the problem, which arises from aspects (i) and (ii), Chapter 5.7.3 is dedicated to it.

5.7.2 Predetermined Mesh Variation

Figure 5.7 illustrates how the mesh variation around a defect looks like. The shown rectangles symbolise single segments. The red coloured segments represent the defect, e.g. segments with a

reduced parallel CIGS absorber resistance. For each simulation in this work a region of highest mesh density at the defect position is chosen, as shown by the blue rectangle, in order to reduce the simulation error. Within the blue rectangle all segments have the size of the smallest segment.

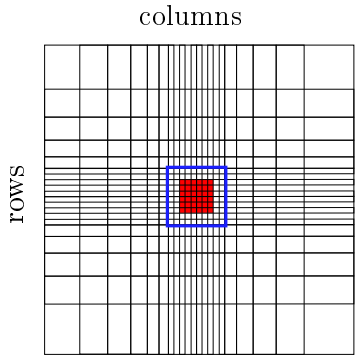

Figure 5.7: *Predetermined variation of rows and columns. The area spanned by the smallest segments (indicated by the blue rectangle) is in every simulation chosen larger than the defect itself (red area) in order to reduce the simulation error according to [6].*

Further away from the defect, both the row size (vertically) and column size (horizontally) of the segments increase. I choose the term "predetermined mesh variation" as the scaling of rows and columns is calculated with a fixed set of equations that are introduced in the following. Figure 5.8 exemplifies the predetermined row variation both schematically and as a simulation result.

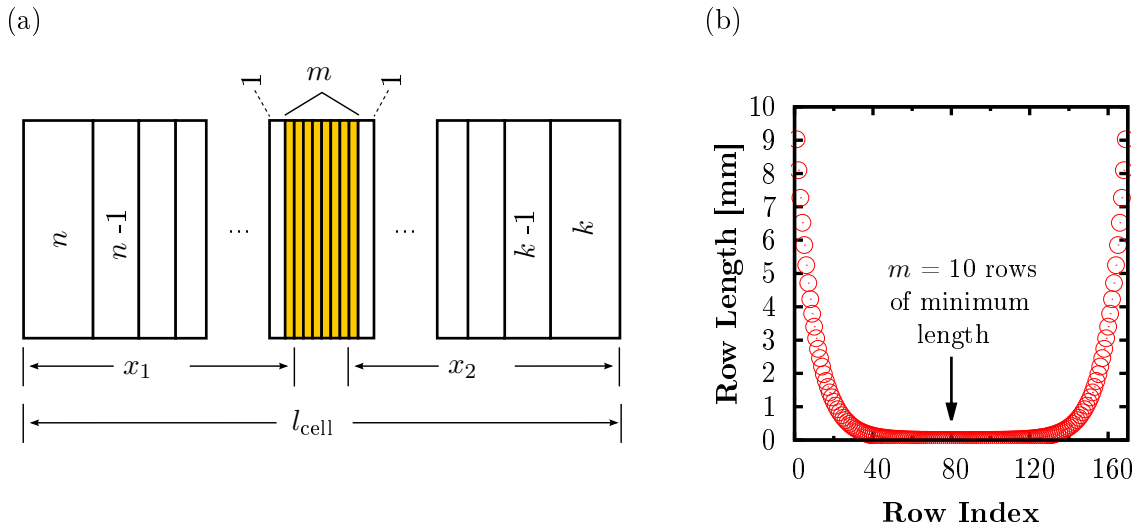

Figure 5.8: *Predetermined variation of rows. (a) Schematic visualisation of predetermined row variation, where $m = 10$ rows of minimum length are positioned at the defect position at the cell centre in order to reduce the simulation error. Further away the row lengths increase. (b) Visualisation of resulting row lengths.*

In Figure 5.8 (a) m rows of constant and minimum length are shown (filled with yellow colour). To the left there are n rows and to the right k rows to be scaled. The further away, with regard to

the m rows, the longer the rows become. The scaling of the left side can be described by

$$\begin{aligned} x_1 &= r_{\min} + r_{\min} \cdot f^1 + r_{\min} \cdot f^2 + ... + r_{\min} \cdot f^{n-1} + r_{\min} \cdot f^n \\ &= r_{\min} \left(1 + \sum_{i=1}^{n} f^i \right), \end{aligned} \tag{5.23}$$

where $r_{\min}$ is the minimum row length and f is a scaling factor. In the same way the right side is given by

$$x_2 = r_{\min} \left(1 + \sum_{j=1}^{k} p^j \right), \tag{5.24}$$

where p is the scaling factor for the right side. The total cell length l_{cell} is given by

$$\begin{aligned} l_{\text{cell}} &= x_1 + r_{\min}(m-2) + x_2 \\ &= r_{\min} \left(1 + \sum_{i=1}^{n} f^i \right) + r_{\min}(m-2) + r_{\min} \left(1 + \sum_{j=1}^{k} p^j \right). \end{aligned} \tag{5.25}$$

If the m rows of minimum length are placed symmetrically in the centre of the cell, then Eq. (5.25) can be simplified by

$$l_{\text{cell}} = r_{\min} \left(m + 2 \sum_{i=1}^{n} f^i \right). \tag{5.26}$$

Furthermore, the NSM supports the modelling of periodically distributed defects. This allows for instance to investigate the influence of a defect density on the device efficiency, as I have shown in a previous work [105]. The variation of rows in case of two periodically distributed defects is shown schematically in Figure 5.9.

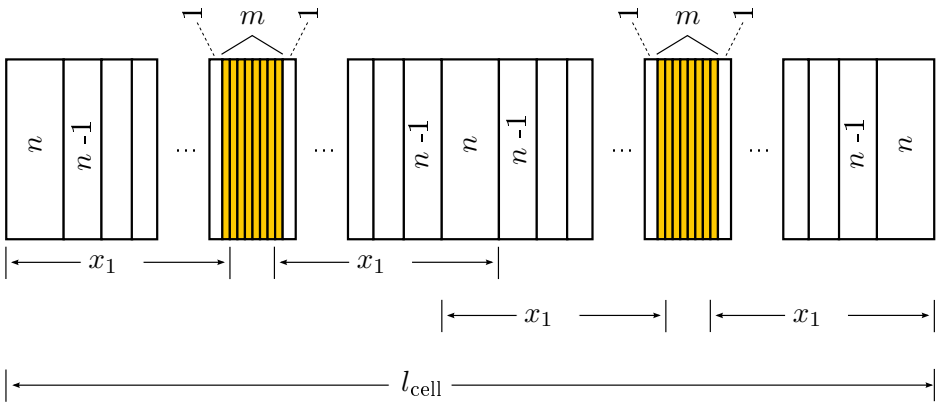

Figure 5.9: *Predetermined periodic variation of rows. Schematic visualization of periodic variation of row lengths for two defects. The shown variation allows to investigate the influence of defect densities on the device efficiency.*

For an arbitrary number a of periodically distributed defects one can write

$$\begin{aligned} l_{\text{cell}} &= 2ax_1 - r_{\min} f^n (a-1) + a (m-2) r_{\min} \\ &= r_{\min} \left[2a \left(1 + \sum_{i=1}^{n-1} f^i \right) + f^n (1+a) + a (m-2) \right]. \end{aligned} \tag{5.27}$$

Equations (5.25) and (5.27) show the calculation of the row and column variation. The scaling factors f and p are calculated based on the variables m, n and $r_{\min}$ which are manually set before the simulation start. Note that I have performed numerous tests to ensure that despite changes of the variables m, n and $r_{\min}$, and therefore the mesh density, the numerical calculation converges to approximately the same solution within reasonable ranges of set row and column numbers.

The manual setting of the variables m, n and $r_{\min}$ is the main disadvantage of the pre-determined mesh variation as the best values for m, n and $r_{\min}$ depend on the modelled defect and its parameters. In order to be on the safe side, the correspondent number m for rows and columns has always been chosen so that the area with smallest segments exceeds the correspondent defect area. This, however, unavoidably impairs the benefit of the scaling of rows and columns with regard to network size and computational time. Hence, the following Chapter 5.7.3 briefly shows another approach (developed in [6]) which addresses the question for the most suitable mesh.

5.7.3 Adaptive Mesh Variation

There are two different approaches to adaptive meshes: (i) The use of sub-grids and (ii) the application of adaptive meshing. A prominent example for (i) is the PARAMESH package (for the programming language Fotrtran 90) which has been published in [106]. PARAMESH subsequently creates "grids within grids", therefore sub-grids, at positions in the mesh where higher mesh densities are needed, and allows to solve the grids with parallel computing.

In contrast, (ii) adaptive meshing, as introduced by Pieters in [6], refines the mesh at certain positions and generates only one new grid that has to be solved in the next step. Hence, while approach (i), e.g. PARAMESH, works with multiple grids, which are typically all of the same size in order to run the same code on multiple cores of the CPU, the approach (ii) creates only one new refined grid which increases with each iteration step. The basic principle of approach (ii) is schematically illustrated in Figure 5.10.

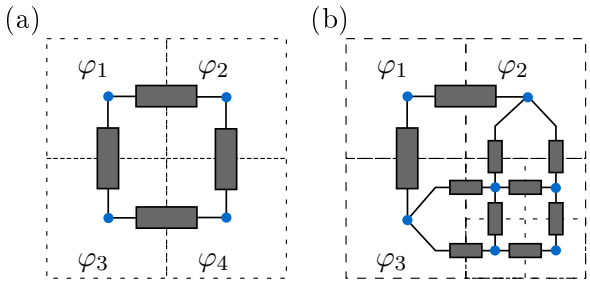

Figure 5.10: *Adaptive mesh. Schematic illustration of adaptive mesh variation developed by Pieters in [6]. It is based on a continuous refinement of the mesh in the regions with highest junction voltage differences between the segments, here between segments 3 and 4, and between segments 2 and 4 respectively. High mesh density is created only where it is necessary in order to reduce the simulation error.*

The initial mesh is comparatively coarse, as illustrated in Figure 5.10 (a) with four segments and the correspondent TCO resistances between the segments. After the first iteration, the differences in junction voltage $\Delta\varphi$ between adjacent segments are calculated. Adjacent segments with the highest $\Delta\varphi$ are selected for a further refinement. In Figure 5.10 (a) the junction voltage differences $\Delta\varphi_{3\text{-}4} = |\varphi_3 - \varphi_4|$ and $\Delta\varphi_{2\text{-}4} = |\varphi_2 - \varphi_4|$ are the highest voltage differences of the network. Thus, $R_{3\text{-}4}$ between segment 3 and 4, and $R_{2\text{-}4}$ between segment 2 and 4 are refined each by two resistors in parallel, as shown in (b). The refinement is continued until the highest simulated $\Delta\varphi$ between two neighbouring segments is below a termination criterion.

5.8 Simulation of EL & DLIT Images

EL images are simulated by approximating the EL intensity ϕ_{EL}

$$\phi_{\mathrm{EL}}(r) \propto \exp\left(\frac{qV_{\text{p-n}}}{k_B T}\right), \tag{5.28}$$

which corresponds to the number of emitted photons at the position r (according to Eq. (4.1)). The DLIT signal, which is described by Eq. (4.7), can be approximated in the NSM by the total locally dissipated electrical power density, i.e.

$$P_{\mathrm{DLIT}} = P_{\mathrm{TCO}} + P_{\mathrm{CIGS}} + P_{\mathrm{Mo}}, \tag{5.29}$$

where P_{TCO}, P_{CIGS}, and P_{Mo} denote the dissipated powers in the TCO front contact, CIGS absorber with CdS/i-ZnO buffer, and Mo back contact respectively. Fig. 5.11 presents in detail how I simulate the DLIT signal of a segment in dependence of current flow and segment geometry. Three segments, labelled by 1, 2 and 3, are shown within one cell.

All segments have the same length l, layer thickness d_{TCO} of the front contact and d_{Mo} of the back contact, but different widths $w_1 \neq w_2 \neq w_3$. For the sake of clarity only the network connections

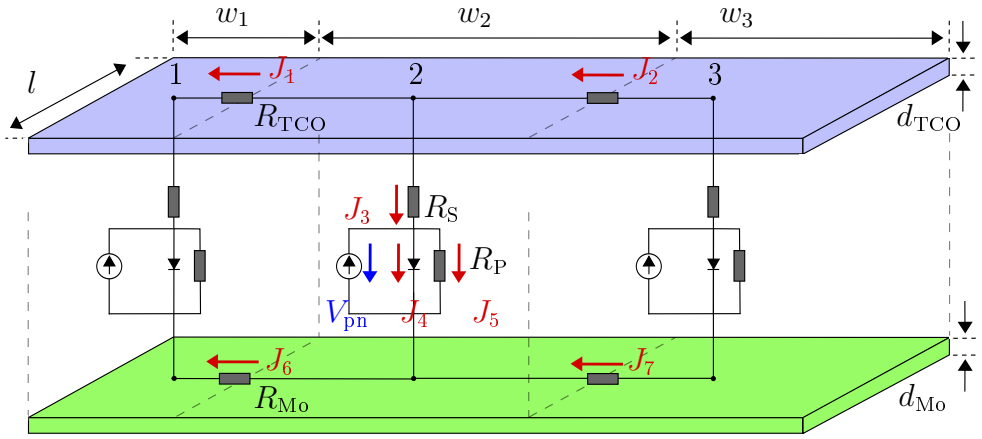

Figure 5.11: *The simulated currents J_1...J_7 are calculated taking into account the segment geometries like length l, width w, and electrode thickness d.*

alongside the width are drawn, but not alongside the length. For the calculation of the dissipated power $P_{\mathrm{DLIT},2}$ (which is assumed to be proportional to the DLIT signal) in segment 2 all currents are taken into account by

$$\begin{aligned} P_{\mathrm{DLIT},2} &= P_1 + P_2 + P_3 + P_4 + P_5 + P_6 + P_7 \\ &= J_1^2 \cdot \rho_{\mathrm{TCO}} \frac{w_2}{2} \frac{1}{l \cdot d_{\mathrm{TCO}}} + J_2^2 \cdot \rho_{\mathrm{TCO}} \frac{w_2}{2} \frac{1}{l \cdot d_{\mathrm{TCO}}} \\ &+ J_3^2 \cdot \frac{\rho_{\mathrm{CIGS,ser}}}{w_2 l} + J_4 \cdot V_{\mathrm{pn}} + J_5^2 \cdot \frac{\rho_{\mathrm{CIGS,par}}}{w_2 l} \\ &+ J_6^2 \cdot \rho_{\mathrm{Mo}} \frac{w_2}{2} \frac{1}{l \cdot d_{\mathrm{Mo}}} + J_7^2 \cdot \rho_{\mathrm{Mo}} \frac{w_2}{2} \frac{1}{l \cdot d_{\mathrm{Mo}}}, \end{aligned} \tag{5.30}$$

where the currents J_3, J_4, and J_5 have the unit A/m^2 and the other currents have the unit A/m. Note that in the actual calculation I also take into account the currents along the length direction, i.e. perpendicular to the direction of J_1, J_2, J_6, and J_7. Figure 5.12 shows the simulated EL and DLIT image of a defect free CIGS module with 3 cells.

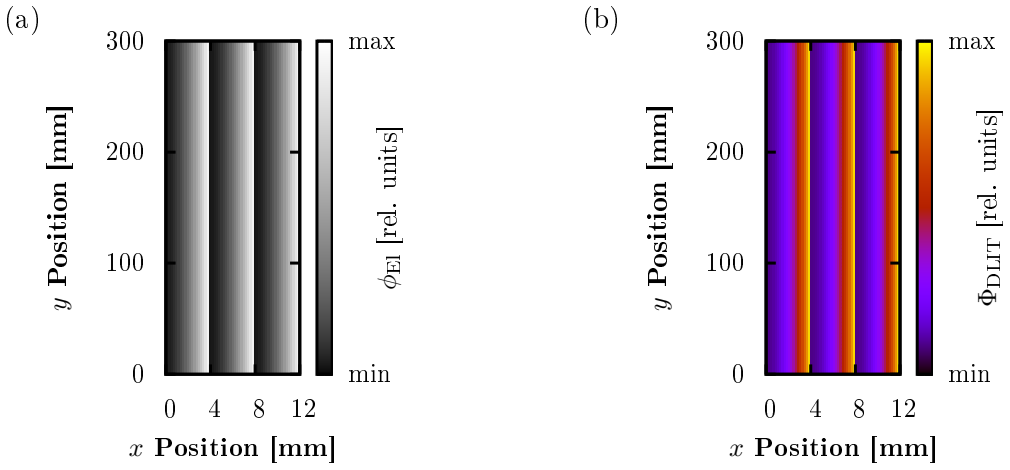

Figure 5.12: *Simulated (a) EL and (b) DLIT image of a defect free module. The axes are not drawn to scale for the sake of a better visibility.*

5.9 Program Implementation

The NSM is implemented in PYTHON [107]. The decision criterion for PYTHON was the accessibility of mathematical libraries which are written in miscellaneous programming languages, mainly in FORTRAN [108] and C/ANSI C/C++ [109]. For instance, the library *numpy.linalg*, which I use in order to solve the system of linear equations $[M][x] = [z]$, is based on the LAPACK [110] library written in FORTRAN. Furthermore, both the *pysparse.umfpack* (implementing UMFPACK [111]) and the *pysparse.superlu* (implementing SUPERLU [112]) libraries, which I use to calculate the LU factorization, are written in C/ANSI C/C++.

5.10 Validation of Network Simulation Model

The NSM in this work has been validated by comparing it to the NSM in [6]. Due to its citation in [113–115], the work of [6] can be regarded as a reliable reference.

First, a plausibility test of a defect free two cell system under (i) forward bias under illumination, and (ii) under forward bias in the dark was performed. For both solar cell operation points, the following three cases have been simulated: (i) $R_{\mathrm{Mo}} < R_{\mathrm{TCO}}$, (ii) $R_{\mathrm{Mo}} = R_{\mathrm{TCO}}$, and (iii) $R_{\mathrm{Mo}} > R_{\mathrm{TCO}}$. The plausibility test has shown sound simulation results of the NSM developed in this work.

Second, a quantitative comparison of a defective two cell system under forward bias in the dark has been performed, which is shown in the following. In order to ensure comparability of the simulations, all material parameters of the two NSM have been chosen identically. A defective parallel resistance R_{P} is modelled, as shown in Table 5.2.

Table 5.2: *Simulated defect parameters. At the defect position the parallel resistance is reduced by 99.99 %.*

Parameter	Symbol	Value	Reference
defect-free CIGS parallel resistivity	$\rho_{CIGS,par}$	0.11 Ωm^2	measured
defective CIGS parallel resistivity	$\rho_{CIGS,par}$	1.1 x 10^{-5} Ωm^2	assumed

The mesh in this work and that of the reference NSM are different, as introduced in Chapter 5.7. In order to compare the simulation results based on two different meshes, a comparison mesh has been defined and both meshes are translated to the comparison mesh. Figure 5.13 illustrates

schematically the translation of the mesh developed in this work to the comparison mesh.

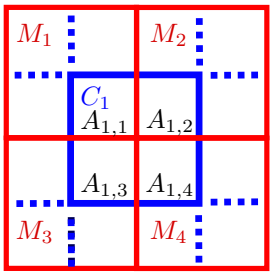

Figure 5.13: *Translation of simulated mesh into comparison mesh. Red coloured mesh containing segments M_{S1} ... M_{S4} is translated into the blue coloured comparison mesh.*

In Figure 5.13 four red coloured segments $M_1 - M_4$ are translated into blue coloured segments of the comparison mesh. The segment C_1 partially overlaps with four red segments $M_1 - M_4$. In order to calculate the resulting potential φ_{C_1}, the potentials $\varphi_{M_1} - \varphi_{M_4}$ are averaged according to the spatial overlap of $M_1 - M_4$ with C_1, which can be expressed by

$$\varphi_{C_1} = \frac{\sum_{i=1}^{n}(A_{1,i} \cdot \varphi_{M_\mathrm{i}})}{\sum_{i=1}^{n} A_{1,\mathrm{i}}}, \tag{5.31}$$

with $n = 4$ for the simple example in Figure 5.13. Eq. (5.31) is consequently applied to all segments in order to allow comparison of the two different meshes.

Figure 5.14 presents the quantitative comparison between the two NSM for a modelled defect of A = 400 µm x 400 µm size in the centre of a cell. Figure 5.14 (a) depicts the simulated junction voltage $V_{\text{p-n}}$ resulting from the NSM developed in this work. The x-axis shows the cell width of 3.8 mm. The y-axis shows the cell length of 300 mm. The axes are not drawn true to scale in order to better visualize the voltage reduction.

The absolute difference $\Delta V_{\text{p-n}}$ in p-n-junction voltage between the two NSM, after relating both simulation results to the comparison mesh, is shown in (b). It turns out that the defect influence is modelled well by my mesh at the defect position in the cell centre with a deviation of $\Delta V_{\text{p-n}} = 2.3 \cdot 10^{-5}$ %. At the cell start alongside the cell width, where $V_{\text{p-n}}$ is highest in the cell, the $\Delta V_{\text{p-n}}$ increases up to 3.5 % and at the cell end alongside the cell width up to 1.5 %. The reason for this increased deviation outside the actual defect area is illustrated in Figure 5.7: At the defect position there is a sufficiently high density of rows and columns, while to the left and to the right the number of columns reduces, which correlates with the increase in $\Delta V_{\text{p-n}}$ in Figure 5.14 (b). Hence, a reduction of $\Delta V_{\text{p-n}}$ is possible by simply increasing the number of columns in the region around the defect.

One can draw the conclusion that with regard to the severness of the shunt reduction of R_{P} by 99.99 % the small deviation at the defect position of only $\Delta V_{\text{p-n}} = 2.3 \cdot 10^{-5}$ % and the average deviation $\Delta \bar{V}_{\text{p-n}} = 0.4$ % prove the validity of my implementation of the NSM.

(a)

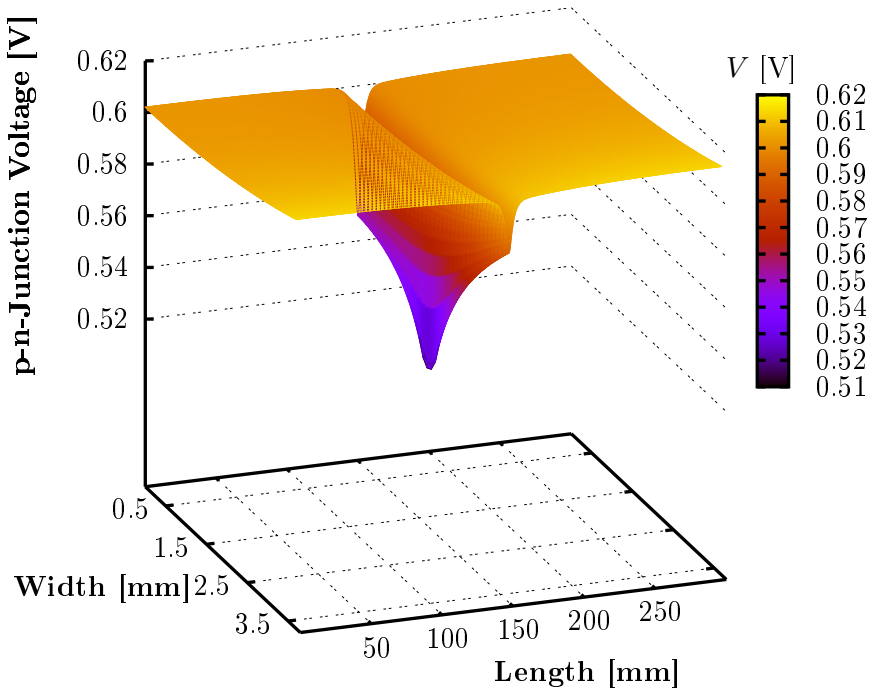

(b)

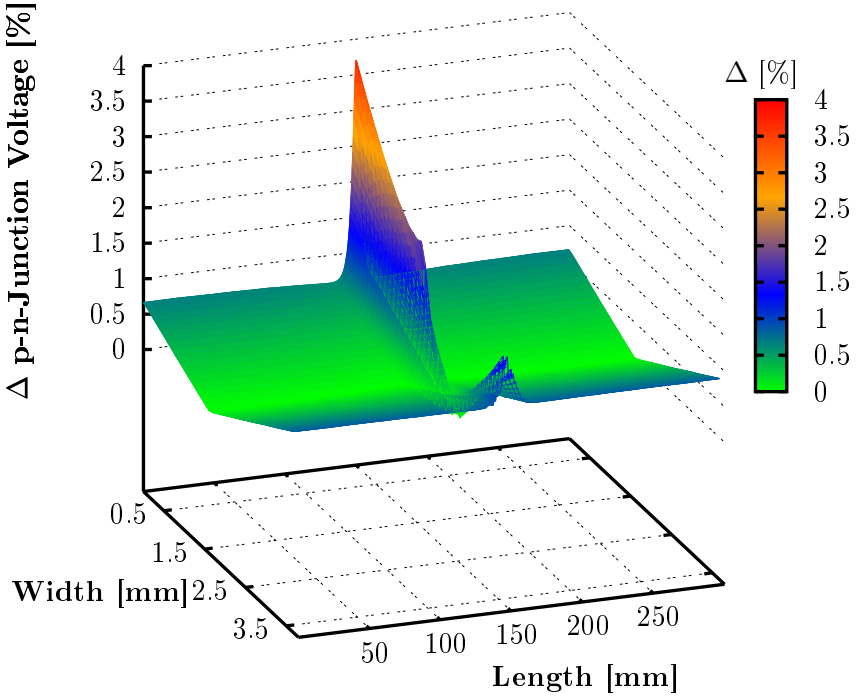

Figure 5.14: *Validation of NSM. For the validation of the NSM, which has been developed in this work, a comparison with the reference network published in [6] is performed . (a) Modelled defect of 400 µm x 400 µm size causes a break down of the p-n-junction voltage in my NSM to values of approximately 0.52 V. (b) Difference in p-n-junction voltage between the two NSM has a maximum of 3.5 % close to the defect and an average of 0.4 % in the affected cell.*

Chapter 6

Implemented, Measured, and Simulated Defects

"The subject of this chapter is the investigation of point defects and scribing defects."

6.1 Introduction

In Chapter 3 I have given a detailed overview of the defects that I investigate in this work and I have summarized the defects in Table 3.1. In order to investigate the defects, I first intentionally implement them in defined ways, which will be introduced in the following, and afterwards measure and quantify the defects.

I implement the point defect types Mo-01, Mo-02, Mo-03, Mo-04, and Mo-05 (summarised under defect ID ***D-1*** in Table 3.1), and the point defect types CIGS-06, CIGS-07, CIGS-08, and CIGS-09 (summarised under defect ID ***D-4*** in Table 3.1). As all aforementioned point defects are basically characterised by at least one missing layer, I imitate the defects by manually removing the correspondent layer(s). Note that this approach can not represent all possible defect origins for the aforementioned defect types, but is a reasonable way to come very close to the actual defective layer structure. As I will show in Chapter 6.2.1, the manual removal of one or more layers can be done in a defined way by piercing the correspondent layer(s) with a mechanical graver. It turns out that the basic difference between the point defects is whether the lack of removed layer(s) leads to a short circuit path, and if it does, how much the resulting layer structure at the defect position can mitigate the short circuit current. The shunt mitigating characteristic is well detectable in EL as it allows the quantification of voltage loss in the cell, which is why I do the complete point defect characterisation with EL measurements.

Furthermore, I implement P1 scribing defects (defect ID ***D-2*** in Table 3.1), P2 scribing defects (defect ID ***D-5*** in Table 3.1), and P3 scribing defects (defect ID ***D-6*** in Table 3.1). All scribing defects are characterised by an interruption of the correspondent scribing line, which is why I imitate the scribing defects by intentionally interrupting the scribing processes, as shown in Chapter 6.3.2. It turns out that the distinction of scribing defects, namely between the P1 and P3 defect, only by

EL investigation is insufficient, which is why I additionally perform DLIT measurements. Although the DLIT measurements improve the distinction between P1 and P3 defects, the correspondent DLIT images can not be intuitively understood. This is because the monolithic series connection is significantly deteriorated at positions of P1 and P3 scribing defects, which leads to abnormal current flows. In order to understand these abnormal current flows, I additionally model the scribing defects in the NSM, and show that the measured EL and DLIT images can well be explained with the simulation results.

In this Chapter the focus is on understanding the defect mechanism i.e. the defect influence on voltages and currents in the defect surrounding, while the defect diagnostics, which is the reliable identification of defects, will be shown later in Chapter 7.

6.2 Point Defects

6.2.1 Implementation of Point Defects

Three CIGS modules of 120 $\times$ 60 cm^2 were produced by the production process described in Chapter 3. In order to introduce the defects, the production sequence was interrupted after each step, and defects were produced by removing locally part of the layer(s). Afterwards, the process sequence was resumed.

The different defect types, as they are introduced in Chapter 3, were distributed evenly on the three modules in order to take into account manufacturing differences between the modules. A distance of 5 cells was allowed between individual defects in order to avoid cross talk effects. After finishing, the modules were cut into mini-modules of a size of 30 $\times$ 30 cm^2 and of 67 cells, each of dimension 0.4 $\times$ 30 cm^2 connected in series, for the sake of easier handling within the EL measurement setup.

Note that the frequent interruption of the process and exposure to the ambient caused additional pollution in the module, e.g. by dust particles. However, these pollutions appear to be passive in the sense that the corresponding area exhibits no photovoltaic activity and does not cause any shunt. This is seen by the multitude of black spots in all EL images in Fig. 6.5. The prepared modules do not exhibit more shunts apart from the intentional ones, which is a further indication that the introduced pollution is mostly passive.

I begin with the first group of point defects that are characterised by a hole at least in the Mo layer. This group of point defects is labelled by defect ID ***D-1*** in Table 3.1 in Chapter 3, and its possible defect origins have been introduced in detail in Chapter 3.2.3 for the defect variants Mo-01 ... Mo-05. I locally remove the Mo layer and every following layer subsequently with a mechanical graver, as shown in Figure 6.1. The absence of the respective layer stack after piercing was verified by illumination from the back of the module.

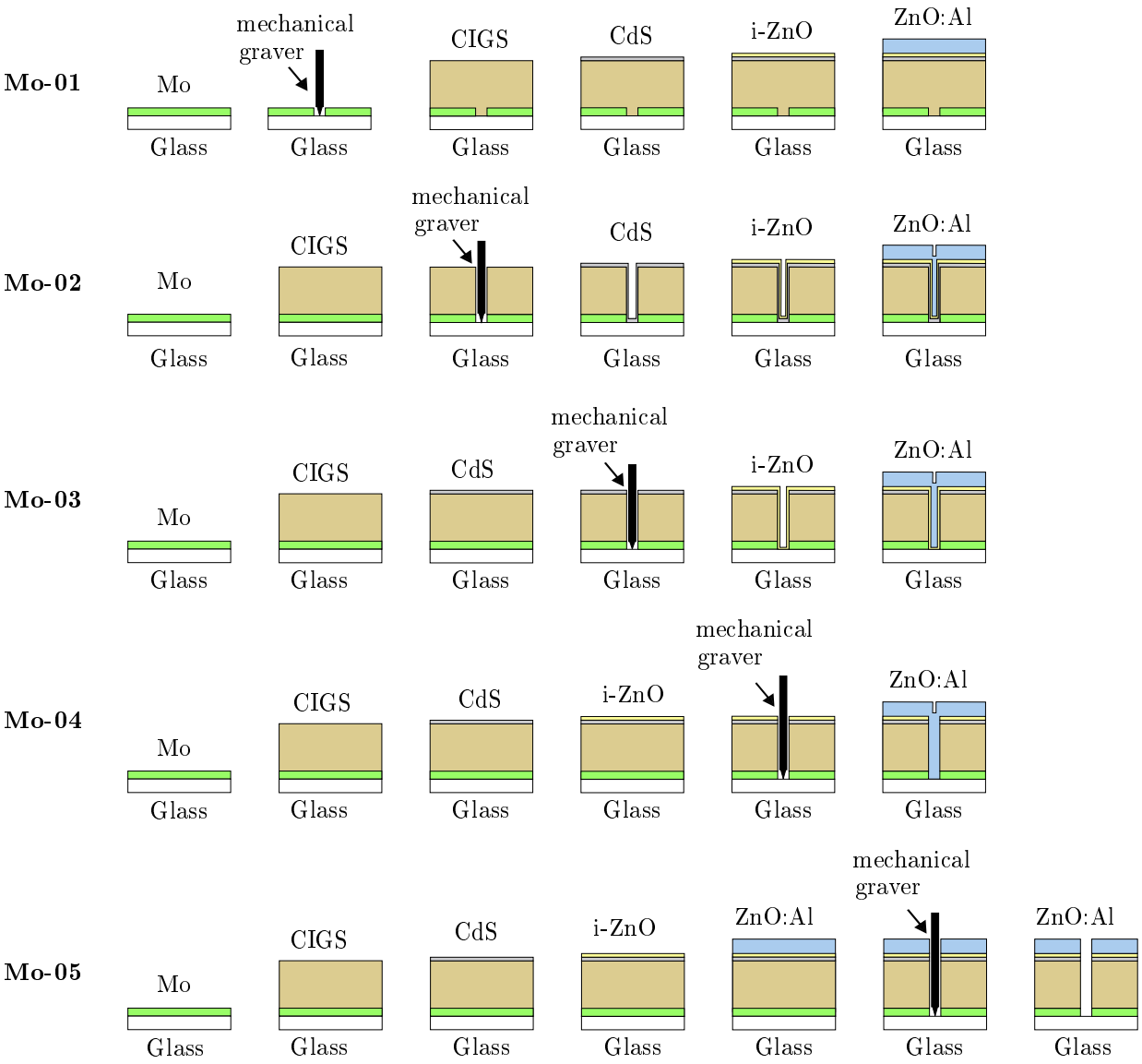

Figure 6.1: *Implementation of Mo point defects.* ***Mo-01*** *is created by piercing of the Mo layer after Mo sputtering.* ***Mo-02*** *is created by piercing of the CIGS and Mo layer after CIGS co-evaporation.* ***Mo-03*** *is created by piercing of the CdS, CIGS, and Mo layer after chemical bath deposition.* ***Mo-04*** *is created by piercing of the i-ZnO, CdS, CIGS, and Mo layer after i-ZnO sputtering.* ***Mo-05*** *is created by piercing all layers after ZnO:Al sputtering.*

The second group of point defects that I investigate is characterised by a hole at least in the CIGS layer. This second group of point defects is labelled by the defect ID ***D-4*** in Table 3.1 in Chapter 3, and I have discussed possible defect origins in Chapter 3.2.6 for its variants CIGS-06 ... CIGS-09. In contrast to ***D-1***, for ***D-4*** the Mo layer is intact, as shown in Figure 6.2.

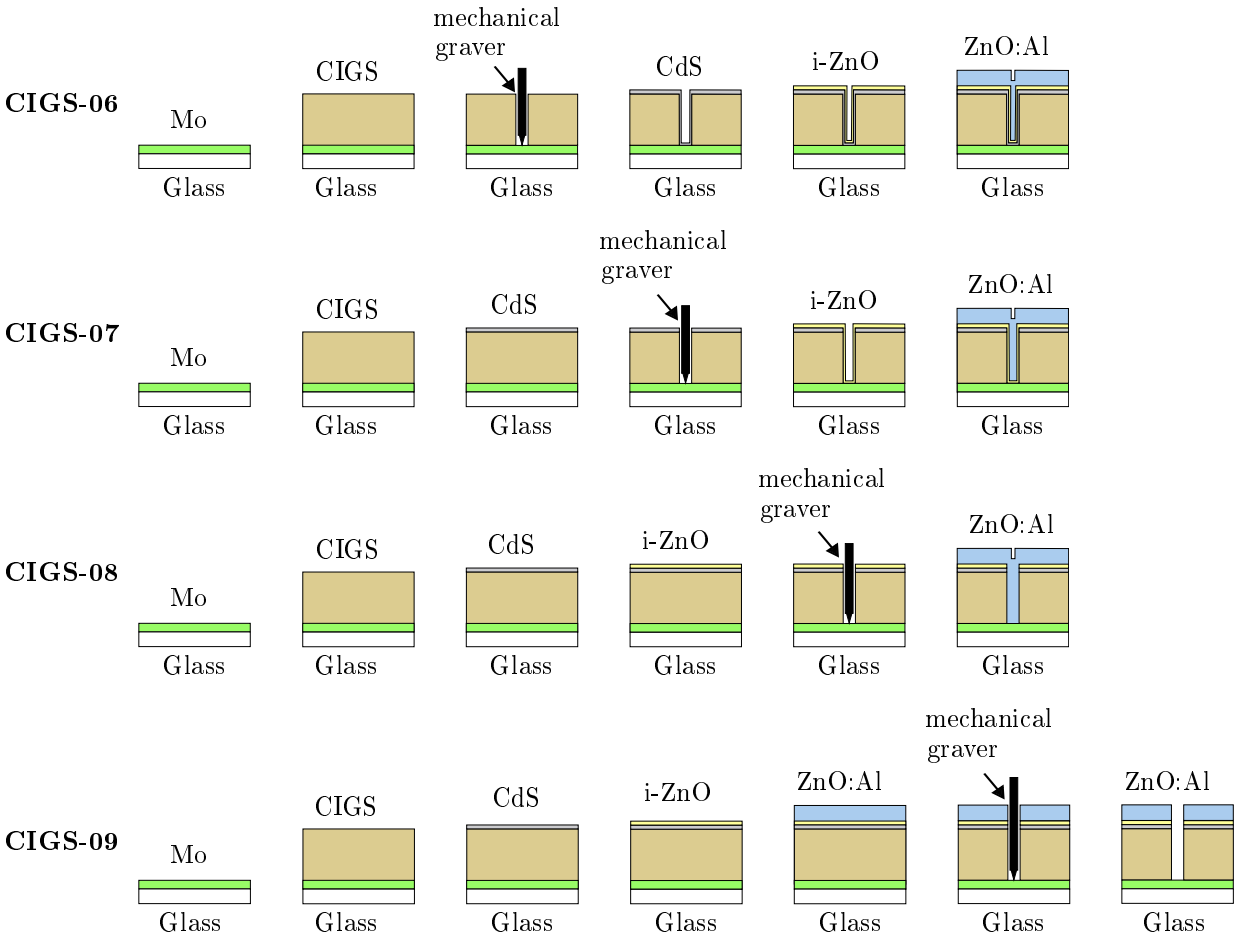

Figure 6.2: *Implementation of CIGS point defects.* ***CIGS-06*** *is created by piercing of the CIGS layer after CIGS co-evaporation.* ***CIGS-07*** *is created by piercing of the CdS and CIGS layer after chemical bath deposition.* ***CIGS-08*** *is created by piercing of the i-ZnO, CdS, and CIGS layer after i-ZnO sputtering.* ***CIGS-09*** *is created by piercing of all layers above the Mo after ZnO:Al sputtering. The piercing for CIGS-06 ... CIGS-09 is done softer than that for Mo-01 ... Mo-05 in order to leave the Mo layer undamaged.*

6.2.2 Pre-Selection of Point Defects

Microscope images of my point defects reveal that the piercing is done in an imperfect way because (i) the tip geometry of the mechanical graver is inhomogeneous, (ii) the graver is not exactly pressed onto the surface in an angle of 90 degrees, and (iii) fractions occur in the Mo due to the mechanical stress. Hence, in order to ensure the comparability between the implemented defects I apply a pre-selection with regard to the defect geometry that I record with a microscope. The pre-selection is based on referring the defect area to an ideal point geometry, while I take into account only those defects that deviate least from this ideal point geometry. This pre-selection procedure requires four steps which are explained in the following and which are visualized in Figure 6.3.

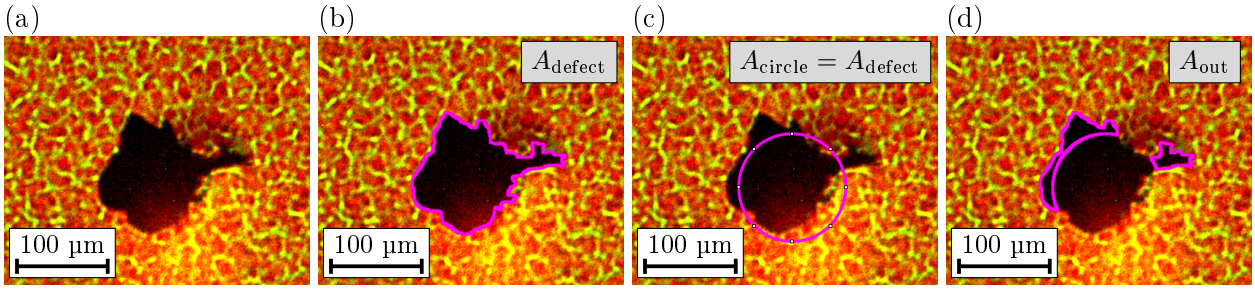

Figure 6.3: *Explanation of defect pre-selection. (a) Microscope image from glass side of a Mo-03 defect before pre-selection. (b) Defect contour is marked, and the defect area and mass point are calculated. (c) Circle is drawn at calculated mass point with calculated defect area. (d) Only the defect area outside the circle is marked. The ratio f of the area A_{out} in d) with regard to the area A_{defect} in (b) is used as exclusion criterion for the pre-selection.*

Fig. 6.3 (a) shows a Mo-03 defect in an microscope image recorded from the glass side. In (b) I determine the defect area and mass point of every single implemented defect by application of automated image processing (AIP) in the software ImageJ [116, 117]. The AIP marks the defect contour with a magenta line and calculcates the aforementioned data for the marked body. In (c) the AIP calculates a circle centered at the calculated defect mass point, while the circle area equals the defect area A_{defect}, as it is shown in (c). Afterwards, the AIP calculates in (d) the defect area A_{out} that is outside the circle area, and relates the outside area to the total defect area by $f = A_{\text{out}}/A_{\text{defect}}$. Defects are excluded from investigation if $f \geq 30$ %, which results in a data set of comparable defect geometries. Fig. 6.4 exemplifies for four different fractions how the pre-selection actually allows to work with similar defect geometries.

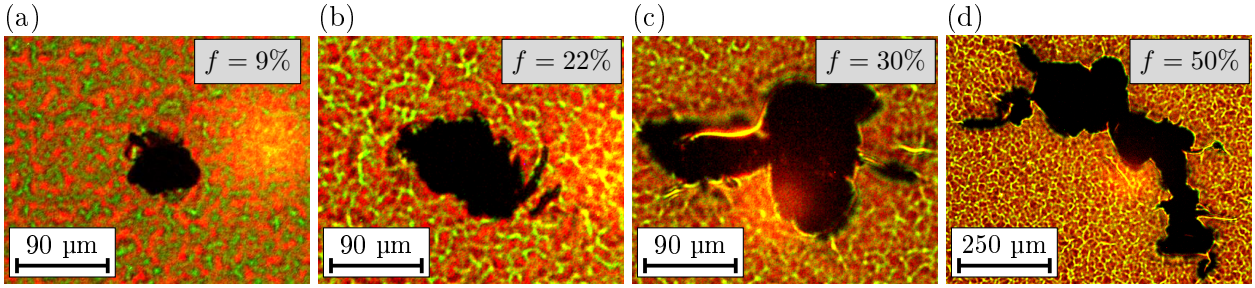

Figure 6.4: *Application of defect pre-selection. The pre-selection allows the defects in (a) and (b), but excludes the defects in (c) and (d) from being taken into account for the following investigation.*

As shown in Fig. 6.4, the pre-selection leads to more similar ratios of the defect circumference to the defect area. As the mechanical graver produces only for small defect areas point-like geometries, the pre-selection furthermore leads to a data set of more similar defect areas, namely small ones with diameters in the region of about 100 µm.

6.2.3 Qualitative Measurement Results

Fig. 6.5 depicts exemplarily one defect sample for each defect type Mo-01 ... CIGS-09. For each defect sample a microscope image (on the left side) and an EL image measured at a current bias of $j = 2.5$ mA/cm^2 (right side) is shown.

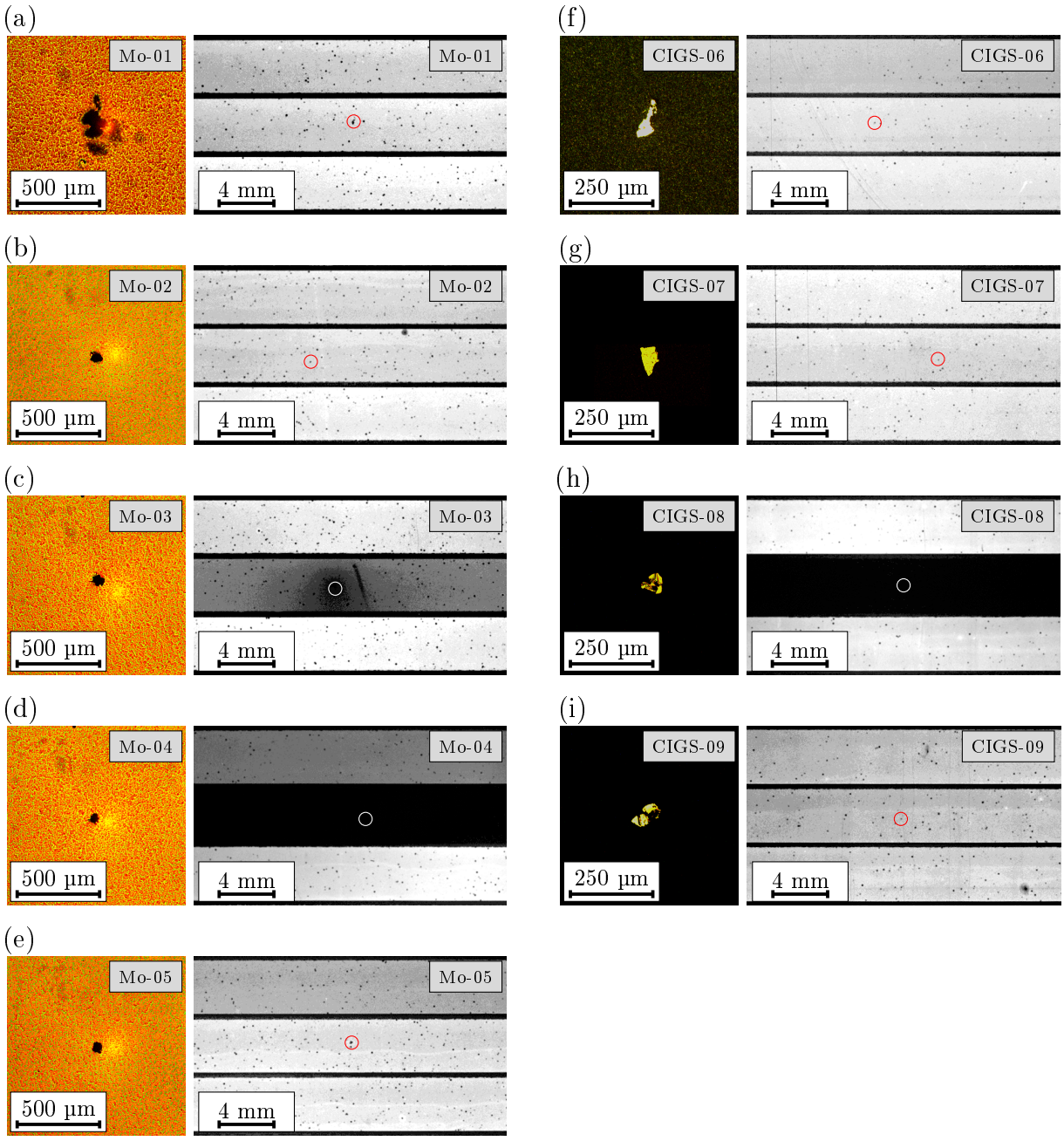

Figure 6.5: *Defect examples for each point defect type Mo-01 ... CIGS-09 with correspondent microscope image (left) and EL image recorded at $j = 2.5$ mA/cm^2 (right). Three defect categories become evident: The first category is formed by the defect types Mo-01, Mo-02, Mo-05, CIGS-06, CIGS-07, and CIGS-09, having no defect influence at all with the exception of the reduced active solar cell area. Second category is represented by Mo-03 with its locally limited defect influence. Defects Mo-04 and CIGS-08 represent the third category as very detrimental shunts that darken the complete middle cell within the image section.*

In Fig. 6.5 the implemented defects are located in the middle cell within each correspondent EL image and their exact position is indicated by a circle. Note, that the frequent interruption of the process and exposure to the ambient caused additional pollution in the module, for example, by dust particles, although these pollutions were essentially passive in the sense that the corresponding area exhibited no photovoltaic activity and did not cause any shunt.

For the defects with missing Mo-01 ... Mo-05, the microscope pictures are taken from the glass side and the defect area displays a reduced reflectance. For the failures with missing CIGS absorber, namely CIGS-06 ... CIGS-09, with the Mo present, pictures are taken from the film side, and the defect area exhibits a higher reflectance at the Mo in the defect than at the CIGS covered area in the defect surrounding.

The EL images are taken at a bias current density of $j = 2.5$ mA/cm^2 (per unit cell area). The defect areas for Mo-01 ... Mo-05 are slightly larger than those for CIGS-06 ... CIGS-09. This is because more pressure needs to be applied in order to pierce the Mo, which eventually led to larger holes. The areas for Mo-01 defects are the largest, as is shown further below in Fig. 6.6. The technical reason for the larger Mo-01 defect areas is the somewhat more slippery contact when pressing a metal graver onto a metal layer (Mo), which leads in my specific experimental setup to a less precise translation of the applied force into a hole than in the other cases Mo-02 ... Mo-05, where further layers are on top of the Mo.

Fig. 6.5 reveals basically three categories of defects: The first category is made up by the defect types Mo-01, Mo-02, Mo-05, CIGS-06, CIGS-07, and CIGS-09, where these defects seem to have no influence on the EL image. The second category is represented by the defect Mo-03, which shows a significant but locally limited shunting behavior. Note that in Fig. 6.5 (c) there is a scratch to the right of the implemented defect type Mo-03, which is not introduced by me but instead is production induced. However, the scratch seems to be electrically inactive as the local reduction in EL signal intensity, and therefore the local junction voltage, is visibly caused by my implemented defect. The third category is made up by the defect types Mo-04 and CIGS-08 which cause such severe shunts that the middle cell in the EL image is completely darkened within the shown image section.

The implemented defects in Fig. 6.5 are not exactly placed in the cell center, which plays no role with regard to the influence on junction voltage for the first defect category (no detrimental effect at all) and the third defect category (detrimental effect is so strong that complete cell is darkened). Only with regard to the second defect category the defect position may play a small role and could slightly influence the size of the darkened area around the defect itself.

6.2.4 Quantitative Measurement Results

While Fig. 6.5 illustrates the effect of the different defect types on the EL image for comparable defect areas, a quantitative comparison of the defect influence on the EL signal for varying defect areas is shown in Fig. 6.6, where the ratio $S_{def}^{avg}/S_{ref}^{avg}$ and the correspondent voltage loss ΔV are shown as functions of the defect area.

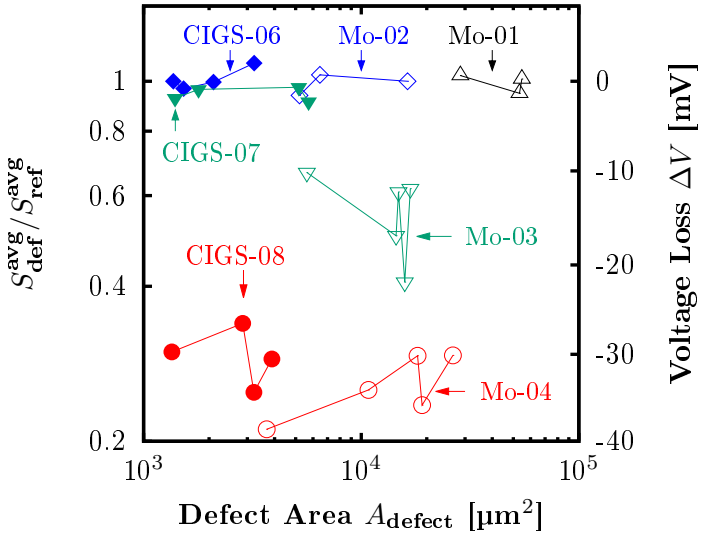

Figure 6.6: *Comparison of the detrimental influence of point defects.*

Note that the defects Mo-05 and CIGS-09 basically form positions where there is no active solar cell and have no influence on currents and voltages. Hence, for the sake of a better visibility I do not show them in Fig. 6.6. With a ratio of $S_{def}^{avg}/S_{ref}^{avg} \approx 1$ and a voltage loss of $\Delta V \approx 0$, the defects Mo-05 and CIGS-09 are in principle represented by the defects Mo-02, and CIGS-06 respectively. In contrast, I show all other defects in Fig. 6.6 and derive the significance of the CdS/i-ZnO buffer combination from defect comparisons in the following.

In analogy to Fig. 6.5, the three defect categories can be observed in Fig. 6.6, too. All AIP preselected defects of defect types Mo-01, Mo-02, CIGS-06, and CIGS-07 (including Mo-05 and CIGS-09) seem to have hardly any effect on the junction voltage and form the first category of harmless defects. In contrast, the representatives of defect type Mo-03 cause a reduction of the EL signal by about the half, and therefore form the second defect category that can be described as semi-detrimental, as the defect influence is locally limited. Eventually, there are the defect types Mo-04 and CIGS-08, forming the third defect category of very detrimental defects, which darken practically the complete cell within the image section. In the following I subsequently compare the defect types in order to gain an understanding of the effects shown in Fig. 6.5.

I first compare the defect types Mo-04 and CIGS-08 in Fig. 6.6, as they are counterparts with regard to missing CIGS, CdS, and i-ZnO. For both Mo-04 (additionally missing Mo) and CIGS-08 the EL emission is reduced by about a factor of 3 to 4, corresponding to voltage losses of 30 – 40 mV. These are considerable shunts that degrade the performance of a considerable cell area (as noted before the given ΔV is the average voltage loss over an area of 0.4×4.8 cm^2. In Mo-04 the doped ZnO:Al obviously comes into direct contact with the Mo back contact at the edges of the defect and causes considerable shunting. The same happens in CIGS-08; the only difference is that the contact area between ZnO:Al and Mo is even larger than for Mo-04. However, the shunts are in both cases so severe that Fig. 6.6 cannot resolve any significant difference between Mo-04 and CIGS-08. Thus, these defects are as detrimental as defects get as the current through the defect is not limited by

the defect resistance itself any more, but by the resistance towards the defect, and as such depends only on the ratio of defect size to electrode size and of the electrode sheet resistances.

Second, I focus on the defect types Mo-03 and CIGS-07 in Fig. 6.6, as they are counterparts with regard to missing CIGS and CdS. The i-ZnO in Mo-03 (additionally missing Mo) shows only moderate shunt mitigation and is less effective than that in CIGS-07. In the case of Mo-03, I assume that flakes or rims at the rugged brink of the removed Mo are not easily covered by the sputtered i-ZnO alone, such that the doped ZnO:Al still makes direct local contact to the Mo back contact. Fig. 6.7 illustrates an exemplary Mo flake recorded by a scanning electron microscope (SEM). It appears unlikely that the vertically sputtered i-ZnO can completely cover the sides of the flake and the cavities that are under the flake, which is necessary in order to provide a sufficient insulation with regard to the ZnO:Al. In contrast to Mo-03, the i-ZnO in CIGS-07 is sputtered on a comparatively smooth Mo surface. The shunt mitigation of CIGS-07, as shown in Fig. 6.6, indicates that i-ZnO can protect smooth Mo surfaces from direct contact with the doped ZnO:Al.

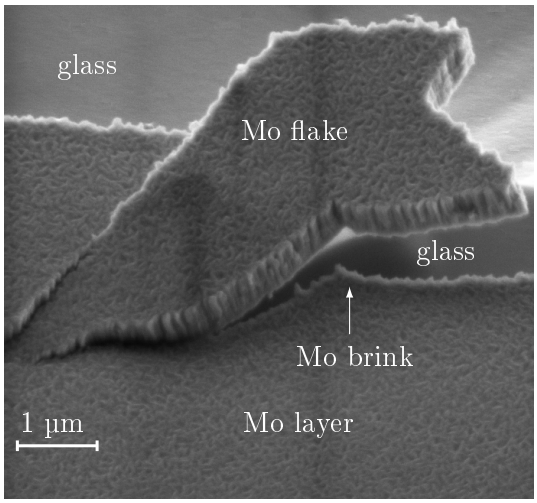

Figure 6.7: *SEM image of Mo flake after local removal of the Mo. It appears unlikely that in Mo-03 the 50 nm thin i-ZnO layer can completely cover flakes of about 600 nm thickness and reliably prevent direct contact between Mo and ZnO:Al. For the sake of a better visibility of the flake, in the shown sample no layers were deposited after Mo removal.*

A comparison of the defect types Mo-02 and Mo-03 in Fig. 6.6 yields that the presence of the CdS in Mo-02 significantly improves the shunt mitigation in contrast to Mo-03. I suggest that during chemical bath deposition (CBD) Mo flakes, and cavities surrounding them, are literally flooded with the chemical solution consisting of thiourea, Cd salt and ammonia [11], and therefore are well covered (in case of flakes) and well filled up (in case of cavities). The stirring of the chemical solution, which is applied in order to homogenize the CdS growth, should be additionally advantageous for covering the inside of the defects, which, in contrast, is less effective in case of only i-ZnO sputtering (like in case of Mo-03) that is basically directed perpendicularly to the substrate surface. Thus, in Mo-02 the following i-ZnO is sputtered on a smoother (or less uneven) surface at the Mo edges (than it is the case without CdS in Mo-03), and therefore can effectively prevent direct contact of ZnO:Al with Mo.

My suggestion of a surface smoothing effect by the CdS for the following i-ZnO layer is consistent with the comparison of the defect types CIGS-06 and CIGS-07 in Fig. 6.6. Both defect types lead practically to the same shunt mitigation of $S_{def}^{avg}/S_{ref}^{avg} \approx 1$ and a voltage loss of $\Delta V \approx 0$. As the Mo surface is already smooth for both CIGS-06 and CIGS-07, the additional CdS layer in CIGS-06 does not add any significant improvement compared to CIGS-07.

6.2.5 Conclusions

I find that the i-ZnO/CdS buffer combination is effective in mitigating the detrimental effect of shunts in CIGS modules that arise from the local absence of the absorber material. The covering coating by the chemical bath deposited CdS plays a role for mitigating shunts if rough edges like in failures Mo-01 ... Mo-05 (damaged Mo) are involved, whereas for relatively smooth topologies the shunt mitigating action of sputter deposited i-ZnO like in CIGS-07 (intact Mo) is sufficient.

6.3 Scribing Defects

6.3.1 Introduction

The interruption of scribing lines leads to a local dysfunction of the monolithic series connection. The defect origins for P1 defects (***D-2***), P2 defects (***D-5***), and P3 defects (***D-6***) have been introduced in the correspondent Chapters 3.2.4, 3.2.9, and 3.2.11 . In the case of the P1 and P3 defects the insulation between the cells is deteriorated which leads to significant changes of the current flow and voltage distribution. In contrast, the P2 scribing defect has only a small effect, as will be shown in Chapter 6.3.3.

In the following Chapter 6.3.2 I first show how I implement the scribing defects. As I have explained in Chapter 6.1, the distinction of P1 and P3 defects in EL images can be difficult which is why I additionally perform DLIT measurements. Although the DLIT mesaurements help to distinguish scribing defects, they can hardly be intuitively understood in the case of P1 and P3 defects. Thus, I model and simulate scribing defects in order to explain the observed measurements. In Chapters 6.3.4.1 and 6.3.4.2 I present for the P1 and P3 scribing defect first the correspondent NSM simulations in order to explain the underlying defect mechanism, and afterwards the correspondent measured EL and DLIT images. This order serves best the understanding of what is happening in the case of scribing defects.

6.3.2 Implementation of Scribing Defects

Figure 6.8 illustrates the implementation of scribing defects schematically.

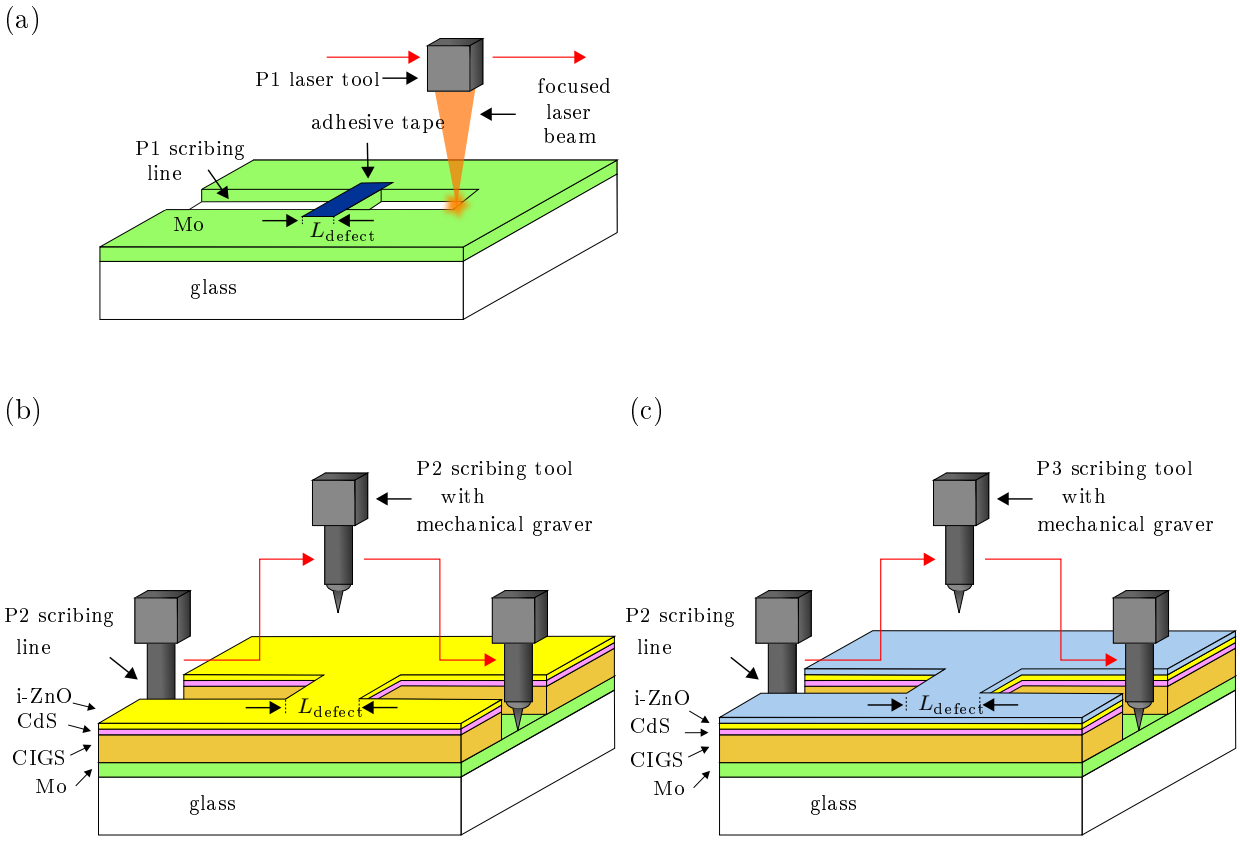

Figure 6.8: *Implementation of scribing defects. (a) P1 scribing defect implementation with a tape that absorbs the laser energy. Here I show P1 film side scribing for the sake of a better visualisation, although P1 substrate side scribing has actually been applied. (b) P2 and (c) P3 scribing defect implementation by drawing back the mechanical graver during scribing process. Red arrow shows the moving direction of the correspondent scribing tool.*

The implementation of P1 scribing defects is shown in Figure 6.8 (a). I position an adhesive tape that locally absorbs the complete laser beam power, and therefore prevents the Mo from being removed. After P1 laser scribing is finished, I remove the tape and the normal module manufacturing continues. By varying the width of the tape I set different lengths L_{defect} of the incomplete P1 laser scribing.

The implementation of P2 scribing defects is shown schematically in Figure 6.8 (b). I create P2 defects by drawing back the mechanical graver during mechanical scribing. I set different scribing defect lengths L_{defect} by varying the distance that the graver moves outside the material. P3 scribing defects are implemented in the same way as P2 scribing defects within the correspondent P3 scribing process.

6.3.3 Measurement Results

The measured DLIT and EL images of defective P1, P2, and P3 lines, which are interrupted over comparable defect lengths L_{defect}, are compared in Figure 6.9. Within both the correspondent DLIT and EL image, the shown P1 and P2 defects are located between the middle and right cell on the vertical centre, while the P3 defect is located between the left and middle cell. I chose this illustration of the defects within a three cell system consequently in the following for both measurement and simulation results, as in case of the P1 and P2 defects the interesting effects take place to the left of the line interruption, while they take place to the right in case of the P3 defect.

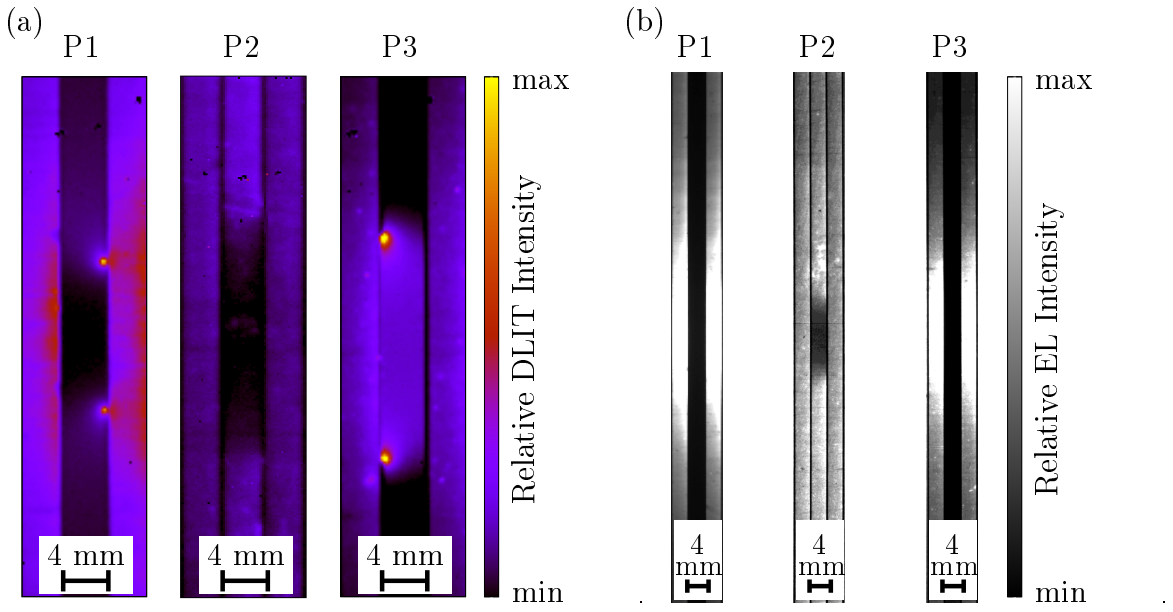

Figure 6.9: *(a) Comparison of DLIT images of scribing defects, measured at $j = 8.3\ mA/cm^2$ for $L_{defect,P1} = 14\ mm$, $L_{defect,P2} = 20\ mm$, and $L_{defect,P3} = 20\ mm$. P1 and P2 defects are located between the middle and right, and the P3 defect between left and middle cell. (b) Comparison of EL images of scribing defects, measured at $j = 8.3\ mA/cm^2$ for $L_{defect,P1} = 14\ mm$, $L_{defect,P2} = 20\ mm$, and $L_{defect,P3} = 20\ mm$. The dark spots in the upper part of each DLIT image are regions of dead pixels in the used DLIT camera sensor.*

The DLIT images in Fig. 6.9 (a) show that two heat centres appear to the left oft the P1 scribing defect, while two heat centres appear to the right of the P3 scribing defect. Furthermore, both the P1 and P3 defect cause a visible cross-talk in the neighbouring cells [118]. In contrast, the P2 defect only leads to a darkening in the middle cell without affecting the surrounding cells. The correspondent EL images are shown in Fig. 6.9 (b).

In both the (a) DLIT and (b) EL images the P1 and P3 defects cause significant cross-talk patterns, while the P2 defect causes only a darkening in the middle cell. The P2 defect mechanism in the DLIT and EL images is obvious. The missing monolithic series connection between the middle and right cell acts like a blocking wall and causes the current to flow around the defect position. Hence, in the middle cell there is a reduced DLIT and EL signal. The EL unveils a slightly higher

intensity above and below the defect site, which is caused by increased current densities due to the currents diverted around the defect site.

However, in order to understand the origin of the most striking attributes, namely the two heat centres in case of the P1 and P3 defect in the DLIT image, I apply in the following network simulations.

6.3.4 Simulation Results

6.3.4.1 Simulation of the P1 Defect

The simulation results for the P1 scribing defect are shown in top view in Fig. 6.10. The horizontal current flow (arrow direction) and current density (arrow colour indicating the unit A/m) in the Mo and TCO electrodes for each NSM segment is shown in Fig. 6.10 (a) and (c). In contrast, Fig. 6.10 (b) shows the current flow and density in A/m^2 vertically through the CIGS and CdS/i-ZnO buffer. The correspondent dissipated power according to Eq. (5.29), and resulting DLIT signal in each segment according to Eq. (5.30), is shown in Fig. 6.10 (d)-(f) in W/m^2. All graphs Fig. 6.10 (a)-(f) present only 50 mm of 150 mm total cell length for the sake of better visibility. The module current flow is from right to left. Within the Mo layer in Fig. 6.10 (a) the interrupted cell edge between the middle and right cell symbolizes the P1 defect, while it is shown as dashed line in Fig. 6.10 (c).

Fig. 6.10 (a) presents how the Mo currents from the top and bottom of the right cell flow towards the defect position and subsequently add up to higher current densities. At the upper and lower end of the line interruption, there is a U-turn of the currents causing the highest current densities. The reason for the U-turn is schematically explained in Fig. 6.11.

Fig. 6.11 contrasts the normal and defective current flow between two Mo potentials $\varphi_{\mathrm{Mo},1}$ and $\varphi_{\mathrm{Mo},2}$. The defect current occurs as long as the red path has a smaller total resistance than the green one, which is caused by the highly resistive i-ZnO forming R_{S} in contrast to the low resistive R_{Mo}. However, far away from the defect position the Mo sheet resistance eventually limits the region where $I_{\mathrm{defect,Mo}}$ occurs.

Fig. 6.10 (b) depicts the highest current densities through the CIGS absorber plus buffer layers within the left and right cell close to the defect position, while the middle cell remains dark as it is bypassed through the Mo layer. The shown current distribution in Fig. 6.10 (b) explains well the correspondent measured EL image for the P1 defect in Fig. 6.9 (b).

In Fig. 6.10 (c) the TCO current flows within the middle cell from left to right, thus in the opposite direction of the module current, which is schematically explained in Fig. 6.12, where (a) illustrates the normal current flow I_{normal} and the defective current flow $I_{\mathrm{defect,TCO}}$ between the potentials φ_{TCO} and φ_{Mo} in the middle cell. Due to the series resistance between φ_{TCO} and φ_{Mo} in the middle cell there is a region around the defect position where the red path through the conductive electrodes has a smaller total resistance than the green one, while the TCO sheet resistance finally limits the region where the defect current occurs. For a defect-free monolithic series connection the potential $\varphi_{\mathrm{C}} < 0$, while in case of a P1 defect at the defect position there is $\varphi_{\mathrm{C}} > 0$, which is why

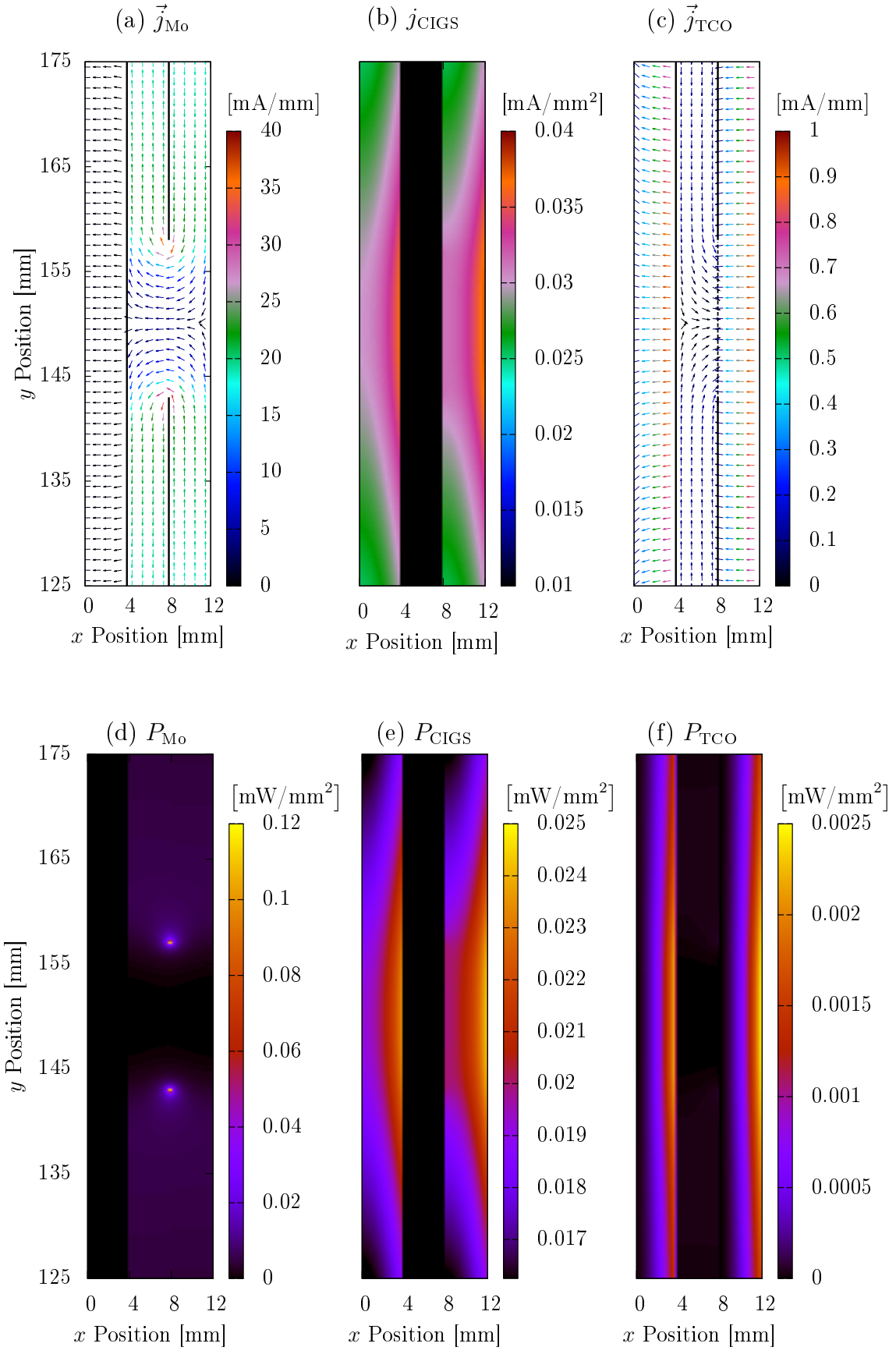

Figure 6.10: *Simulation of a P1 defect of 14 mm length with j_{DLIT} = 8.3 mA/cm^2. (a) Horizontal current flow within Mo. (b) Vertical current flow through CIGS plus buffer layers. (c) Horizontal current flow within TCO. Correspondent power dissipation is shown in (d) - (f).*

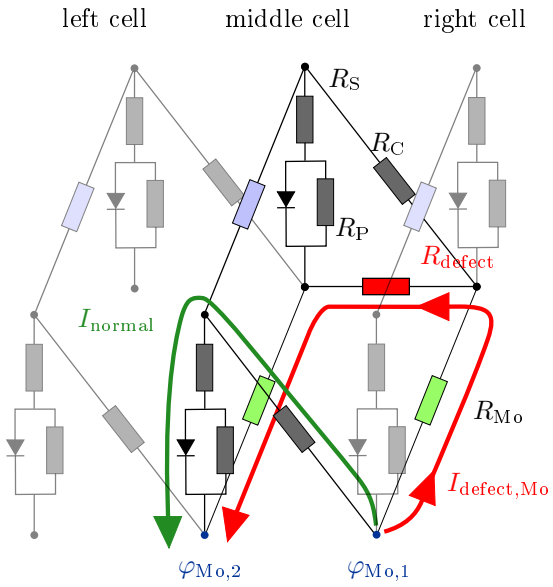

Figure 6.11: *Schematic Mo currents in case of P1 defect. Normal current flow I_{normal} from right to middle cell between potentials $\varphi_{Mo,1}$ and $\varphi_{Mo,2}$ in the Mo layer is shown by the green arrow. The defective current flow $I_{defect,Mo}$ results from a lower resistance alongside the red current path compared to the green one.*

$I_{\mathrm{defect,TCO}}$ does not enter the Mo layer in the right cell through R_C before the defect position, as shown in Fig. 6.12 (a).

Note that the defect currents shown in Fig. 6.11 and Fig. 6.12 overlay and together form the U-turn at the defect edges in Fig. 6.10 (a), although $I_{\mathrm{defect,TCO}}$ is small compared to $I_{\mathrm{defect,Mo}}$, as the comparison of the colour bars in Fig. 6.10 (a) and (c) shows.

Fig. 6.10 (d) presents that the U-turns at the upper and lower P1 defect edges cause two centres of increased dissipated power. Fig. 6.10 (e) and (f) contain that the power dissipation within the CIGS absorber plus buffer layer, and the TCO layer respectively, corresponds to the current densities shown in (b) and (c). While in a defect free case most of the power is dissipated in the TCO sheet resistance and in the CIGS series resistance, our simulation results in Fig. 6.10 (d)-(f) show that in case of a P1 scribing defect most of the power is dissipated at the upper and lower defect edges within the Mo layer.

Hence, the simulated current flow in Fig. 6.10 (b) explains the measured EL image in Fig.6.9 (b) for the P1 defect, while the simulated current flows in Fig. 6.10 (d)-(f) explain the two heat centres between middle and right cell in the measured DLIT image for the P1 defect in Fig. 6.9.

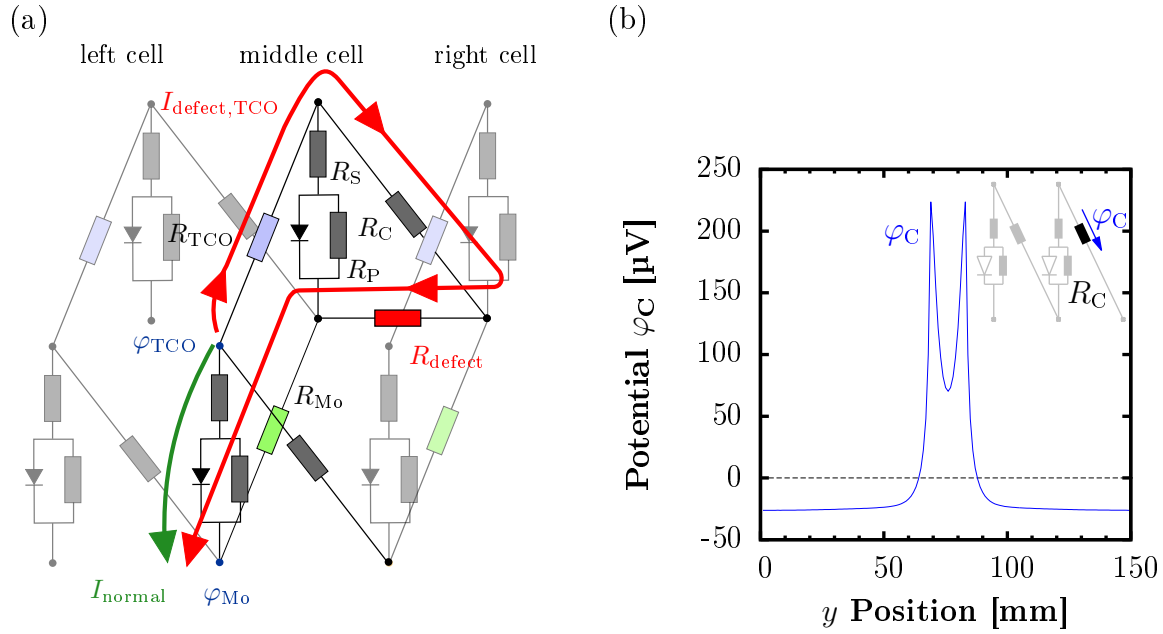

Figure 6.12: *Schematic TCO currents in case of P1 defect. (a) The normal current flow I_{normal} within the middle cell between the potentials φ_{TCO} and φ_{Mo} is shown by the green arrow, while the defective current flow $I_{defect,TCO}$ is shown by the red arrow. The change in current flow occurs as the total resistance along the red current path is smaller. (b) Simulated potential φ_C across the resistor R_C. A potential $\varphi_C < 0$ blocks any current flow from TCO to Mo layer through R_C. Only close to the defect there is $\varphi_C > 0$ and $I_{defect,TCO}$ can flow from middle to right cell through R_C.*

6.3.4.2 Simulation of the P3 Defect

In analogy to Fig. 6.10, the Fig. 6.13 depicts the simulation results for the P3 scribing defect that is located between the left and middle cell.

With regard to the current flow, two striking attributes can be observed: First, the Mo current in Fig. 6.13 (a) in the middle cell flows, with regard to the module current direction, into reverse direction, and in the right cell from upper and lower cell edge towards the P3 defect. Second, in Fig. 6.13 (c) the TCO current in the middle cell flows towards the P3 defect and forms a U-turn at the defect edges. Both effects are explained schematically in Fig. 6.14.

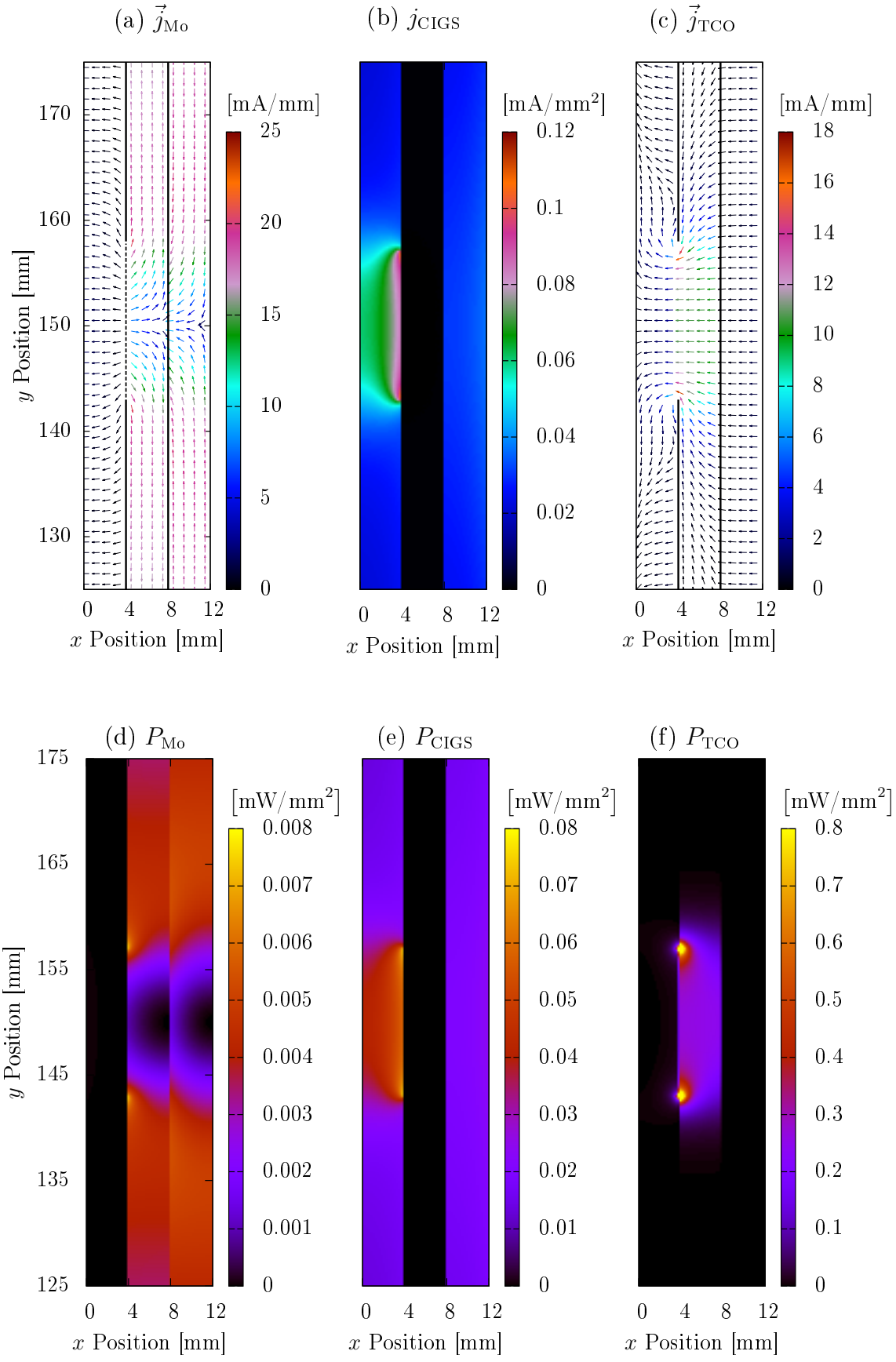

Figure 6.13: *Simulation of a P3 defect of 14 mm length with j_{DLIT} = 8.3 mA/cm^2. (a) Horizontal current flow within Mo. (b) Vertical current flow through CIGS plus buffer layers. (c) Horizontal current flow within TCO. Correspondent power dissipation is shown in (d) - (f).*

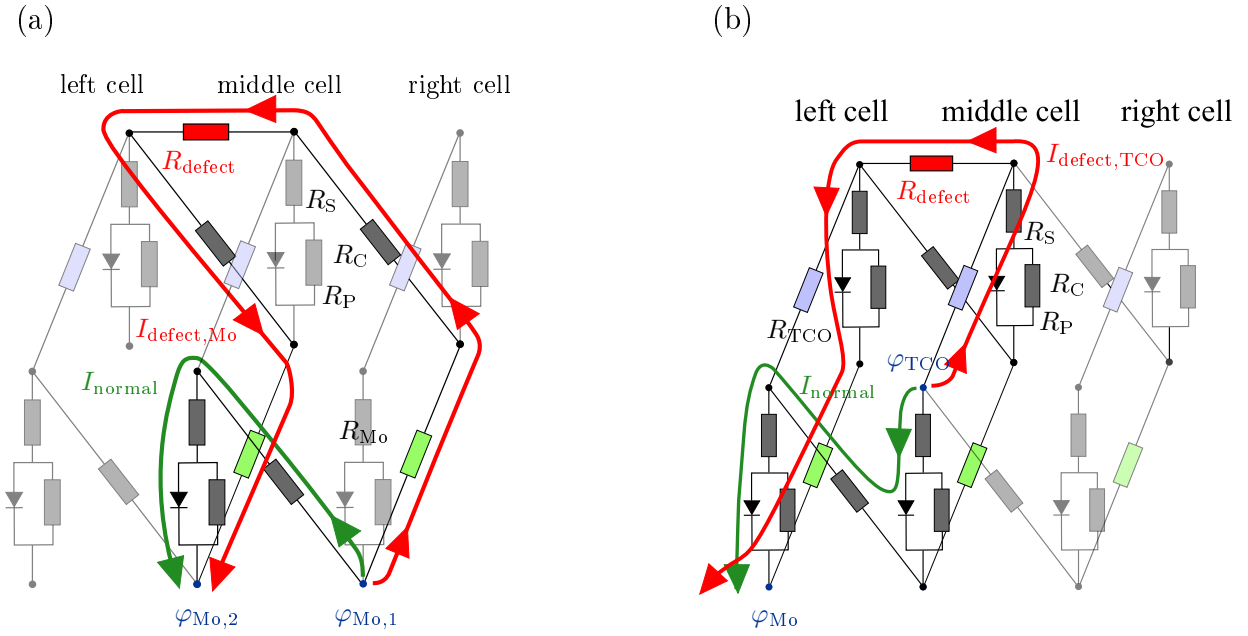

Figure 6.14: *Schematic Mo and TCO currents in case of a P3 defect. (a) The normal current flow I_{normal} from the right to the middle cell between the potentials $\varphi_{Mo,1}$ and $\varphi_{Mo,2}$, as shown by the green arrow, is locally bypassed by the red path due to a smaller total resistance. (b) Additionally, the normal current flow I_{normal} from the middle to the left cell between the potentials φ_{TCO} and φ_{Mo}, as shown by the green arrow, is also locally bypassed by the red path due to a smaller total resistance.*

Fig. 6.14 (a) illustrates the normal current I_{normal} and the defect current $I_{\mathrm{defect,Mo}}$ between the Mo potentials $\varphi_{\mathrm{Mo,1}}$ in the right cell and $\varphi_{\mathrm{Mo,2}}$ in the middle cell in case of a P3 defect. Up to a certain distance from the P3 defect the red path has a smaller total resistance than the green one. The same defect mechanism applies to the current between the potentials φ_{TCO} to φ_{Mo} in Fig. 6.14 (b). Both defect currents in Fig. 6.14 (a) and (b) overlay and form the U-turns in the TCO layer at the defect edges, as shown in Fig. 6.13 (c), which leads to the two characteristic heat centres in Fig. 6.13 (f).

Comparison of Fig. 6.13 (d), (e), and (f) yields that the P3 defect leads to the highest power dissipation in the TCO layer, which explains the two visible heat centres at the defect edges between the left and middle cell in the measured DLIT image in Fig. 6.9 (a).

6.3.5 Comparison of Simulated and Measured DLIT Images

In the following I eventually compare the simulated and measured DLIT images. In Section 6.3.4 I have shown simulations of the P1 and P3 defect for the same defect length $L_{\mathrm{P1}} = L_{\mathrm{P3}} = 14$ mm, for the sake of comparability of the simulated current vector fields and dissipated powers within each layer. However, my available real CIGS samples do not provide identical line interruptions and cell lengths of the CIGS samples, which is why I simulate in Fig. 6.15 (a) an interruption of $L_{\mathrm{P1}} = 14$ mm for the P1 defect in a CIGS sample with a cell length $L_{\mathrm{cell}} = 300$ mm, and in

Fig. 6.15 (b) an interruption of $L_{P3} = 20$ mm for the P3 defect in a CIGS sample with a cell length $L_{cell} = 230$ mm. Thus, Fig. 6.15 basically allows the utmost comparability between the DLIT simulation and DLIT measurement (with regard to both P1 and P3 defects), while Fig. 6.10 and Fig. 6.13 allow the utmost comparability between the correspondent simulations.
The y-axis in Fig. 6.15 (a) is valid for all four images and shows 50 mm alongside the cell length, while the x-axes show the width of three cells. The simulated images in (a) and (c) show the simulated power P_{th} in mW/mm^2, which can basically be calculated as the sum of the dissipated powers in the Mo electrode, absorber, and TCO electrode, as shown in Fig. 6.10 (d)-(f) for the P1 defects and in Fig. 6.13 (d)-(f) for the P3 defects.
The measured DLIT images in (b) and (d) present the camera signal S_{DLIT} which is not calibrated to mW/mm^2 and is therefore given in arbitrary units.

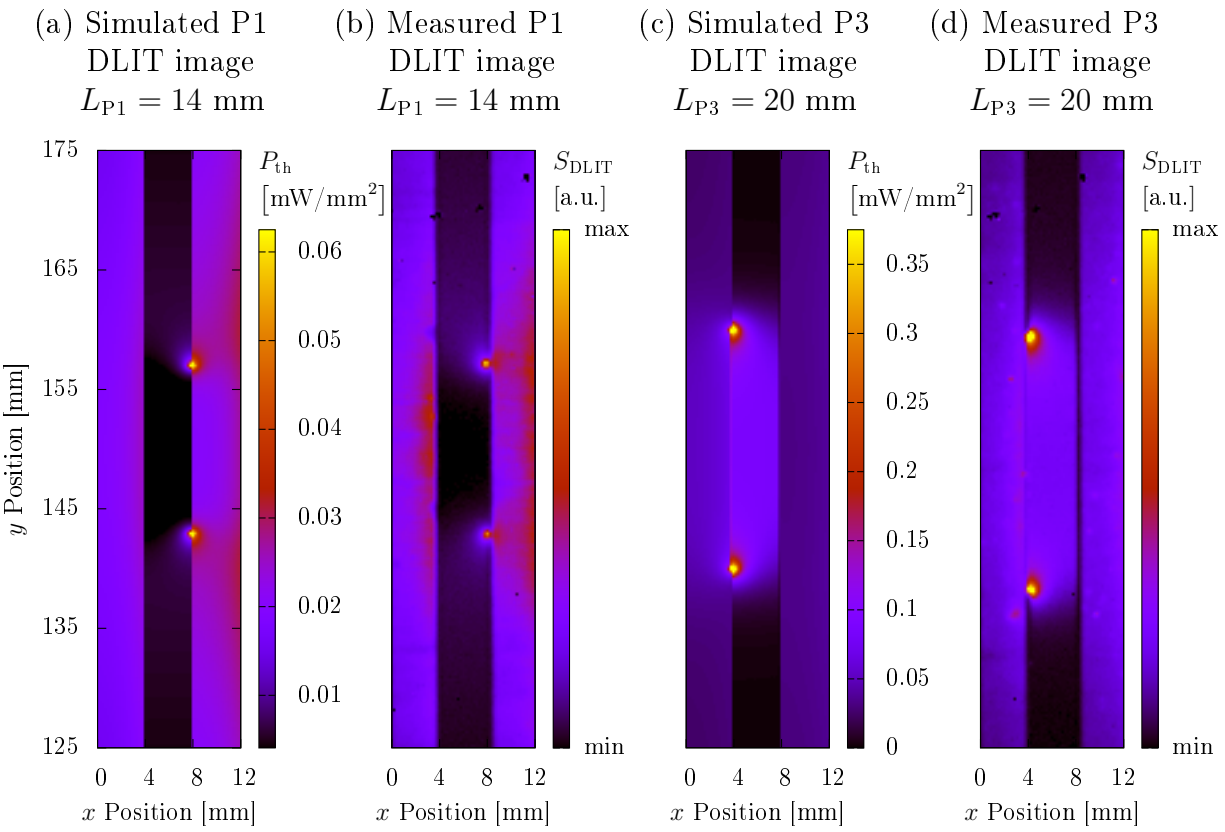

Figure 6.15: *Comparison of simulated and measured P1 and P3 defects. The simulated DLIT images are based on the sum of the dissipated powers in the single Mo, absorber, and TCO layers, as it has been exemplified for the P1 defect in Fig. 6.10 (d)-(f), and for the P3 defect in Fig. 6.13 (d)-(f), respectively. In (a) the simulated DLIT image of a 14 mm long P1 scribing defect is shown and contrasted with the correspondent DLIT measurement in (b). In (c) the simulation of a 20 mm long P3 defect is presented next to the correspondent DLIT measurement in (d). The y-axis in a) is valid for all four images. Both simulations and measurements are shown for $j_{DLIT} = 8.3$ mA/cm^2. The used DLIT camera is not calibrated which is why its signal S_{DLIT} is shown in arbitrary units. To draw a conclusion, the simulations do pretty precisely match with the real measurements.*

Furthermore, the measured DLIT images in (b) and (d) show several dark spots in the region $y \approx 165 - 173$ mm among each cell and $y \approx 137$ mm in the right cell, which are dead pixels in the camera sensor and therefore have nothing to do with the CIGS sample itself.
Both (a) and (b) show that the heat dissipation within the absorber (including the buffer layers) takes place only within the left and right cell in case of the P1 defect. Within the middle cell only the two heat centres are visible.
While in the measured DLIT image in (b) the heat centres are located within the darkened region between left and right cell, they are symmetrically located on the cell transition itself in our simulation in (a). The reason is that in our simulation, although we take into account the dimensions of the P1, P2, and P3 line correctly for the calculation of the correspondent resistances R_{P1}, R_{C}, and R_{P3}, the scribing lines are geometrically located above each other between the first segment in the middle cell and the first node in the right cell close to the cell transition. In contrast, in the measured image in (b) the complete so called dead area, which is spanned from P1 to P3 line (and the distances in between), appears dark, which means that the darkened middle cell appears wider than the neighbouring cells and therefore the two heat centres seem to be within the middle cell.
Moreover, note that we do not try to match single simulation parameters (like ρ_{Mo}) to the measured DLIT image in b) as this is a different kind of work which has to be done preferably in EL image analysis [81]. Instead, here we focus on providing a qualitative explanation of the defect mechanism.
The measurement of the P3 defect in (d) yields an increased DLIT signal close to the defect in the middle cell, while the rest of the middle cell remains dark. We have explained this with decreasing currents through the absorber in the middle cell in Fig. 6.13 (e), and an increased power dissipation in the TCO electrode in the region of the P3 defect, especially at the ends of the line interruptions, where, in analogy to the P1 defect within the Mo electrode, within the TCO electrode the two heat centres occur, as simulated in Fig. 6.13 (f).
To draw a conclusion, the simulated images in Fig. 6.15 very well match the real measurements.

6.3.6 Conclusions

This chapter studies the defect mechanisms of P1, P2, and P3 scribing failures. I find characteristic patterns in measured DLIT images for each scribing defect type. Based on simulations with the network simulation model, I give a detailed explanation of the measured DLIT by correlating it with complex current flow patterns as they uniquely result from P1, P2 and P3 defects.

The most remarkable finding is that P1 defects basically lead to two heat centres in the DLIT image which are located to the left of the affected P1 scribing line (assuming a module current from right to left), while P3 defects lead to two heat centres in the DLIT image which are located to the right of the affected P3 scribing line. In contrast, the P2 defect acts only as a current blocking wall in both the correspondent EL and DLIT image.

The results suggest that the knowledge about the characteristic DLIT defect patterns can be used for a defect diagnostics, which is discussed more detailed in the following chapter.

Chapter 7

Defect Detection and Identification

"The subject of this chapter is the identification of defects by characteristic defect patterns in EL and DLIT measurements."

7.1 Introduction

Chapter 6 has introduced point defects and scribing line defects, and the results have contributed to the understanding of the defect mechanism. In this chapter I discuss how some of these defects can not only be detected in EL and DLIT measurements, but also identified and distinguished from each other. Hence, this chapter will yield a defect diagnostic.

The appearance of defects depends on (i) the measurement resolution, (ii) the defect geometry, (iii) the defect position, and (iv) the interaction of defects. While (i) is only limited by technical means, I investigate (ii)-(iv), that are often closely linked to each other, in the following Chapter.

7.2 Identification of P1 Defects

Fig. 7.1 (a) shows the microscope image of a P1 line where the laser scribing has been interrupted on a length of $L_{\mathrm{P1}} = 412$ µm. The visible fractures in the Mo layer occur during Cu(In,Ga)Se_2 absorber deposition due to thermally induced mechanical stress between the Mo layer with a thermal expansion coefficient of $\alpha_{\mathrm{Mo}} = 5.2 \times 10^{-6}$ K^{-1} [119] and glass with $\alpha_{\mathrm{glass}} = 9.1 \times 10^{-6}$ K^{-1} [120]. Hence, the actually conductive Mo remnant in Fig. 7.1 (a) is smaller than 412 µm.

These fractures are also visible in Fig. 7.1 (b), where the concatenated microscope image of a P1 line interruption of $L_{\mathrm{P1}} = 5$ mm is shown. Note that the fracture lengths are negligible in Fig. 7.1 (b), as they are much smaller than 5 mm.

A comparison of the correspondent EL images in Fig. 7.1 (a) and (b) yields that the P1 defect causes a significant cross-talk even for small L_{P1} of only a few µm. The two EL images in Fig. 7.1 (a) and (b) show generally the same brightness pattern, while the correspondent DLIT images yield the striking difference of one heat centre in (a) and two heat centres in (b). I have explained the

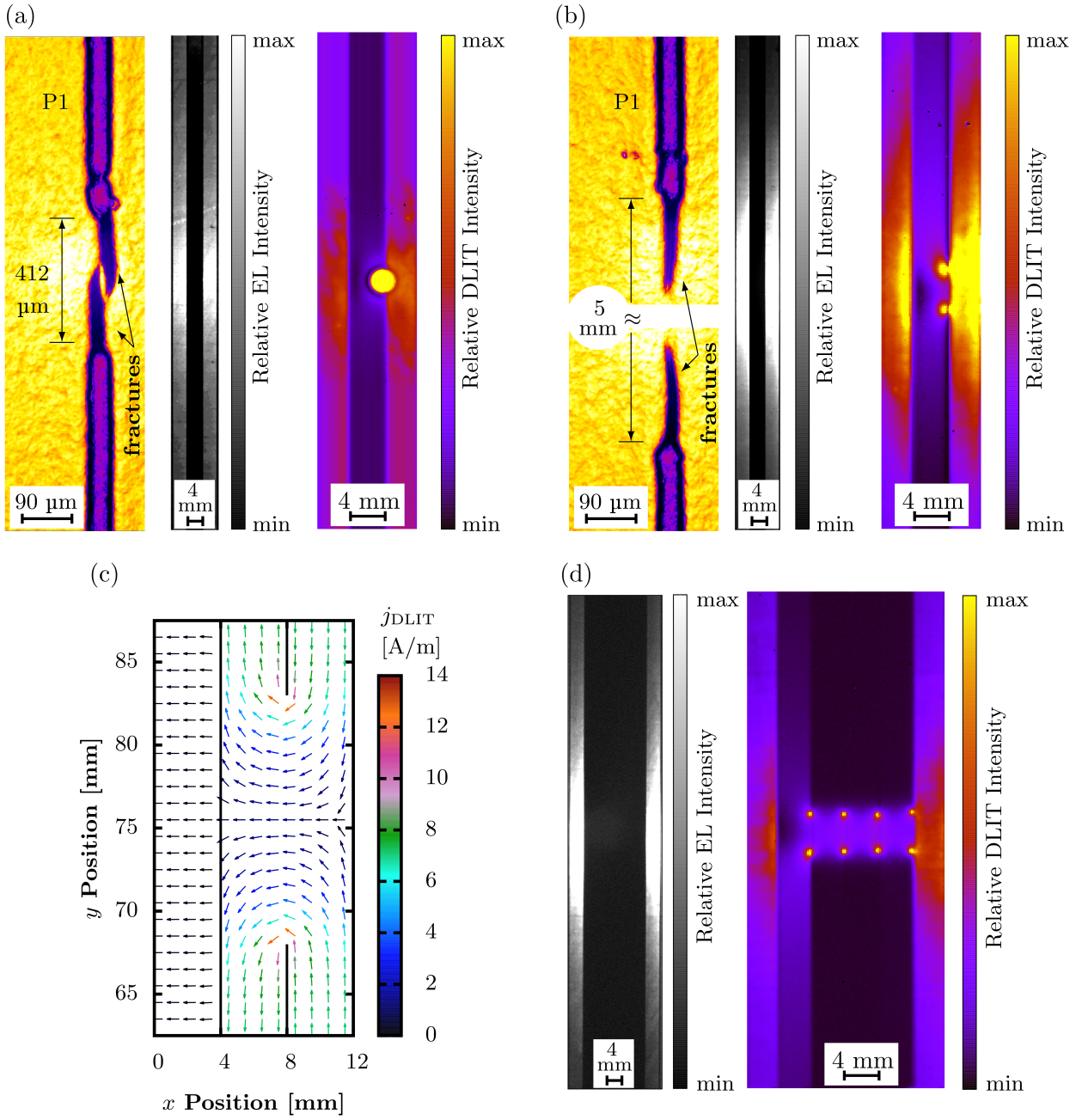

Figure 7.1: *P1 failure appearance for (a) $L_{P1} = 412\ \mu m$ and (b) $L_{P1} = 5$ mm in microscope (recorded and illuminated from glass side), EL, and DLIT (both measured at $j = 8.3\ mA/cm^2$) images. Microscope image in (b) is combined from two images due to the long L_{P1}, and defects in (a), (b), and (c) are located between middle and right cell. (c) Simulated current flow in Mo back electrode. (d) EL and DLIT of four subsequent P1 failures of $L_{P1} = 5$ mm (also measured at $j = 8.3\ mA/cm^2$).*

creation of the two heat centres in Fig. 7.1 (b) in detail with my NSM in Chapter 6.3.4. Fig. 7.1 (c) exemplifies the current flow within the Mo back electrode for a simulation of $L_{P1} = 14$ mm (I simulate a longer P1 defect for the sake of better visibility) and depicts that the currents flowing from the upper and lower cell edges towards the defect cause the U-turns and therefore highest current densities at the defect edges. The heat centres are consequently located at the defect edges between the middle and right cell.

The two heat centres can not be distinguished in DLIT for $L_{P1} < 1.0$ mm as the heat diffusion leads to a thermal blurring that makes the two lateral heat centres appear as one single heat centre, while the heat centres are distinguishable for approximately $L_{P1} > 1.0$ mm.

In the production environment that we work in, the glass substrates are transported on rolls which can leave rather long smudges. These smudges can absorb the laser beam energy during glass side scribing [42], and thus can lead to interruptions in the P1 line. Due to the length of the smudges several adjacent P1 lines may be interrupted, as shown in Fig. 7.1 (d) with the EL and DLIT image of four adjacent P1 defects, all of $L_{P1} = 5$ mm. The characteristic EL and DLIT patterns for a single P1 defect are consequently enhanced by the number of additional subsequent P1 defects. Thus, the number of darkened cells in EL and of heat centre pairs in DLIT correspond to the number of adjacent P1 failures.

7.3 Identification of P2 Defects

Fig. 7.2 depicts the appearance of P2 defects for (a) $L_{P2} = 45$ µm and (b) $L_{P2} = 30$ mm. The EL and DLIT image in Fig. 7.2 (a) show that the P2 defect is practically not visible for small defect lengths in the range of µm. However, the P2 defect becomes visible when its length is in the range of mm, as it is shown in Fig. 7.2 (b), where the locally missing P2 line blocks the current flow and leads to a darkening in the middle cell both in EL and DLIT. The current that has to flow around the P2 defect causes a slightly increased EL signal in the middle cell near the defect edges in Fig. 7.2 (b).

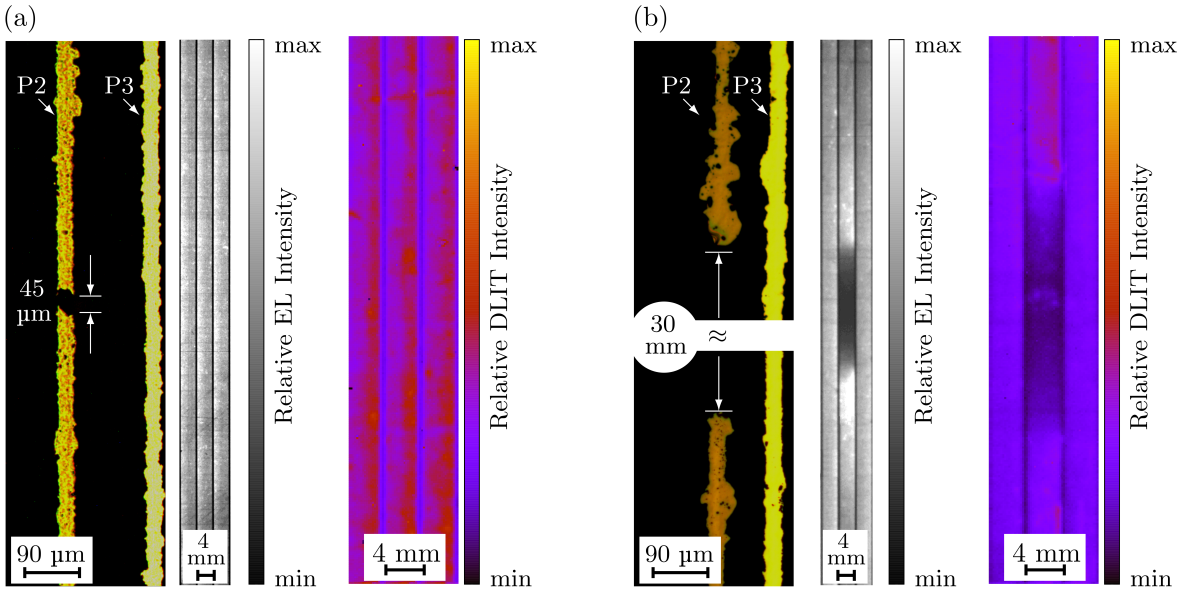

Figure 7.2: *P2 defect appearance for (a) $L_{P2} = 45$ µm and (b) $L_{P2} = 30$ mm in microscope, EL, and DLIT images (EL and DLIT measured at $j = 8.3$ mA/cm^2). P2 defects are located at vertical centre between middle and right cell. Microscope images are recorded/illuminated from film side, microscope image in (b) is combined from two images due to the long L_{P2}.*

7.4 Identification of P3 Defects

In Fig. 7.3 the microscope, EL, and DLIT images of three P3 defects with (a) $L_{P3} = 25$ µm, (b) $L_{P3} = 328$ µm, and (c) $L_{P3} = 4$ mm, which are all located at the cell transition between left and middle cell, are shown. The EL and DLIT image in Fig. 7.3 (a) depict that the ZnO:Al sheet resistance prevents any visibility of P3 defect lengths in the range of a few µm.

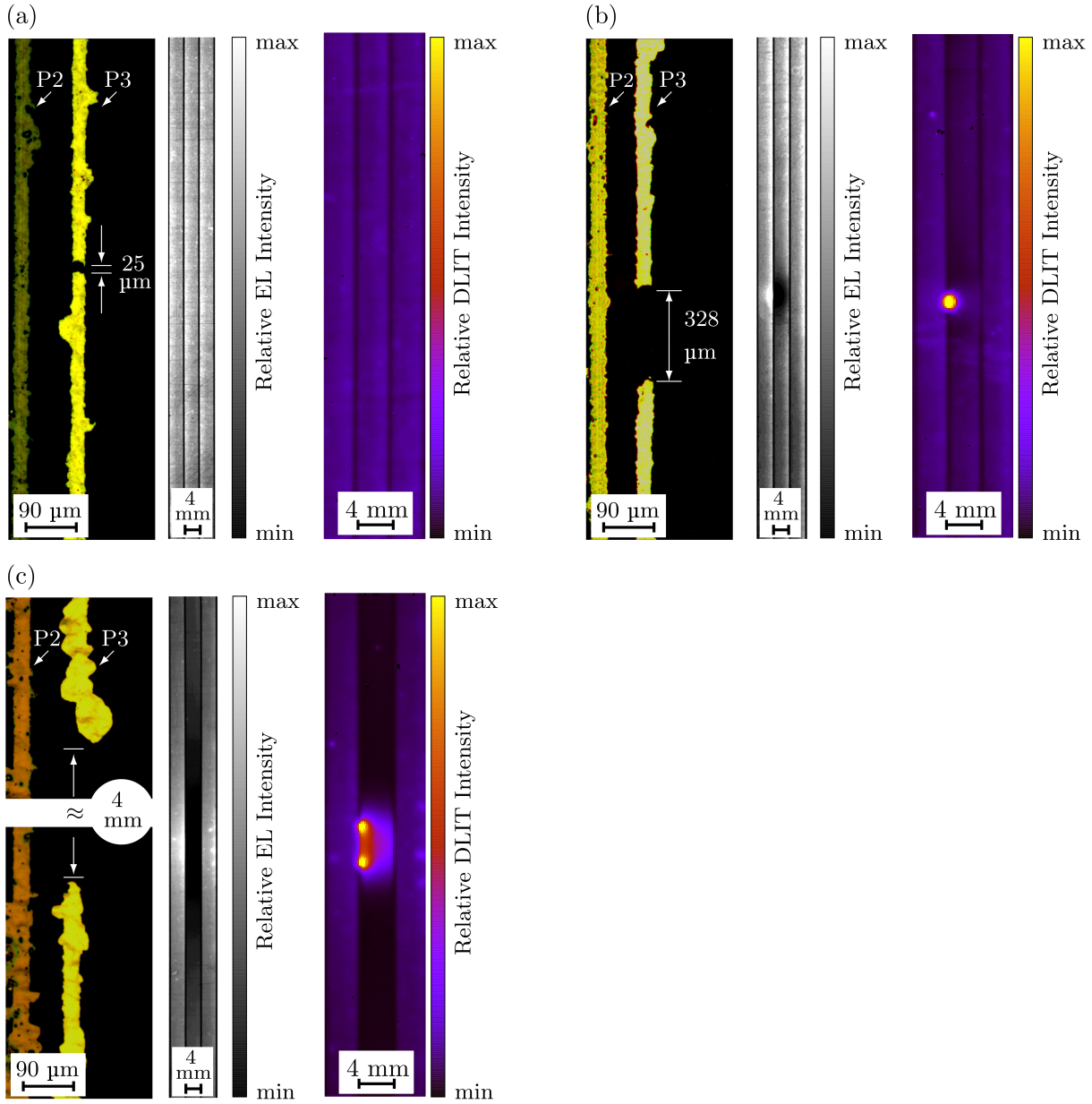

Figure 7.3: *P3 defect appearance for (a) $L_{P3} = 25$ µm, (b) $L_{P3} = 328$ µm, and (c) $L_{P3} = 4$ mm in microscope, EL, and DLIT images. The P3 defect is positioned at the vertical centre between the left and middle cell. The EL and DLIT is measured at $j = 8.3$ mA/cm^2. Microscope images are recorded/ illuminated from film side, and microscope image in (c) is combined from two images due to the long L_{P3}. Only for $L_{P3} > 1$ mm the P3 defect can be reliably identified in the DLIT by two heat centres to the right of the affected cell transition, while in case of P1 defects the heat centres appear to the left of the affected cell transition.*

For P3 defect lengths in the range of several hundred µm, as shown in Fig. 7.3 (b), the defect causes in the EL image a darkening in the middle cell and cross talk is visible in the left cell. The correspondent DLIT image in Fig. 7.3 (b) shows one heat centre which is why this scenario can simply be mistaken for a small shunting defect within the middle cell close to the cell transition between the left and middle cell, as I will show in Chapter 7.5. For P3 defect lengths in the range of mm, as exemplified in Fig. 7.3 (c), the cross talk in the EL image becomes stronger and affects both neighbouring cells, and the correspondent DLIT image shows two heat centres. The creation, position and appearance of the two heat centres in case of the P3 defect has been introduced in Chapter 6.3.4.2. The scribing defect appearances from Fig. 7.1 - 7.3, are summarised quantitatively in Table 7.1.

Defect type	Defect length	Measure-ment	Characteristics
P1	$L_{P1} < 1$ mm	Optical	Visible
		EL EL	"Bright-Dark-Bright" pattern
		DLIT	One heat centre to the left
	$L_{P1} \geq 1$ mm	Optical	Visible
		EL	"Bright-Dark-Bright" pattern
		DLIT	Two heat centres to the left
P2	$L_{P2} < 1$ mm	Optical	Visible
		EL	Not visible
		DLIT	Not visible
	$L_{P2} \geq 1$ mm	Optical	Visible
		EL	Darkened middle cell
		DLIT	Darkened middle cell
P3	$L_{P3} < 100$ µm	Optical	Visible
		EL	Not visible
		DLIT	Not visible
	100 µm $\leq L_{P3} <$ 1 mm	Optical	Visible
		EL	"Bright-Dark" pattern
		DLIT	One heat centre to the right
	$L_{P3} \geq 1$ mm	Optical	Visible
		EL	"Bright-Dark-Bright" pattern
		DLIT	Two heat centres to the right

Table 7.1: *Found identification ranges for P1, P2, and P3 scribing defects. The transitions between the identification ranges are estimated based on my experiments, and therefore strongly depend on the EL and DLIT measurement resolutions I have chosen. Furthermore, the identification ranges will vary in dependence of the individual material parameters of each CIGS manufacturer, e.g. on the sheet resistance of the Mo and TCO electrodes.*

7.5 Identification of Point Defects

The distinction of point defect types Mo-01 ... CIGS-09 is discussed with the help of Figure 7.4.

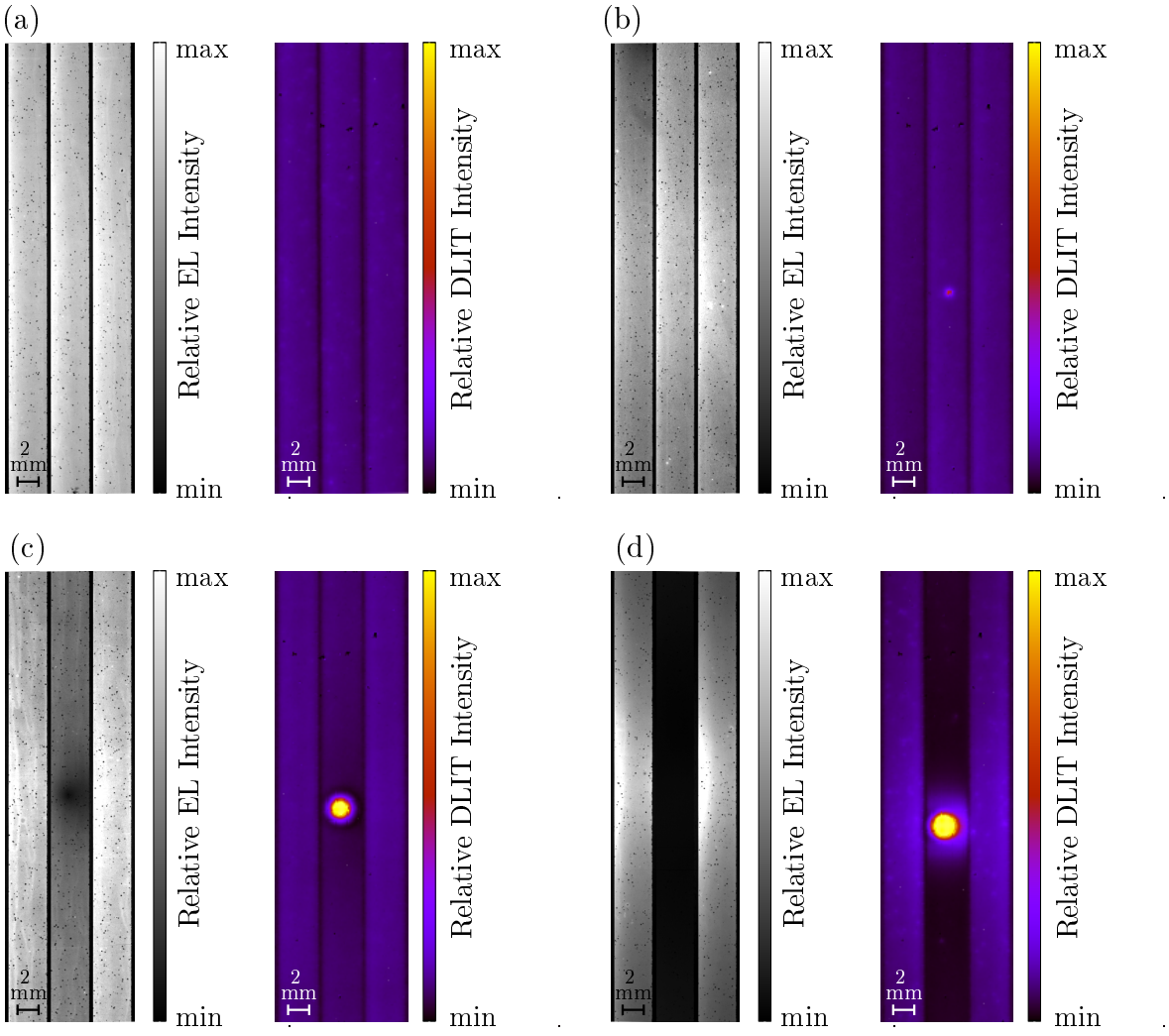

Figure 7.4: *EL and DLIT of point defect types (a) Mo-01 (with a diameter of 277 µm), (b) Mo-02 (with a diameter of 127 µm), (c) Mo-03 (with a diameter of 148 µm), and (d) Mo-04 (with a diameter of 141 µm), all measured at $j = 8.3\ mA/cm^2$.*

The images in Figure 7.4 (a) are representative for the defect types Mo-01, Mo-05, and CIGS-09, where at least one electrode is missing, which leads to inactive solar cell areas that neither cause shunts in EL nor heat centres in DLIT.

I have shown in Figure 6.6 in Chapter 6 that the defect type Mo-02 with a diameter of 127 µm leads to a ratio $S_{\mathrm{def}}^{\mathrm{avg}}/S_{\mathrm{ref}}^{\mathrm{avg}} \approx 1$ and $\Delta\bar{V}_{\mathrm{p\text{-}n}} \approx 0$, which means that the defect is practically invisible in the EL image of Figure 7.4 (b). In contrast, in the DLIT image of Figure 7.4 (b) the dissipated heat is already detectable. Further detailed EL and DLIT measurements at much higher resolutions and applying the de-convolution of thermal heat diffusion in DLIT measurement, as presented by Breitenstein [86] and Siegloch [88], are required to explain this phenomenon precisely. In general, the change of the thermal emissivity ε at the Mo-02 defect position (as it lacks the Mo and CIGS absorber layer) compared to its surrounding, could for very small shunt currents and thus voltage

reductions, as indicated by the EL image, explain why the defect appears more pronounced in the DLIT. But as stated before, a future investigation will include much higher DLIT resolutions than have been applied in this work, and thus the exact explanation of Figure 7.4 (b) is beyond the scope of this work.

Figures 7.4 (c) and (d) show for the defect type Mo-03 with a diameter of 148 µm and the defect type Mo-04 with a diameter of 141 µm that a further decreasing of $S_{\mathrm{def}}^{\mathrm{avg}}/S_{\mathrm{ref}}^{\mathrm{avg}} \approx 1$ is linked with an increased signal at the defect position and more darkened area around the defect position in the middle cell within the correspondent DLIT images.

I find experimentally that it is not possible to distinguish between the point defect types Mo-02, Mo-03, Mo-04, CIGS-06, CIGS-07, and CIGS-08 based on EL and DLIT, as the effect of the defect feature size and the specific shunt characteristic of each point defect type overlay in the images.

7.6 Identification of Cu-rich Debris

Cu-rich debris, a contamination occurring during CIGS absorber deposition, has been introduced in Chapter 3 with the defect ID ***D-3*** in Table 3.1, and its origin has been introduced in Chapter 3.2.6. In the following I discuss under which circumstances the Cu-rich debris can be identified in EL and DLIT images.

I demonstrate the influence of the size and position of Cu-rich debris in Fig. 7.5, where the debris is located (a) within the cell centre, (b) close to the cell centre, and (c) on a P1 scribing line.

The width of the Cu-rich debris in Fig. 7.5 (a) spans with its 3 mm almost the complete width of the middle cell. The correspondent EL image in Fig. 7.5 (a) depicts a "bright-darkened-bright" pattern that can be either mistaken for a P1 scribing defect, as I have shown it in Fig. 7.1 (b), or a P3 scribing defect, as I have shown it in Fig. 7.3 (c). Thus, a reliable diagnostics additionally requires the correspondent DLIT image in Fig. 7.5 (a) where the increased heat dissipation within the middle cell indicates a point-like shunt, and the lack of the DLIT patterns shown in Fig. 7.1 (b) and Fig. 7.3 (c) excludes the possibility of scribing defects. Note that the EL image in Fig. 7.5 (a) undoubtedly indicates that the Cu-rich debris is located only within the middle cell, but not within the neighbouring left and right cell, as otherwise the two neighbouring cells should contain darkening due to shunts, too. The DLIT image in Fig. 7.5 (a) even unveils that the Cu-rich debris is spread over the middle cell as two drops. The advantage of DLIT images (in contrast to EL images) to display more accurately the shape and size of the Cu-rich debris in $CuInGaSe_2$ modules has been presented already in [121].

Fig. 7.5 (b) also shows Cu-rich debris within the middle cell, but this time the diameter of the Cu drop is only approximately 100 µm, as visible in the microscope image, and the debris is located about 300 µm close to the P1 scribing line. The consequence of the small debris size and its position is that both the corresponding EL and DLIT image in Fig. 7.5 (b) can be mistaken for a P3 scribing defect as shown in Fig. 7.3 (b). Here only a microscope analysis can solve the issue and avoid confusion.

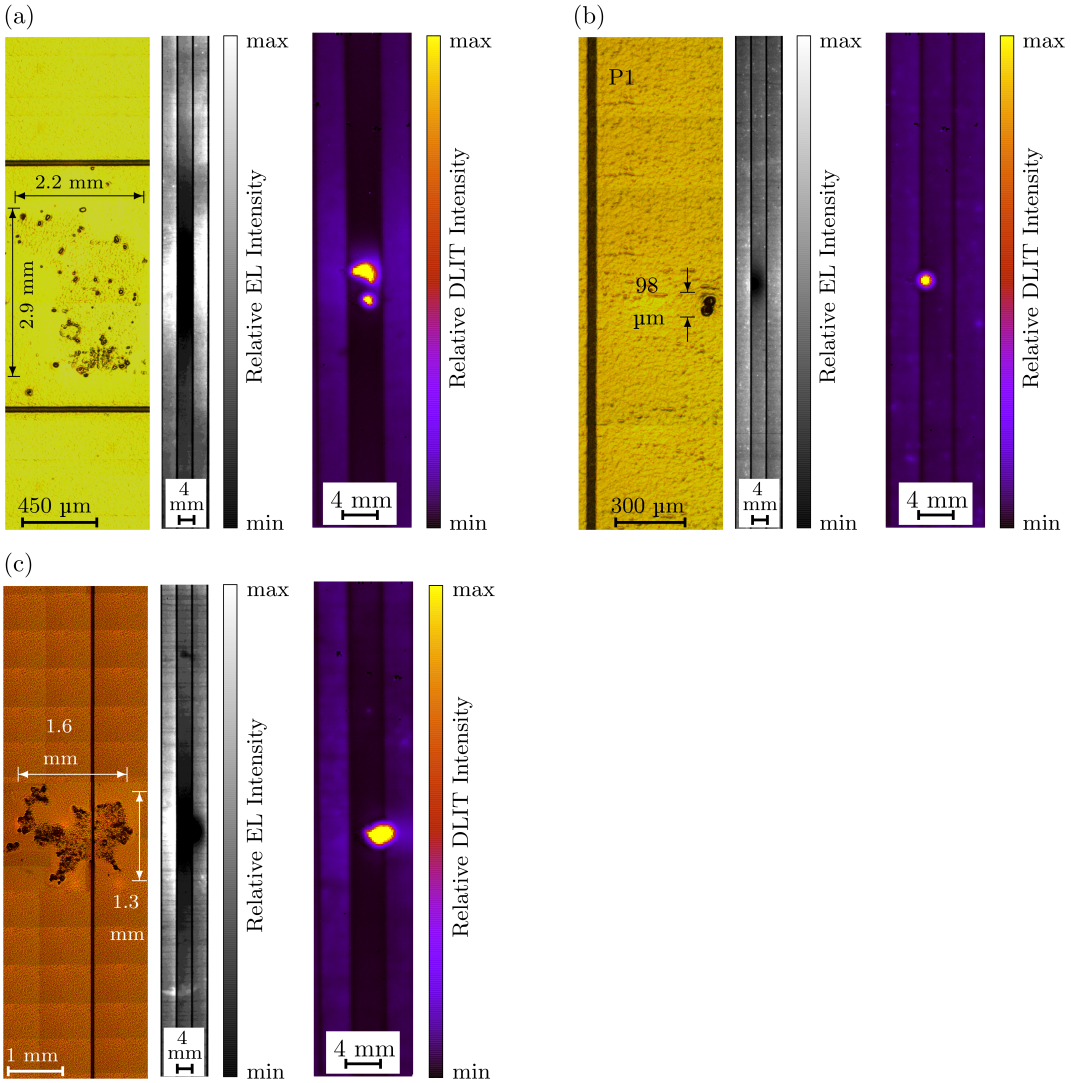

Figure 7.5: *Appearance of Cu-rich debris (a) located within the cell centre, (b) located close to the cell centre, and (c) located on the P1 scribing line. Defects in (a) and (c) can be clearly identified, while (b) is too similar to small P3 scribing defects. All microscope images are recorded and illuminated from the glass side. Microscope image in (c) is combined from multiple images in order to illustrate the complete debris. Different colours of the reflecting Mo are due to different illumination intensities.*

The most exceptional defect appearance occurs when Cu-rich debris falls onto a P1 scribing line, as shown in Fig. 7.5 (c) for the cell transition between the middle and right cell. While the DLIT image could theoretically belong to either small P1 or P3 scribing defects, as shown in Fig. 7.1 (a) and Fig. 7.3 (b), it is the EL image in Fig. 7.5 (c) that unveils a unique defect appearance. The left cell shows a visible brightness increase as a consequence of the cross-talk, the middle cell shows a darkening at the defect position, and the right cell shows an ellipsoidal darkening at the defect position. In order to explain this EL brightness pattern I apply the NSM and find the scenario shown in Fig. 7.6 to be a sound explanation for the measured EL image in Fig. 7.5 (c).

In Fig. 7.6 (a) the Cu-rich debris is schematically illustrated after Cu(In,Ga)Se_2 co-evaporation, and in Fig. 7.6 (b) after all layers have been deposited. We draw the Cu-rich debris to penetrate the Mo layer as we can see the debris in the microscope image in Fig. 7.5 (c) through the glass.

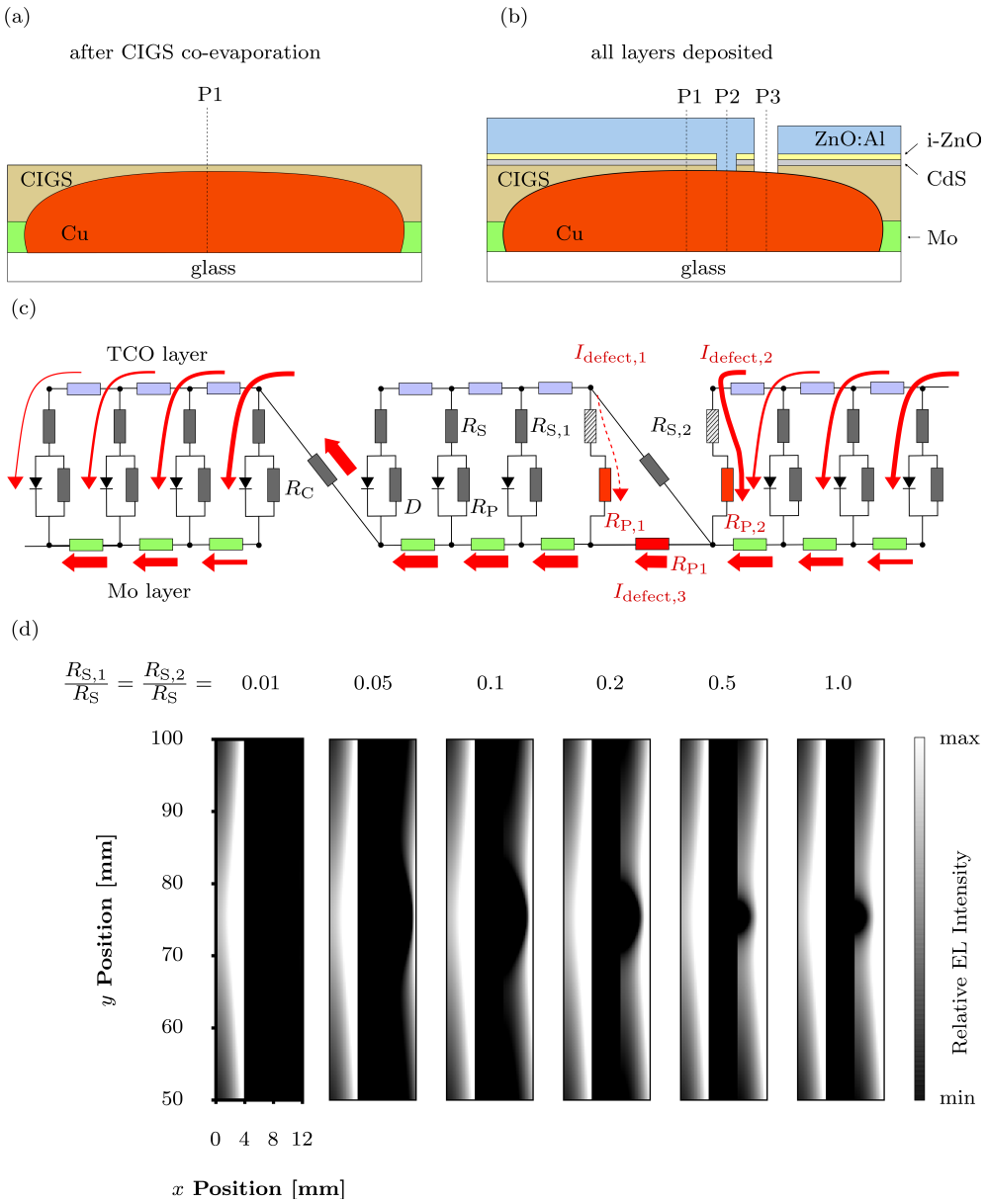

Figure 7.6: *Cu-rich debris on P1 line and neighbouring cells. Schematic layer structure shows the Cu-rich debris (a) after CIGS deposition and (b) after all layers have been deposited. (c) In the NSM the layer structure from (b) is modelled by locally reduced parallel resistivity of the CIGS (red resistances $R_{P,1}$ and $R_{P,2}$) in the left and right cell, and R_{P1} which models a P1 defect. (d) EL simulation matches the measured EL in Fig. 7.5 (c) for an intact series resistance of the CdS/i-ZnO buffer combination.*

Furthermore, in the schematic drawing it does not matter whether the Cu falls onto the module and afterwards Cu(In,Ga)Se_2 is still deposited onto the Cu, or the Cu falls onto the module at the end of the Cu(In,Ga)Se_2 co-evaporation. This is because only the deposition of the following CdS/i-ZnO buffer combination is relevant for the shunting behaviour as I have shown in Chapter 6.2. Although I draw the CdS/i-ZnO buffer combination in Fig. 7.6 (b) schematically at the defect position above the Cu-rich debris, I actually do regard different degrees of the buffer intactness by varying its local series resistance in the NSM.

Fig. 7.6 (c) presents the modelling of the defect in the NSM. At the defect position (in the middle and right cell close to the correspondent cell transition) I locally remove the diode characteristic as there is no intact p-n-junction due to the Cu. The conductivity of the Cu-rich debris is modelled by the two red resistances $R_{\mathrm{P},1}$ and $R_{\mathrm{P},2}$ with the specific electrical resistivity of Cu $\rho_{\mathrm{Cu}} = 58.1 \cdot 10^{-6}$ Ωm instead of the parallel resistivity $\rho_{\mathrm{CIGS,par}} = 0.11$ Ωm of the Cu(In,Ga)Se_2 absorber. Thus, the Cu-rich debris is modelled to cause a short circuit path in both the left and right cell close to the cell transition, which is indicated by the resulting defect currents $I_{\mathrm{defect},1}$ and $I_{\mathrm{defect},2}$.

As I want to regard a possible inefficient covering of the surface at the Cu-rich debris (no matter to which extend it is Cu(In,Ga)Se_2 or Cu) by the CdS/i-ZnO buffer combination, I locally vary the series resistance that is formed by the buffer combination, as indicated in Fig. 7.6 (c) by the dashed-patterned resistances $R_{\mathrm{S},1}$ and $R_{\mathrm{S},2}$. I investigate ratios from $R_{\mathrm{S},1}/R_{\mathrm{S}} = R_{\mathrm{S},2}/R_{\mathrm{S}} = 0.01$ ... 1.0, where R_{S} is the buffer series resistance in the defect free case.

Additionally, I model scenarios both with and without a P1 scribing failure between the middle and right cell by introducing the resistance R_{P1} with the resistivity of Cu $\rho_{\mathrm{Cu}} = 58.1 \cdot 10^{-6}$ Ωm, which takes into account that the Cu-rich debris can locally connect the two neighbouring Mo back electrodes. I assume the contact resistance between Cu and Mo to be very low and therefore neglect it for the sake of simplicity.

Fig. 7.6 (d) presents the simulated EL images for the correspondent ratios $R_{\mathrm{S},1}/R_{\mathrm{S}} = R_{\mathrm{S},2}/R_{\mathrm{S}}$. The simulated EL images in Fig. 7.6 (d) are quite comparable to the measured EL image in Fig. 7.5 (c) for $R_{\mathrm{S},1}/R_{\mathrm{S}} = R_{\mathrm{S},2}/R_{\mathrm{S}} \geq 0.5$. In contrast, my simulations without P1 scribing failure, and therefore without R_{P1}, yield completely different EL images than those in Fig. 7.5 (c), and instead only show local darkening in both the middle and right cell which is approximately of the same size.

An important observation is that the CdS/i-ZnO buffer combination apparently covers the defect position well and therefore reduces the darkening of the right cell in EL to a small region around the defect. However, in the middle cell the buffer combination plays no role for the EL as the Mo back electrode of the middle cell is shunted anyway, and therefore there can practically be no charge carrier recombination that could cause an EL signal.

We have investigated more than two hundred cases where Cu-rich debris has fallen on a P1 scribing line and the correspondent EL images always showed an EL brightness pattern very similar to that in Fig. 7.5 (c). To draw a conclusion, what we observe in Fig. 7.5 (c) in a real EL measurement and in Fig. 7.6 (d) for an EL simulation with $R_{\mathrm{S},1}/R_{\mathrm{S}} = R_{\mathrm{S},2}/R_{\mathrm{S}} \geq 0.5$ is an overlay of two shunting defects in each the middle and right cell, plus a P1 failure between the middle and right cell, caused by the Cu-rich debris.

7.7 Conclusions

I have presented how several defect types can be identified with the combination and comparison of EL and DLIT measurements.

For P1 defects (see Chapter 7.2), P2 defects (see Chapter 7.3), and P3 defects (see Chapter 7.4) I have defined identification ranges and presented the correspondent characteristic scribing defect appearance within these ranges (see Table 7.1). The found identification ranges contribute to the reliable identification of and distinction between scribing defects.

With regard to point defects (see Chapter 6.2) two groups can be identified: those which lead to inactive solar cell area (Mo-01, Mo-05, CIGS-09), and those which lead to short circuit paths in cells (Mo-02, Mo-03, Mo-04, CIGS-06, CIGS-07, CIGS-08). I have shown representatives of both groups in Figure 7.4 and explained that the distinction between the two groups is possible by a combination of EL and DLIT, while the distinction between the point defects within these two groups is not possible.

Finally, I have shown that the identification of Cu-rich debris depends on its position within the cell. One can distinguish between the Cu-rich debris in the cell centre, as shown in Figure 7.5 (a), close to a cell transition, as illustrated in Figure 7.5 (b), and on a P1 scribing line, as contained in Figure 7.5 (c). Here only the case of a Cu-rich debris in the cell centre and on a P1 scribing line can be reliably diagnosed.

The shown results can be used as a practical guide for the implementation and calibration of an automated software-based defect diagnostics of EL and DLIT measurements, e.g. in mass production sites.

Chapter 8

Repair of Defective P1 Scribing

"The subject of this chapter is the repair of incomplete P1 Mo scribing lines as it can occur inherently during module production, or can be done electrically on purpose."

8.1 Introduction

An advantage of laser scribing is that compared to mechanical scribing, where an uncontrollable chipping at the line edges requires safety margins between the lines in order to avoid short circuiting, the lines can be placed closer to each other [122]. With currently used line widths for CIGS in the range of approximately 40 - 50 µm, the total interconnect width, which is spanned by the three scribing lines and which does not contribute to the photovoltaic conversion efficiency, has been reduced from previously about 300 µm [123, p. 301-302] to currently about 180 µm.

As a result of thinner lines the process windows tend to become smaller with regard to material parameter and process variations. For instance, the P1 scribing is, with regard to the minimum required laser peak fluence, sensitive to the inherent stress in the Mo layer, which depends on the Ar gas pressure during direct current (DC) magnetron sputtering with a metal Mo target [41], as shown in Chapter 3.2.3.

In case of the P1 scribing, which is the second processing step of a CIGS module, such material or process deviations and the possible resulting line interruptions of even only a few µm can cause sever shunting due to the high conductivity of the Mo electrode, as shown in Chapters 6 and 7. This is precarious as the glass substrate and sputtered Mo layer already make up more than 30% of the module material costs [124].

Thus, it is worthwhile to investigate how a reliable monolithic series connection can be achieved even with having in mind further reductions of the interconnection width. While scribing defects ideally should be avoided, there is also the possibility to repair them. In this Chapter I present two ways of P1 defect repair. The first way is an engineering approach where I melt and evaporate the Mo remnant which leads to a sufficient insulation. The second way is to create insulating fractures in the Mo by thermally induced mechanical stress. Both ways are novel and have been discovered and developed in this thesis.

8.2 Electrical Repair

8.2.1 Introduction

By applying a current sufficiently high to both melt and afterwards evaporate the Mo remnant at the position of incomplete P1 scribing, a sufficient insulation between two neighbouring Mo back contacts can be achieved. In the following I present schematically the setup which I have developed in this work, and I introduce a first order approximation that describes the theory of the electrical repair of incomplete P1 scribing. I introduce in detail variations of the electrical repair technique and show its potential with regard to an application in a real CIGS mass production site.

8.2.2 Experimental Setup

In order to have a comprehensive set of P1 scribing defects, with multiple defect samples of each scribing line interruption length, I intentionally implement the P1 defects. I place adhesive tapes on the substrate glass where the tapes locally absorb the laser energy during glass side scribing [41, 42]. The two neighbouring cells are connected to a voltage source by contact pins, and the repair current I_{rep} results from the applied voltage V_{rep} and the Mo resistance between the contact pins, as is schematically shown in Fig. 8.1.

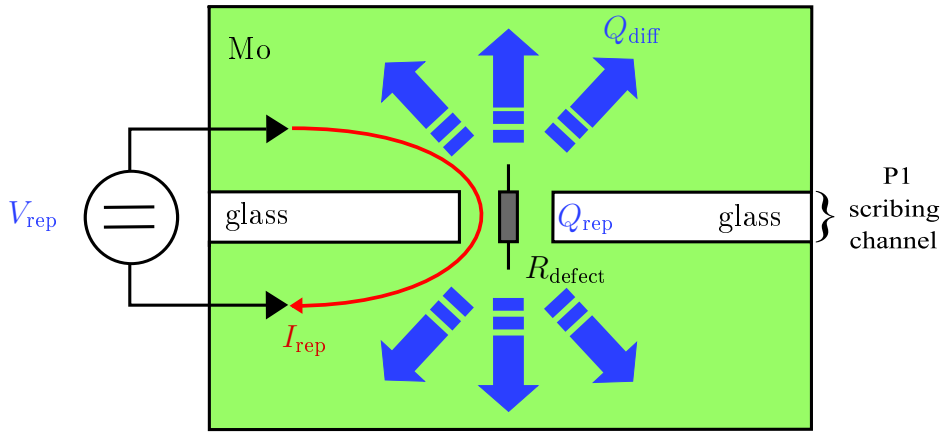

Figure 8.1: *Setup for electrical repair of P1 defects. A voltage source V_{rep} is connected to the Mo back electrodes of two neighbouring cells, and the repair current I_{rep} results from the Mo resistance between the contact pins. The heat energy Q_{rep} is used for the repair, while Q_{diff} diffuses into the surrounding Mo.*

8.2.3 Theory

In the following I first describe the changes of the Mo's states, namely from solid to gaseous. Afterwards, I explain my first order approximation of the electrical repair process and show the comparison between approximation and real measurements.

8.2.3.1 Changes of States

The Mo remnant at the position of incomplete P1 scribing can be considered as an idealised rectangle and forms with its resistivity ρ_{res} the resistance

$$R_{\mathrm{defect}} = \rho_{\mathrm{res}} \frac{w}{hL}, \tag{8.1}$$

as shown schematically in Fig. 8.2.

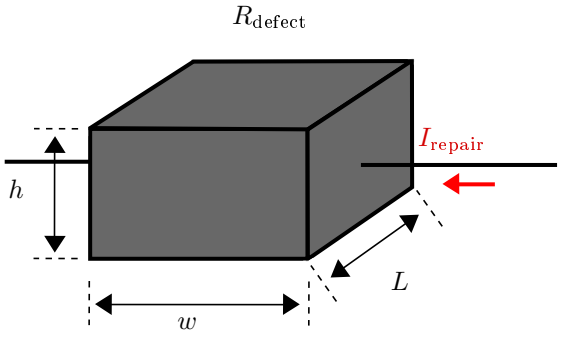

Figure 8.2: *Schematic illustration of Mo remnant in incomplete P1 channel as a rectangle body with height h, width w of the P1 line, and length L along the P1 line. The applied repair current I_{rep} flows through the Mo remnant which forms a resistance R_{defect}.*

The heat energy Q_{rep} that is dissipated in the resistance R_{defect}, and which finally leads to its melting and evaporation, is given by Joule's first law

$$Q_{\mathrm{rep}} = I_{\mathrm{rep}}^2 R_{\mathrm{defect}} t_{\mathrm{rep}}. \tag{8.2}$$

Depending on the dissipated heat energy, the state of Mo changes from solid to liquid, and eventually to gaseous. The Mo remnant is heated from initial room temperature $T_{\mathrm{initial}} = 300$ K to its melting point T_{melt} by applying the heat energy

$$Q_{\mathrm{solid}} = m c_{\mathrm{p}} \left(T_{\mathrm{melt}} - T_{\mathrm{initial}}\right), \tag{8.3}$$

where m is the mass of the Mo remnant, calculated with the mass density ρ_{mass} by

$$m = \rho_{\mathrm{mass}} h w L, \tag{8.4}$$

and c_{p} is the specific heat capacity of Mo. Applying the melting energy Q_{melt} causes the change of the Mo state from solid to liquid which is described by

$$Q_{\mathrm{melt}} = m H_{\mathrm{f}}, \tag{8.5}$$

where H_{f} is the heat of fusion of Mo. Dissipating Q_{liquid}, the Mo heats up to its boiling point T_{boil} by

$$Q_{\text{liquid}} = mc_{\text{p}} \left(T_{\text{boil}} - T_{\text{melt}}\right). \tag{8.6}$$

Finally, the evaporisation energy Q_{evap} changes the Mo's state from liquid to gaseous by

$$Q_{\text{evap}} = mH_{\text{e}}, \tag{8.7}$$

where H_{e} is the Mo's heat of evaporisation. Consequently, Q_{rep} is given by

$$Q_{\text{rep}} = Q_{\text{solid}} + Q_{\text{melt}} + Q_{\text{liquid}} + Q_{\text{evap}}. \tag{8.8}$$

The values of the aforementioned Mo material parameters, which we use for the following approximation, are listed in Table 8.1.

Table 8.1: *Mo material parameters and their values that we use for the first order approximation. The resistivity ρ_{res}, density ρ_{mass}, specific heat capacity c_p, heat of fusion H_f, heat of vaporisation H_v, melting point T_{melt}, and boiling point T_{boil} are taken from literature sources.*

Mo Parameter	Value	Reference
ρ_{res}	53.4×10^{-9} Ωm	[119]
ρ_{mass}	10.28 kg·m^{-3}	[125]
c_{p}	250 J·kg^{-1}·K^{-1}	[125]
H_{f}	3.9 $\times 10^5$ J·kg^{-1}	[126]
H_{e}	598 kJ·kg^{-1}	[119]
T_{melt}	2896 K	[125, 127–129]
T_{boil}	4912 K	[119, 130]

8.2.3.2 First Order Approximation

In my first order approximation I first neglect the heat exchange between the Mo remnant and its surrounding. Thus, $Q_{\text{diff}} = 0$ means that there is no heat diffusion from the Mo remnant into its surrounding and all heat energy is only dissipated within the Mo remnant.

Second, I assume a constant atmospheric pressure so that I can apply the literature values from Table 8.1.

Third, I assume that the Mo remnant passes the three states: solid, liquid and gaseous. However, for the sake of completeness I mention that at room temperature [131] and during heating [132] Mo oxide layers of 15 - 20 nm thickness can be formed which can behave differently. For instance, Mo trioxide MoO_3, a result of the reaction

$$Mo + 3\ O_2 \rightarrow 2\ MoO_3, \tag{8.9}$$

can directly sublimate at $T \geq 600$ K. Nonetheless, these oxide layers form at most only 2% of the total Mo remnant height of 1 µm and the high temperature oxidation described in [132] takes longer than the duration of the electrical repair in the range of seconds, which is why I can neglect direct sublimation in the following consideration.

Fourth, I approximate the change of the Mo's resistivity ρ_{res} during the repair process. Fig. 8.3 presents the resistivity ρ_{res} as a curve concatenated of measurement data from the references [133] and [134].

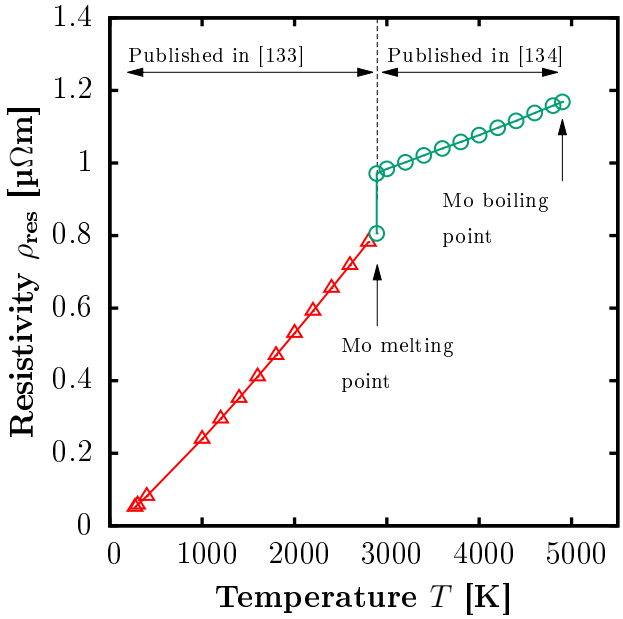

Figure 8.3: *The first order approximation takes into account the temperature dependence of the Mo's resistivity. The measurement data is extracted from references [133] and [134].*

Fig. 8.3 shows that the specific resistivity ρ_{res} of Mo increases during the electrical repair by more than about one order of magnitude. For a detailed discussion of ρ_{res} as a function of the temperature, for instance the change of ρ_{res} at the melting point, I refer to [135–139].

Consequently, I distinguish the specific resistivity in the following by ρ_{solid} in the solid state, ρ_{melt} during melting, ρ_{liquid} in the liquid state, and ρ_{evap} during evaporation. In addition to the assumption of no heat exchange with the surrounding by $Q_{diff} = 0$, I work in my first order approximation with averaged values of ρ_{res} within each state based on the data in [133] and [134], i.e. with $\bar{\rho}_{solid} = 0.4$ µΩm in the solid state, $\bar{\rho}_{melt} = 0.9$ µΩm during melting, $\bar{\rho}_{liquid} = 1.1$ µΩm in the liquid state, and for the sake of simplicity we assume $\bar{\rho}_{evap} = \bar{\rho}_{liquid} = 1.1$ µΩm during evaporation.

My first order approximation describes the relation between the repair time t_{rep} and the repair current I_{rep}. As I apply in my experimental setup the voltage V_{rep}, which leads to the repair current I_{rep} in dependence of R_{defect} (see Fig. 8.1), I can write the repair time t_{rep} as function of the repair current according to Joule's law by

$$t_{\mathrm{rep}} = \frac{Lh}{w} \sum_{\mathrm{i}=1}^{4} \frac{1}{I_{\mathrm{rep,i}}^2} \frac{Q_{\mathrm{i}}}{\rho_{\mathrm{i}}}, \tag{8.10}$$

where $i = 1$ stands for the solid phase, $i = 2$ stands for the melting phase, $i = 3$ stands for the liquid phase, and $i = 4$ stands for the gaseous phase, as introduced before in Eq. (8.3)-(8.7). Note that due to applied constant repair voltage V_{rep}, and the change in ρ_{res} during electrical repair, the repair current $I_{\mathrm{rep,i}}$ must be regarded individually for each of the four states by

$$\begin{aligned} I_{\mathrm{rep},1} &= I_{\mathrm{solid}}, & I_{\mathrm{rep},2} &= I_{\mathrm{rep}} \frac{\bar{\rho}_{\mathrm{melt}}}{\bar{\rho}_{\mathrm{solid}}}, \\ I_{\mathrm{rep},3} &= I_{\mathrm{rep}} \frac{\bar{\rho}_{\mathrm{liquid}}}{\bar{\rho}_{\mathrm{solid}}}, & I_{\mathrm{rep},4} &= I_{\mathrm{rep}} \frac{\bar{\rho}_{\mathrm{evap}}}{\bar{\rho}_{\mathrm{solid}}}. \end{aligned} \tag{8.11}$$

The comparison of my first order approximation with the real electrical repairs of seven P1 line interruptions, each of length $L = 350$ µm, is shown Fig. 8.4. For real experiments with comparatively small repair currents $I_{\mathrm{rep}} < 0.8$ A I observe high repair durations t_{rep} in the range of seconds. The repair duration increases for decreasing repair currents as the required heat energy Q_{rep} is dissipated more slowly in the Mo remnant, which consequently means more time for the heat diffusion into the surrounding Mo. Hence, the heat diffusion $Q_{\mathrm{diff}} \neq 0$ is the reason why the measured relation between the repair current and resulting repair time in Fig. 8.4 differs from the approximated one for $I_{\mathrm{rep}} \leq 0.8$ A. In contrast, for higher repair currents $I_{\mathrm{rep}} \geq 1$ A I observe that my first order approximation is in good agreement with the measured electrical repair. The higher repair currents make the Mo remnant dissipate Q_{rep} faster, and therefore there is less time for heat diffusion into the surrounding, which makes the real situation come closer to the assumptions in my first order approximation.

Note that with regard to an application in a real mass production site I do not want the electrical repair process to be a potential bottleneck and therefore prefer repair durations as short as possible. Hence, my first order approximation describes the actually relevant case of a high repair current I_{rep} leading to a short repair duration t_{rep}.

8.2.4 Results and Discussion

8.2.4.1 Repair by Constant Current

Fig. 8.5 shows the repair of three positions of incomplete P1 scribing, each of length $L = 350$ µm, by applying different constant repair currents I_{rep}. In accordance to Joule's first law, the repair duration t_{rep} in Fig. 8.5 decreases with increasing repair current I_{rep}. The correspondent microscope images of the repaired defects are shown in Fig. 8.6.

Fig. 8.6 presents microscope images of the three defects in Fig. 8.5 after the electrical repair. The shortest repair duration of $t_{\mathrm{rep}} = 0.068$ s in (a) leads to the smallest heat diffusion into the sur-

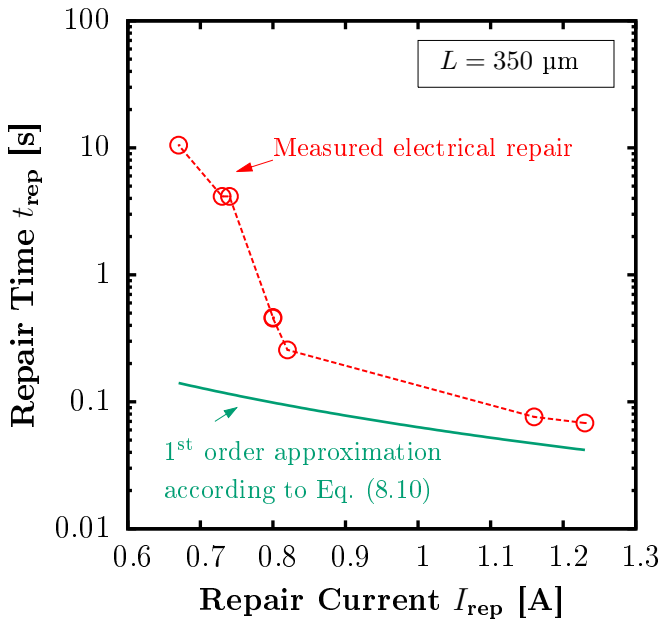

Figure 8.4: *Comparison of approximated and measured electrical repair for $L = 350$ µm. The first order approximation describes the real measurements well for repair currents $I_{rep} \geq 1$ A. In contrast, at smaller repair currents I_{rep} the repair duration t_{rep} increases and heat diffusion Q_{diff} into the surrounding cannot be neglected any more.*

rounding, where only slight thermally induced Mo fractions are visible. The melted and evaporated area is about as thin as the P1 scribing line itself.

In (b) and (c) the thermally affected areas are visibly larger. This indicates that increasing repair durations t_{rep} lead to more heat diffusion Q_{diff} into the surrounding. The abrupt disruptions in

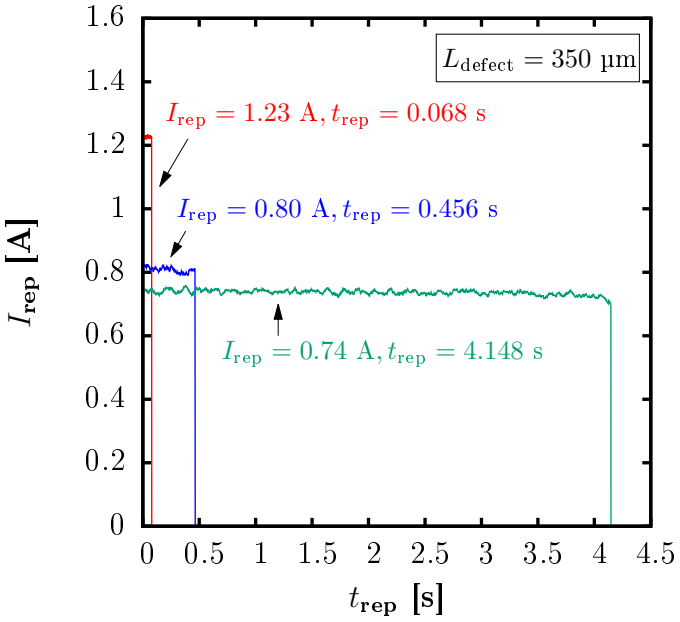

Figure 8.5: *Constant current repair of three P1 defects with $L = 350$ µm. Three different repair currents I_{rep} are applied and lead to different repair durations t_{rep}.*

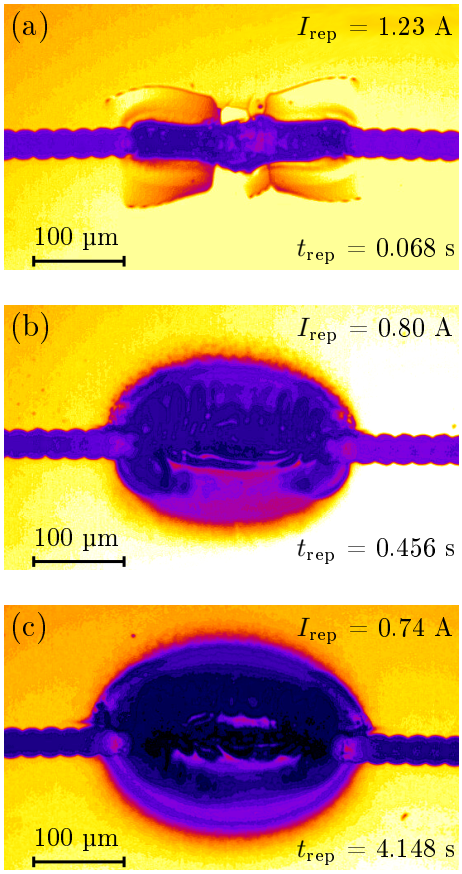

Figure 8.6: *Microscope images of electrically repaired P1 defects of $L = 350$ µm from Fig. 8.5. A short repair duration of $t_{rep} = 0.068$ s leads to less heat diffusion into the surrounding Mo than for $t_{rep} = 0.456$ s and $t_{rep} = 4.148$ s. Measured correspondent EL images prove successful electrical insulation for each repair.*

Fig. 8.5 indicate a sufficient insulation between the neighbouring Mo back electrodes. Additionally, we have measured the correspondent EL images which prove not only successful electrical insulation but also absolutely normal solar cell operation at the repair positions.

8.2.4.2 Process Window

From Fig. 8.4, 8.5, and 8.6 we extract that higher constant repair currents lead to smaller thermally affected areas around the repaired defect positions. Although we have not observed aversive effects of the relatively small thermally affected areas at the repair positions, we prefer to keep these zones small due to loss of active solar cell area, or a potential negative effect of the oxidised Mo on the contact with the CIGS absorber. Hence, at a first glance one would opt for repair currents as high as possible, and therefore configure high repair voltages V_{rep}.

However, in my experiments with very high repair currents I clearly observe arcing between the neighbouring Mo back electrodes which affects even larger areas than those shown in Fig. 8.6. Note that I did not investigate the exact arching mechanism, but only observed it visually. Physically it is the applied voltage V_{rep} that exceeds the dielectric strength of the P1 scribing line, namely 3 MV/m in air. However, in order to discuss the repair process only for two parameters, namely

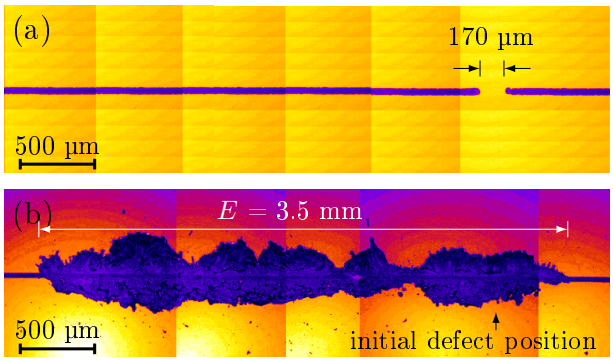

Figure 8.7: *Large damaged Mo area as a result of arcing during repair with I_{rep} = 3.6 A applied to $L = 170$ µm. P1 line is shown (a) before and (b) after electrical repair. The contact pins were placed to the left of the defect. Both microscope images consist of multiple single images which causes the repetitive horizontal brightness distribution.*

the repair current and repair time, I neglect in the following the voltage V_{rep} and discuss only the repair current that would result from applying V_{rep} to the resistance between the two contact pins, which I measured before each measurement. I exemplify the detrimental effect of arcing in the microscope images in Fig. 8.7 (both microscope images are concatenated from multiple images). In Fig. 8.7 (a) and (b) configuring a repair current $I_{\text{rep}} = 3.6$ mA has lead to arcing which has damaged a large Mo area along the current path. The damaged Mo area exceeds the defect size by orders of magnitude and must therefore be avoided. I introduce the dimension E in (b) as an easily measurable extension of the thermally affected area along the P1 line, here $E = 3.5$ mm. In order to avoid the detrimental arcing and its consequences, as shown in Fig. 8.7, I experimentally investigate a process window for the applicable repair current, which is shown in Fig. 8.8.

For the process window in Fig. 8.8 I define the repair time $t_{\text{rep}} \geq 30$ s as lower process limit because this is the module production cycle time of the CIGS mass production site that I performed my experiments at. The green striped area indicates repair currents I_{rep} which lead to repair durations $t_{\text{rep}} \geq 30$ s. However, note that this lower process limit is chosen arbitrarily and can be defined differently.

Furthermore, I define the elongation $E \geq 3$ mm of the damaged Mo area along the P1 line as the higher process limit, as I want to limit the damaged area in the surrounding of the Mo remnant. The red chequered area indicates repair currents I_{rep} which lead to $E \geq 3$ mm. Similarly to the lower process limit, this higher process limit can be defined differently if required.

In my measurements I find a process window of 1.5 A between the lower and upper process limits. Hence, even if the upper and lower process limits are moved depending on the specific Mo parameters of a manufacturer, there is a sufficiently wide and therefore feasible process window. Note that the experimentally found upper and lower process limits depend linearly from the defect length L. This linear dependence $I_{\text{rep}} \propto L$ can be also seen if one inserts Eq. (8.3) - (8.7) into Eq. (8.2), and substitutes the Mo's remnant mass by $m = \rho_{\text{mass}} whL$ and the Mo's remnant resistance by

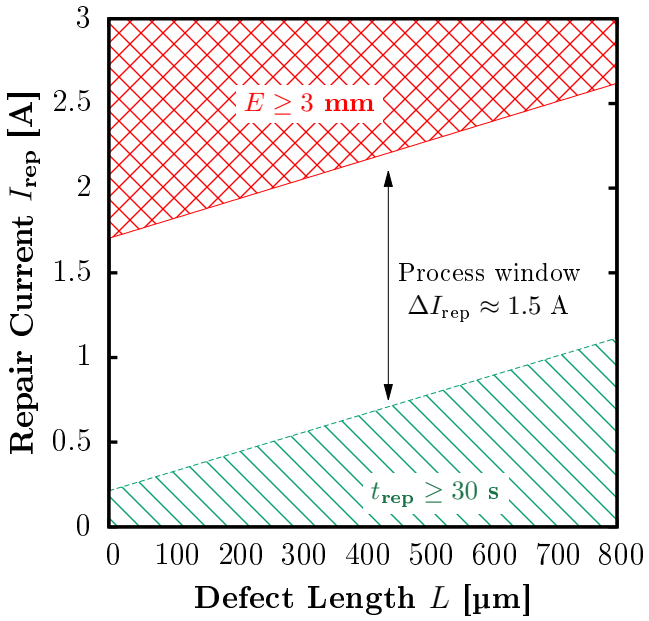

Figure 8.8: *Process window for electrical repair with constant current. Green striped area represents electrical repair currents that lead to $t_{rep} \geq 30$ s as lower process limit, and red chequered area represents repair currents that lead to $E \geq 3$ mm along the P1 scribing line as higher process limit. I find a usable process window of approximately 1.5 A.*

$R = \rho_{\mathrm{res}} w/(hL)$. I find that the lower and upper process limits can be described by

$$I_{\mathrm{rep,min}}(L) = 0.21\ \mathrm{A}\ + L \cdot 1.1 \frac{\mathrm{mA}}{\mu\mathrm{m}} \tag{8.12}$$

$$I_{\mathrm{rep,max}}(L) = 1.71\ \mathrm{A}\ + L \cdot 1.1 \frac{\mathrm{mA}}{\mu\mathrm{m}} \tag{8.13}$$

Consequently, a disadvantage of the constant current repair procedure is that the defect length L needs to be known in order to configure the repair current I_{rep} within the process window. Knowing the defect length L, however, would require a microscopic recording of all P1 lines as the defect positions are unknown in the beginning. As the current module design of CIGS modules contains 136 P1 scribing lines (each of 1.2 m length), the microscopic recording would mean a bottle neck for the repair process time and is therefore not feasible. In order to overcome this problem, I introduce in the following the electrical repair by a current ramp.

8.2.4.3 Repair by Current Ramp

Fig. 8.9 shows the electrical repair of three P1 scribing defects, each of $L = 400$ µm defect length, by one constant repair current and by two repair current ramps. The red current ramp has a slope of 9.0 A/s and finishes repair after 168 ms at $I_{\mathrm{rep,top}} = 1.48$ A, while the blue current ramp has a slope of 0.55 A/s and finishes repair after 1.83 s at $I_{\mathrm{rep}} = 1.11$ A.

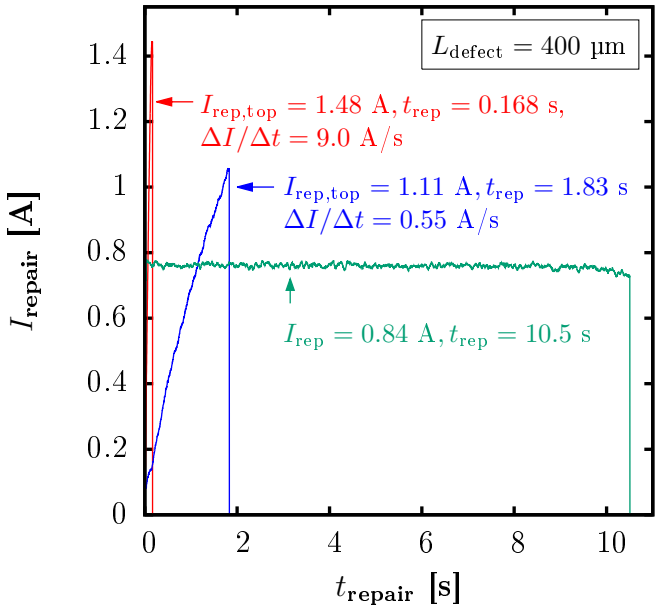

Figure 8.9: *Comparison of current ramp and constant current for the repair of P1 defects of $L = 400$ µm. Current ramps repair defects faster and at higher $I_{rep,top}$.*

In contrast, the constant current repair (green curve) is done at $I_{\text{rep}} = 0.84$ A and takes 10.5 s. One can extract that a higher slope of the ramp leads to a higher $I_{\text{rep,top}}$ and a shorter t_{rep}, which can be explained for short t_{rep} (neglecting heat diffusion into the surrounding) by

$$Q_{\text{rep}} = R_{\text{defect}} \int_{t=0}^{t=t_{\text{rep}}} I_{\text{rep}}\,(t)^2 dt \tag{8.14}$$

In Eq. (8.14) the required heat energy Q_{rep} is earlier reached for higher slopes at a higher $I_{\text{rep,top}}(t = t_{\text{rep}})$. The effect of the slope on the heat diffusion into the surrounding Mo is visualised in Fig. 8.10. Obviously, current ramps with higher slopes repair P1 defects with less heat diffusion into the surrounding.

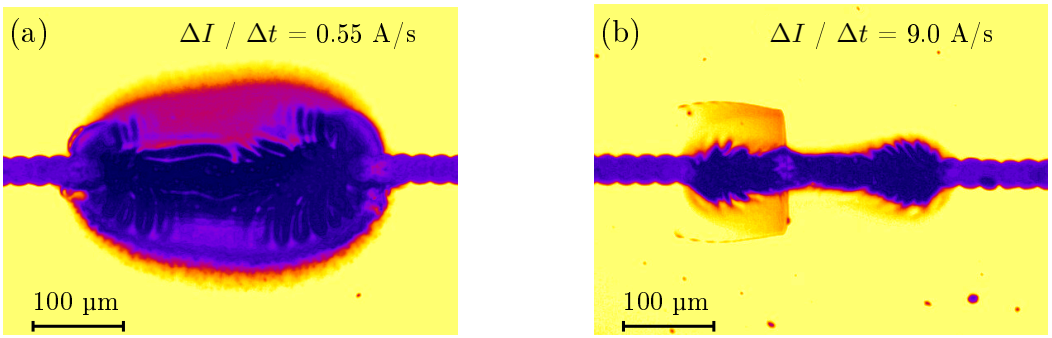

Figure 8.10: *Less heat diffusion by higher slope in current ramps. As a higher slope reduces the repair duration, there is less heat diffusion in the surrounding Mo. The microscope images correspond to the two current ramps shown in Fig. 8.9 for the repair of $L = 400$ µm.*

Consequently, the elongation E of the thermally affected area along the P1 line is minimised, as $I_{\mathrm{rep,top}}$ per se adjusts to L. I show the adjustment of $I_{\mathrm{rep,top}}$ in Fig. 8.11 for different defect lengths and a slope of 9.0 A/s, which was the maximum configurable value in my experimental setup.

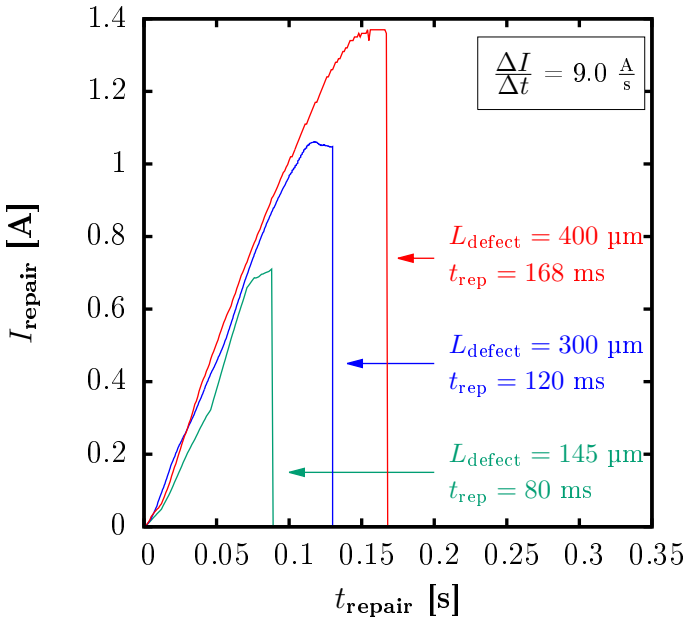

Figure 8.11: *Current ramps per se adjust $I_{rep,top}$ to L and lead to smallest possible Q_{rep}.*

In addition to the adjustment of $I_{\mathrm{rep,top}}$ to the defect length L, the use of current ramps frees me from the necessity of knowing the defect position and defect number per P1 scribing line, as I present in the following.

8.2.4.4 Repair of Multiple Failures

In the following I show how current ramps adjust the repair process to multiple defects per P1 scribing line, exemplified for two P1 defects in Fig. 8.12. Fig. 8.12 (a) depicts the microscope image of a P1 line with two interruptions, in the following referred to as left and right defect. Note that each microscope image is concatenated from multiple single images, which is the reason for the repetitive horizontal brightness distribution. In this example the measured defect lengths are $L = 280$ µm for the left defect, $L = 580$ µm for the right defect, and the distance between the two defects is 16 mm.

In Fig. 8.12 (b) the correspondent equivalent circuit for the repair of both defects is illustrated schematically. The voltage source is connected to the Mo layer on the left side which means that the repair current I_{rep} splits up into I_1 through the left defect and I_2 through the right defect. The defects are represented by R_{D1} and R_{D2}, while the Mo sheet resistance is regarded by $R_{\mathrm{Mo,1}}$ ... $R_{\mathrm{Mo,4}}$. The currents through the defects are

$$\frac{I_1}{I_2} = \frac{R_{\mathrm{Mo,2}} + R_{\mathrm{D2}} + R_{\mathrm{Mo,3}}}{R_{\mathrm{D1}}}. \tag{8.15}$$

Here because of the defect sizes, R_{D1} and R_{D2} are of the same order of magnitude. Due to the distance between contact pins and defects, and between left and right defect respectively, there is

$R_{\mathrm{D,i}} << R_{\mathrm{Mo,j}}$ for $i = 1, 2$ and $j = 1...4$. Hence, we expect that

$$I_1 >> I_2 \tag{8.16}$$

and that the left defect is repaired first, which results in the new equivalent electrical circuit in Fig. 8.12 (c). The defect current through the right defect becomes $I_2 = I_{\mathrm{rep}}$ and finally leads to the completely repaired P1 line in Fig. 8.12 (d).

Fig. 8.12 (e) depicts the real measured repair current I_{rep} during the total repair time $t_{\mathrm{rep}} \approx$ 82 ms. A break down of I_{rep} is visible in the moment when the left defect is repaired. During the repair of the right defect the repair current I_{rep} increases again and finally abruptly stops at $t = t_{\mathrm{rep}}$. The reason for the break down of I_{rep} after the repair of the left defect is the change in the total resistance R_{tot} of the schematically shown electrical circuit. The circuit shown in Fig. 8.12 (b), before repair of the left defect, has a total resistance of

$$R_{\mathrm{tot,unrep}} = R_{\mathrm{Mo,1}} + \frac{R_{\mathrm{D1}}\left(R_{\mathrm{Mo,2}} + R_{\mathrm{D2}} + R_{\mathrm{Mo,3}}\right)}{R_{\mathrm{D1}} + R_{\mathrm{Mo,2}} + R_{\mathrm{D2}} + R_{\mathrm{Mo,3}}} + R_{\mathrm{Mo,4}}, \tag{8.17}$$

while the circuit in Fig. 8.12 (c) after the repair of the left defect has a total resistance of

$$R_{\mathrm{tot,rep,D1}} = R_{\mathrm{Mo,1}} + R_{\mathrm{Mo,2}} + R_{\mathrm{D2}} + R_{\mathrm{Mo,3}} + R_{\mathrm{Mo,4}}, \tag{8.18}$$

and therefore $R_{\mathrm{tot,unrep}} < R_{\mathrm{tot,rep,D1}}$. Assuming an infinitesimal time duration δt, one can define a time window from t^- to t^+ around the moment of repair of the left defect at $t = t_{\mathrm{rep,D1}}$ by

$$t^- = t_{\mathrm{rep,D1}} - \delta t/2 \tag{8.19}$$

$$t^+ = t_{\mathrm{rep,D1}} + \delta t/2, \tag{8.20}$$

in which the applied repair voltage V_{rep} of our voltage source can be assumed to be constant by

$$V_{\mathrm{rep}}\left(t^-\right) = V_{\mathrm{rep}}\left(t^+\right) = V_{\mathrm{rep}}\left(t_{\mathrm{rep,D1}}\right). \tag{8.21}$$

Consequently, this means for the repair current in the moment of repair of the left defect

$$I_{\mathrm{rep}}\left(t^-\right) = \frac{V_{\mathrm{rep}}\left(t_{\mathrm{rep,D1}}\right)}{R_{\mathrm{tot,unrep}}} > I_{\mathrm{rep}}\left(t^+\right) = \frac{V_{\mathrm{rep}}\left(t_{\mathrm{rep,D1}}\right)}{R_{\mathrm{tot,rep,D1}}}, \tag{8.22}$$

which explains both the break down of I_{rep} and the change of the ramp's slope in Fig. 8.12 (e) after the left defect has been repaired.

It actually plays no role which defect is repaired first, as it will be always the one that represents the smaller resistance in the parallel circuit. Therefore, even if the defect to the right was repaired first (although it is sound to assume that the left one was repaired first due to the aforementioned geometries), the measured I_{rep} in Fig. 8.12 (e) would look similar.

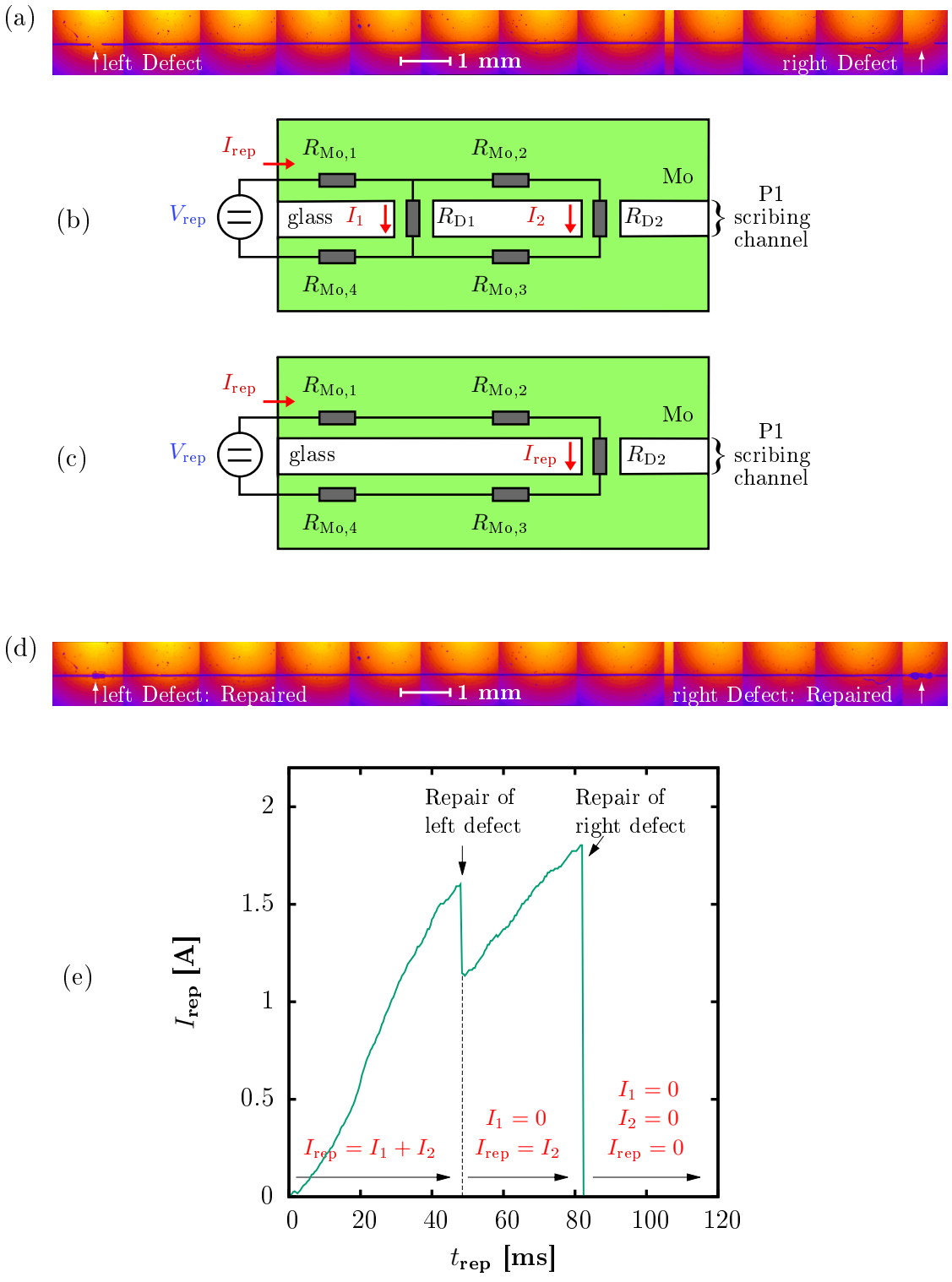

Figure 8.12: *Schematic repair of two defects on one P1 line. (a) P1 line with two defects and (b) its schematic equivalent circuit before repair. (c) Schematic circuit after repair of first defect. (d) P1 line after repair of right defect. (e) Measured repair current during repair time. The partial break-down in I_{rep} indicates the repair of the first defect, and the complete break-down indicates the repair of the second defect. The microscope images in (a) and (d) are concatenated from multiple single images which is the reason for the repetitive horizontal brightness distribution.*

Keeping the resistance between contact pin and defect small means keeping V_{rep} small and therefore reduces the danger of arcing. Hence, for the automated inline repair setup we place multiple contact pins on each of the neighbouring Mo back electrodes and find that this configuration effectively prevents the arcing effect.

Hence, the repair current measurement reliably yields whether there is any defect at all: if there is no defect, there is no current flow. Furthermore, we can determine how many defects have been repaired, as the number of repaired defects equals the number of break downs in the measured I_{rep}.

8.2.5 Conclusions

I have demonstrated the electrical repair of incomplete P1 scribing lines and shown that a comparatively simple setup allows to repair faulty P1 scribing lines in an early stage of the CIGS module production. By applying current ramps, a repair process is realised that is independent from the actual defect geometries, number, and their positions, which makes no additional microscope measurements necessary.

Finally, by constantly recording the repair current I_{rep} for each scribing line, one obtains statistical information about the defect occurrence and position of affected P1 lines, which can be used as a feedback loop in order to improve the scribing equipment or scribing process.

8.3 Thermal Repair

8.3.1 Introduction

During CIGS co-evaporation the substrate and the deposited Mo layer are heated up to about 700°C. I have found that the Mo remnant within P1 scribing defects can manifest a fracture after CIGS co-evaporation, and that this fracture is insulating the neighbouring cells. In the following I discuss the theory of mechanical stress and strain, and I present a first order approximation that shows that the origin of these fractures is most likely thermally induced mechanical stress in the Mo. Afterwards I present measurements of the inherent thermal repair of P1 defects, and I show how the found phenomenon can be used intentionally for an even improved thermal repair.

8.3.2 Stress and Strain Theory

For a better understanding of the mechanism that causes the fractures in the Mo, it is necessary to consider the stress and strain in both the Mo and the glass substrate. Therefore, I introduce the stress-strain test in this chapter, which is a standard measurement in materials science. The stress-strain tests of Mo and float glass in the literature have yielded the material parameters given in Table 8.2. These material parameters can be used for a first order approximation of the stresses occurring in the Mo during CIGS deposition, as I will show in Chapter 8.3.3.

In materials science the behaviour of a material under tensile load is tested with tensile-test machines, where a tensile load is applied to a small specimen of the material, and the resulting deformations are measured [140–142]. For a quantitative analysis of the measurement a stress-strain diagram is drawn. The stress σ is defined by

$$\sigma = \frac{F_{\text{tensile}}}{A}, \tag{8.23}$$

where F_{tensile} is the tensile force onto a cross section area A of the material which is tested. The strain or elongation ϵ is defined by

$$\epsilon = \frac{\Delta L}{L_0}, \tag{8.24}$$

where ΔL is the specimen's absolute change in length and L_0 is its initial length. A test specimen and the corresponding stress-strain diagram are schematically shown in Figure 8.13.

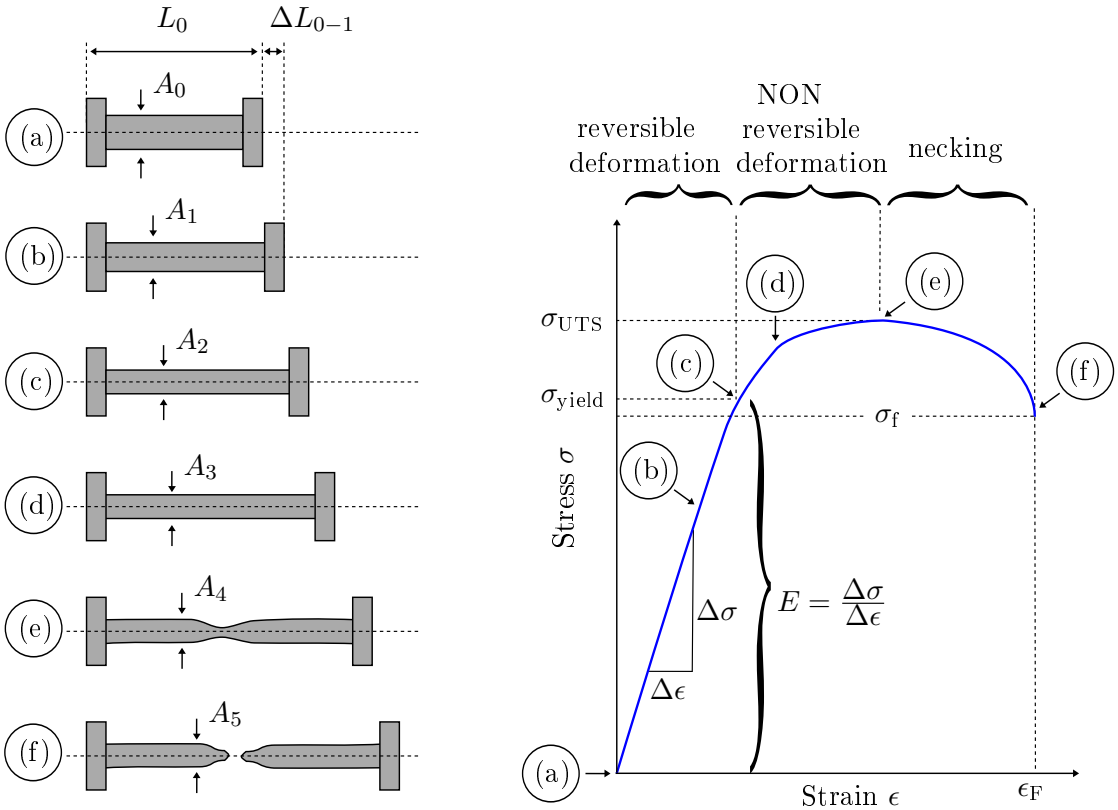

Figure 8.13: *Schematic stress-strain-test. A specimen is stressed in position (a) - (f), as shown in the left part. The correspondent stress-strain-diagram is shown in the right part [143].*

Figure 8.13 schematically illustrates on the left side a specimen, and on the right side the correspondent stress-strain diagram. The diagram shows the stress σ as function of strain ϵ. The specimen is deformed at constant speed by providing a pure tensile force F_{tensile} [144].

Position (a) shows the initial length L_0 of the specimen. Between positions (a) and (c) there is the elastic region, where the stress σ is proportional to the strain ϵ. Hooke's law describes the linear

slope E, also called Young's modulus [145], in the elastic region by

$$E = \frac{\Delta\sigma}{\Delta\epsilon}. \tag{8.25}$$

Within the elastic region the elongation is uniform, which means for the specimen cross section area $A_0 < A_1 < A_2$.

At position (c) the elastic limit is reached. If the load is removed before or at the elastic limit in (c), the specimen will return to its initial shape in (a). In contrast, any stress above the elastic limit will cause it to deform permanently.

Point (c) is called yielding point with the correspondent yield strength σ_{yield}. Applying stress slightly above point (c) can cause the specimen to enter the yielding phase (not shown in Figure 8.13). For the sake of visibility (it occurs only within a small range of ϵ) and simplicity (it would require a detailed physical explanation that is beyond the scope of this work) I neglect the yielding phase and instead refer to [146], where it has been explained the first time.

From point (d) to (e) the stress rises monotonically but the slope decreases until it reaches a maximum in point (e). The phase from (d) to (e) is called strain hardening and the point (e) is called ultimate tensile strength σ_{UTS}. The elongation from (c) to (e) is non uniform which means for the specimen cross section area $A_3 = A_4 = A_5$.

When the ultimate tensile strength σ_{UTS} in (e) is exceeded, the cross sectional area A decreases only in a localized region of the specimen (shown in the left part of Figure 8.13), which is why the phase from (e) to (f) is called necking. The measured stress reduces slightly in the necking phase, which is explained in detail in [143, 145]. At point (f) the specimen breaks and the correspondent stress is called fracture stress σ_{f}.

Both the strain ϵ_{perp} perpendicular to the load (pulling direction in the left part of Figure 8.13) and the strain ϵ_{par} parallel to the load, can be obtained from stress-strain tests [142]. The ratio of the two strains

$$\nu = \frac{\epsilon_{\text{perp}}}{\epsilon_{\text{par}}} \tag{8.26}$$

is called Poisson's ratio ν. The strain ϵ_{perp} causes a decrease of the cross section area from A_0 to A_5 (first uniform and afterwards in the necking region), while the strain ϵ_{par} causes an enlargement of the specimen length from L_0 to L_5. Mechanical parameters measured in stress-strain tests for deposited Mo layers and float glass are listed in Table 8.2.

Table 8.2: Stress-strain test parameters *of Mo and float glass. Yield strength and ultimate strength have been measured by a Mo manufacturer [147] for Mo layers sputtered under the same conditions as used in CIGS production sites.*

Material	Parameter	Variable	Value	Reference
Mo	Young's modulus	E^{Mo}	320 GPa	[147]
Mo	Yield strength	$\sigma^{\mathrm{Mo}}_{\mathrm{yield}}$	0.62 GPa	[147]
Mo	Ultimate tensile strength	$\sigma^{\mathrm{Mo}}_{\mathrm{UTS}}$	0.76 GPa	[147]
Mo	Poisson's ratio	ν^{Mo}	0.3	[143]
float glass	Young's modulus	E^{glass}	70 GPa	[148, 149]
float glass	Poisson's ratio	ν^{glass}	0.22	[149]

8.3.3 First Order Approximation of Stress in Mo

Figure 8.14 shows microscope images of the Mo layer before and after CIGS deposition, recorded in the cell centre and from the glass side. Microscope images recorded before CIGS deposition show a smooth Mo surface, as presented in (a). After CIGS deposition, most of the Mo surface on the module appears slightly rugged, as shown in (b). However, there are also multiple regions that appear like stretch marks, as exemplified in (c). I did not find any systematics to correlate the dislocations from (c) with their position on the module, and the results varied from module to module within the same batch manufactured with the same process parameters.

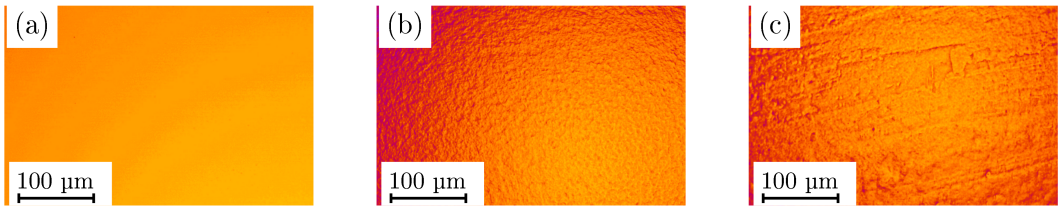

Figure 8.14: *Microscope images of (a) a smooth Mo surface before CIGS deposition, (b) a slightly rugged Mo surface after CIGS deposition, and (c) a Mo surface after CIGS deposition clearly showing dislocations or stretch marks. No systematics could be found in order to explain the differences between (b) and (c). All images are recorded from glass side and from the same CIGS module.*

Although the microscope images in Fig. 8.14 indicate that it is not possible to predict the change of the Mo layer during CIGS deposition, obviously there is an irreversible deformation of the Mo, which means that its yield strength $\sigma^{\mathrm{Mo}}_{\mathrm{yield}}$ must have been exceeded. I suggest that the origin of the Mo's irreversible deformation is thermally induced mechanical stress during CIGS deposition which I approximate in the following with a first order approximation. I begin with a simple

two layer system consisting of only the glass substrate and the Mo layer, which complies with our experiment on intentional thermal repair. I will show that the theoretically approximated mechanical stress exceeds the Mo's yield strength $\sigma_{\text{yield}}^{\text{Mo}}$ and therefore can explain the irreversible deformation. Afterwards I discuss the influence of an additional deposited CIGS layer on the mechanical stress within the Mo layer.

Figure 8.15 shows schematically a square material composite and occurring stresses, as they are assumed in the following first order approximation inside of the Mo layer and float glass. The four stresses $\sigma_{\text{-x}}^{\text{glass}}$, $\sigma_{\text{+x}}^{\text{glass}}$, $\sigma_{\text{-y}}^{\text{glass}}$, and $\sigma_{\text{+y}}^{\text{glass}}$ are imposed by the Mo layer onto the float glass, and $\sigma_{\text{-x}}^{\text{Mo}}$, $\sigma_{\text{+x}}^{\text{Mo}}$, $\sigma_{\text{-y}}^{\text{Mo}}$, and $\sigma_{\text{+y}}^{\text{Mo}}$ are imposed by the float glass onto the Mo layer. The following approximations for the calculation of stresses are taken from Bürgel [143]. The elongation of the material composite into z-direction is not hampered [143, p. 31], and therefore

$$\sigma_{\text{z}}^{\text{Mo}} = \sigma_{\text{z}}^{\text{glass}} = 0. \tag{8.27}$$

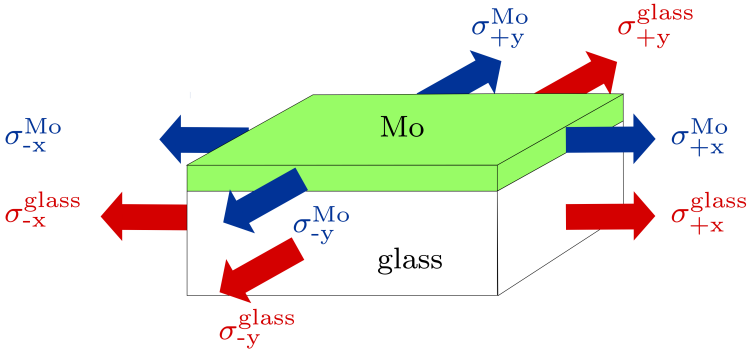

Figure 8.15: *Schematic square material composite consisting of Mo layer on float glass substrate, as assumed in the first order approximation. The thermally induced elongation of glass imposes the stress σ^{Mo} onto the Mo layer into x- and y-direction, and the Mo layer imposes σ^{glass} onto the glass substrate.*

For quasi-isotropic materials the modulus of elasticity is equal into all directions [143, p. 33], which means for the stresses into x- and y-direction

$$\sigma_{\text{-x}}^{\text{glass}} = \sigma_{\text{+x}}^{\text{glass}} = \sigma_{\text{-y}}^{\text{glass}} = \sigma_{\text{+y}}^{\text{glass}} = \sigma^{\text{glass}} \tag{8.28}$$

$$\sigma_{\text{-x}}^{\text{Mo}} = \sigma_{\text{+x}}^{\text{Mo}} = \sigma_{\text{-y}}^{\text{Mo}} = \sigma_{\text{+y}}^{\text{Mo}} = \sigma^{\text{Mo}}. \tag{8.29}$$

The equilibrium of forces [143, p. 36] states that

$$F^{\text{Mo}} + F^{\text{glass}} = 0 \tag{8.30}$$

$$\sigma^{\text{Mo}} A^{\text{Mo}} + \sigma^{\text{glass}} A^{\text{glass}} = 0, \tag{8.31}$$

where F^{Mo} is the force imposed by the float glass onto a cross section area A^{Mo} of the Mo layer into x- or y-direction, and vice versa. We assume the material composite not to warp [143, p. 34]

in order to estimate the resulting stress, i.e. the elongation ϵ of both materials into all directions is supposed to be the same by

$$\epsilon_{\text{-x}}^{\text{glass}} = \epsilon_{\text{+x}}^{\text{glass}} = \epsilon_{\text{-y}}^{\text{glass}} = \epsilon_{\text{+y}}^{\text{glass}} = \epsilon^{\text{glass}} \tag{8.32}$$

$$\epsilon_{\text{-x}}^{\text{Mo}} = \epsilon_{\text{+x}}^{\text{Mo}} = \epsilon_{\text{-y}}^{\text{Mo}} = \epsilon_{\text{+y}}^{\text{Mo}} = \epsilon^{\text{Mo}} \tag{8.33}$$

$$\epsilon^{\text{glass}} = \epsilon^{\text{Mo}}. \tag{8.34}$$

We neglect temperature gradients within the composite [143, p. 35], which allows to approximate the thermally induced elongations ϵ for both materials by

$$\epsilon^{\text{glass}} = \alpha^{\text{glass}}\Delta T + \frac{\sigma^{\text{glass}}}{E^{\text{glass}}} - \nu^{\text{glass}}\frac{\sigma^{\text{glass}}}{E^{\text{glass}}} \tag{8.35}$$

$$\epsilon^{\text{Mo}} = \alpha^{\text{Mo}}\Delta T + \frac{\sigma^{\text{Mo}}}{E^{\text{Mo}}} - \nu^{\text{Mo}}\frac{\sigma^{\text{Mo}}}{E^{\text{Mo}}}. \tag{8.36}$$

Substituting Eq. (8.31), (8.35), and (8.36) into Eq. (8.34) yields the induced stresses in both the glass and the Mo layer by

$$\sigma^{\text{glass}} = \frac{\Delta T E^{\text{Mo}}\left(\alpha^{\text{Mo}} - \alpha^{\text{glass}}\right)}{\frac{E^{\text{Mo}}}{E^{\text{glass}}}\left(1-\nu^{\text{glass}}\right) + \frac{A^{\text{glass}}}{A^{\text{Mo}}}\left(1-\nu^{\text{Mo}}\right)} \tag{8.37}$$

$$\sigma^{\text{Mo}} = \frac{\Delta T E^{\text{glass}}\left(\alpha^{\text{glass}} - \alpha^{\text{Mo}}\right)}{\frac{E^{\text{glass}}}{E^{\text{Mo}}}\left(1-\nu^{\text{Mo}}\right) + \frac{A^{\text{Mo}}}{A^{\text{glass}}}\left(1-\nu^{\text{glass}}\right)}. \tag{8.38}$$

The thickness of the glass is $d^{\text{glass}} = 3$ mm and that of the Mo is $d^{\text{Mo}} = 500$ µm, hence $A^{\text{Mo}}/A^{\text{glass}} \approx 0$ which means that there is practically no stress imposed by the Mo layer onto the glass substrate. Inserting the thermal expansion coefficients $\alpha^{\text{Mo}} = 5.2 \times 10^{-6}$ 1/K [119] for Mo and $\alpha^{\text{glass}} = 9.1 \times 10^{-6}$ 1/K [120] for float glass into Eq. (8.38) yields the thermally induced mechanical stress σ^{Mo} in the Mo layer, as shown by the red curve as function of temperature change ΔT in Figure 8.16.

Obviously, the Mo's yield strength $\sigma_{\text{yield}}^{\text{Mo}} \approx 0.62$ GPa [147] is exceeded at approximately $\Delta T = 350$ K, which is the prerequisite for an irreversible deformation as shown in Fig. 8.14 (b) and (c). Furthermore, the ultimate tensile strength $\sigma_{\text{UTS}}^{\text{Mo}} \approx 0.76$ GPa [147] is exceeded at approximately $\Delta T = 400$ K, which is required for the creation of fractures like those that cause the thermal repair of incomplete P1 scribing lines. The actual CIGS co-evaporation requires $\Delta T \approx 650$ K which leads to

$$\sigma_{\text{CIGS}}^{\text{Mo}} \approx 187\%\ \sigma_{\text{yield}}^{\text{Mo}} \approx 152\%\ \sigma_{\text{UTS}}^{\text{Mo}}. \tag{8.39}$$

In reality the stress within the Mo is less due to warping of the glass substrate which allows a stress relaxation within the material composite [11, 143]. Furthermore, I observe in my experiments that the CIGS absorber layer deposited onto the Mo additionally hampers the creation of fractures, which

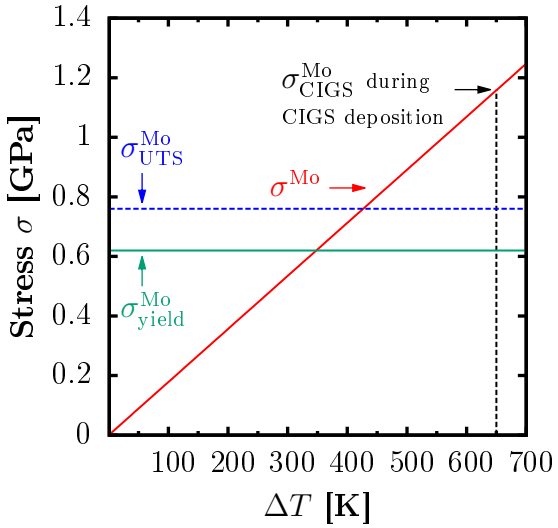

Figure 8.16: *First order approximation of thermally induced mechanical stress σ^{Mo} imposed by the glass onto the Mo layer. The yield strength σ^{Mo}_{yield} required for irreversible deformation is exceeded at approximately $\Delta T = 350$ K, and the ultimate tensile strength σ^{Mo}_{UTS} required for creation of fractures at approximately $\Delta T = 400$ K. The actual CIGS deposition takes place at approximately $\Delta T = 650$ K with room temperature as reference.*

can be explained with the additional friction between Mo and CIGS that must be overcome for the creation of fractures. These two effects, namely warping and stabilisation by the CIGS absorber layer, explain why the intact Mo layer may show irreversible deformations but not fractures, as exemplified in Fig. 8.14.

However, in case of incomplete P1 lines the Mo remnant can be imagined as a thin bond connecting two neighbouring Mo electrodes that are by magnitudes of order both longer, namely 1.2 m versus some µm, and wider, namely 4 mm versus about 50 µm. Hence, although some relaxation is present in reality, the two Mo cell back electrodes can with their elongation impose additional stress on a figuratively very weak bond between them, which makes fractures in the bond possible, as our experiments show.

8.3.4 Experimental Setup

The P1 line interruptions, which I show in our experiments, with lengths of up to approximately 100 µm occur inherently during the manufacturing process. Additionally, I implement scribing defects with lengths of up to 1 mm deliberately by placing adhesive tape on the glass side which absorbs the laser energy during glass side scribing [41, 42]. Beside the intentionally implemented line interruptions, the CIGS modules were manufactured normally in a real mass production site [33].

The insulation capability was investigated by EL, where after biasing the sample, a pause period was kept before each EL measurement until $\delta V/\delta t \approx 0$, in order to minimise the influence of metastable tranciences [83].

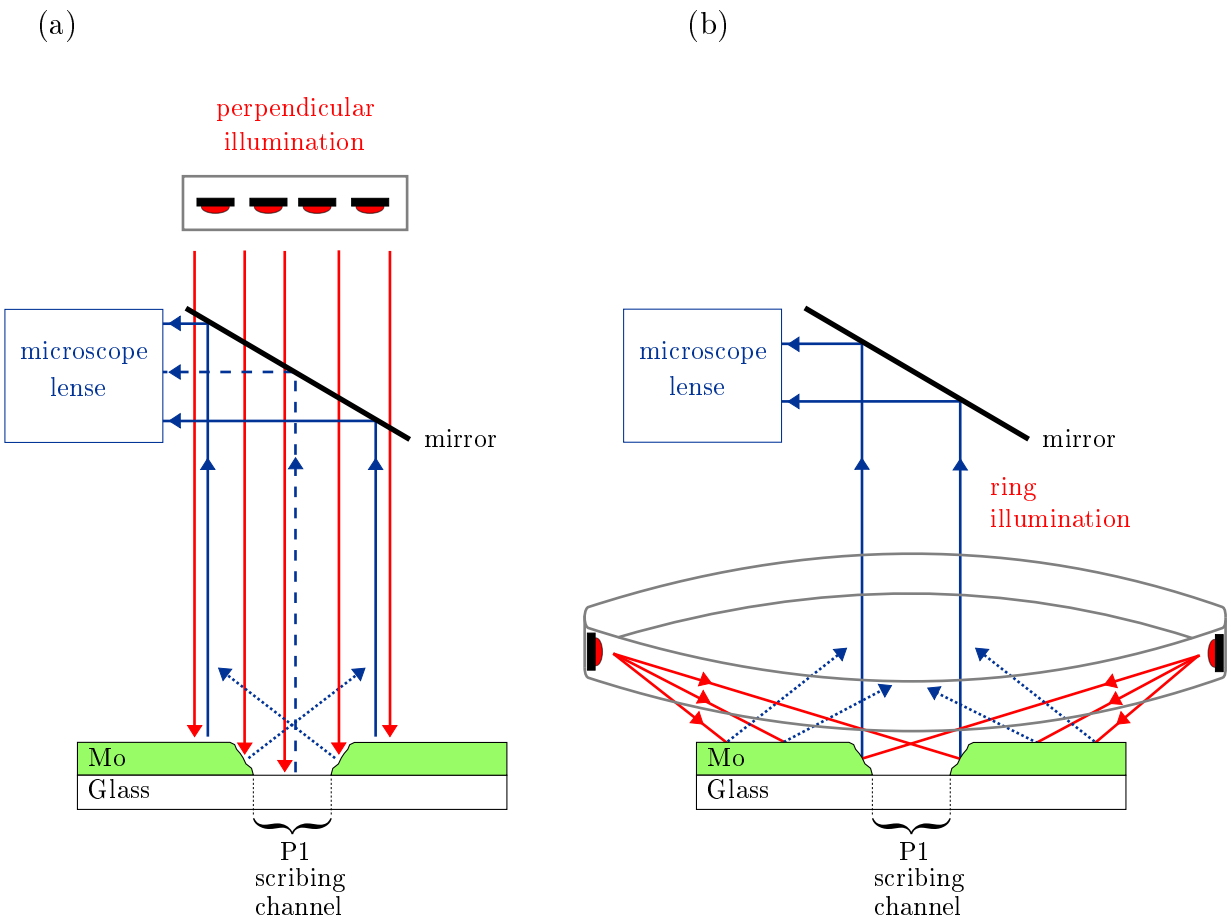

Figure 8.17: *Schematic illumination setup for microscope images. Red arrows represent the illumination, while blue arrows represent the reflected light. (a) Illumination perpendicular to the Mo layer. The Mo reflects the illumination (solid blue arrows), while the reflection on glass inside the P1 line is low (dashed blue arrow). At the inclined edge of the P1 line, the light is reflected to the sides (dotted blue arrows) which makes the edges appear dark in the microscope image. (b) Ring illumination is also reflected by the Mo layer, but does not reach the mirror due to the angle of the reflected light (dotted blue arrows). Instead, the edges of the P1 line can reflect the light into the direction of the mirror (solid blue arrow). The resulting image looks like Figure 8.19 (f).*

For the microscope investigation of the fractures two different illumination setups were used which are shown in Figure 8.17. While the perpendicular illumination in Figure 8.17 (a) is used to show large areas on the Mo layer, the ring illumination in (b) is used to show more precisely the actual width of the thin fracture.

8.3.5 Inherent Thermal Repair

Fig. 8.18 depicts five different P1 scribing defects of finished CIGS thin-film modules. For P1 scribing defect lengths of 16 - 57 µm in (a)-(c) one can observe that after the CIGS absorber deposition a small fracture between the left and the right end of the interrupted laser line occurs. As the P1 scribing defect is characterised by a significant cross-talk in the EL image even for interruptions of

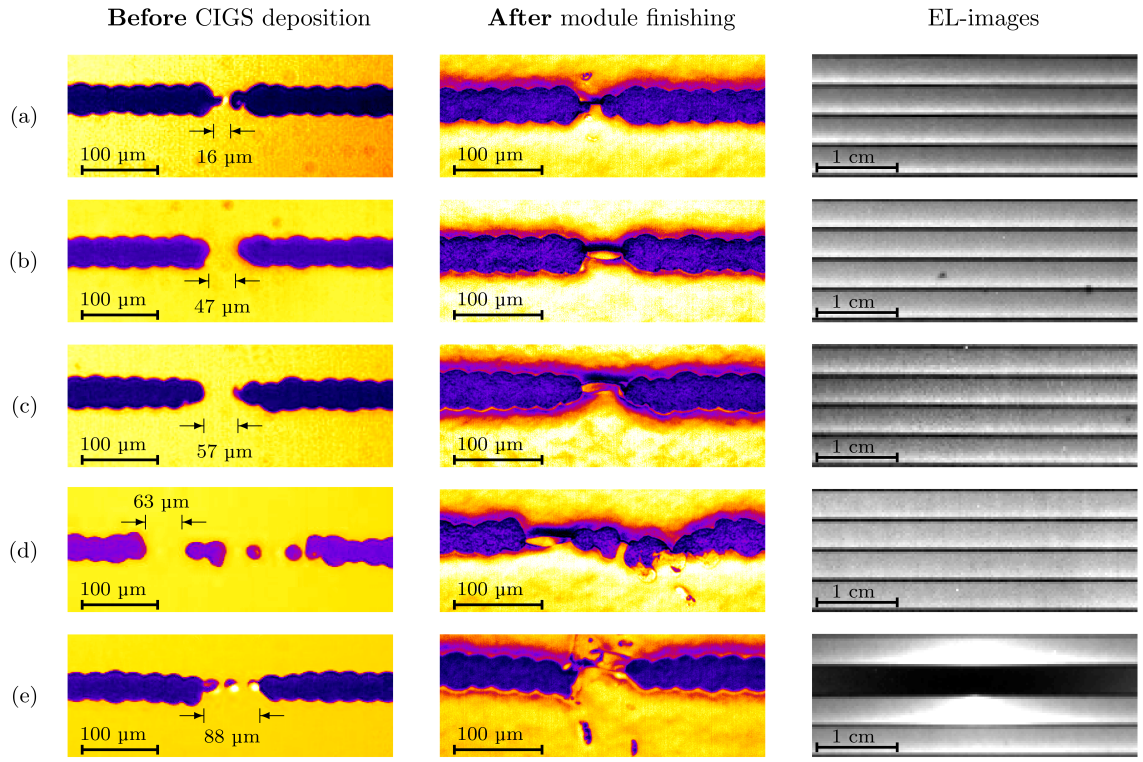

Figure 8.18: *Inherent thermal repair of incomplete P1 scribing. Microscope images show the defect position before CIGS deposition (second column) and after finishing the CIGS module (third column). The EL-images (fourth column) show sufficient electrical insulation for defect lengths up to $L_{defect} \approx 63$ µm. In each EL image the repaired defect position is located in the centre between the second and third cell. For $L_{defect} \approx 88$ µm the characteristic P1 EL defect pattern appears.*

only a few µm (see Chapters 6 and 7), the correspondent EL images in Fig. 8.18 prove that the fractures sufficiently insulate the adjacent Mo back electrodes in (a)-(c).

Fig. 8.18 (d) shows multiple P1 scribing line interruptions of which the largest one, with $L_{\mathrm{defect}} \approx 63$ µm, is labelled in the microscope image before CIGS absorber deposition. Obviously, the fracture can occur during CIGS deposition even between multiple small P1 line interruptions and still effectively isolate the two neighbouring cells. The first P1 scribing defect length for which the correspondent EL image indicates an insufficient cell isolation in the Mo layer is 88 µm in Fig. 8.18 (e).

The results in Fig. 8.18 are representative for several hundred measured P1 defects, that I found in multiple modules which have been processed in different production batches. The mean value for the P1 line interruption width that could not be thermally repaired any more was approximately 70 µm.

8.3.6 Intentional Thermal Repair

In the following I show how the principle of thermal repair can be used intentionally in order to ensure insulation between Mo back electrodes even when there are P1 line interruptions. In the

correspondent experiment the P1 scribing was applied with intentionally introduced interruptions of up to 1 mm length. Afterwards, the CIGS module passed a real CIGS co-evaporation chamber with realistic industry process parameters like heating and conveyor motion speed. However, I left the CIGS precursor gas tanks empty, which means that no CIGS was deposited. This experimental approach allows to investigate only the influence of the temperature and to exclude the effect of the CIGS layer.

Figure 8.19 (a) - (e) depicts P1 scribing interruptions of 50 - 940 µm as recorded after the glass substrate, containing the P1 scribed Mo layer, passed the CIGS deposition chamber and cooled down to room temperature. In (b) - (e) two or more fractures originating from the left and right end of the interrupted line can be observed, which I do not observe in case of the inherent repair showed in Fig. 8.18. Note that the image resolution in Figure 8.19 (a) - (e) is only half of the resolution that I chose in Fig. 8.18 in order to record the complete interruption.

In Fig. 8.19 (a) - (e) the samples are illuminated perpendicularly, which causes a bright image where there is the plain reflecting Mo layer. The glass in the P1 scribing line channel reflects less light than the Mo and therefore appears darker than the surrounding. The inclined edges of the P1 scribing line appear darkest as they scatter the incoming light to the sides.

In contrast, a ring illumination is used in Figure 8.19 (f) in order to record the actual fracture width in (e) at the left end of the interrupted line, which is labelled by the red rectangle, more

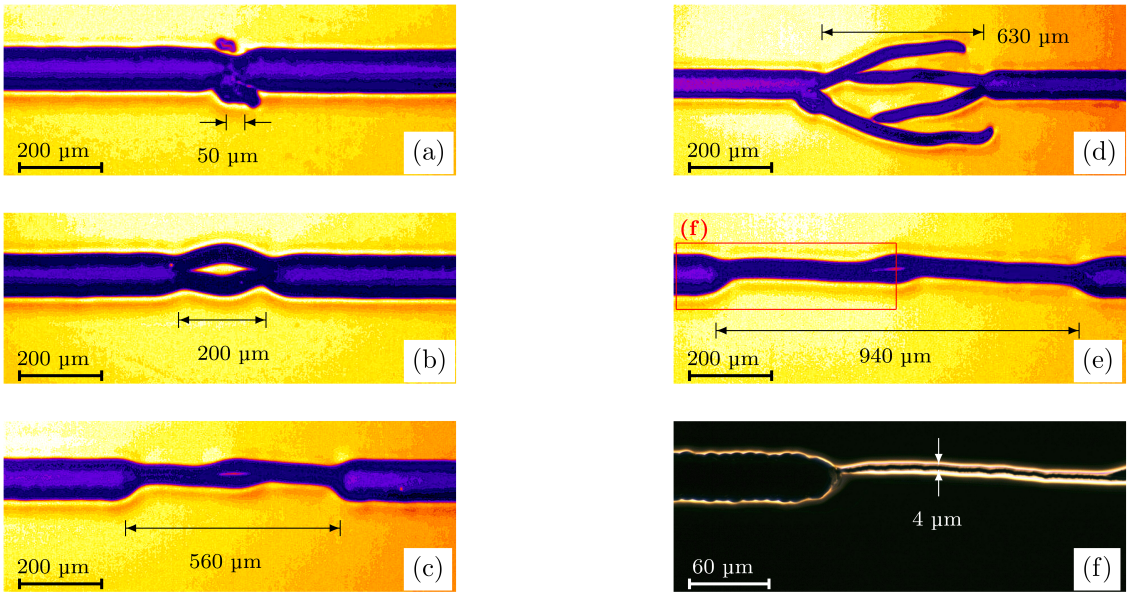

Figure 8.19: *Intentional thermal repair of incomplete P1 scribing. I deliberately implement P1 scribing interruptions of up to 1 mm length. Afterwards, the glass substrate passes the CIGS co-evaporation chamber and temperature ramp but with empty precursor gas tanks. In (a) - (e) five P1 scribing interruptions are recorded from the Mo film side. Fractures are visible for interruptions of up to 940 µm. (a) - (e) are recorded with perpendicular microscope illumination. (f) shows the left end of the scribing line in (e), but with a ring illumination which highlights the inclined edges of the laser line and of the fracture. The setup in (f) allows to determine the fracture width as approximately 4 µm.*

precisely. The ring illumination can be placed above the sample in a way that allows to record only the light scattered at the inclined edges of the Mo within the scribing channel, which is an alternative way to determine the actual fracture width, and suitable for automated image processing algorithms as there is only a bright and dark signal level. Our measurements yield that the mean value of the fracture width that provides sufficient insulation is approximately 4 µm.

Thus, with the same temperature treatment the absence of a deposited CIGS absorber layer allows us to thermally repair significantly longer P1 line interruptions, namely about 1 mm versus 70 µm.

8.3.7 Conclusions

The thermal repair of incomplete P1 scribing lines, which significantly affect the cell's electrical performance, by fractures in the Mo remnant occurring during CIGS co-evaporation has been studied.

A first order approximation suggests that thermally induced mechanical stress during the heating and cooling period, as it is applied for the CIGS co-evaporation, causes the fractures in the Mo.

I observe for our material and process parameters an inherent repair of P1 line interruptions of up to approximately 70 µm length.

In contrast, a heating (and therefore cooling) ramp before the actual CIGS co-evaporation allows due to the absence of the stabilising CIGS layer an intentional thermal repair of P1 line interruptions of up to approximately 1 mm length.

The most important finding is that mean fracture widths of only approximately 4 µm can sufficiently insulate two neighbouring Mo back electrodes. This means that a further reduction of the P1 line width, and thus of the entire interconnection width, is possible, which would lead to more active solar cell area and thus a higher electrical efficiency of the module.

8.4 Conclusions

I have investigated two mechanisms for the repair of P1 defects: a thermal repair and an electrical repair.

The fortunate situation in case of the thermal repair is that it is an inherent process taking place during CIGS absorber deposition for defect lengths of up to $L_{\mathrm{defect}} \approx 60$ µm. With the experiments on intentional thermal repair in Chapter 8.3.6 I have proven that the creation of fractures, which are observed after CIGS co-evaporation at positions of incomplete P1 scribing, is thermally induced.

Furthermore, my experiments show that the intentional thermal repair can repair significantly longer P1 scribing line interruptions than the inherent thermal repair (1 mm versus 60 µm), most likely because of the absence of the CIGS layer during intentional repair which stabilises the Mo (as shown in the Chapters 8.3.5 and 8.3.6).

Its simplicity with regard to technical realisation, and its reliability for the repair of P1 scribing line interruptions of up to 1 mm length, make the thermal repair a potential candidate for a repair tool inside of the production line.

The insulating fractures that I observe are of approximately 4 µm width, while in contrast the P1 laser lines are of 45 µm width. Nonetheless, fractures between the ends of interrupted laser lines provide sufficient electrical insulation of the neighbouring cells, as I have shown with the EL images of Figure 8.18. This indicates that the P1 line width can be further reduced in future in order to reduce the dead area loss per series connection line.

An alternative to the intentional thermal repair is the electrical repair, where a current I_{rep} is driven through the P1 defect until the Mo remnant is melted and evaporated. The electrical repair works for defect lengths up to $L_{\mathrm{defect}} \approx 1$ mm, too.

My experiments show that the application of a current ramp (see Figure 8.11) allows an electrical repair process with a practically self-adjusted highest repair current $I_{\mathrm{rep,top}}$.

A beneficial characteristic of the electrical repair is that for $I_{\mathrm{rep}} > 0$ A it can be determined if there are P1 defects at all, on which P1 lines they are, and, with regard to detectable current break downs, how much P1 defects per P1 line have been repaired.

Chapter 9

Conclusions and Outlook

I have investigated the the use of EL and DLIT as diagnostic tools to identify various defects that can occur in the production process. My investigation of deliberately implemented defects shows that characteristic defect patterns can be found in EL and DLIT measurements, which allow a reliable defect identification. The conclusion from this insight is that it would be advantageous to design future measurement setups to measure both EL and DLIT. An advantage would be that the module needs only to be positioned once and the spatially resolved EL and DLIT images can be conveniently overlayed. The DLIT measurement duration in the range of minutes, which exceeds the current CIGS production cycle time of currently about half a minute, is no obstacle for a quality control because not every single module has to be measured. Instead, random samples, which represent a complete production batch that is produced with the same parameters, are sufficient. The next consequent step would be to implement an automated image processing which scans the measured EL and DLIT images for the characteristic defect patterns.

I have correlated the applied scribing tool contact pressure during mechanical P2 and P3 scribing with the mechanical wear of the used graver tip with scanning electron microscope (SEM) and energy dispersive X-ray (EDX) measurements. The results indicate that the applied scribing tool contact pressure in the process which is used in this work is typically a factor 2-3 higher than required. Manufacturers apply these high contact pressures in order to ensure that the mechanical graver has a continuous contact to the substrate during the scribing process, despite the waviness of the substrate, which is a result of the glass warping due to the high temperatures during CIGS co-evaporation. However, the high contact tool pressure accelerates the mechanical wear of the mechanical gravers, and thus can lead even earlier to defective mechanical P2 and P3 scribing, if the graver is not changed on time.

My experimental results suggest that the nature of the chemical bath deposition makes the CdS layer cover easily rough surfaces or fill up cavities like holes in the Mo or the CIGS absorber. Thus, the CdS chemical bath deposition provides a surface smoothing and allows the sputtered i-ZnO to form a uniform and unbroken layer that prevents contact between the ZnO:Al and CdS, or between ZnO:Al and Mo respectively. This result is in agreement with the common observation that CIGS modules still have comparatively high efficiencies although their correspondent EL images reveal multiple defects. These defects may be caused by a locally damaged absorber and locally lead to

voltage reductions, but their detrimental influence is apparently well mitigated by the i-ZnO/CdS buffer layer combination. Controlled model experiments, like those performed in the present thesis on point defects, could also be useful for the development and evaluation of alternative Cd-free buffer combinations.

The present work also sheds light on the significance of defect geometry for defect identification. The scribing defect length L_{defect} of P1, P2, and P3 defects strongly determines whether a scribing defect can be reliably detected and identified in EL and DLIT images. Independent from their defect geometry, shunting point defects can not be reliably distinguished and identified. While the point defect type determines the defect resistivity, the geometry influences the actual defect resistance. In EL and DLIT measurements these two parameters can not reliably be distinguished and therefore a reliable identification of point defects is not possible. Only electrically inactive point defects can be distinguished from shunting ones. In contrast, in case of Cu-rich debris not the defect geometry but its position within the cell, or on the P1 line respectively, is relevant for its reliable identification.

My simulation software allows to model and simulate photovoltaic modules based on the principle of network simulation model. Analysis of the simulation performance shows that the simulation duration t scales almost linearly with the number of equations n to be solved in the non-linear system of equations, by $t \propto n^{1.08}$, which is close to the linear optimum. This almost linear behaviour is achieved by avoiding the calculation of the Jacobian matrix, usage of sparse matrices, and the usage of efficient memory allocation during runtime. The correctness of my simulation has been shown by comparison with a reference simulation [6].

Finally, I have found two ways to repair incomplete P1 lines, namely a thermal and an electrical repair. Fortunately, the thermal repair is an inherent process taking place during CIGS co-evaporation. The thermal repair is based on thermally induced mechanical stress, which I have proven with experiments on intentionally heated modules that contained P1 defects. While the inherent thermal repair works only for defect lengths up to $L_{\mathrm{defect}} \approx 60$ µm (due to the mechanically stabilising CIGS layers on top of it), the intentional thermal repair works for defect lengths even up to $L_{\mathrm{defect}} \approx 1$ mm (here the stabilising CIGS layer is missing). My experiments on the thermal repair yield that fractures of about 4 µm thickness are sufficient to insulate the Mo back contacts of neighbouring cells. This means that the current P1 thickness of about 45 µm can be further reduced in order to reduce the dead area loss per series connection line. In addition to the thermal repair, I have developed an electrical repair which is based on melting and evaporating the Mo remnant at the P1 defect position by electrical current. The experiments on electrical repair yield that it is as efficient for scribing defect lengths up to $L_{\mathrm{defect}} \approx 1$ mm as the intentional thermal repair. Additionally, the electrical repair allows an automated detection of defects, locating affected scribing lines, and counting the number of defects per affected scribing line with the setup which has been developed in this work. Both the intentional thermal repair and the electrical repair have the potential to be used as a reliable inline repair tool in a production site due to their simplicity, high efficiency, and reliability in P1 shunt prevention.

List of Publications

Publications in Journals

1 B. Misic, B. E. Pieters, J. P. Theisen, A. Gerber and U. Rau, *Shunt mitigation in ZnO:Al/i-ZnO/CdS/Cu(In,Ga)Se_2 solar modules by the i-ZnO/CdS buffer combination*, Phys. Status Solidi (a) 212(3), page 541-546, 2015.

2 B. Misic, B. E. Pieters, U. Schweiter, A. Gerber and U. Rau, *Defect Diagnostics of Scribing Failures and Cu-rich Debris in Cu(In,Ga)Se_2 Thin Film Modules with Electroluminescence and Thermography*, IEEE J. Photov. 5(4), page 1179-1187, 2015.

3 B. Misic, B. E. Pieters and U. Rau, *Electrical Repair of Incomplete Back Contact Insulation (P1) in Cu(In,Ga)Se_2 Photovoltaic Thin Film Modules*, IEEE J. Photov. 5(4), page 1197-1205, 2015.

4 B. Misic, B. E. Pieters and U. Rau, *Thermal Repair of Incomplete Back Contact Insulation (P1) in Cu(In,Ga)Se_2 Photovoltaic Thin Film Modules*, ASME J. Sol. Energy Eng 137(6), page 061004-061004-7, 2015.

5 B. Misic, B. E. Pieters, A. Gerber and U. Rau, *Thermography and Electroluminescence Imaging of Scribing Failures in Cu(In,Ga)Se_2 Thin Film Solar Modules*, Phys. Status Solidi (a) 212(12), page 2877–2888, 2015.

Publications in Conference Proceedings

1 B. Misic and K. Orgassa and U. Schweitzer and J. Müller and C. Kuhn and D. Manz and U. Rau, *Network simulation for analysis and visualization of shunt defects in Cu(In,Ga)Se_2 thin film modules*, in Proc. of the 25th European Photov. Solar Energy Conf. (2010) 3670-3675.

---

2 B. Misic and H. Kästner and U. Schweitzer and A. Kümmerer and J. Müller and A. Marienfeld and K. Orgassa and W. Henschel and C. Kuhn and D. Manz and T. Kirchartz and U. Rau, *TCO scribing defects in electroluminescence images of CIGS solar thin film modules*, in Proc. of the 26th European Photov. Solar Energy Conf. (2011) 2974-2980.

---

3 B. Misic and U. Schweitzer and R. Modlmeir and J. P. Theisen and H. Kästner and A. Marienfeld and T. Marschner and B. Pieters and U. Rau, *Scribing defects in CIGS modules*, in Proc. of the 27th European Photov. Solar Energy Conf. (2012) 2179 - 2191.

Curriculum Vitae

Boris Misic, geboren am 11.11.1980 in Stuttgart

Bildungsweg	
1987-1991	Ostheimer Grundschule, Stuttgart
1991-2000	Zeppelin-Gymnasium, Stuttgart (Abiturnote: 1.8)
2002-2009	Studium der Elektrotechnik und Informationstechnik an der Universität Stuttgart (Gesamtnote: "Sehr gut")
2006	Studienarbeit am Institut für Hochspannungstechnik und Energieübertragung (Note: 1.3)
2008	Diplomarbeit bei T-Solar, Ourense (Spanien) Betreuung durch Institut für Physikalische Elektronik (Note: 1.0)
2015	Promotion an der RWTH Aachen (Note: "Sehr gut")
Beruflicher Werdegang	
2001-2002	Behindertenpfleger in der Individuellen Schwerstbehindertenassistenz (ISA) der Evangelischen Gesellschaft Stuttgart e.V.
2002	Industriepraktikum bei Robert Bosch GmbH Feuerbach
2008	Industriepraktikum bei Robert Bosch GmbH Schwieberdingen
2009-2012	Manz AG, Reutlingen (Doktorand)
2013-2014	IEK-5 Forschungszentrum Jülich (Doktorand)
2014	IEK-5 Forschungszentrum Jülich (Post-Doc)
seit 2015	Robert Bosch GmbH Leonberg (Forschung & Entwicklung)
Auszeichnungen	
2000	Scheffelpreis der literarischen Gesellschaft Karlsruhe
2009	Otto F. Scharr-Preis für Energietechnik
2015	Titelbild der Physica Status Solidi (a) Ausgabe März 2015 mit *"Shunt mitigation in ZnO:Al/i-ZnO/CdS/Cu(In,Ga)Se_2 solar modules by the i-ZnO/CdS buffer combination"*

Appendix A

LU Factorisation

The Gaussian elimination method is a common method for solving linear systems of equations. Its computational realisation is often done as LU factorisation [99–101] which I apply in the calculation of my NSM, too. In this chapter I briefly introduce its basic principle for a general example of a matrix $M \in \mathbb{R}^{3x3}$. The linear system of equations

$$\begin{aligned} \begin{bmatrix} M \end{bmatrix} \quad \begin{bmatrix} x \end{bmatrix} \quad &= \begin{bmatrix} z \end{bmatrix} \\ \begin{bmatrix} m_{11} & m_{12} & m_{13} \\ m_{21} & m_{22} & m_{23} \\ m_{31} & m_{32} & m_{33} \end{bmatrix} \quad \begin{bmatrix} x_1 \\ x_2 \\ x_3 \end{bmatrix} \quad &= \begin{bmatrix} z_1 \\ z_2 \\ z_3 \end{bmatrix} \end{aligned} \tag{A.1}$$

that results from my NSM (see Chapter 5.1) can be solved by multiplying Eq. (A.1) with two elimination matrices $[L_1]$ and $[L_2]$. The first multiplication is given by

$$\begin{bmatrix} L_1 \end{bmatrix} \begin{bmatrix} M \end{bmatrix} \begin{bmatrix} x \end{bmatrix} = \begin{bmatrix} z^{(2)} \end{bmatrix} \tag{A.2}$$

which is in detail

$$\begin{aligned} \begin{bmatrix} 1 & 0 & 0 \\ -l_{21}^{(1)} & 1 & 0 \\ -l_{31}^{(1)} & 0 & 1 \end{bmatrix} \begin{bmatrix} m_{11} & m_{12} & m_{13} \\ m_{21} & m_{22} & m_{23} \\ m_{31} & m_{32} & m_{33} \end{bmatrix} \quad \begin{bmatrix} x_1 \\ x_2 \\ x_3 \end{bmatrix} \quad &= \begin{bmatrix} z_1^{(1)} \\ z_2^{(2)} \\ z_3^{(2)} \end{bmatrix} \\ \begin{bmatrix} m_{11}^{1} & m_{12}^{(1)} & m_{13}^{(1)} \\ 0 & m_{22}^{(2)} & m_{23}^{(2)} \\ 0 & m_{32}^{(2)} & m_{33}^{(2)} \end{bmatrix} \quad \begin{bmatrix} x_1 \\ x_2 \\ x_3 \end{bmatrix} \quad &= \begin{bmatrix} z_1^{(1)} \\ z_2^{(2)} \\ z_3^{(2)} \end{bmatrix} \\ \begin{bmatrix} M_2 \end{bmatrix} \quad \begin{bmatrix} x \end{bmatrix} \quad &= \begin{bmatrix} z^{(2)} \end{bmatrix} \end{aligned} \tag{A.3}$$

and yields a matrix $[M_2]$ where the first column entries in the second and third row are eliminated. In order to additionally remove the second column entry in the third row, the second multiplication is performed by

$$\begin{bmatrix} L_2 \end{bmatrix} \begin{bmatrix} M_2 \end{bmatrix} \begin{bmatrix} x \end{bmatrix} = \begin{bmatrix} z^{(3)} \end{bmatrix} \tag{A.4}$$

which is in detail

$$\begin{bmatrix} 1 & 0 & 0 \\ 0 & 1 & 0 \\ 0 & -l_{32}^{(2)} & 1 \end{bmatrix} \begin{bmatrix} m_{11}^{1} & m_{12}^{(1)} & m_{13}^{(1)} \\ 0 & m_{22}^{(2)} & m_{23}^{(2)} \\ 0 & m_{32}^{(2)} & m_{33}^{(2)} \end{bmatrix} \begin{bmatrix} x_1 \\ x_2 \\ x_3 \end{bmatrix} = \begin{bmatrix} z_1^{(1)} \\ z_2^{(2)} \\ z_3^{(3)} \end{bmatrix}$$

$$\begin{bmatrix} m_{11}^{1} & m_{12}^{(1)} & m_{13}^{(1)} \\ 0 & m_{22}^{(2)} & m_{23}^{(2)} \\ 0 & 0 & m_{33}^{(3)} \end{bmatrix} \begin{bmatrix} x_1 \\ x_2 \\ x_3 \end{bmatrix} = \begin{bmatrix} z_1^{(1)} \\ z_2^{(2)} \\ z_3^{(3)} \end{bmatrix}$$

$$\Big[M_3\Big] \quad \Big[x\Big] \quad = \Big[z^{(3)}\Big] \tag{A.5}$$

The matrices $[L_1]$ and $[L_2]$ are called elimination matrices and their correspondent elimination factors $l_{i,j}$ are given by

$$l_{i,j} = \frac{m_{i,j}}{m_{j,j}} \tag{A.6}$$

In Eq. (A.5) one obtains an upper triangular matrix $[U]$ by

$$\Big[M_3\Big] = \begin{bmatrix} m_{11}^{1} & m_{12}^{(1)} & m_{13}^{(1)} \\ 0 & m_{22}^{(2)} & m_{23}^{(2)} \\ 0 & 0 & m_{33}^{(3)} \end{bmatrix} = \Big[U\Big] = \begin{bmatrix} u_{11} & u_{12} & u_{13} \\ 0 & u_{22} & u_{23} \\ 0 & 0 & u_{33} \end{bmatrix} \tag{A.7}$$

and Eq. A.7 can be solved by

$$\begin{aligned} x_3 = & \quad \tfrac{1}{u_{33}} z_3^{(3)} \\ x_2 = & \quad \tfrac{1}{u_{22}} \Big[z_2^{(2)} - u_{23} x_3 \Big] \\ x_1 = & \quad \tfrac{1}{u_{11}} \Big[z_1^{(1)} - u_{13} x_3 - u_{12} x_2 \Big] \end{aligned} \tag{A.8}$$

which can be generally written for a matrix $M \in \mathbb{R}^{nxn}$ as

$$x_i = \begin{cases} \tfrac{1}{u_{i,i}} \cdot \left[z_i^{(i)} - \sum_{i}^{n-1} u_{i,i+1} \cdot x_{i+1} \right] & , \text{ for } i < n \\ \\ \tfrac{1}{u_{i,i}} \cdot z_i^{(i)} & , \text{ for } i = n \end{cases} \tag{A.9}$$

The two multiplications in Eq. A.2 and Eq. A.4 can be combined by

$$\Big[L_1\Big] \Big[L_2\Big] \Big[M\Big] = \Big[U\Big] \tag{A.10}$$

Bringing both elimination matrices to the right side with

$$\Big[L\Big] = \Big[L_1^{-1}\Big] \Big[L_2^{-1}\Big] \tag{A.11}$$

yields

$$\Big[M\Big] = \Big[L\Big]\,\Big[U\Big] \tag{A.12}$$

which gives this method its name: LU factorization. If a LU-decomposition of $[M]$ can be found, then it is enough to solve the following two systems of equations

$$\Big[L\Big]\,\Big[y\Big] = \Big[z\Big] \tag{A.13}$$

$$\Big[U\Big]\,\Big[x\Big] = \Big[y\Big] \tag{A.14}$$

in order to calculate the vector $[x]$. Eq. (A.13) is solved in forward substitution and Eq. (A.14) in backward substitution. This finally yields the vector $[x]$ which contains the currents I_k^i of my NSM. The matrix $[y]$ is only introduced to conveniently solve for $[x]$.

There would be much more to say about this method like the restriction of non zero pivots a_{kk}^k and the application of partial pivoting, for example. But any further discussion would go far beyond the scope of this thesis. For more details see [99–101].

Bibliography

[1] D. M. Chapin, C. S. Fuller, and G. L. Pearson, J. Appl. Phys. 25(5), page 676–677, 1954.

[2] A. Luque and S. Hegedus, *Handbook of Photovoltaic Science and Engineering.* Wiley, 2nd edition, 2011.

[3] P. Jackson, D. Hariskos, R. Wuerz, W. Wischmann, and M. Powalla, Physica Status Solidi (RRL) 8(3), page 219–222, 2014.

[4] M. A. Green, K. Emery, Y. Hishikawa, W. Warta, and E. D. Dunlop, Prog. in Photovoltaics 22(7), page 701–710, 2014.

[5] A. Chirilă, P. Reinhard, F. Pianezzi, P. Bloesch, A. R. Uhl, C. Fella, L. Kranz, D. Keller, C. Gretener, H. Hagendorfer, D. Jaeger, R. Erni, S. Nishiwaki, S. Buecheler, and A. N. Tiwari, Nature Materials 12(12), page 1107–1111, 2013.

[6] B. E. Pieters, IEEE J. Photovolt. 1(1), page 93–98, 2011.

[7] T.P. Seward and T. Vascott, *High Temperature Melt Properties Database for Process Modeling.* Wiley, Hoboken New Jersey, 2006.

[8] K. Orgassa, H. W. Schock, and J. H. Werner, Thin Solid Films 431-432, page 387–391, 2003.

[9] J. Malmström, S. Schleussner, and L. Stolt, Appl. Phys. Lett. 85(13), page 2634, 2004.

[10] M. Gloeckler and J. R. Sites, J. Phys. Chem. Solids 66, page 1891–1894, 2005.

[11] R. Scheer and H. W. Schock, *Chalcogenide Photovoltaics.* WILEY-VCH, Weinheim, 2012.

[12] W. N. Shafarman, R. Klenk, and B. E. McCandless, J. Appl. Phys. 79(9), page 7324–7328, 1996.

[13] S. H. Wei and A. Zunger, J. Appl. Phys. 78(6), page 3846–3856, 1995.

[14] O. Lundberg, M. Edoff, and L. Stolt, Thin Solid Films 480, page 520–525, 2005.

[15] O. Zelaya-Angel, J. J. Alvarado-Gil, R. Lozada-Morales, H. Vargas, and A. F. Silva, Appl. Phys. Lett. 64(3), 1994.

[16] M. Kroemer, Procedings of the IEEE 51(12), page 1782–1783, 1963.

[17] J. Tersoff, Phys. Rev. B 30(8), page 4874–4877, 1984.

[18] P. Bhattacharya, *Semiconductor optoelectronic devices.* Prentice Hall, 1994.

[19] U. Rau and H. W. Schock, Appl. Phys. A(69), page 131–147, 1999.

[20] H. W. Schock and R. Noufi, Prog. in Photovoltaics 8(1), page 151–160, 2000.

[21] U. Rau and M. Schmidt, Thin Solid Films 387(1-2), page 141–146, 2001.

[22] A. Pimentel, E. Fortunato, A. Gonçalves, A. Marques, H. Águas, L. Pereira, I. Ferreira, and R. Martins, Thin Solid Films 487(1–2), page 212–215, 2005.

[23] K. Ottosson, *The role of i-ZnO for shunt prevention in Cu(In,Ga)Se2-based solar cells.* Master's thesis, University of Uppsala, 2006.

[24] S. Ishizuka, K. Sakurai, A. Yamada, K. Matsubara, P. Fons, K. Iwata, S. Nakamura, Y. Kimurab, T. Baba, H. Nakanishi, T. Kojima, and S. Niki, Sol. Energy Mater. Sol. Cells 87(1-4), page 541–548, 2005.

[25] J. Kessler, O. Lundberg, J., Wennerberg, and L. Stolt, Proc. of the 16th PVSEC Glasgow, page 775–778, 2000.

[26] M. D. Kempe, K. M. Terwilliger, and D. Tarrant, 33rd IEEE Photovoltaic Specialists Conference, page 1–6, 2008.

[27] F.J. Pern, Angew. Makromol. Chem. 252(1), page 195–216, 1997.

[28] G. J. Jorgensen, K. M. Terwilliger, J. A. DelCueto, S. H. Glick, M. D. Kempe, J. W. Pankow, F. J. Pern, and T. J. McMahon, Sol. Energy Mater. Sol. Cells 90(16), page 2739–2775, 2006.

[29] K. Ishaque, Z. Salam, and H. Taheri, Sol. Energy Mater. Sol. Cells 95(2), page 586–594, 2011.

[30] M. Powalla, D. Hariskos, E. Lotter, M. Oertel, J. Springer, D. Stellbogen, B. Dimmler, and R. Schäffler, Thin Solid Films 431–432(0), page 523–533, 2003.

[31] M. Powalla and B. Dimmler, Thin Solid Films 361–362(0), page 540–546, 2000.

[32] M. Powalla and B. Dimmler, Sol. Energy Mater. Sol. Cells 75, page 27–34, 2003.

[33] M. Powalla, M. Cemernjak, J. Eberhardt, F. Kessler, R. Kniese, H.D. Mohring, and B. Dimmler, Sol. Energy Mater. and Sol. Cells 90(18-19), page 3158–3164, 2006.

[34] P. Huang, C. Huang, M. Lin, C. Chou, C. Hsu, and C. Kuo, Int. J. of Photoenergy, page 1–8, 2013.

[35] R. Sundaramoorthy, F. J. Pern, A. L. Lazcano, S. Glynn, C. DeHart, B. To, J. Pankow, and T. Gessert, IEEE PVSEC 361–362, page 2506–2511, 2000.

[36] F. Erfurth, Z. Jehl, M. Bouttemy, N. Dahan, P. Tran-Van, I. Gerard, A. Etcheberry, J. Greffet, M. Powalla, G. Voorwinden, D. Lincot, J. F. Guillemoles, and N. Naghavi, Appl. Surf. Sci. 258(7), page 3058–3061, 2012.

[37] G. Gordillo, F. Mesa, and C. Calderon, Braz. J. of Physics 36, page 982–985, 2006.

[38] S. A. Pethe, E. Takahashi, A. Kaul, and N. G. Dhere, Sol. Energy Mater. Sol. Cells 100, page 1–5, 2012.

[39] J. H. Scofield, A. Duda, D. Albin, B. L. Ballard, and P. K. Predecki, Thin Solid Films 260(1), page 26–31, 1995.

[40] H. E. Bennett and A. H. Guenther, *Laser Induced Damage in Optical Material.* ASTM International, 1985.

[41] C.Linke, H. Köstenbauer, E. Franzke, J. Winkler, L. Klaiber, F. Carrasco, and C. Neugebauer, Proc. of the 26th PVSEC Hamburg, page 2971–2973, 2011.

[42] J. Bovatsek, A. Tamhankar, R. S. Patel, N. M. Bulgakova, and J. Bonse, Thin Solid Films 518, page 2897–2904, 2010.

[43] J. E. Shelby, *Introduction to Glass Science and Technology.* The Royal Society of Cambridge, 2^{nd} edition, 2005.

[44] S. Kundu and L. C. Olsen, Thin Solid Films 471(1–2), page 298–303, 2005.

[45] J. Haarstrich, H. Metzner, M. Oertel, C. Ronning, T. Rissom, C. A. Kaufmann, T. Unold, H. W. Schock, J. Windeln, W. Mannstadt, and E. Rudigier-Voigt, Sol. Energy Mater. Sol. Cells 95(3), page 1028–1030, 2011.

[46] M. Contreras, B. Egaas, K. Ramanathan, J. Hiltner, A. Swartzlander, F. Hasoon, and R. Noufi, Prog. Photovolt: Res. Appl. 7, page 311–316, 1999.

[47] R. E. Smallwood, *Refractory metals and their applications.* ASTM International, 1984.

[48] W. K. Metzger, I. L. Repins, M. Ropero, P. Dippo, M. Contreras, R. Noufi, and D. Levi, Thin Solid Films 517(7), page 2360–2364, 2009.

[49] M. Froment and D. Lincot, Electrochim. Acta 40(10), page 1293–1303, 1995.

[50] P. C. Rieke and S. B. Bentjen, Chem. Mater. 5, page 43–53, 1993.

[51] M. Weber, J. Krauser, A. Weidinger, J. Bruns, C. H. Fischer, W. Bohne, J. Röhrich, and R. Scheer, J. Electrochem. Soc. 146(6), page 2131–2138, 1999.

[52] A. Kylner, A. Rockett, and L. Stolt, Solid State Phenomena 51-52, page 553–540, 1996.

[53] C. Heske, D. Eich, R. Fink, E. Umbach, T. Buuren, C. Bostedt, L. J. Terminello, S. Kakar, M. M. Grush, T. A Callcott, F. J. Himpsel, D. L. Ederer, R. C. C. Perera, W. Riedl, and F. Karg, Appl. Phys. Lett. 74(10), page 1451–1453, 1999.

[54] B. N. Colding, Ann. CIRP, page 35–40, 1991.

[55] W. F. Hastings and P. L. B. Oxley, Ann. CIRP, page 33–38, 1976.

[56] H. Opitz and W. König, Proc. of the 8th Int. MTDR Conference, page 173–190, 1967.

[57] J. T. Burwell and C. D. Strang, J. Appl. Phys. 23(1), page 18–28, 1952.

[58] L. Lasa and J. M. Rodriguez-Ibabe, Scripta Materialia 46(6), page 477–481, 2002.

[59] M. Nouari, G. List, F. Girot, and D. Coupard, Wear 255(7–12), page 1359–1368, 2003.

[60] J. A. Arsecularatne, L. C. Zhang, and C. Montross, Int. J. Mach. Tools Manuf. 46, page 482–491, 2006.

[61] B. T. Chao and K. J. Trigger, Trans. ASME J. Eng. Ind. 81, page 139–151, 1959.

[62] M. C. Shaw, Proc. of the seminar on metal cutting, OECD, Paris, 1966.

[63] T. Kurimoto and G. Barrow, Ann. CIRP, page 19–25, 1982.

[64] W. Grzesik and P. Nieslony, Int. J. Mach. Tools Manuf. 44, page 889–901, 2004.

[65] P. L. B. Oxley, *Mechanics of Machining: An analytical approach to assessing machinability.* Ellis Horwood Limited, 1989.

[66] E. M. Trent and P. K. Wright, *Metal Cutting.* Butter-Heinemann, 4^{th} edition, 2000.

[67] N. Narutaki and Y. Yamane, Bull. JSPE 10(3), page 95–100, 1976.

[68] N. H. Cook and P. N. Nyak, Trans. ASME Ser. B 88, page 93–100, 1966.

[69] T. N. Loladze, Proc. of the 8th Int. MTDR Conference, page 821–843, 1967.

[70] W. F. Hastings, P. Mathew, and P. L. B. Oxley, Proc. of the 20th Int. MTDR Conference, page 313–320, 1979.

[71] P. Mathew, Int. J. Mach. Tools Manuf. 29(4), page 481–497, 1989.

[72] H. Takeyama and R. Murata, Trans. ASME J. Eng. Ind. 85, page 33–38, 1963.

[73] E. Lassner, *Tungsten: properties, chemistry, technology of the element, alloys, and chemical compounds.* Kluwer Academic, 1998.

[74] P. Jackson, R. Würz, U. Rau, J. Mattheis, M. Kurth, T. Schlötzer, G. Bilger, and J. H. Werner, Prog. Photovoltaics 15(6), page 507–519, 2007.

[75] M. Ruckh, D. Hariskos, U. Ruhle, H. W. Schock, R. Menner, and B. Dimmler, Procedings of the 25th IEEE Photovoltaic Specialist Conference, page 825, 1996.

[76] J. N. Duenow, T. A. Gessert, D. M. Wood, B. Egaas, R. Noufi, and T. J. Coutts, MRS Proceedings 1012, page 1012–Y01, 2007.

[77] S. O. Kucheyev, J. E. Bradby, J. S. Williams, C. Jagadish, and M. V. Swain, Appl. Phys. Lett. 80(6), page 956–958, 2002.

[78] T. M. H. Tran, B. E. Pieters, M. Schneemann, J. P. Theisen, R. Schäffler, A. Gerber, and U. Rau, Proc. of the 27th PVSEC Hamburg, page 2372–2376, 2012.

[79] U. Rau, D. Abou-Ras, and T. Kirchartz, *Advanced Characterization Techniques for Thin Film Solar Cells.* Wiley, 2011.

[80] U. Rau, Phys. Rev. B 76, page 085303, 2007.

[81] T. Kirchartz A. Helbig, R. Schaeffler, J. H. Werner, and U. Rau, Sol. Energy Mater. Sol. Cells 94, page 979–984, 2010.

[82] A. Okamoto, T. Minemoto, and H. Takakura, JJAP 50, page 04DP10–1, 2011.

[83] T. M. H. Tran, B. E. Pieters, C. Ulbrich, A. Gerber, T. Kirchartz, and U. Rau, Thin Solid Films 535, page 307–310, 2013.

[84] J. C. Mullikin, L. J. van Vliet, H. Netten, F. R. Boddeke, G. van der Feltz, and I. T. Young, Proc. SPIE 2173, page 73–84, 1994.

[85] M. Kasemann, W. Kwapil, M. C. Schubert, H. Habenicht, B. Walter, M. The, S. Kontermann, S. Rein, O. Breitenstein, J. Bauer, A. Lotnyk, B. Michl, H. Nagel, A. Schutt, J. Carstensen, H. Foll, T. Trupke, Y. Augarten, H. Kampwerth, R. A. Bardos, S. Pingel, J. Berghold, W. Warta, and S. W. Glunz, 33rd IEEE Photovoltaic Specialists Conference, page 1–7, 2008.

[86] O. Breitenstein, *Lock-in Thermography.* Springer, Heidelberg, 2nd edition, 2010.

[87] M. Planck, Entropie 144(190), page 164, 1914.

[88] M. Siegloch, *Failure Analysis of Thin Film Solar Modules using Lock-in Thermography.* PhD thesis, RWHT Aachen, 2014.

[89] J. C. Krapez, Proc. QIRT, page 148–153, 1998.

[90] A. Zekry and A. Al-Mazroo, IEEE Trans. Electron Devices 43(5), page 691–700, 1996.

[91] V. G. Karpov, A. D. Compaan, and D. Shvydka, Appl. Phys. Lett. 80(22), page 4256–4258, 2002.

[92] G. T. Koishiyev and J. R. Sites, Sol. Energy Mater. Sol. Cells 93(3), page 350–354, 2009.

[93] A. Wagner, *Photovoltaik Engineering.* Springer, Heidelberg, 2nd edition, 2006.

[94] W. J. McCalla and W. G. Howard Jr., IEEE JSSCS SC-6, page 14–19, 1971.

[95] C. G. Broyden, Math. Comp 19(92), page 577–593, 1965.

[96] C. W. Ho, A. E. Ruehli, and P. A. Brennan, IEEE TCAS CAS-22, page 504–509, 1975.

[97] L. M. Wedepohl and L. Jackson, ESEJ 11(3), page 84–92, 2002.

[98] K. M. Chandy, U. Herzog, and L. Woo, IBM J. Res. Dev. 19, page 36–42, 1975.

[99] W. Dahmen and A. Reusken, *Numerik für Ingenieure und Naturwissenschaftler.* Springer, Heidelberg, 2006.

[100] A. Quarteroni, R. Sacco, and F. Saleri, *Numerical Mathematics.* Springer, Heidelberg, 2nd edition, 2006.

[101] M. Hanke-Bourgeois, *Grundlagen der numerischen Mathematik und des wissenschaftlichen Rechnens.* Teubner, Wiesbaden, 2nd edition, 2006.

[102] L. Phillips, *Gnuplot Cookbook.* Packt Publishing, 2012.

[103] B. Galiana, C. Algora, I. Rey-Stolle, and I.G. Vara, IEEE Trans. Electron Devices 52(12), page 2552–2558, 2005.

[104] P. Ordejón, D. A. Drabold, R. M. Martin, and M. P. Grumbach, Phys. Rev. B 51, page 1456–1476, 1995.

[105] B. Misic, K. Orgassa, U. Schweitzer, J. Müller, C. Kuhn, D. Manz, and U. Rau, Proc. of the 25th PVSEC Valencia, page 3670–3675, 2010.

[106] P. MacNeice, K. M. Olson, C. Mobarry, R. Fainchtein, and C. Packer, Comput. Phys. Commun. 126(3), page 330–354, 2000.

[107] T.E. Oliphant, Comp. Sci. Eng. 9(3), page 10–20, 2007.

[108] F.E. Allen, IBM J. Res. Dev. 25(5), page 535–548, 1981.

[109] B. W. Kernigham and D. M. Ritchie, *The C Programming Language.* Prentice Hall, 2nd edition, 1988.

[110] E. Anderson, Z. Bai, J. Dongarra, A. Greenbaum, A. McKenney, J. Du Croz, S. Hammerling, J. Demmel, C. Bischof, and D. Sorensen, Proc. of the 1990 ACM/IEEE Conference on Supercomputing, page 2–11, 1990.

[111] T. A. Davis, ACM Trans. Math. Softw. 30(2), page 196–199, 2004.

[112] X. S. Li, ACM Trans. Math. Softw. 31(3), page 302–325, 2005.

[113] T. Lanz, M. Bonmarin, M. Stuckelberger, C. Schlumpf, C. Ballif, and B. Ruhstaller, IEEE J. Quantum Electron. 19(5), page 1–8, 2013.

[114] S. Dongaonkar and M.A. Alam, IEEE J. Photovolt. 4(1), page 324–332, 2014.

[115] H. Nesswetter, P. Lugli, A.W. Bett, and C.G. Zimmermann, IEEE J. Photovolt. 3(1), page 353–358, 2013.

[116] J.M.M. Pérez and J. Pascau, *Image Processing with ImageJ*. Packt Publishing, 2013.

[117] Caroline A Schneider, Wayne S Rasband, Kevin W Eliceiri, Johannes Schindelin, Ignacio Arganda-Carreras, Erwin Frise, Verena Kaynig, Mark Longair, Tobias Pietzsch, Stephan Preibisch, et al., Nature Methods 9(7), 2012.

[118] T. M. H. Tran, *Quantitative analysis of spatially resolved electroluminescence of Cu(In,Ga)Se_2 and a-Si:H thin film solar cells and modules*. PhD thesis, RWTH Aachen, 2014.

[119] W.F. Gale and T.C. Totemeier, *Smithells metals reference book*. Elsevier Butterworth-Heinemann, Massachusetts, 8$^{\text{th}}$ edition, 2003.

[120] T.P. Seward and T. Vascott, *High temperature glass melt property database for process modeling*. Wiley, 2005.

[121] T. M. H. Tran, B. E. Pieters, M. Siegloch, A. Gerber, C. Ulbrich, T. Kirchartz, R. Schäffler, and U. Rau, Proceedings of the 26th EUPVSEC Hamburg, page 2981–1085, 2011.

[122] P-O Westin, Uwe Zimmermann, Marta Ruth, and Marika Edoff, Sol. Energy Mat. Sol. Cells 95(4), page 1062–1068, 2011.

[123] A. McEvoy, L. Castañer, and T. Markvart, *Solar cells: materials, manufacture and operation*. Academic Press, 2$^{\text{nd}}$ edition, 2012.

[124] M. Powalla and B. Dimmler, Thin Solid Films 387, page 251–256, 2001.

[125] C.K. Gupta, *Extractive Metallurgy of Molybdenum*. Taylor & Francis, FL, 1992.

[126] JL McClure and A Cezairliyan, Int. J. Thermophys. 11(4), page 731–737, 1990.

[127] M Pirani and H Alterthum, Z. Elektrochem. 29, page 5–8, 1923.

[128] A. G. Worthing, Phys. Rev. 25, page 846–857, 1925.

[129] RE Bedford, G Bonnier, H Maas, and F Pavese, Metrologia 33(2), page 133, 1996.

[130] C Zwikker, Physica 7, page 71, 1927.

[131] M. Gritsch, C. Brunner, K. Piplits, H. Hutter, P. Wilhartitz, A. Schintlmeister, and H. P. Martinz, Fresenius' J. Anal. Chem. 365(1-3), page 188–194, 1999.

[132] N. Birks, G.H. Meier, and F.S. Pettit, *Introduction to the High Temperature Oxidation of Metals*. Cambridge University Press, 2006.

[133] A. G. Worthing, Phys. Rev. 28(1), page 190, 1926.

[134] U. Seydel and W. Fucke, *Die Bestimmung thermophysikalischer Daten hochschmelzender Metalle mit schnellen Pulsaufheizexperimenten*. Mannhold, Düsseldorf, 1980.

[135] J. M. Ziman, Philosophical Magazine 6(68), page 1013–1034, 1961.

[136] J.M. Ziman, Advances in Physics 13(49), page 89–138, 1964.

[137] T. E. Faber and J. M. Ziman, Philosophical Magazine 11(109), page 153–173, 1965.

[138] J. M. Ziman, *The Physics of Metals: Volume 1, Electrons*. Univ. Press, Cambridge, 1969.

[139] T. E. Faber, *Introduction to the theory of liquid metals*. Univ. Pr., Cambridge, 1972.

[140] J. M. Gere, *Mechanics of materials*. Thomson Brooks Cole, Belmont California, 6$^{\text{th}}$ edition, 2004.

[141] C. H. Jenkins and S.K. Khanna, *Mechanics of materials: a modern integration of mechanics and materials in structural design*. Elsevier Acad. Press, Amsterdam, 2005.

[142] W. F. Riley, L. D. Sturges, and D. H. Morris, *Mechanics of materials*. Wiley, Hoboken New Jersey, 6$^{\text{th}}$ edition, 2007.

[143] R. Bürgel, *Lehr- und Übungsbuch Festigkeitslehre*. Vieweg, Wiesbaden, 2005.

[144] N. E. Dowling, *Mechanical behavior of materials: engineering methods for deformation, fracture, and fatigue*. Pearson Prentice Hall, Upper Saddle River New Jersey, 3$^{\text{rd}}$ edition, 2007.

[145] R. C. Hibbeler, *Mechanics of materials*. Pearson Prentice Hall, Upper Saddle River New Jersey, 6$^{\text{th}}$ edition, 2005.

[146] A. H. Cottrell and B. A. Bilby, Proc. Phys. Soc. A 62(1), page 49–62, 1949.

[147] Plansee Composite Materials GmbH. *Technical documentation molybdenum*, 2012.

[148] Saint-Gobain, *Glazing Manual*. `www.saint-gobain.com`, Technical report, 2012.

[149] Valley Design corp, *Technical documentation*. `www.valleydesign.com`, Technical report, 2012.

Danksagung

Ich habe drei Jahre dieser Dissertation in der Industrie bei der Firma Manz AG verbracht, bevor ich sie am IEK-5 am Forschungszentrum Jülich abgeschlossen habe. Während der Zeit meiner Dissertation habe ich von vielen Menschen Unterstützung und Wertschätzung erhalten, wofür ich mich an dieser Stelle bedanken möchte.

Danke an meine beiden Lehrer und meinen Betreuer

Ich möchte mich bei Professor Dr. Uwe Rau bedanken, der mir sein Vertrauen geschenkt hat und mir ermöglicht hat, diese Arbeit anzufertigen

Ebenso möchte ich mich bei meinem Betreuer Dr. Bart Pieters für die gewissenhafte Betreuung bedanken.

Letztlich danke ich Prof. Dr. Jürgen H. Werner, der mit seinen Vorlesungen den Weg für diese Arbeit geebnet hat.

Danke an die vielen ehemaligen Kollegen

Ich möchte mich bei Ulrich Schweitzer bedanken, der mit seiner Arbeit den Grundstein für meine Programmierung gelegt hat.

Genauso möchte ich mich bei Andreas Kümmerer, Henning Kästner, Reiner Modlmeir, Jean-Patrick Theisen und Francesco Carrasco bedanken, mit denen ich in der Zeit bei der Manz AG Tag für Tag zusammen gearbeitet habe. Ihr wart wunderbare Wegbegleiter und es war mir eine Freude, Euch an meiner Seite gehabt zu haben.

Mulţumesc Ana

Te pup şi te iubesc mult, mult, mult!

Hvala mojim dragim roditeljima

Dragi moji roditelji, ja vama sve zahvaljujem.

Hvala za vaše strpljenje i za vašu ljubav.

Ja sam vaš Boki, i ja vas volim.